U.S. Department of Transportation
Federal Highway Administration

PRECAST CONCRETE SEGMENTAL LINERS FOR LARGE DIAMETER ROAD TUNNELS

Laboratory Testing

FHWA-HIF-24-003
December 2023

Technical Report Documentation Page

1. Report No. FHWA-HIF-24-003	2. Government Accession No.	3. Recipient's Catalog No.	
4. Title and Subtitle **Precast Concrete Segmental Liners for Large Diameter Road Tunnels: Laboratory Testing**		5. Report Date December 11, 2023	
		6. Performing Organization Code:	
7. Author(s) Michael A. Mooney, Haotian Zheng, Clay J. Naito, Spencer E. Quiel, Joseph Ouyang, John Wisniewski		8. Performing Organization Report No.	
9. Performing Organizations Name and Address **Colorado School of Mines** 1500 Illinois St Golden, CO 80401 **Lehigh University** 27 Memorial Dr W Bethlehem, PA 18015 **WSP USA, Inc.** One East Pratt Street, Suite 300 Baltimore, MD 21202		10. Work Unit No.	
		11. Contract or Grant No. DTFH6114D00048	
12. Sponsoring Agency Name and Address Office of Bridges and Structures 1200 New Jersey Ave, SE Washington, DC 20590		13. Type of Report and Period Final Report 09, 2020 – 12, 2023	
		14. Sponsoring Code DOT/FHWA/HIF	
15. Supplementary Notes Cover photo: SR 99 Tunnel, Seattle, Washington. Photo: John Wisniewski.			
16. Abstract An experimental program was undertaken to examine thrust jack load, joint rotation stiffness and chloride ingress under pressure in large diameter steel fiber reinforced concrete (SFRC) and hybrid SFRC + steel rebar reinforced liner segments. Thrust jack load testing on 450 mm thick segments showed that (a) radial bursting stress governs SFRC segment failure; (b) maximum radial bursting stress occurs at a distance of 0.4-0.5 times the segment thickness from the thrust jack load pad while maximum transverse bursting stress occurs at a distance of one-half the segment width from the thrust jack load pad; and (c) the perimeter rebar improves radial bursting stress capacity and shifts the governing condition to transverse bursting stress and mid-width of the segment. A comparison shows that the use of residual tensile strength in ACI 544.7R-16 simplified equations leads to considerable underestimation of ultimate radial-based thrust jack pad load capacity. Radial joint rotation testing on the 450 mm thick segments showed linear positive moment – rotation response (constant rotation stiffness) and nonlinear negative moment – rotation response (decreasing stiffness with increasing rotation). The commonly used Janssen model was found to underestimate joint rotation stiffness for most ranges of rotation and axial (hoop) forces. Janssen's model was also found to underestimate the observed large rotation moments by a factor of approximately two at all axial force levels. Pressurized salt ponding durability testing on SFRC specimens showed that higher hydraulic pressures induced higher chloride concentrations within uncracked SFRC specimens. The chloride ion diffusion coefficient under 500 kPa pressure was 8-10 times greater than that at atmospheric pressure. Cracks on the order of 0.1 mm thickness exhibited chloride concentrations at potentially harmful levels, 70 mm deep in SFRC specimens after 60 days of exposure. A design scheme for field monitoring of full ring behavior is provided and detailed in the report.			
17. Key Words Tunnel lining, steel fiber reinforced concrete, thrust jack load, radial joint bending, durability	18. Distribution Statement No restrictions.		
19. Security Classif. (of this report) UNCLASSIFIED	20. Security Classif. (of this page) UNCLASSIFIED	21. No. of Pages	22. Price

Form DOT F 1700.7(8-72) Reproduction of completed page authorized

FOREWORD

The Federal Highway Administration (FHWA) sponsors research on suggested practices for use of large diameter precast concrete segmental tunnel linings in highway tunnels. The basic technology of conventionally reinforced precast concrete segments is relatively mature for smaller diameter tunnels. It has been in use in the United States for nearly 40 years (and even longer in other parts of the world). However, recent advances in the use of steel fibers for concrete reinforcement, joint hardware and details, gasket technology, high-strength concrete mixes, and material durability encourage more studies to identify suggested practices and details for use of precast concrete segmental tunnel linings in large-diameter tunnels. The work of this research includes a literature search to identify gaps in the current body of knowledge, computer modeling and laboratory research, and engagement of industry stakeholders through a workshop to solicit input on the research plans. The work is built on prior work performed to codify design approaches for tunnel boring machine (TBM) excavated tunnels.

The objective of this research is to provide technical expertise to advance the current state of practice for the analysis, design, detailing, fabrication, installation, inspection, and maintenance of precast concrete segmental tunnel linings for large diameter highway TBM-tunnels in the United States. The research project includes several elements:

1. Conducting a literature search and developing a literature synthesis of the current state of practice (published report titled “Precast Concrete Segmental Liners for Large Diameter Road Tunnels – Literature Survey and Synthesis,” FHWA-HIF-20-035);
2. Developing computer modeling and laboratory testing workplans;
3. Soliciting input from technical organizations, designers, contractors and researchers regarding the workplans through an industry workshop (published report titled “Precast Concrete Segmental Liners for Large Diameter Road Tunnels – Workshop Report,” FHWA-HIF-20-036); and
4. Executing the research workplans and summarizing the research in a series of reports.

This document presents the results from the laboratory testing component including thrust jack loading, joint loading, and durability testing. In addition, the design of an in-situ lining instrumentation and testing plan is provided.

Notice

This document is disseminated under the sponsorship of the U.S. Department of Transportation in the interest of information exchange. The U.S. Government assumes no liability for the use of the information contained in this document.

Non-Binding Contents

Except for the statutes and regulations cited, the contents of this document do not have the force and effect of law and are not meant to bind the States or the public in any way. This document is intended only to provide information regarding existing requirements under the law or agency policies.

Quality Assurance Statement

The Federal Highway Administration (FHWA) provides high-quality information to serve Government, industry, and the public in a manner that promotes public understanding. Standards and policies are used to ensure and maximize the quality, objectivity, utility, and integrity of its information. FHWA periodically reviews quality issues and adjusts its programs and processes to ensure continuous quality improvement.

Disclaimer for Product Names and Manufacturers

The U.S. Government does not endorse products or manufacturers. Trademarks or manufacturers' names appear in this document only because they are considered essential to the objective of the document. They are included for informational purposes only and are not intended to reflect a preference, approval, or endorsement of any one product or entity.

ACRONYMS

AASHTO	American Association of State Highway and Transportation Officials
ACI	American Concrete Institute
ASTM	American Society for Testing Materials
BART	Bay Area Rapid Transportation
DAUB	Deutscher Ausschuss für unterirdisches Bauen e. V.
CBBT	Chesapeake Bay Bridge Tunnel
CBJV	Chesapeake Tunnel Joint Venture
CK	Cracked
CT	Computerized Tomography
CNN	Convolutional Neural Networks
DFOS	Distributed Fiber Optic Sensing
DIN	Deutches Institut fur Normung
EN	Eurocode
FEM	Finite Element Modeling
HD	Horizontal Displacement
IC	Ion Chromatography
LA	Los Angeles
LAN	Local Area Networks
LIDAR	Light Detection and Ranging
LRFD	Load Resistance Factor Design
LoRa	Long Range Communication
LVDT	Linear Variable Differential Transformer
NaCl	Sodium Chloride
PCTL	Precast Concrete Tunnel Lining
RC	Reinforced Concrete
RILEM	The International Union of Laboratories and Experts in Construction Materials, Systems and Structures
SFRC	Steel Fiber Reinforced Concrete
TBD	To Be Determined
TBM	Tunnel Boring Machine
UCK	Uncracked
VD	Vertical Displacement

ACKNOWLEDGMENTS

The FHWA is the source of all figures and photographs within this document unless noted otherwise.

UNIT CONVERSIONS

SI* (MODERN METRIC) CONVERSION FACTORS

APPROXIMATE CONVERSIONS TO SI UNITS

Symbol	When You Know	Multiply By	To Find	Symbol
		LENGTH		
in	inches	25.4	millimeters	mm
ft	feet	0.305	meters	m
yd	yards	0.914	meters	m
mi	miles	1.61	kilometers	km
		AREA		
in^2	square inches	645.2	square millimeters	mm^2
ft^2	square feet	0.093	square meters	m^2
yd^2	square yard	0.836	square meters	m^2
ac	acres	0.405	hectares	ha
mi^2	square miles	2.59	square kilometers	km^2
		VOLUME		
fl oz	fluid ounces	29.57	milliliters	mL
gal	gallons	3.785	liters	L
ft^3	cubic feet	0.028	cubic meters	m^3
yd^3	cubic yards	0.765	cubic meters	m^3
		NOTE: volumes greater than 1000 L shall be shown in m^3		
		MASS		
oz	ounces	28.35	grams	g
lb	pounds	0.454	kilograms	kg
T	short tons (2000 lb)	0.907	megagrams (or "metric ton")	Mg (or "t")
		TEMPERATURE (exact degrees)		
°F	Fahrenheit	5 (F-32)/9 or (F-32)/1.8	Celsius	°C
		ILLUMINATION		
fc	foot-candles	10.76	lux	lx
fl	foot-Lamberts	3.426	candela/m^2	cd/m^2
		FORCE and PRESSURE or STRESS		
lbf	poundforce	4.45	newtons	N
lbf/in^2	poundforce per square inch	6.89	kilopascals	kPa

APPROXIMATE CONVERSIONS FROM SI UNITS

Symbol	When You Know	Multiply By	To Find	Symbol
		LENGTH		
mm	millimeters	0.039	inches	in
m	meters	3.28	feet	ft
m	meters	1.09	yards	yd
km	kilometers	0.621	miles	mi
		AREA		
mm^2	square millimeters	0.0016	square inches	in^2
m^2	square meters	10.764	square feet	ft^2
m^2	square meters	1.195	square yards	yd^2
ha	hectares	2.47	acres	ac
km^2	square kilometers	0.386	square miles	mi^2
		VOLUME		
mL	milliliters	0.034	fluid ounces	fl oz
L	liters	0.264	gallons	gal
m^3	cubic meters	35.314	cubic feet	ft^3
m^3	cubic meters	1.307	cubic yards	yd^3
		MASS		
g	grams	0.035	ounces	oz
kg	kilograms	2.202	pounds	lb
Mg (or "t")	megagrams (or "metric ton")	1.103	short tons (2000 lb)	T
		TEMPERATURE (exact degrees)		
°C	Celsius	1.8C+32	Fahrenheit	°F
		ILLUMINATION		
lx	lux	0.0929	foot-candles	fc
cd/m^2	candela/m^2	0.2919	foot-Lamberts	fl
		FORCE and PRESSURE or STRESS		
N	newtons	0.225	poundforce	lbf
kPa	kilopascals	0.145	poundforce per square inch	lbf/in^2

TABLE OF CONTENTS

LIST OF FIGURES

LIST OF TABLES

1 INTRODUCTION

A recently completed literature review and synthesis (FHWA, 2020) identified three large diameter (greater than 12 m) tunnel liner topics for further experimental investigation: (a) transient thrust jack load-induced bursting stress, (b) radial joint behavior, and (c) high water pressure driven chloride ingress.

1.1. Transient Thrust Jack Loading

Tunnel boring machines (TBMs) apply thrust jack loading to the leading edge face of the most recently installed ring (Figure 1-1). This thrust jack force is needed to support face pressure, to pull the trailing gear, to overcome shield friction, and to move the TBM forward during excavation. These TBM jacking loads induce tensile stresses (also known as bursting stresses) in the precast concrete tunnel lining (PCTL) segments that might result in longitudinal cracks in the segments. This is of particular concern in large-diameter tunnels because the magnitude of thrust jack force increases with cross-sectional tunnel area and with depth (due to water pressure). The magnitude of total thrust jack force increases with diameter squared, yet the ring end/bearing area against which thrust jacks apply this load increases predominantly with diameter and with thickness, though liner thickness does not increase significantly with diameter. Accordingly, large-diameter tunnel lining typically experiences higher thrust jack pad stresses and greater tensile bursting stresses than the more common 6-7 m diameter tunnels. The transient thrust jack forces can become one of the governing load cases for large diameter segment design.

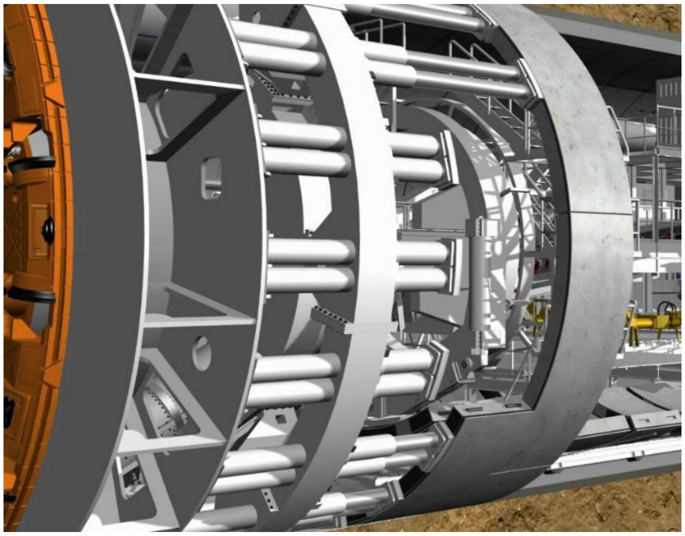

© 2015 Herrenknecht

Figure 1-1. Illustration of TBM thrust jacking loads applied to ring end/bearing area of recently installed segments.

In this study, thrust jack load testing was performed on full scale PCTL segments cast with similar dimensions and steel fiber reinforced concrete (SFRC) mix design as the Chesapeake Bay Bridge Tunnel (CBBT) project. The 12.6 m outside diameter lining is comprised of a 9 plus 1 segment plus key arrangement with 450 mm thickness. In addition to SFRC-only segments, a hybrid SFRC plus perimeter reinforcement bar arrangement was cast and tested. Segments were instrumented and loaded to failure to characterize behavior. The behavior was compared to ACI 544.7R-16[1], a common design specification used for thrust jack loading.

1.2. Radial Joint Behavior

The influence of radial (longitudinal) joint behavior is significant in segmental lining system response, e.g., for deformation, flexural stiffness, and internal load development. In addition, this influence is amplified in large diameter tunnel rings. However, the behavior of radial joints in large diameter segmental lining rings and the influence of both radial and circumferential joint behavior on the overall performance of segmental lining (e.g., stiffness, deformation, and internal moment generation) is an area of limited understanding. Most experimental joint research conducted has focused on smaller, metro-size tunnels, in a typical range of 6-7 m diameter.

Large diameter rings typically have thicker segments (typically 450-600 mm) compared to metro-size tunnels (typically 250-300 mm). Because overlying ground and building settlement limits are the same regardless of tunnel diameter, large-diameter segmental joints experience different deformations and normalized convergence than metro-size tunnels. Typically, large diameter linings have more segments (9-10 segments on average, as high as 13) compared to metro-size tunnels (5-7 segments). Large diameter segments also have lower segment slenderness ratios (arc length/thickness) than metro-size segments.

Given the noted difference between large diameter and metro-size diameter lining systems combined with the lack of research on the influence of joint behavior, there exists a gap in knowledge that can benefit from further experimental study. For example, several joint rotation behavioral models have been considered over the years; the (Janssen,1983) model is a commonly used theoretical model for small diameter tunnels. However, the applicability of Janssen's model to large diameter tunnels is unclear.

Radial joint behavior was examined experimentally by testing joint assemblies similar to those of the CBBT project. Joint assemblies were subjected to positive and negative bending moments for a variety of hoop loads. The results are compared to predictions by the Janssen model.

---

[1] Use of ACI 544.7R-16, Report on Design and Construction of Fiber-Reinforced Precast Concrete Tunnel Segments is not a Federal requirement.

1.3. Chloride Ion Ingress under Pressure

The AASHTO Load and Resistance Factor Design (LRFD) Road Tunnel Design and Construction Guide specifications[2] suggest designing for a service life for the structure of 150 years. However, little is known about the durability performance of concrete segments, including reinforcement steel corrosion, over that period of time. Further, large diameter road tunnels are bored deeper and therefore are subject to high groundwater pressures. And, many road tunnels are bored under the seabed or near coasts, and therefore are exposed to salt water. The influence of elevated pressure on chloride ion penetration is unclear. Typical test methods to examine chloride ion penetration are performed under atmospheric pressure.

Chloride ion penetration, and the resulting corrosion, through concrete containing micro-cracking could benefit from further research. Micro-cracking is typically permitted by the owner in segmental lining design. The presence of cracks could accelerate chloride ion penetration and reinforcement corrosion. However, the influence of micro-cracking is not considered in chloride ion testing and durability design calculations.

Salt ponding testing under pressure was undertaken to examine chloride ion penetration under more field-realistic conditions. SFRC cores with and without cracking were immersed in pressurized saline water (1-5 bar) for 60 days. Chloride concentration was measured and examined versus sample depth to characterize ingress. The results are compared with *fib* model code practice, which serves as a basis for the Eurocode for concrete structures.

1.4. Report Organization

This report is organized into five chapters and four appendices. Chapter 2 documents the results from thrust jack load testing including a comparison to ACI design methods. Chapter 3 presents the results from radial joint load testing including a comparison to Janssen's model. Pressurized salt pond testing is documented in Chapter 4.

In addition to experimental investigation of these three topics in the laboratory on individual segments, joints or cores, experimentally characterizing full PCTL ring response may be necessary to truly understand behavior. It could be cost prohibitive, however, to perform full-scale testing of large diameter rings in a laboratory setting. Field testing within large diameter tunnel projects provides cost-effective opportunities for full scale testing. Chapter 5 presents the design of a field monitoring and testing plan to characterize full ring behavior.

Appendices are included to provide detailed documentation of: (A) SFRC tensile strength back calculation; (B) thrust jack load test results; (C) radial joint load test results; and (D) radial joint gasket and bolt test results.

---

[2] Use of AASHTO LRFD Road Tunnel Design and Construction Guide Specifications, First Edition, 2017 is not a Federal requirement.

2 BEHAVIOR DURING TRANSIENT THRUST JACK LOADING

2.1. Introduction

TBMs impart the requisite longitudinal loading to excavate the ground through a series of main thrust jacks (Figure 2-1). The thrust jacks exert considerable bearing load on the leading edge of the most recently installed lining ring. Thrust jack load magnitudes generally increase with the excavated area of the TBM. Therefore, while the lining bearing area for thrust force increases with tunnel diameter D multipied by tunnel lining thickness t, the total TBM thrust force grows with D^2. As the diameter reaches 12 m and greater, TBM thrust force can become the governing and critical overall lining load case.

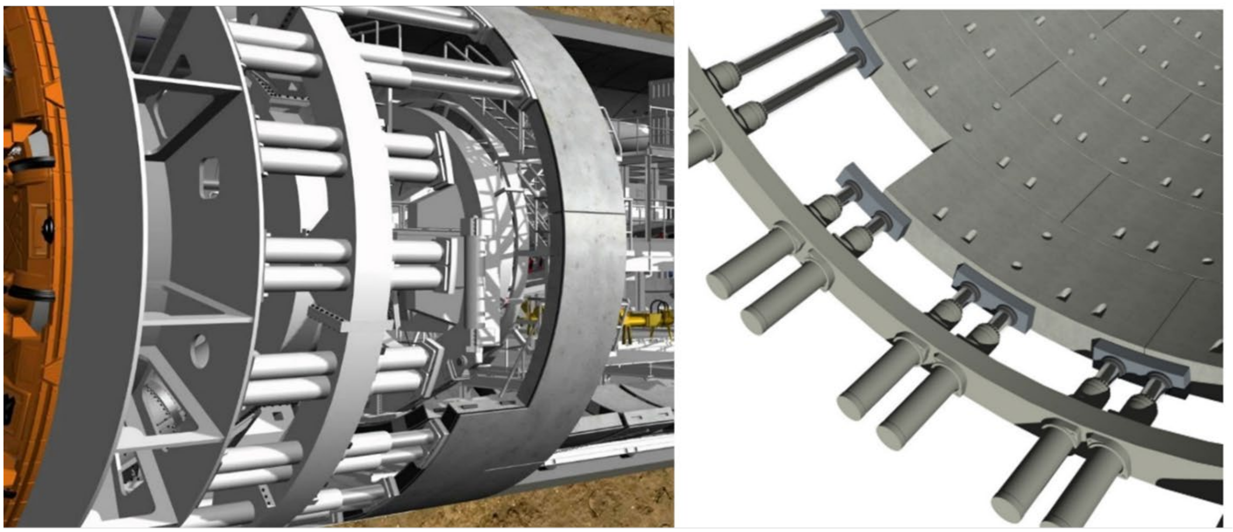

© 2015 Herrenknecht

© 2007 Groeneweg

(a)

(b)

Figure 2-1. Illustrations of TBM thrust jacking loads applied to ring end/bearing area of recently installed segments.

Thrust jack load testing was performed on four precast concrete tunnel lining (PCTL) segments. The segments were cast using the geometry and concrete mix design used for the Chesapeake Bay Bridge Tunnel (CBBT) project. The tunnel includes a 12.8 m outside diameter tunnel lining with 9 plus 1 PCTL segment arrangement (Figure 2-2). Each segment is 4.06 m long circumferentially, 2.0 m wide and 457 mm thick. The key segment is 2.03 m long circumferentially, 2.0 m wide and 457 mm thick. Two reinforcement designs were investigated, including: (a) steel fiber reinforced concrete (SFRC) and (b) hybrid SFRC plus perimeter reinforcement bar (SFRC plus RC). The segments were instrumented to measure radial and circumferential strains during testing. Surface crack widths were measured during loading.

This chapter details the test program conducted and the test results observed. The chapter summarizes current ACI thrust jack load design procedures and compares observed results with ACI predictions. Implications for modifications to the current ACI design procedures for large diameter lining segments are discussed. The SFRC segments meet the design criteria for serviceability at maximum thrust jack load, and the additional reinforcement does not improve the segment performance under thrust load.

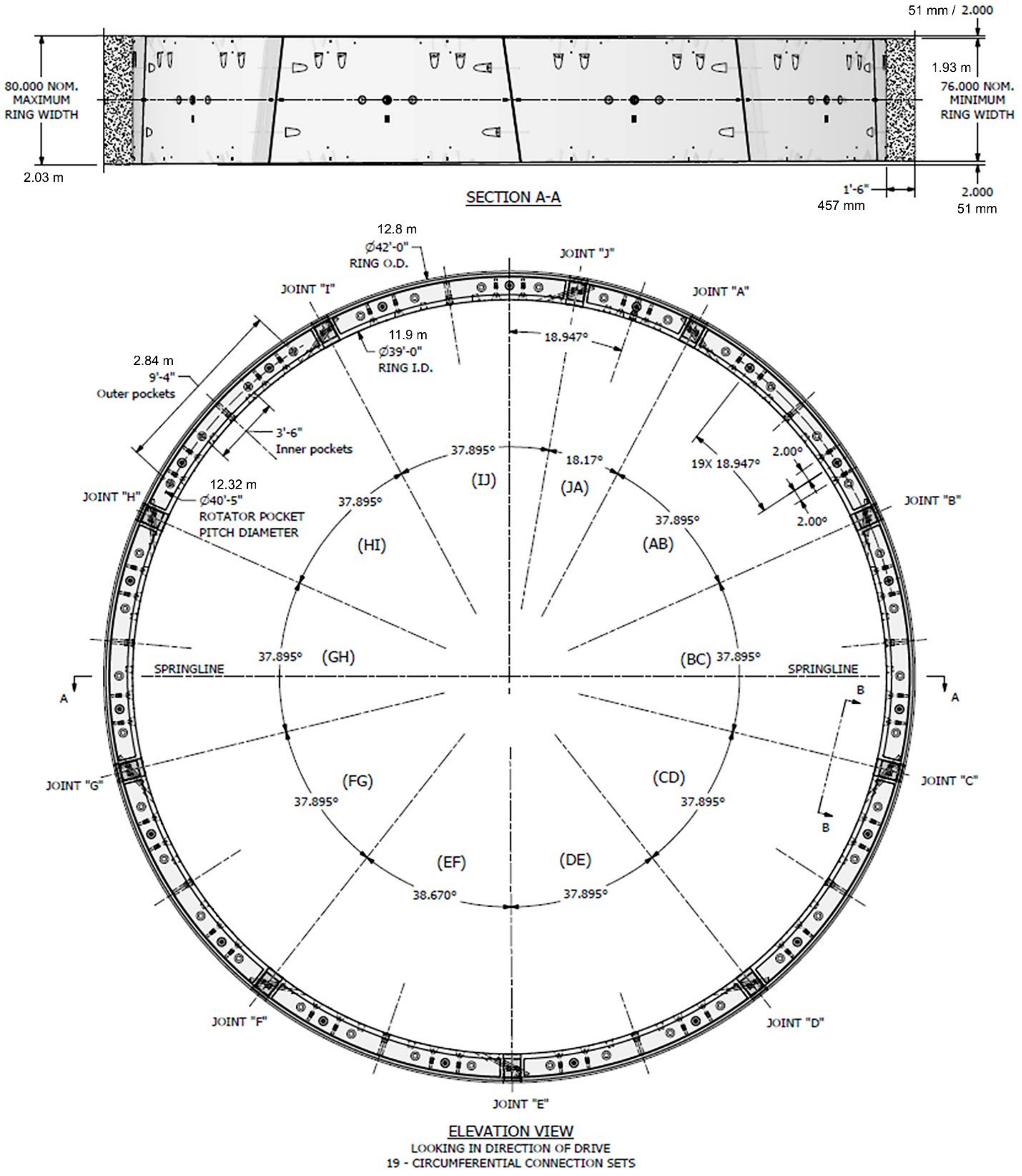

© 2018 Chesapeake Bay Bridge and Tunnel

Figure 2-2. Schematic of 12.8 m (42.0 ft) outside diameter, 457 mm (18 inches) thick tunnel lining comprised of nine full-size segments and one keystone.

2.2. Test Program

2.2.1. Segments Tested

SFRC and SFRC plus RC segments were used during testing (Figure 2-3). The SFRC mix design included a cementitious content of 445 kg/m^3 and a w/c ratio of 0.35. Multi-hook 4D steel fiber was used. The fiber content was 38.6 kg/m^3 with fiber geometry 61 mm length, 0.75 mm diameter and a fiber aspect ratio of 80. As summarized in Table 2-1, the average uncracked elastic modulus is 30.9 GPa, obtained from compressive tests on SFRC samples. The average compressive strength of the SFRC mix design determined by CSI Concrete Systems, Hudson, New Hampshire was 66 MPa, matching well with 64 MPa compressive strength determined from segment cores. The average splitting tensile strength, measured from segment cores, was 7.1 MPa and similar to the mix design splitting tensile strength of 7.3 MPa determined by CSI. Crack mouth opening displacement tests were performed on the mix design according to the BS EN 14651 procedure.

Figure 2-3. Batch of precast tunnel lining segments used for thrust jack testing. Segment dimensions are 4.06 m (13.5 ft) long, 2.0 m (6.5 ft) wide and 457 mm (18 inches) thick.

Table 2-1. SFRC material properties presented as mean plus/minus standard deviation.

Property	**CSI-measured value (MPa)**	**Measured from cores (MPa)**
Young's modulus	Not Measured	30,940 ± 1,550
Compressive strength	65.6 ± 5.2	64.3 ± 9.5
Splitting tensile strength	7.34 ± 0.17	7.10 ± 0.85
CMOD peak $f_{t,fl}$	7.12 ± 0.32	Not Applicable
CMOD 0.5 mm $f_{R,1}$	4.57 ± 0.83	Not Applicable
CMOD 1.5 mm $f_{R,2}$	6.53 ± 1.52	Not Applicable
CMOD 2.5 mm $f_{R,3}$	6.96 ± 1.49	Not Applicable
CMOD 3.5 mm $f_{R,4}$	6.28 ± 1.30	Not Applicable

* ± reflects standard deviation

Peak flexural strength at first cracking of the SFRC was reported to be 7.1 MPa while residual flexural strengths ranged from 4.6 to 7.0 MPa depending on the magnitude of crack mouth opening displacement. See Appendix A for details. The back-analyzed peak and residual SFRC tensile strengths based on EN 14651 were found to be approximately 4.3-5.4 MPa and 1.2-2.8 MPa, respectively, and depended on the back-analysis methodology used. The tensile strain limit at peak tensile cracking was therefore estimated to be 140 to 180 με, depending on the 4.3 to 5.4 MPa assumed peak tensile strength.

A hybrid SFRC plus perimeter rebar reinforcement design (i.e., SFRC plus RC) was developed and cast using the same SFRC and casting process in Virginia. The reinforcement is shown in Figure 2-4 and consisted of intrados and extrados circumferential *ϕ*25 (US #8) bars in two rows, both within 127 mm of the leading and trailing edges. Radially oriented *ϕ*19 (US #6) bars were welded to the circumferential rebar. The intent of the rebar was to provide bursting stress support immediately below the thrust jack load pads.

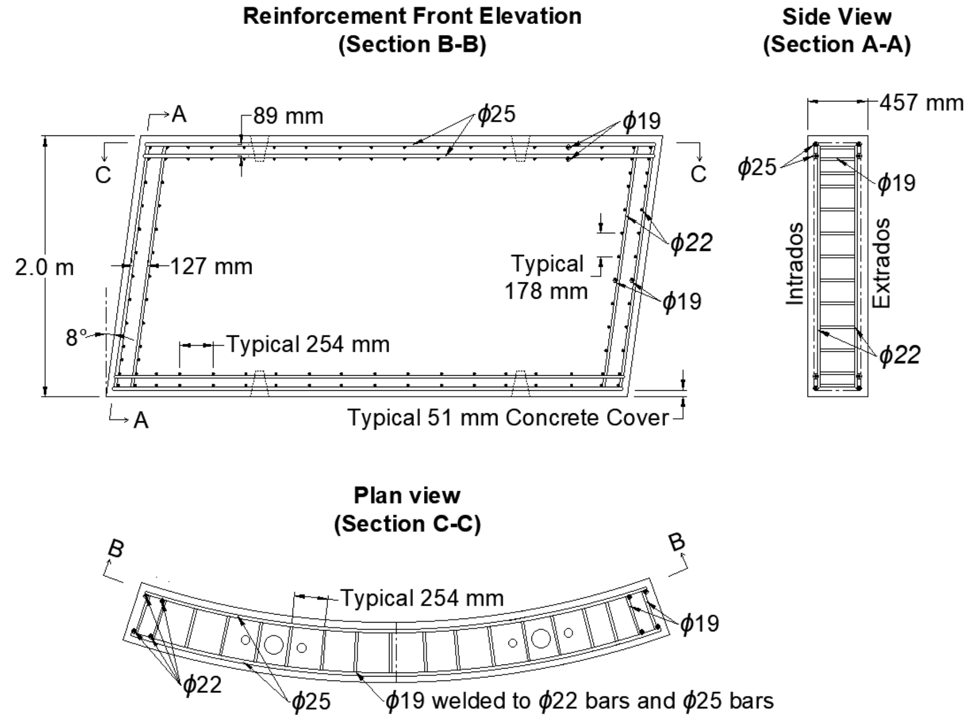

Figure 2-4. Reinforcement cage used in the hybrid SFRC plus RC segments (units in meters unless noted).

2.2.2. Desired Testing Arrangement

The test setup aimed to replicate field thrust jack loading conditions where each segment is loaded by multiple thrust jack load pads (Figure 2-1). Figure 2-5 shows the CBBT project thrust jack load configuration sketched onto a photo of the ring mockup prepared at the CBBT project site by CBJV. Except for the keystone, all segments are loaded by two thrust jack loading pads. Segments are typically loaded by the two thrust jack loading pads simultaneously; however, there may be instances where only one thrust jack load pad is engaged at a time due to alignment or operational conditions during construction. Given the upsets (i.e., portions of segment ends that protrude) on the segment circumferential joints (red region in Figure 2-6), thrust jack load is transferred from the segment leading edge (where thrust jack pad loading acts) to distinct contact regions on the trailing edge as illustrated in Figure 2-5.

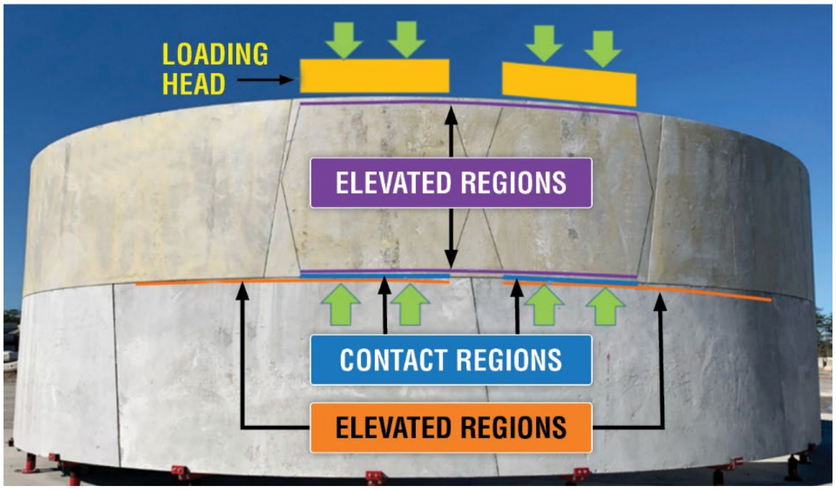

Figure 2-5. Tunnel boring machine thrust jack loading arrangement superimposed on CBBT tunnel lining mockup ring on project site.

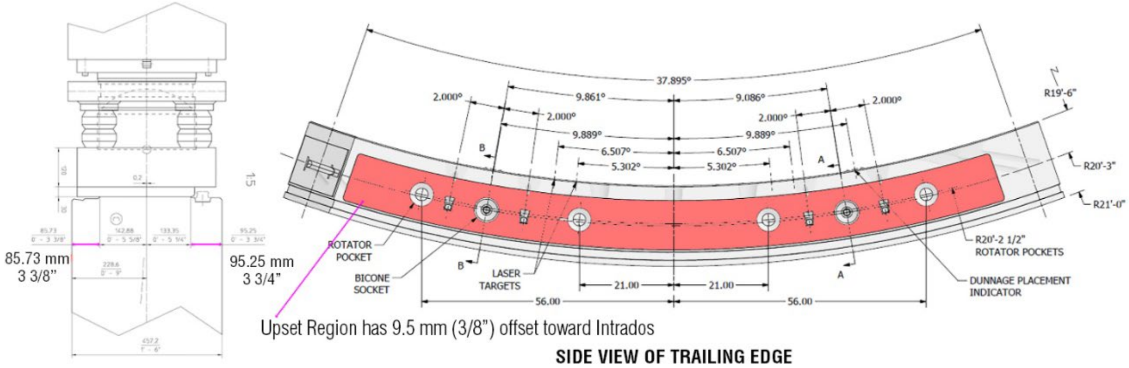

Figure 2-6. Upset region and jack application detail for edge of liners.

As evidenced by the geometry illustrated and the load transfer paths dictated by segment upsets, there is only minor overlap in concrete stress due to the adjacent load pads. The radial and transverse bursting stresses below each load pad are induced by that load pad with little contribution from the adjacent load pad. The exception to this is the area (contact regions in Figure 2-5) between the load pads where tensile spalling stresses on the segment's leading edge are the result of the two adjacent thrust jack loaded pads.

2.2.3. Test Frame and Procedure

Segments were tested using a 22 MN capacity load frame. Double pad and single pad loading configurations were adopted during testing (see Figure 2-7). The CBBT project TBM has an ultimate jack pad load capacity of 9.55 MN and was constrained to 8.42 MN during operation. The load frame was able to exceed the TBM-installed capacity during double pad loading (11 MN per pad force) and during single pad loading. The single pad configuration was used to load segments to bursting stress failure.

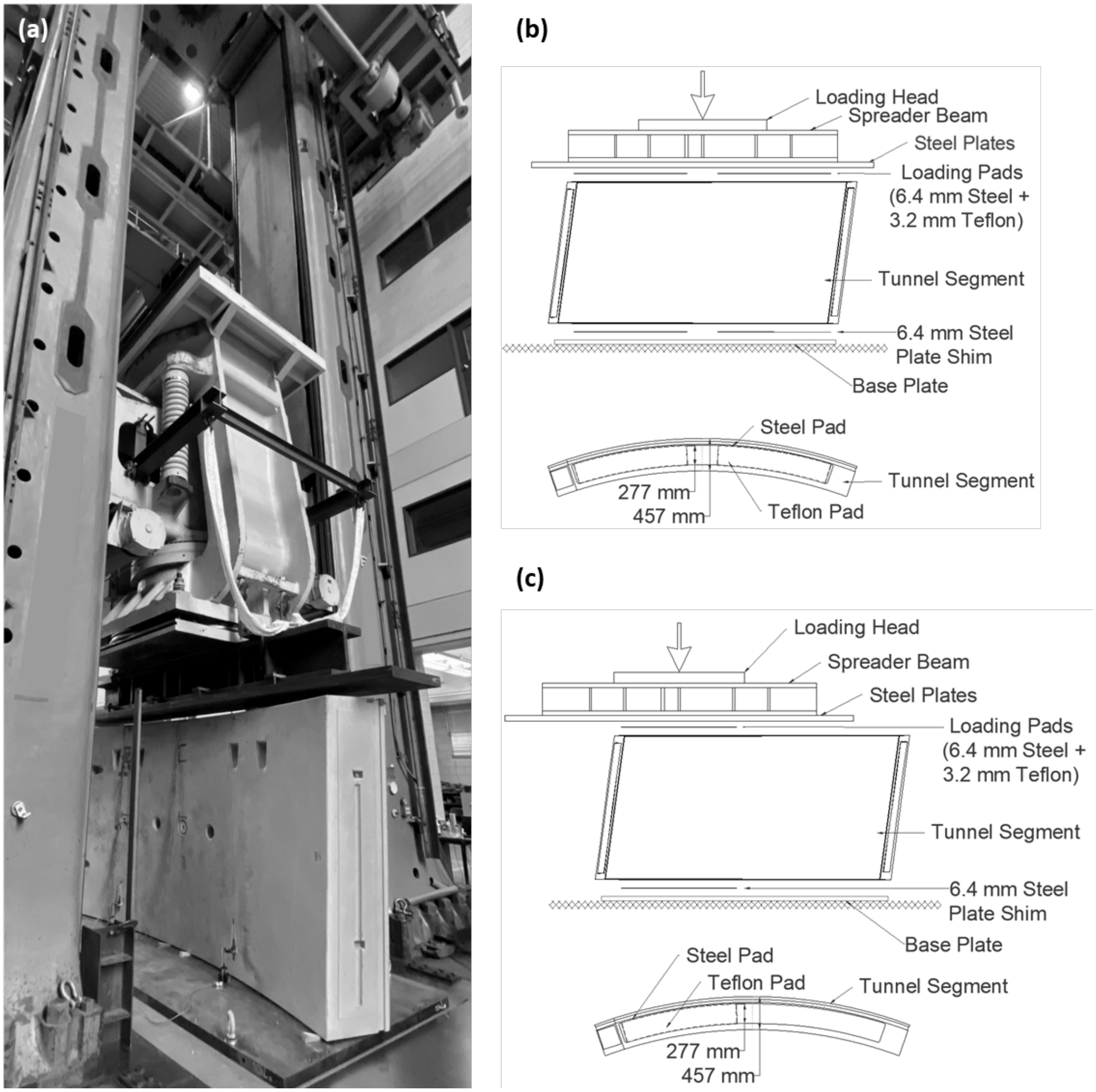

Figure 2-7. (a) 22 MN thrust jack test assembly;
(b) double load pad configuration applying up to 11 MN per load pad;
(c) single load pad configuration applying up to 22 MN to one load pad.

2.2.4. Instrumentation

PCTL test segments were outfitted with external and internal strain gages and external displacement sensors (linear variable differential transformers, LVDTs) to measure radial and transverse bursting stresses. Figure 2-8 and Figure 2-9 show instrumentation layouts to measure radial and transverse bursting strains at various distances below each thrust jack load pad as well as between load pads. Up to four columns of gages were used on each segment including beneath the center of each load pad, at the center of the segment, and at the edge of the load pad as shown in Figure 2-8 and Figure 2-9. For radial strain, foil-type gages were installed by pre-drilling 16 mm diameter holes to a depth of 254 mm along segment thickness direction from the intrados surface. Sensors were inserted and epoxy was applied to seal the hole and bond the gage to the concrete. Distributed fiber optic sensor-type gages were also installed by pre-drilling 16 mm diameter holes through the entire 457 mm segment thickness, inserting fiber optic cables and applying epoxy to bond the fiber to the concrete. In addition, crack widths were regularly measured on the intrados and extrados faces of the segments using a crack comparator gage.

2.3. Test Results

Two SFRC and two hybrid SFRC plus RC segments were subjected to thrust jack loading throughout six tests. The following sections describe the observed behavior. The detailed measurements from each test are provided in Appendix B.

2.3.1. SFRC Behavior

When subjected to thrust jack loading, the SFRC segment showed a distinct ultimate radial bursting stress failure (illustrated in Figure 2-10) at an approximate thrust jack pad load magnitude of 20.3 MN. At thrust jack pad load levels above 10.5 MN and below this abrupt ultimate failure at 20.3 MN, the segment exhibited intrados and extrados cracking with crack widths that start to exceed the design code allowed levels (typically 0.2 mm is allowed). Crack widths are summarized as a function of thrust load in Figure 2-11. The longitudinal cracking shown in Figure 2-11 is caused by transverse bursting stresses. Early onset cracking due to radial bursting stress is not visible on the extrados and intrados because these cracks manifest internally in the transverse (circumferential) direction. Such cracking likely occurred well before the ultimate failure at 20.3 MN. In addition, no cracks were observed on the extrados and intrados surfaces at thrust jack pad load levels up to and including the 9.55 MN capacity of the CBBT TBM.

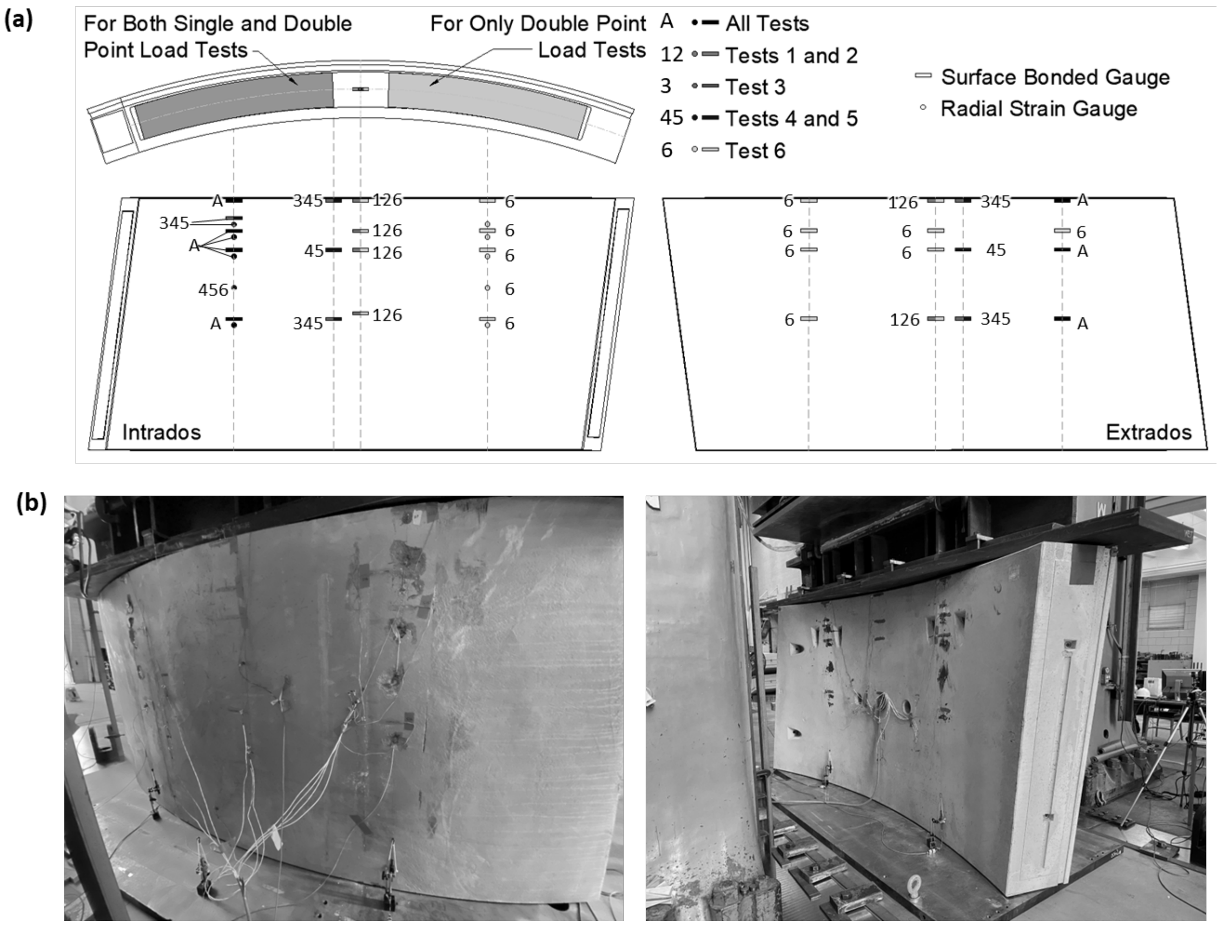

Figure 2-8. (a) Segment instrumentation layout for thrust jack loading including radial and tangential strain gages on the segment intrados and extrados, and (b) photos of radial and tangential strain gages and displacement transducers on the segment intrados and extrados.

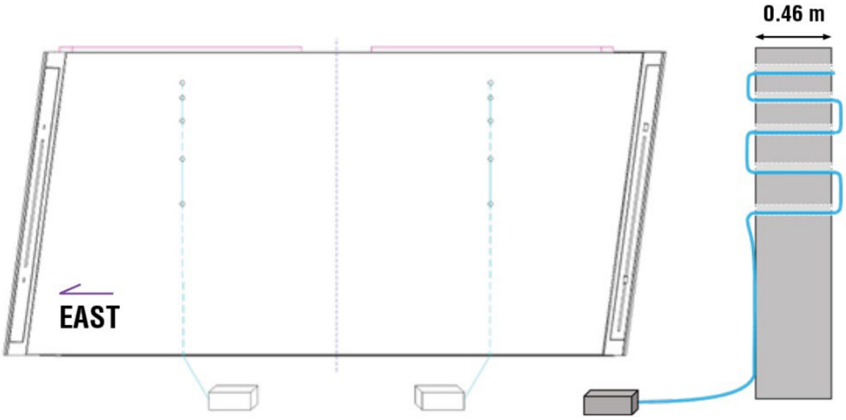

Figure 2-9. Distributed fiber optic sensing for radial strain measurements.

Figure 2-10. View after radial bursting stress failure of SFRC segment: (a) Leading edge where radial bursting stress induced cracking is clear; (b) side of the segment where radial bursting stresses (along thickness direction) exceeded the tensile capacity of the SFRC.

Radial and transverse strain behavior was measured at multiple discrete depths below the thrust jack load pad. Measured radial strains reached the estimated tensile strength/strain limit of 180 με at a depth of approximately 0.2 m beneath the thrust jack load pad. This depth, approximately equal to 0.45 times the segment thickness, is consistent with the ACI 318-14[3] and DAUB estimations of 0.5 and 0.4 times the segment thickness, respectively, in both cases assuming no eccentric loading.

Per fiber optic strain sensing, the measured radial strains reached the 180 με tensile strain limit at thrust jack load levels averaging 8 MN (plus or minus 1 MN given variability in strain measurements). This is considerably lower than the 20.3 MN ultimate failure described above and does not convey the ultimate thrust capacity of the segment. Exceeding the SFRC tensile strain limit of 180 με radially indicates that circumferentially oriented internal cracks are occurring and radial bursting stress redistribution is occurring. While these internal circumferential cracks may not manifest at the extrados/intrados surface, they may intersect with existing radially oriented cracks to introduce an ingress pathway and durability risk.

Measured transverse strain reached 180 με at a depth of 1.0 m below the thrust jack load pad (Figure 2-11). This depth to maximum transverse strain, referred to as d_{burst} in ACI 544.7R-16[1], is clearly different from the observed depth to maximum radial strain, and is not conveyed as such in design codes. The transverse strain reached 180 με at a thrust jack load of approximately 17.6 MN. This load level exceeding 180 με is consistent with the observation of measured crack widths

---

[3] Use of ACI 318-14, Building Code Requirements for Structural Concrete, is not a Federal requirement.

≥ 0.2 mm, as the maximum allowed crack width typically prescribed in tunnel lining design specifications (e.g., AASHTO, 2017[1]).

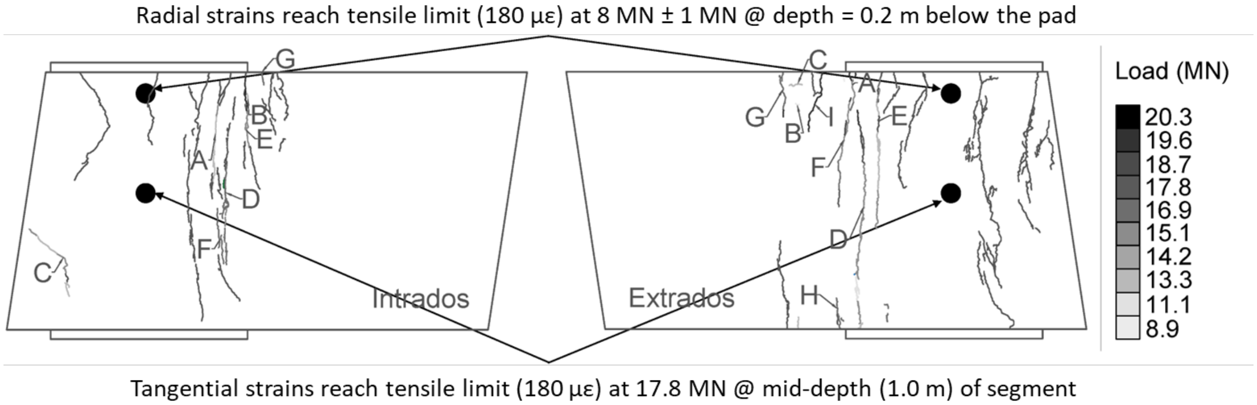
Radial strains reach tensile limit (180 με) at 8 MN ± 1 MN @ depth = 0.2 m below the pad

Tangential strains reach tensile limit (180 με) at 17.8 MN @ mid-depth (1.0 m) of segment

Figure 2-11. Crack width records during single thrust jack pad loading and locations of maximum observed bursting strains.

Table 2-2. Crack width records during thrust jack pad loading corresponding to Figure 2-11

Load (MN)	Intrados Crack Width (mm)							Extrados Crack Width (mm)								
	A	B	C	D	E	F	G	A	B	C	D	E	F	G	H	I
4.5	0.00	0.00	0.00	0.00	0.00	0.00	0.00	0.00	0.00	0.00	0.00	0.00	0.00	0.00	0.00	0.00
8.9	0.00	0.00	0.00	0.00	0.00	0.00	0.00	0.10	0.05	0.10	0.00	0.00	0.00	0.00	0.00	0.00
11.1	0.05	0.00	0.00	0.00	0.00	0.00	0.00	0.10	0.08	0.15	0.23	0.00	0.00	0.00	0.00	0.00
13.3	0.10	0.05	0.10	0.00	0.00	0.00	0.00	0.10	0.10	0.18	0.23	0.15	0.00	0.00	0.00	0.00
15.1	0.15	0.05	0.15	0.10	0.10	0.00	0.10	0.10	0.10	0.18	0.23	0.18	0.18	0.00	0.00	0.00
16.9	0.23	0.08	0.15	0.15	0.10	0.10	0.10	0.10	0.10	0.18	0.25	0.18	0.18	0.10	0.15	0.00
17.8	0.23	0.10	0.15	0.15	0.10	0.10	0.10	0.10	0.10	0.18	0.64	0.25	0.18	0.10	0.15	0.00
18.7	0.23	0.10	0.15	0.15	0.18	0.10	0.10	0.10	0.10	0.18	0.76	0.30	0.51	0.10	0.18	0.00
19.6	0.25	0.15	0.15	0.15	0.18	0.10	0.10	0.18	0.15	0.23	0.81	0.30	0.51	0.15	0.23	0.18

2.3.2. Hybrid SFRC Plus RC Behavior

One hybrid SFRC plus RC segment was loaded to 22 MN thrust jack load and did not exhibit the abrupt ultimate radial bursting stress failure that the SFRC segment experienced. The capacity of the test rig prevented loading the hybrid segment any further. The measured internal radial strains at depths = 0.2 m below the load pad remained at or below 180 με. The rebar in the radial direction (Figure 2-4) is located in this vicinity and is supporting this tensile stress. As shown in Figure 2-12, longitudinal cracking emerges at 17.6 MN thrust jack pad loading. These longitudinal cracks are due to transverse bursting stresses. The measured transverse strains within the segment reached 180 με at 17.6 MN near the 1.0 m mid-depth of the segment (Figure 2-13), where the locations correspond to the red dots shown in Figure 2-12. In this area, there is no rebar to provide additional tensile load capacity. This demonstrates that, while the rebar cage with perimeter reinforcement provides important additional radial bursting stress capacity beyond what SFRC can provide, this essentially shifts the governing limit state to transverse bursting stress failure at mid segment. The SFRC transverse bursting stress capacity is only slightly greater than the radial bursting stress capacity. Therefore, the benefit of a perimeter rebar cage is limited insofar as significantly improving bursting stress capacity, even if it is beneficial to avoid the observable cracks caused by radial bursting stress.

When a full ring of segments is installed, adjacent segments provide beneficial confinement in the transverse (circumferential) direction, while there remains no confinement in the radial direction. This circumferential direction confinement likely boosts the transverse bursting stress capacity. However, there are many cases, such as in continuous tunneling, where thrust jack loading is imparted to segments before the full ring is installed. This indicates that in design practice, neglecting circumferential confining gives conservative prediction of thrust performance of PCTL segments.

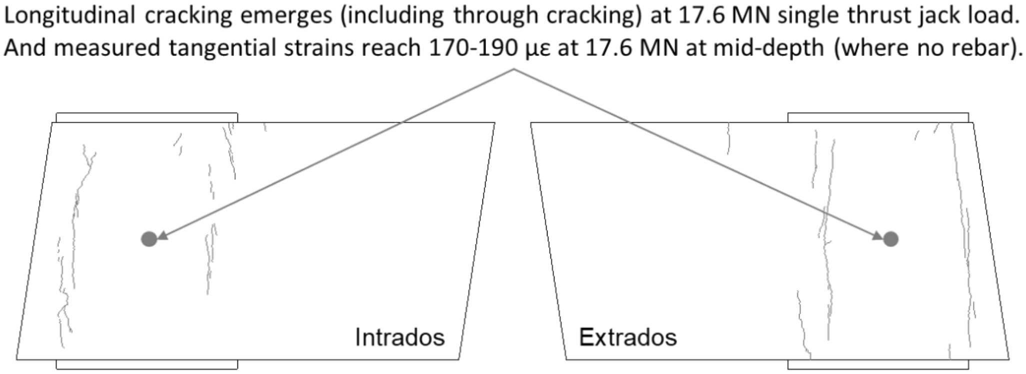
Longitudinal cracking emerges (including through cracking) at 17.6 MN single thrust jack load.
And measured tangential strains reach 170-190 με at 17.6 MN at mid-depth (where no rebar).

Figure 2-12. Hybrid segment crack width records and locations of maximum observed bursting stresses.

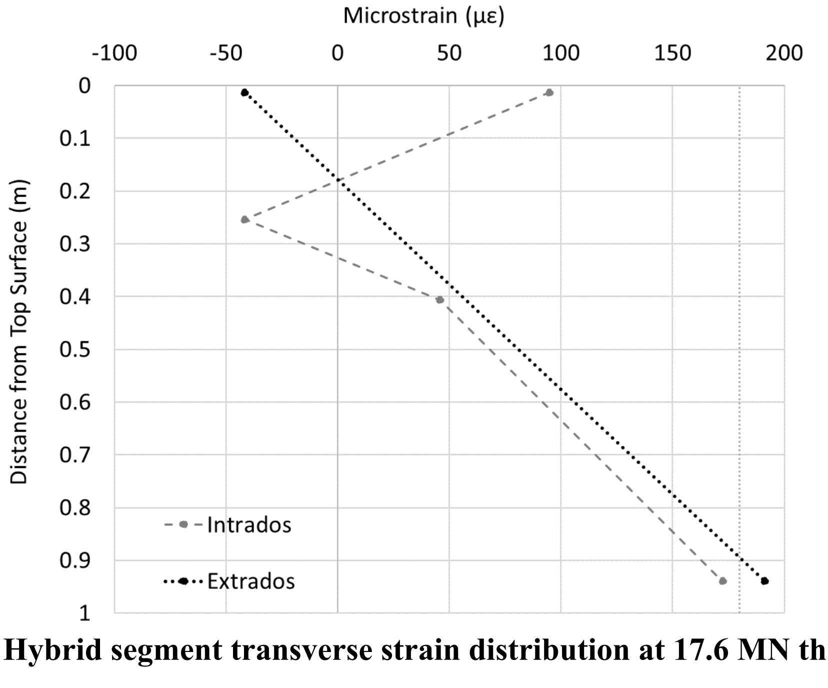

Figure 2-13. Hybrid segment transverse strain distribution at 17.6 MN thrust jack load.

2.4. Implications on Current Design Practice

2.4.1. ACI Design Approach

ACI-544-7R-16[1] summarizes the state of practice for bursting stress analysis. Four methods are suggested to assess bursting stress: (a) ACI 318-14[3] simplified equations; (b) German tunneling committee (DAUB) equations; (c) Iyengar (1962) diagram analysis; or (d) finite element analysis. The simplified equations to estimate the bursting force T_{burst} and depth d_{burst} where T_{burst} occurs are provided by ACI 318-14[3] equation (2-1) and DAUB equation (2-2). Figure 2-14 from ACI 544.7R-16[1], illustrates the pertinent parameters. Figure 2-14(a) from ACI 318-14[3] illustrates a post-tensioning beam girder application (from which the simplified formulations were derived) while Figure 2-14(b) from the German tunneling committee more directly illustrates thrust jack load application across the segment thickness.

$$T_{burst} = 0.25F_{jack}\left(1-\frac{h_{anc}}{h}\right);\ d_{burst} = 0.5(h-2e_{anc}) \qquad (2\text{-}1)$$

$$T_{burst} = 0.25F_{jack}\left(1-\frac{h_{anc}}{h-2e_{anc}}\right);\ d_{burst} = 0.4(h-2e_{anc}) \qquad (2\text{-}2)$$

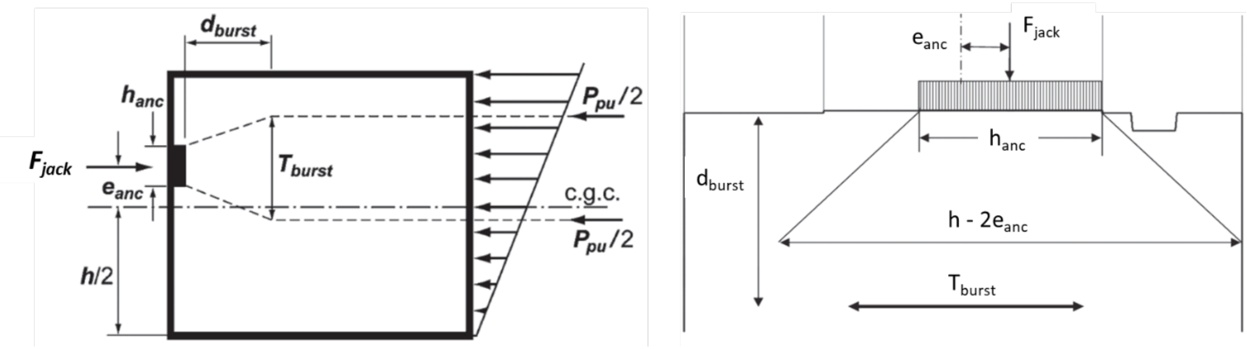

© 2014 ACI 318-14[3]

(a) (b)

Figure 2-14. Bursting force estimation via simplified equations suggested by (a) ACI 318-14[3] and (b) the German tunneling committee.

Equation (2-3) and equation (2-4) are provided in ACI 544.7R-16[1] to calculate the maximum radial (r) and transverse (t) bursting stresses based on T_{burst} and d_{burst}. The maximum bursting stress developed in the radial ($\sigma_{p,r}$) and transverse ($\sigma_{p,t}$) directions employ the geometry terms illustrated in Figure 2-15. Here, the strength reduction factor ϕ = 0.7 is included for the ACI context of comparing the achieved factored stress with a SFRC tensile strength σ_p. If $\sigma_{p,r}$ or $\sigma_{p,t}$ is greater than $\phi\sigma_p$ then reinforcing bars are provided to supplement the SFRC.

$$\sigma_{p,r} = \frac{T_{burst}}{\phi a_l d_{burst}} \qquad (2\text{-}3)$$

$$\sigma_{p,t} = \frac{T_{burst}}{\phi h_{anc}\, d_{burst}} \qquad (2\text{-}4)$$

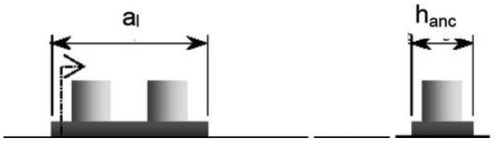

Figure 2-15. Thrust load pad geometry terms incorporated into ACI 544.7R-16[1] bursting stress calculations. a_l is the length of the load pad in the transverse (circumferential) direction while h_{anc} is the load pad dimension in the radial direction.

Equation (2-3) and equation (2-4) from ACI 544.7R-16[1] suggest there is one unique value of T_{burst} and one unique value of d_{burst} used to estimate both radial and transverse bursting stress. The abovementioned equations and the accompanying Figure 2-15 from ACI 544.7R-16[1] are applicable to radial bursting stress and the corresponding radial bursting stress governing T_{burst} estimation. The estimations of d_{burst} in equation (2-1) and (2-2), at a depth equal to $0.4h$ (DAUB) and $0.5h$ (ACI 318-14[3]), assuming e_{anc}= 0, match with the measured depth to maximum radial bursting stress (Figure 9). However, the measured depth to maximum transverse bursting stress is significantly greater than the radial d_{burst} (Figure 2-11 and Figure 2-12) and is not governed by the segment thickness as denoted in equations (2-1) and (2-2). ACI uses the same d_{burst} term for transverse bursting stress or at least does not distinguish transverse bursting stress, therefore suggesting that the maximum tensile stress in the transverse direction occurs close to the load pad at a similar depth as the radial maximum bursting stress. This discrepancy will be addressed in the following section.

2.4.2. Clarification of Radial and Transverse Bursting Stress

Figure 2-16 and Figure 2-17 are provided to clarify the implementation of the ACI 318-14[3] and DAUB simplified equations for SFRC radial and transverse bursting, respectively. Each figure illustrates the geometry for the depth d_{burst} where T_{burst} acts in each direction, as well as pad thickness and other dimensional terms adopted. From the ACI 544-7R-16[1] stated bursting stress equations (2-3) and (2-4), equations for radial bursting stress $\sigma_{p,r}$ and transverse bursting stress $\sigma_{p,t}$ are provided. Using the adopted and unfactored (ϕ=1.0) SFRC tensile strength σ_p, the ultimate thrust jack pad load $F_{j,u}$ can be estimated both for radial bursting stress control and transverse bursting stress control. Allowable thrust jack pad loads can also be determined by introducing appropriate load and resistance factors (not included here).

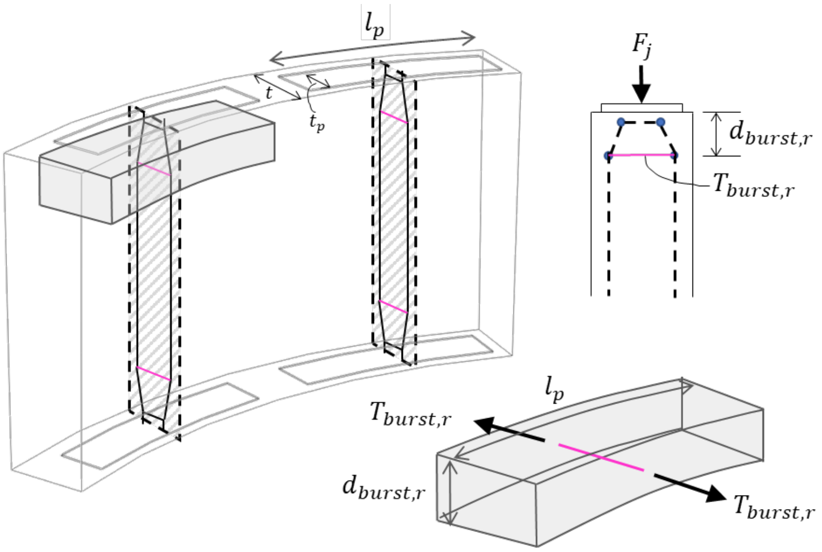

Figure 2-16. Illustration of ACI 318-14[3] and DAUB approach to radial thrust jack bursting.

Table 2-3 Equations of ACI 318-14[3] and DAUB approach to radial thrust jack bursting.

Parameter	**ACI 318-14[3]**	**DAUB**
Radial bursting force $T_{burst,r}$	$T_{burst,r} = 0.25F_j\left(1-\frac{t_p}{t}\right)$	$T_{burst,r} = 0.25F_j\left(1-\frac{t_p}{(t-2e_r)}\right)$
Depth to max radial bursting force $d_{burst,r}$	$d_{burst,r} = 0.5(t-2e_r)$	$d_{burst,r} = 0.4(t-2e_r)$
Radial bursting stress $\sigma_{p,r} = \frac{T_{burst,r}}{l_p d_{burst,r}}$	$\sigma_{p,r} = \frac{F_j\left(1-\frac{t_p}{t}\right)}{2l_p(t-2e_r)}$	$\sigma_{p,r} = \frac{F_j\left(1-\frac{t_p}{(t-2e_r)}\right)}{1.6l_p(t-2e_r)}$
Ultimate thrust jack pad capacity per radial bursting $F_{j,u}$ when $\phi = 1.0$ and $e_r = 0$	$F_{j,u} = \frac{2l_p(t-2e_r)\sigma_p}{1-\frac{t_p}{t}}$	$F_{j,u} = \frac{1.6l_p(t-2e_r)\sigma_p}{1-\frac{t_p}{(t-2e_r)}}$

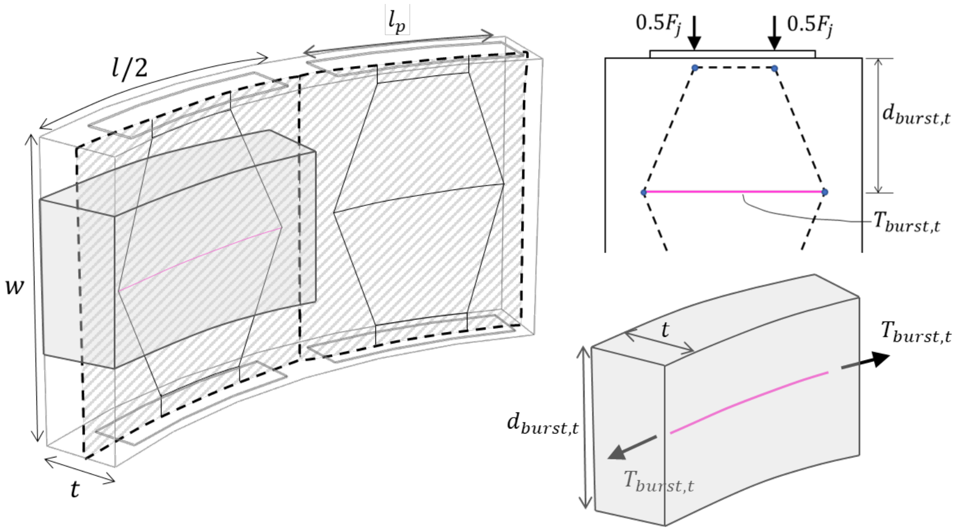

Figure 2-17. Illustration of ACI 318-14[3] and DAUB approach to transverse thrust jack bursting.

Table 2-4 Equations of ACI 318-14[3] and DAUB approach to transverse thrust jack bursting.

Parameter	**ACI 318-14[3]**	**DAUB**
Transverse bursting force $T_{burst,t}$	$T_{burst,t} = 0.25F_j\left(1-\frac{l_p}{l/2}\right)$	$T_{burst,t} = 0.25F_j\left(1-\frac{t_p}{(t-2e_t)}\right)$
Depth to max transverse bursting force $d_{burst,t}$	$d_{burst,t} = 0.5(w/2-2e_t)$	$d_{burst,t} = 0.4(w/2-2e_t)$
Transverse bursting stress $\sigma_{p,t} = \frac{T_{burst,t}}{t \cdot d_{burst,t}}$	$\sigma_{p,t} = \frac{F_j\left(1-\frac{l_p}{l/2}\right)}{tw}$	$\sigma_{p,t} = \frac{0.25F_j\left(1-\frac{t_p}{(l/2-2e_t)}\right)}{0.2tw}$
Ultimate thrust jack capacity per transverse bursting $F_{j,u}$ when ϕ = 1.0 and $e_t = 0$	$F_{j,u} = \frac{w\,t\,\sigma_p}{1-\frac{2l_p}{l}}$	$F_{j,u} = \frac{0.8\,w\,t\,\sigma_p}{1-\frac{2l_p}{l}}$

Figure 2-18 summarizes the Iyengar approach to estimating radial bursting stress derived from an analytical modeling approach for post-tensioning anchors (Iyengar, 1962). Here, Iyengar's term a is equivalent to the segment thickness t, β is the thrust jack pad width t_p, and b is the transverse dimension over which the thrust jack load is applied, equivalent to l_p. σ_{cm} is the average compressive stress acting over an area ab equals $t_p l_p$ at a distance/depth a from the thrust jack pad. To this end Iyengar's analysis assumes the applied thrust jack load becomes uniform at a distance t_p below the pad and that there is no load spreading transversely/circumferentially. The bursting tensile stress is termed σ_{cx} in Iyengar's diagram, and its magnitude is a function of a/x

and β/a. For β/a = 0.6, as is the case in the performed thrust jack load tests, the maximum bursting stress occurs at a distance $0.5t_p$ below the pad. The bursting stress magnitude is provided by the curves shown in Figure 16. Converting to terminology in Figure 2-16 and Figure 2-17, the radial bursting stress is calculated as:

$$\sigma_{p,r} = \frac{\sigma_{cx}}{\sigma_{cm}} \frac{F_j}{t\, l_p} \tag{2-5}$$

Iyengar's diagram is not appropriate for transverse bursting stress given the assumptions made in deriving the estimated response.

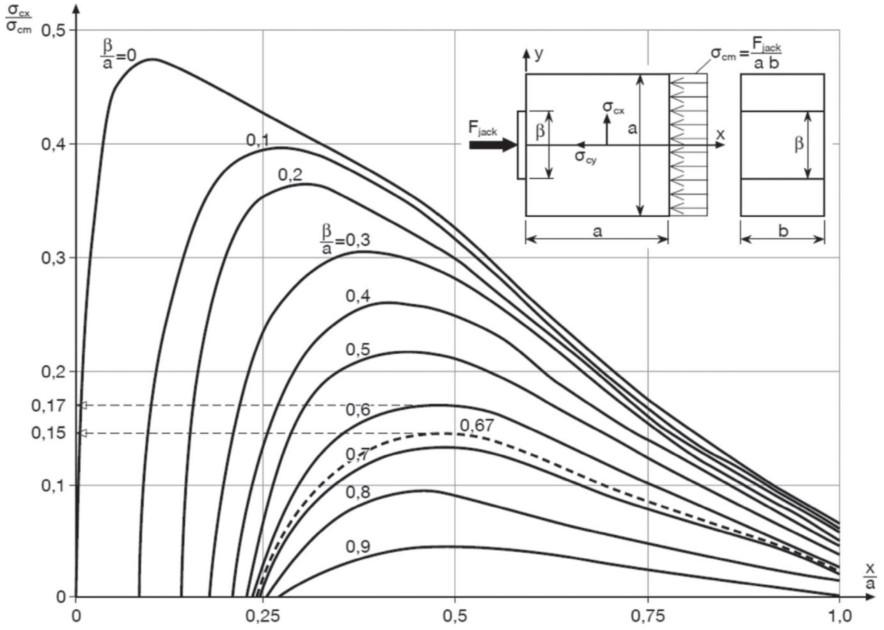

© 2016 ACI 544.7R-16[1]

Figure 2-18. Iyengar diagram to estimate radial bursting stress (from ACI 544.7R-16[1]).

2.4.3. Findings in Context of ACI Design Procedure

The bursting stress results collected during SFRC thrust jack load testing are directly compared with magnitudes estimated using ACI 544.7R-16[1]. A summary of the experimental findings presented in a design context are summarized in Table 2-5.

Ultimate radial bursting failure occurred at a thrust jack pad load of 20.3 MN. Per the crack width criteria of 0.2 mm cited in the AASHTO LRFD Road Tunnel Design and Construction Guide Specifications[2], transverse bursting failure occurred at 16.7 MN. Crack width-based radial bursting failure is undeterminable because the resulting circumferential cracks are internal and not observable on the intrados and extrados faces. The 180 με tensile strain limit associated with the 5.4 MPa peak tensile strength was measured radially at a thrust jack pad load of 8 MN and transversely at a thrust jack pad load of 17.6 MN. The transverse strain limit and 0.2 mm transverse cracking occurred at similar thrust jack pad load. The occurrence of the radial tensile strain limit would induce internal cracking that would not manifest at the surface. To this end, the significance of these cracks in regard to segment durability, i.e., chloride ingress, is not as clear as in the case of transverse cracks that manifest at the surface.

Table 2-5. Observed radial and transverse bursting stress failure in SFRC testing.

Limit state criterion	Radial	Transverse	Notes
Ultimate capacity failure	20.3 MN	-	Clear radial bursting stress failure near load pad.
Cracking/crack width > 0.2 mm	Undeterminable	16.7 MN	Cracking due to radial bursting stress is internal and runs circumferential; not observable on surfaces
SFRC tensile strength (5.4 MPa) exceeded	8 MN*	17.6 MN	Transverse is coincident with surface crack formation; not possible to observe associated tensile cracking.

* ± 1 MN and based on fiber optic sensing

The thrust jack load capacity was estimated using suggested ACI 544.7R-16[1] methods, namely the ACI 318-14[3] and DAUB simplified formulas and Iyengar diagram described in Section 2.4.2. The following segment and thrust jack load pad inputs were used: l = 4.06 m, w = 2.0 m, $t = h$ = 457 mm, t_p = 275 mm, l_p = 1.6 m, e_t = 0, e_r = 5 mm. No stress reduction was adopted to provide an estimate of capacity, i.e., ϕ = 1.0.

Multiple values of tensile strength were explored given the lack of clarity in ACI 544.7R-16[1] and differing philosophies in the tunnel design community. The peak and residual σ_p were back-calculated from notched beam test results. Appendix A summarizes the estimation of SFRC tensile strength. The results presented in Table 2-6 show that radial bursting stress is the controlling failure mode over transverse bursting failure for the SFRC segments according to the ACI 318-14[3] and DAUB estimates. Transverse bursting failure is estimated to occur at a 20 percent greater thrust jack pad load in SFRC. The DAUB estimation of T_{burst} capacity is lower than ACI 318-14. The Iyengar approach predicts the highest radial-governed T_{burst}. For transverse bursting stress capacity, $d_{burst,t}$ equals 1.0 m is adopted in equation (2-4) based on experimental results. The use of $d_{burst,r}$ in equation (2-4) would lead to much higher transverse bursting stress capacity than conveyed in Table 2-6. These methods give relatively similar thrust load levels corresponding to the stress limits, with an approximate variation of 14 percent.

Table 2-6. Ultimate thrust jack load capacity according to ACI 544.7R-16[1] (no partial safety factors)

Parameter	ACI 318-14[3]	DAUB	Iyengar
Radial			
Peak σ_p (5.5 MPa)	19.9 MN	16.5 MN	23.3 MN
Residual σ_p (2.1 MPa)	7.6 MN	6.3 MN	8.9 MN
Split Tensile σ_p (7.1 MPa)	25.7 MN	21.3 MN	30.0 MN
Transverse*			
Peak σ_p (5.5 MPa)	23.3 MN	18.6 MN	NA
Residual σ_p (2.1 MPa)	8.9 MN	7.1 MN	NA
Split Tensile σ_p (7.1 MPa)	30.0 MN	24.0 MN	NA

* using $d_{burst,t}$ = 1.0 m. Tangential capacity much higher if using $d_{burst,t} = d_{burst,ra}$

A comparison of Table 2-6 results with measured results (Table 2-5) shows that the SFRC ultimate limit state (20.3 MN thrust jack pad load) is best estimated by ACI 318-14[3] when using the back-calculated peak tensile strength and DAUB when using split tensile strength. The use of residual tensile strength as suggested by ACI 544.7R-16[1] leads to significant underestimation of ultimate thrust jack pad load capacity. Specifically, ACI 318-14[3] and DAUB methods estimate 7.6 MN and 6.3 MN thrust jack pad load limits compared to the 20.3 MN actual limit state.

2.5. Summary and Suggestions

Thrust jack load testing on 457 mm thick SFRC and hybrid SFRC plus RC segments showed that: (a) radial bursting stress governs SFRC thrust jack failure; (b) maximum radial bursting stress occurs at a distance of 0.4-0.5 times the segment thickness from the thrust jack load pad; (c) maximum transverse bursting stress occurs at a distance from the thrust jack load pad of one-half the segment width; (d) perimeter rebar improves radial bursting stress capacity and shifts the governing condition to transverse bursting stress at mid-width of the specimen.

A comparison with the ACI 544.7R-16[1] design methodologies shows that the use of residual tensile strength in the simplified design equations in ACI 544.7R-16[1] can lead to considerable underestimation of ultimate radial-based thrust jack pad load capacity. The results presented are based on limited testing. Further testing may confirm findings and better inform this critical load case for large diameter segmental lining.

Modifications to transverse bursting force, depth and stress definitions in ACI 544.7R-16[1]should be considered because ACI 544.7R-16[1], as currently written, suggests the use of a similar d_{burst} for radial and transverse analysis. The test results suggest this may be incorrect.

3 RADIAL JOINT BEHAVIOR DURING SERVICE LOADING

3.1. Introduction

This chapter examines the moment-rotation behavior of radial (longitudinal) joints in large diameter precast concrete tunnel lining (PCTL). Under service load conditions, the tunnel ring is subject to combinations of axial and bending demands in the circumferential direction of the liner. One important area where large diameter rings may behave differently is in overall stiffness reduction due to the segmental nature of the rings (Mooney et al., 2020). Hence, the flexural performance of the liner is controlled by the response of the radial joints between PCTL segments. Moment-rotation is generally determined to evaluate the flexural performance of tunnel liner joints, as shown in Figure 3-1.

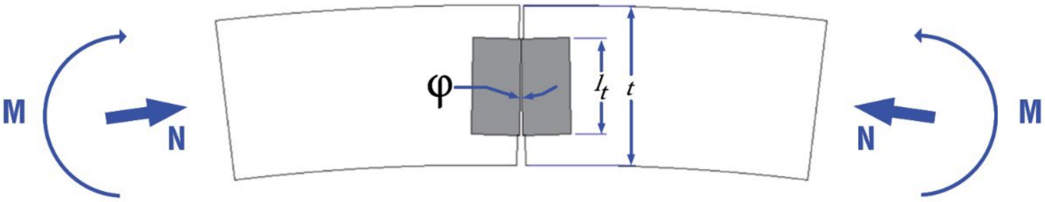

Figure 3-1. Illustration of positive moment-rotation.

(Janssen, 1983) developed a theoretical solution based on flexural bearing and decompression of an elastic concrete joint. His approach allows for the determination of the joint moment-rotation behavior as a function of the axial force applied and can be used for modeling the response of a tunnel subject to external loads transverse to the longitudinal axis of the tunnel. The Janssen model assumes that the contact area can be modeled as a concrete beam with the same dimensions as contact area, which has zero tensile stress capacity (Groeneweg, 2007). The derivation of Janssen's model, documented in German in (Janssen, 1983), is summarized in English by (Groeneweg, 2007). Janssen's moment-rotation model can be expressed as:

$$M = \frac{b \cdot l_t^2 \cdot E_c}{12} \cdot \varphi \qquad (closed\ joint) \tag{3-1}$$

$$M = \left(1 - \sqrt{\frac{8 \cdot N}{9 \cdot b \cdot l_t \cdot E_c \cdot \varphi}}\right) \cdot \frac{N \cdot l_t}{2} \qquad (opened\ joint) \tag{3-2}$$

where M is the applied moment at the joint, N is the applied axial force (e.g., thrust load), φ is the joint rotation (in radians), E_c is the elastic modulus of concrete, b is the length of the joint (into the page), and l_t is the height of the joint.

Rearranging, the initial linear rotational stiffnesses before and after joint opening can be expressed as:

$$k_{joint} = \frac{b \cdot l_t^2 \cdot E_c}{12} \qquad (closed\ joint) \tag{3-3}$$

$$k_{joint} = \frac{9 \cdot b \cdot l_t \cdot E_c \cdot M}{8 \cdot N} \cdot \left(\frac{2 \cdot M}{N \cdot l_t} - 1\right)^2 \qquad (opened\ joint) \tag{3-4}$$

The linear rotational stiffness of the segment before reaching the cracking moment can be expressed as:

$$k_{segment} = \frac{w \cdot t^2 \cdot E_c}{12} \tag{3-5}$$

where w is the width of the segment and t is the thickness of the segment.

Joint opening initiates when the strain at the extreme fiber reaches zero. This can be determined using either the closed or open joint moment-rotation relationships. The rotation at incipient joint opening or the ratio of moment to axial force that would result in incipient joint opening is given by equation (3-6):

$$\varphi = \frac{2 \cdot N}{b \cdot l_t \cdot E_c} \left(or\ \frac{M}{N} \geq \frac{l_t}{6}\right) \tag{3-6}$$

According to the Janssen $M - \varphi$ model, the joint stiffness transitions from linear-elastic behavior to nonlinear behavior once the axial (i.e. thrust or normal) force is no longer within the core of the contact area. This occurs when the ratio of applied moment to axial force (i.e., the eccentricity) is larger than 1/6 of joint height (equation (3-6)). In the nonlinear response, the joint $M - \varphi$ behavior is also controlled by the axial force at the joint. Nonlinear rotational stiffness increases with axial force (Mooney et al. 2020).

This chapter summarizes the test results and widely used Janssen model and compares observed results with the theoretical solutions from Janssen model. Details on the mechanics of the Janssen model are provided in following sections. Note that a number of assumptions inherent in the model do not accurately represent the actual joint tested. Deviations that may need to be considered include the presence of both the radial bolts and the compression gasket, eccentricity between the segment and the contact surface, the general assumption that the joint is fully closed under all axial load levels, and the reduced bearing area due to the radial alignment rod pockets. None of these issues are examined herein.

3.2. Test Program

A series of radial joint tests were performed on joint assemblies of SFRC segments. The segments examined in this study have an elastic modulus of 30.9 GPa and the following geometric properties: the length of the joint b equals 1800 mm, the height of the joint l_t equals 276 mm, the width of the segment w equals 1980 mm, and the segment thickness t equals 457 mm. A joint test assembly consists of two cut panels and one unaltered joint as shown in Figure 3-2. The joints were tested with and without radial bolts to obtain the initial linear $M - \varphi$ when subjected to axial (normal) force levels of 674, 1070, 1460, 1850 and 2250 kN/m. Nonlinear joint behavior was examined when subjected to axial force levels of 674, 1460 and 2250 kN/m. Note that the axial joint demands are calculated with respect to the overall segment width of 1.98 m. Both positive and negative bending tests were performed to determine the initial linear rotational stiffness. Nonlinear joint behavior tests were only conducted in the positive bending direction. For clarity, positive bending, also referred to as sagging, is described in this report as producing compression on the extrados and decompression/opening on the intrados of the joint. Negative bending, also referred to as hogging, is described in this report as producing compression on the intrados and decompression/opening on the extrados of the joint. Three identical assemblies were used to characterize radial joint behavior through a series of six tests. The test matrix is summarized in Table 3-1.

Table 3-1: Joint rotation test matrix.

Assembly	Test	Description
Assembly 1	Pretest	Calibration and nondestructive evaluation of setup and loading scheme
	1	Positive $M - \varphi$ at N = 1460 kN/m axial load with radial bolts
	2	Positive $M - \varphi$ at N = 674 kN/m axial load with radial bolts
Assembly 2	3	Negative/Positive joint rotation stiffness evaluation at N = 674, 1070, 1460, 1850 and 2250 kN/m axial load with radial bolts
	4	Positive $M - \varphi$ at N = 2250 kN/m axial load with radial bolts
	4a	Negative $M - \varphi$ at N = 2250 kN/m axial load with radial bolts
Assembly 3	5	Negative/Positive joint rotation stiffness evaluation at N = 674, 1070, 1460, 1850 and 2250 kN/m axial load without radial bolts
	6	Positive $M - \varphi$ at N = 1460 kN/m axial load without radial bolts
	6a	Negative $M - \varphi$ at N = 1460 kN/m axial load without radial bolts

The test assembly consists of a joint between two full scale panels. To create a testing assembly that can be examined in the laboratory the panels had to be cut. The assembly concept is illustrated in Figure 3-2. To facilitate application of axial load and vertical reaction supports, the CBBT segments were cut as illustrated in Figure 3-2 and Figure 3-3. The first cut on segments was intended to allow for axial thrust application in the circumferential direction, and the second cut was made to create a flat surface for vertical reaction support in the setup. As shown in Figure 3-2 and Figure 3-3, the full-size segments were cut to a length of 1.75 m long circumferentially, and radial joint contact area remained unaltered.

3.2.1. Segment and Radial Joint Properties

As-designed SFRC segments from the CBBT project were used for the joint flexure evaluation; these segments have no additional conventional reinforcement. The segments used for this testing were from the same fabricator mentioned in Chapter 2. The SFRC mix design included a cementitious content of 445 kg/m^3 and a w/c ratio of 0.35. Multi-hook 4D steel fiber was used. The fiber content was 38.5 kg/m^3 with 61 mm length, 0.75 mm diameter and a fiber aspect ratio of 80. The average compressive strength of the SFRC mix design was 65 MPa, matching well with 64 MPa compressive strength determined from segment cores. The average splitting tensile strength, measured from segment cores, was 7.1 MPa and reasonably similar to the mix design splitting tensile strength of 7.6 MPa. Crack mouth opening displacement tests were performed on the mix design according to the BS EN 14651 procedure[4]. The average elastic modulus is 30.9 GPa as obtained from compressive tests. Further details on the material properties and the methods used for determination can be found in Appendix A.

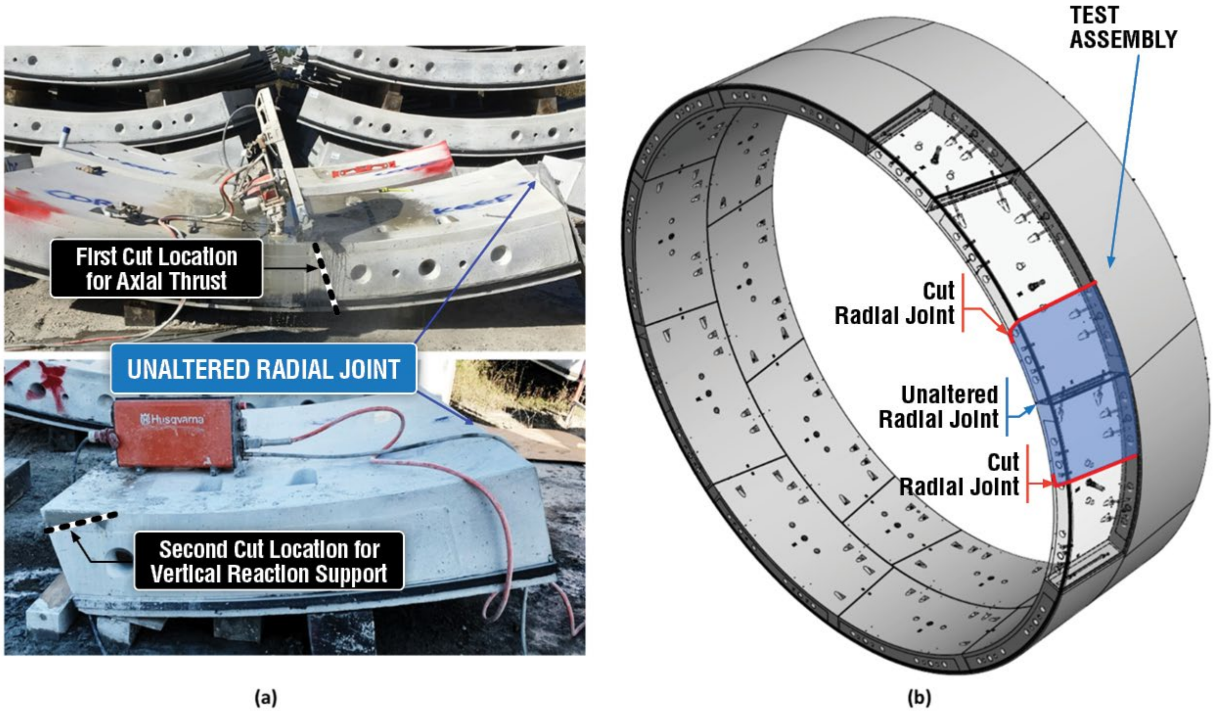

Figure 3-2. (a) On-site segment cutting and (b) test assembly configuration.

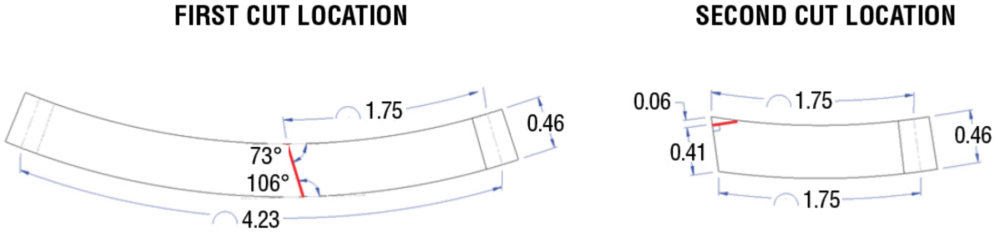

Figure 3-3. Segment cutting detail (dimensions in m).

The joints examined in this study are illustrated in Figure 3-4. Each ring consists of ten segments with flat ends (8 rhomboidal segments, 1 counter key and 1 key) and ten joints. The radial joints are oriented at an 8-degree skew (Figure 3-5). Assembly of segments at the radial joints is aligned with a steel guide rod located at the geometric center of each segment (Figure 3-5). The 40 mm

---

[4] The use of this procedure is not a Federal requirement.

diameter guide rods are located within a pocket with a diameter of 41.6 mm, thus preventing any localized bearing at the region. Segments are connected at each radial joint with two bolts offset at 510 mm and skewed at 29° as shown in Figure 3-5. Note that the bolts are located at the mid-thickness of the segment instead of the center of joint contact area. In practice, the bolts are often removed after all segments are in place, to mitigate the risk of loosening and detachment during service. The longitudinal joints have a raised (4.8 mm) region which is in contact with the adjacent segment. This region is referred to as the contact surface and measures 1800 mm by 276 mm. The contact surface is eccentric from the centroid of the section by 4.8 mm toward the intrados as shown in Figure 3-5.

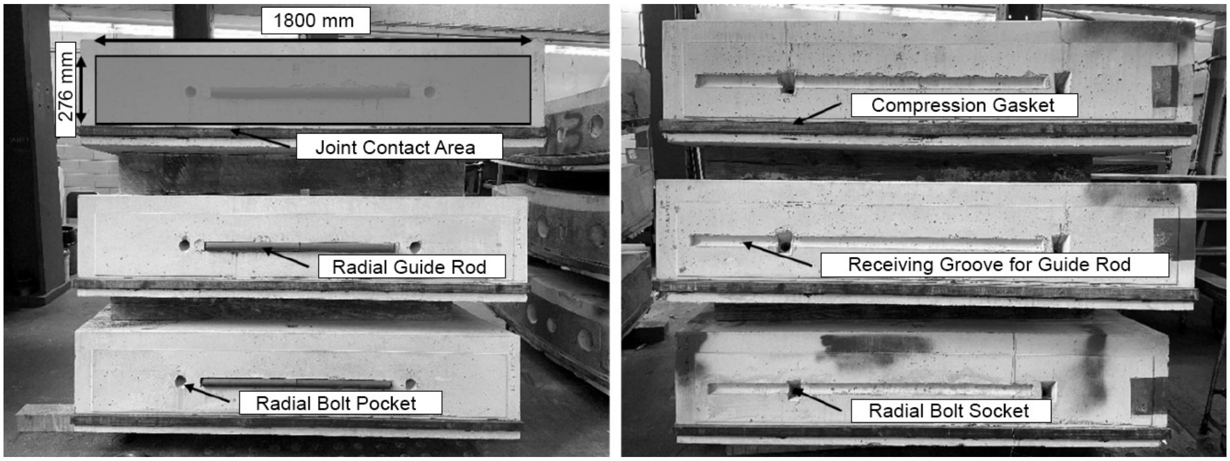

Figure 3-4. Joint face details from test sections.

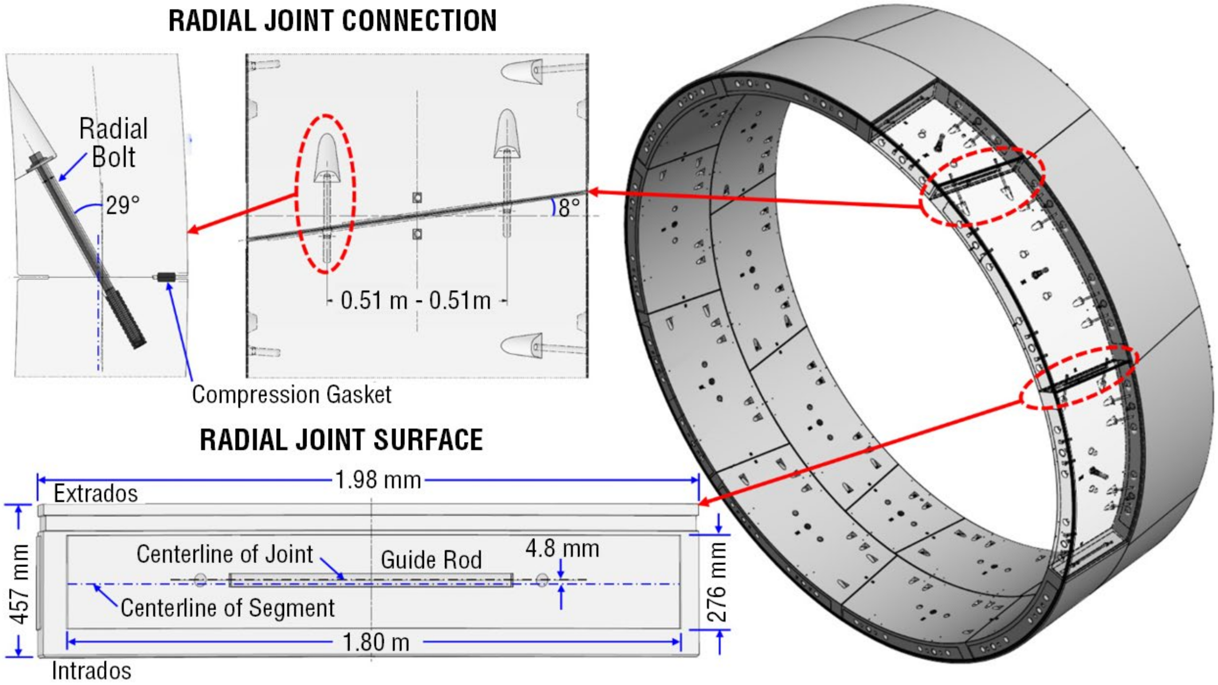

Figure 3-5. Joint connection of CBBT ring.

3.2.2. Test Setup and Assembly

The axial and bending loads at the radial joint were simulated by connecting two segments in an assembly. The radial joint and segment ends comprising the joint was unaltered. The axial thrust was applied with two 1.3 MN capacity through-hole jacks, which provided horizontal loading using two outbound post-tensioning bars as shown in Figure 3-6.

(a) FRONT ELEVATION OF ASSEMBLY (SOUTH SIDE)

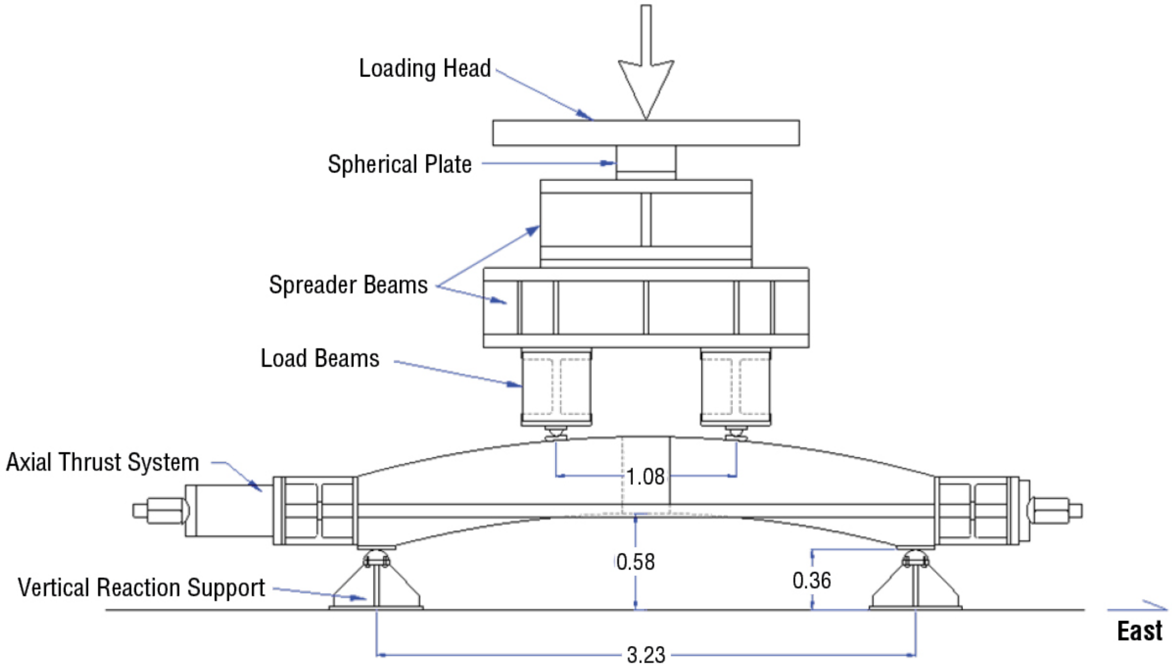

(b) PLAN VIEW OF ASSEMBLY (LOAD FRAME EXCLUDED)

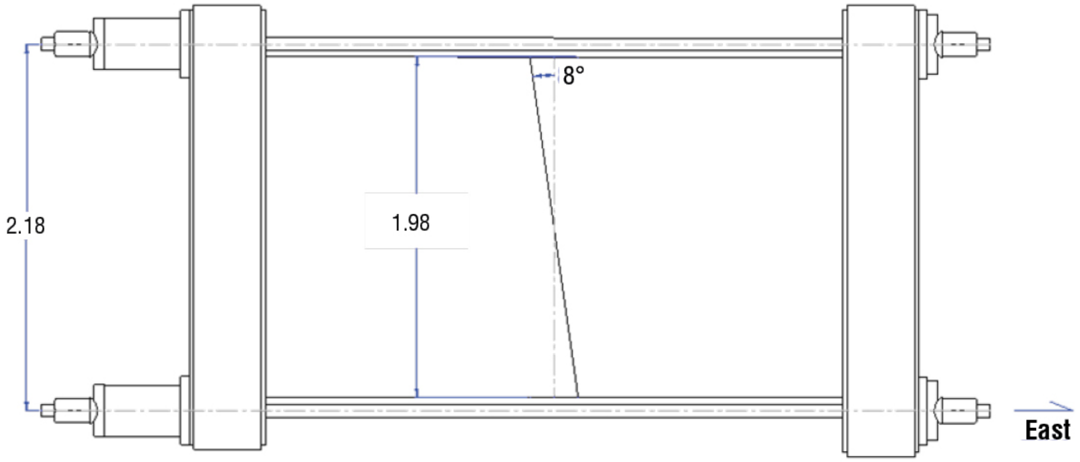

Figure 3-6. (a) Elevation view and (b) plan view of test configuration (units: m)

The axial load was applied to the cut surfaces, which were fabricated parallel to the radial joints. Joint flexure was generated simultaneously by the eccentric axial load and a vertical load applied using a Baldwin 22 MN capacity universal testing machine[5]. The vertical load was spread to create 1/3-point flexural loading on the segments. The full setup is illustrated in Figure 3-7.

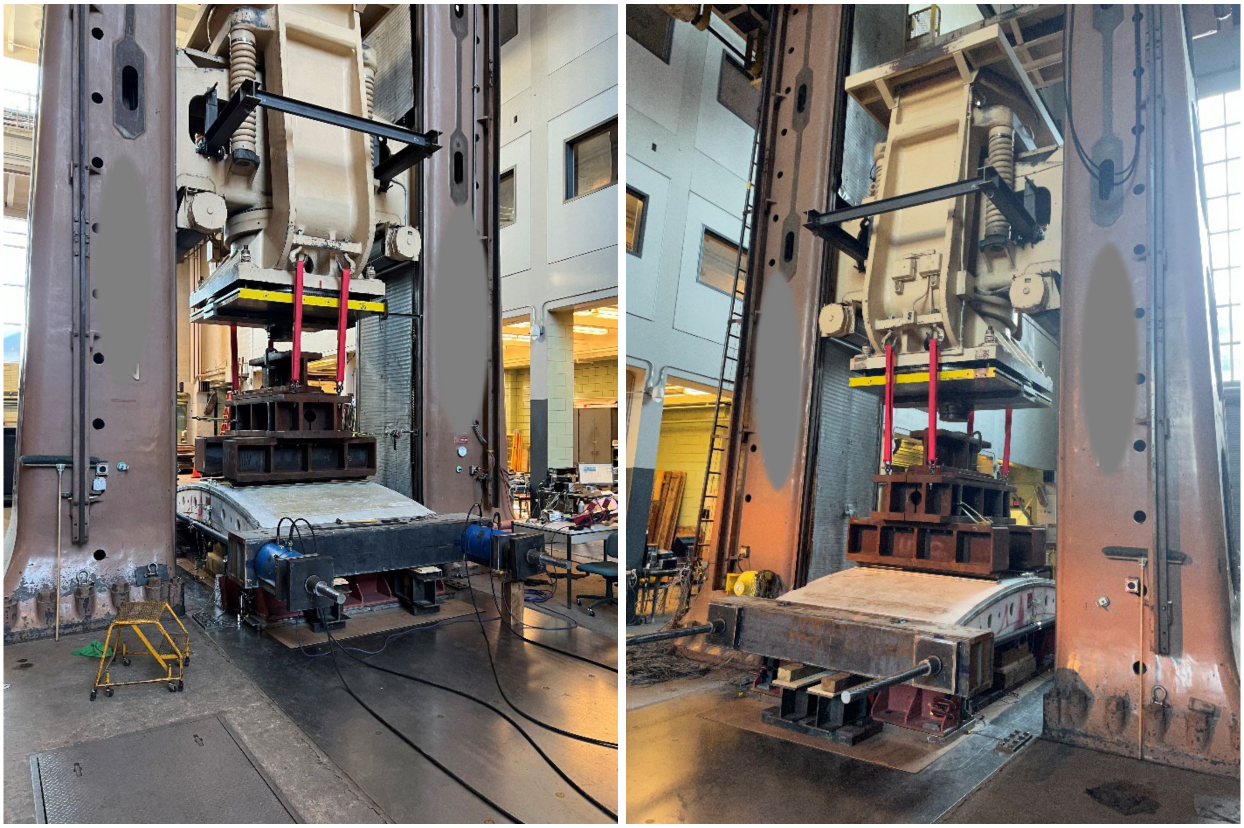

(a) (b)

Figure 3-7. Radial joint test assembly: (a) west side and (b) east side.

3.2.3. Instrumentation

Assemblies were outfitted with linear variable differential transformers (LVDTs) to measure joint openings, rotation meters to compare with LVDT data, displacement transducers for monitoring purposes, surface strain gages for monitoring purposes and bolt strain gages to measure the strain in bolts. The layout of LVDTs (L*i*, where *i* is the sensor number), vertical and horizontal displacement transducers (VD*i* and HD*i*) and rotation meters (R*i*) is shown in Figure 3-8. The bolt strain gages were installed in a 1-mm predrilled hole at the depth of 64 mm from the bolt head.

---

[5] The name of the equipment used is included for informational purposes only and is not intended to reflect a preference, approval, or endorsement of any one product or entity

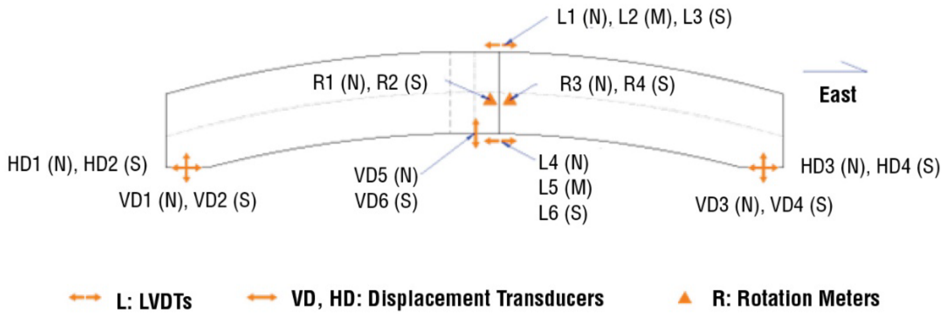

Figure 3-8. Assembly instrumentation layout (N: North, M: Middle, S: South).

The rotation was measured through LVDTs, while the rotation meters were only used as a reference to compare with the LVDT data due to relatively low precision. The calculated rotation using LVDT data can be expressed as:

$$\varphi = \frac{1}{3} \cdot \left(\frac{(L_4 - L_1)}{d_1} + \frac{(L_5 - L_2)}{d_2} + \frac{(L_6 - L_3)}{d_3} \right) \tag{3-7}$$

where L_1 through L_6 are the displacement measured by LVDTs, and d_1 through d_3 are the distance between top and bottom LVDTs. It is important to note that the joint is at an 8-degree skew. The nonlinear geometric action was not directly examined.

3.2.4. Testing Procedure

To apply realistic loads to the joint, a multistep loading procedure was conducted. The initialization consisted of aligning the panels, installing the radial bolts loosely in their pockets, and supporting the panels on temporary vertical jacks. The joint assembly geometry applied vertical force F_y, horizontal force F_x and dimensions including eccentricity e are shown in Figure 3-9. The axial thrust system was then engaged to apply adequate axial load to overcome the moment at the joint induced by self-weight of the segment. The axial load was stepwise increased to the target axial thrust force needed for each test. During each step the hogging moment generated by the eccentricity of the horizontal load was counterbalanced by the vertical load to ensure that a net zero moment was present at the joint. When radial bolts were used, they were tightened when subjected to 674 kN/m axial load. This level was chosen based on preliminary observations which indicated that the gap between the two segments generated by the gasket compression, was closed. Once the target axial load was reached, the axial jacks were set to load control that can remain at a constant axial load level, and joint flexure was applied using the vertical loads. Hogging was facilitated by reducing the vertical load, while sagging was facilitated by increasing the vertical load on the segments. The vertical loads were applied at a rate between 22 and 89 kN/min.

3.3. Joint Rotation Model

Based on the test configuration, the load application can be simplified as shown in Figure 3-9. The vertical load, F_y, provides positive bending moment, and the horizontal load, F_x, due to its eccentricity, provides negative bending moment. The expression of applied moment at the joint can be expressed as:

$$M = \frac{F_y \cdot L_1}{2} - F_x \cdot e$$
$$(F_x = N) \tag{3-8}$$

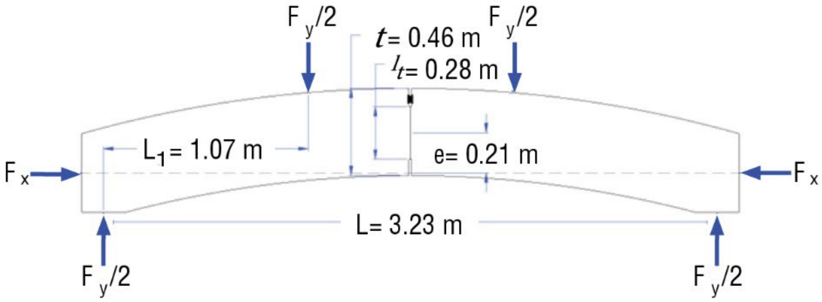

Figure 3-9. Load application configuration.

3.4. Test Results

The following sections describe the observed joint moment-rotation behavior. The detailed measurements of bolt and gasket testing are provided in Appendix D.

3.4.1. Elastic Moment-Rotation Behavior

The results of the testing program are examined relative to elastic material behavior and nonlinear joint opening response. The Janssen model predictions are included to provide a relative comparison for each test.

An initial series of joint rotation tests were conducted where the stress levels were maintained below the elastic compressive stress of the concrete. The $M - \varphi$ behaviors of these joints with and without bolts at five axial force load levels are presented in Figure 3-10 to Figure 3-14. At each axial load level and upon reaching M equals 0 per equation (3-8), F_y was gradually reduced to induce a negative moment (per equation (3-8)) (Figure 3-1). The maximum achievable negative moment, determined by setting F_y equals 0 in equation (3-8), is limited by the test setup, i.e., F_y was applied only in gravity direction. F_y was then increased to apply a positive moment. The responses are nonlinear due to decompression and opening of the joint, when the rotation exceeds the criterion for the closed/opened joint.

The $M - \varphi$ responses over the range of N values employed during testing show the following. The positive $M - \varphi$ behavior is practically linear while the negative $M - \varphi$ response exhibits a nonlinear response, i.e., decreasing rotational stiffness with increasing rotation at rotations lower than the expected opening values. While subtle differences exist, the radial joint generally exhibits similar magnitudes of rotational stiffness during positive M and negative M loading. The noted exception is at very low loads where rotational stiffness is greater during negative M loading than during similar magnitudes of positive M loading. Rotational stiffness increases considerably with increasing N during both positive M and negative M loading. This is evident both during full joint contact (closed joint) and partial contact (open joint). The Janssen model predicts a much different $M - \varphi$ response and considerably higher joint rotation stiffness than observed experimentally for $N \leq 1460$ kN/m. Janssen's model matches quite well with observed $M - \varphi$ response when $N \geq 1850$ kN/m.

The tests with and without bolts were performed on different assemblies. The assemblies with and without bolts generally exhibit similar $M - \varphi$ behavior. The use of bolts should conceptually increase the rotational stiffness since the bolt provides a spring resistance at an eccentricity from the compression face. The initial elastic rotational stiffness during negative M loading is greater with bolts, in all cases except for the low 674 kN/m axial load case. During positive M loading, however, the use of bolts results in a lower rotational stiffness. This is an unexpected result but could be associated with the location of the radial bolts relative to the compression zone in each bending direction. For example, since the bolts are located above the centroid of the contact surface, they will have a larger moment arm in the negative bending direction than in the positive bending direction. This difference in moment arm may impact how they influence the rotation stiffness.

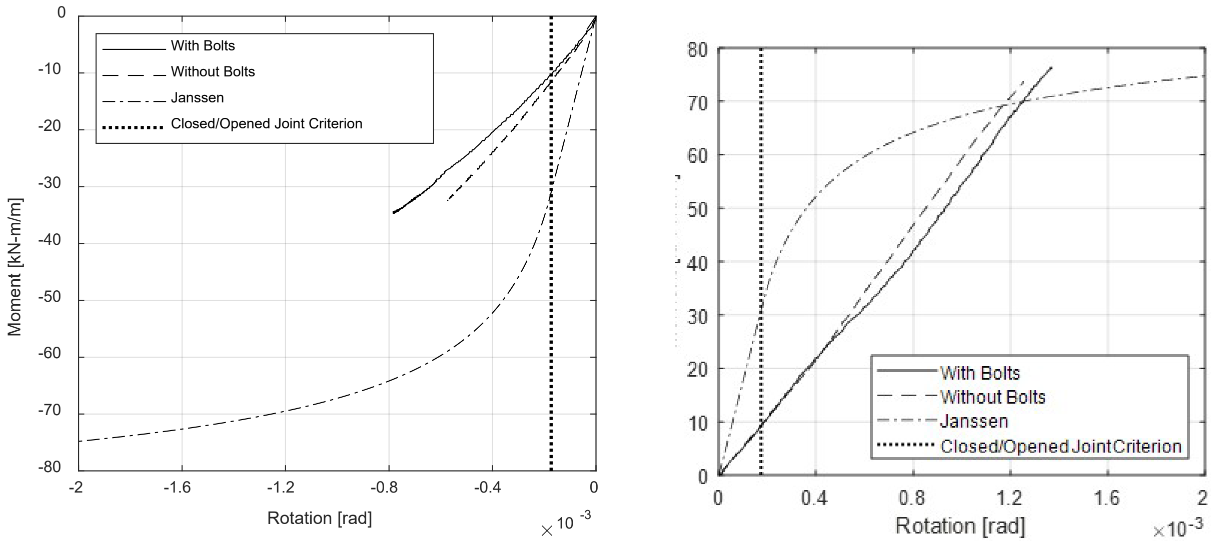

(a) (b)

Figure 3-10. Negative (a) and positive (b) moment-rotation curves for N = 674 kN/m axial force level.

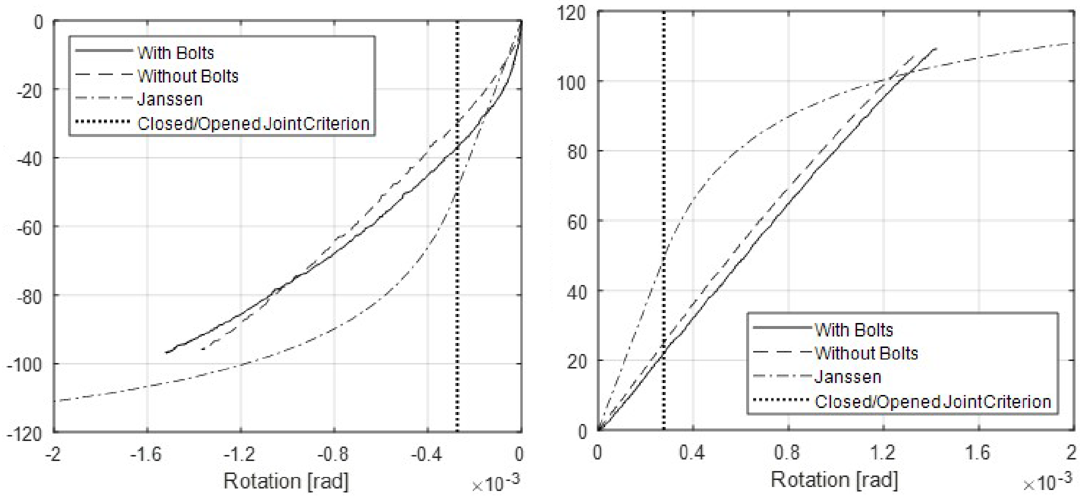

(a) (b)

Figure 3-11. Negative (a) and positive (b) moment-rotation curves at N = 1070 kN/m axial force level.

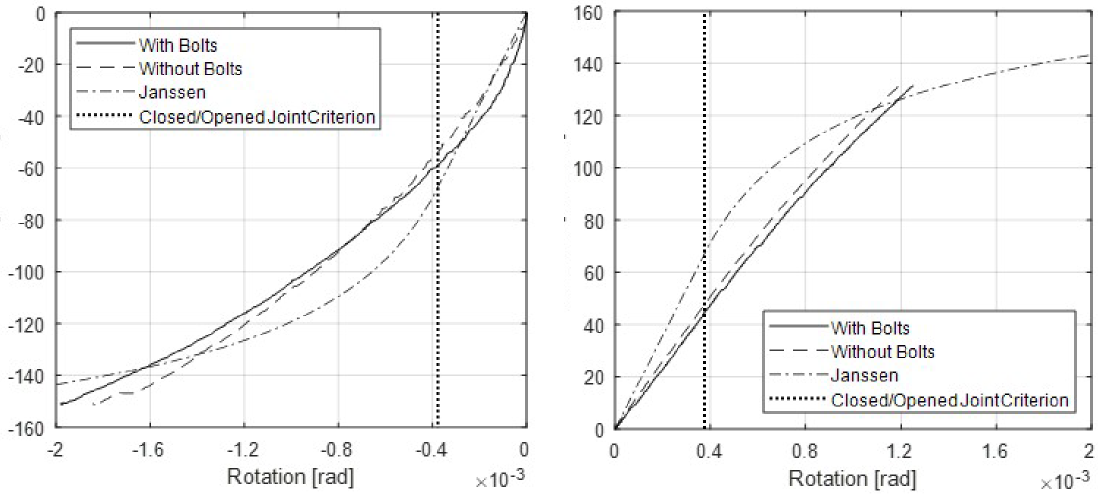

(a) (b)

Figure 3-12. Negative (a) and positive (b) moment-rotation curves at N = 1460 kN/m axial force level.

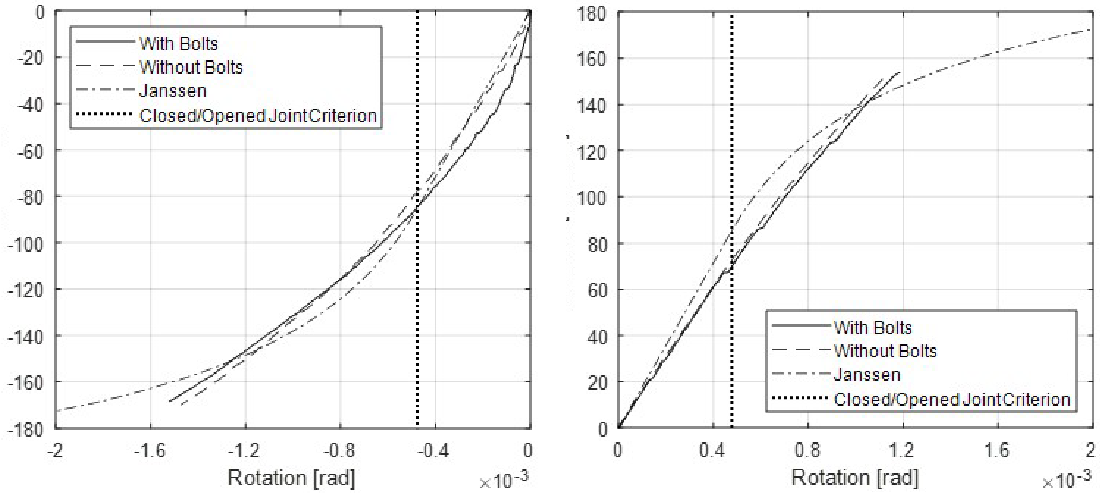

(a) (b)

Figure 3-13. Negative (a) and positive (b) moment-rotation curves at *N* = 1850 kN/m axial force level.

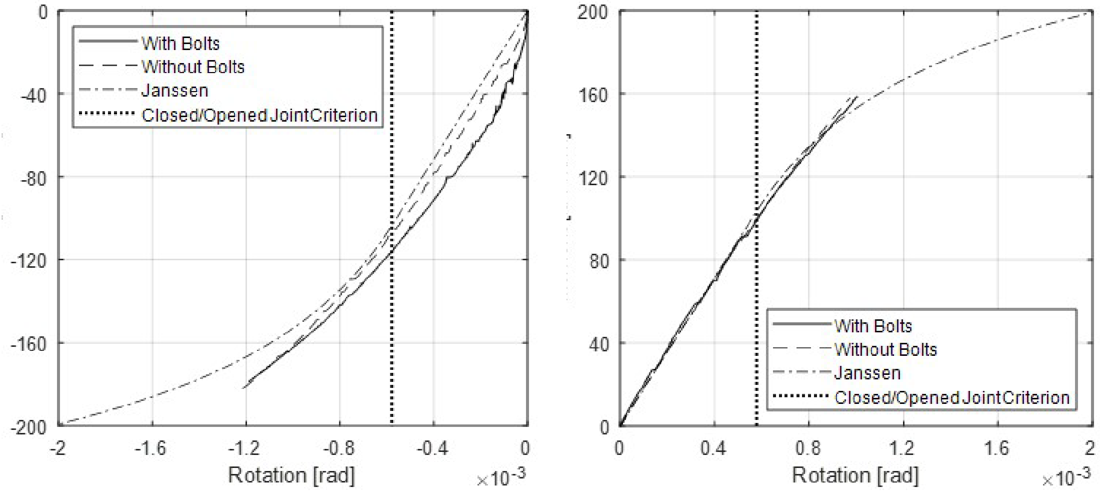

(a) (b)

Figure 3-14. Negative (a) and positive (b) moment-rotation curves at *N* = 2250 kN/m axial force level.

The secant rotational stiffness for each experimental case was determined as summarized in Table 3-2. To compare with the Janssen model, the rotational stiffness is determined at the expected joint opening rotation for each axial load level. The rotation levels at which the stiffness values are determined are summarized in Table 3-2. The expected joint rotation at opening is based on equation (3-6).

Table 3-2: Secant joint rotational stiffness at expected joint opening rotation.

Axial load N [kN/m (total axial kN)]	Expected Joint Rotation at Opening [x 10^{-3} rad]	Measured joint secant rotational stiffness [MN-m/m/rad]			
		$-M$ with bolts	$-M$ without bolts	$+M$ with bolts	$+M$ without bolts
674 (1330)	0.174	57.1	66.8	56.3	57.4
1070 (2110)	0.275	130	105	82.1	92.2
1460 (2890)	0.376	151	139	120	128
1850 (3670)	0.477	173	165	152	155
2250 (4450)	0.587	196	183	173	176

The secant rotational stiffness for each axial load level with and without bolts in both negative and positive bending is plotted in Figure 3-15. The Janssen rotational stiffness of the joint at opening (per equation (3-3)) is independent of axial load and for the geometry and measured constitutive properties is estimated to be 179 MN-m/m/rad. In comparison, the elastic stiffness of the solid portion of the segment is estimated to be 539 MN-m/m/rad. As illustrated, the measured stiffness increases with axial load level. This behavior is not captured in the Janssen model. The stiffness values are also presented as relative to the Janssen model by plotting the ratio of measured joint rotational secant stiffness compared to theoretical solutions of joint stiffness and segment stiffness in Figure 3-16. The segment stiffness is determined based on the elastic rotational stiffness of the entire segment cross section. Once the joint is open, Janssen's model indicates that the rotational stiffness increases with higher axial force level, as expressed in equation (3-4).

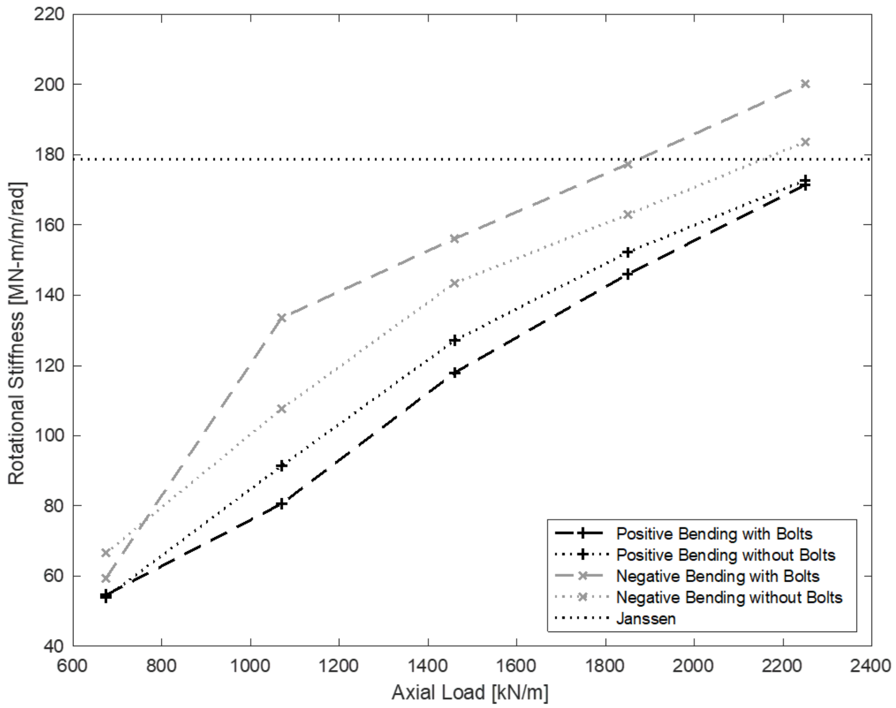

Figure 3-15. Secant rotational stiffness at expected opening rotation under various axial load levels.

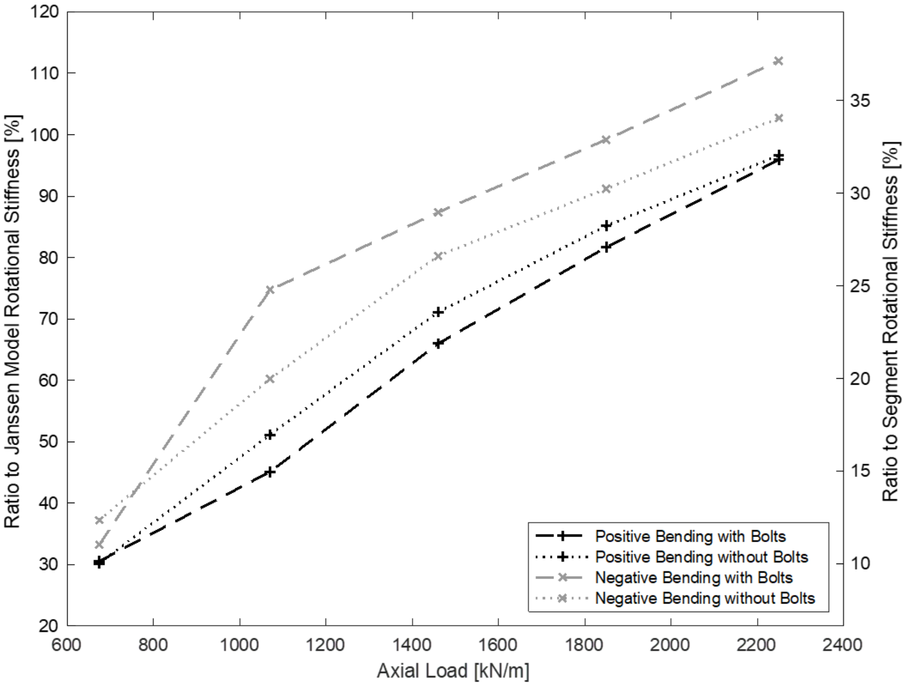

Figure 3-16. Ratio to the rotational stiffness of Janssen model and SFRC segment.

3.4.2. Moment-Rotation Behavior Beyond Expected Opening

The positive moment-rotation behavior at three axial force levels is plotted in Figure 3-17. These tests were conducted to joint rotation levels significantly greater than the assumed rotation at the joint opening. The theoretical solutions based on Janssen's model are also plotted. The tangent stiffness was computed through the rotation history and compared with Janssen's model. As shown in Figure 3-18, the initial measured stiffness is lower than Janssen's prediction but becomes greater than Janssen's prediction at rotations greater than approximately 0.001 radians. The experimental results show considerably greater eventual joint moment capacity than is estimated by Janssen's model. The Janssen model provides a reasonable estimate of joint rotation stiffness up to 0.005 rad for $N \geq 1460$ kN/m. The tests were stopped when the response exhibited low rotational stiffness due to stability concerns in the laboratory.

The damage to the joint for each case was minimal. Following the test, the assembly was removed and photos of the contact surfaces were taken. Damage consisted of hairline cracking (less than 0.1 mm) at the compression face of the contact area. Localized cracks greater than 0.1 mm were observed around the radial bolts as illustrated in Figure 3-19. The close-in damage details marked in Figure 3-19 are presented in Figure 3-20. Damage only occurred within the joint face, thus observations of when it occurred was not available.

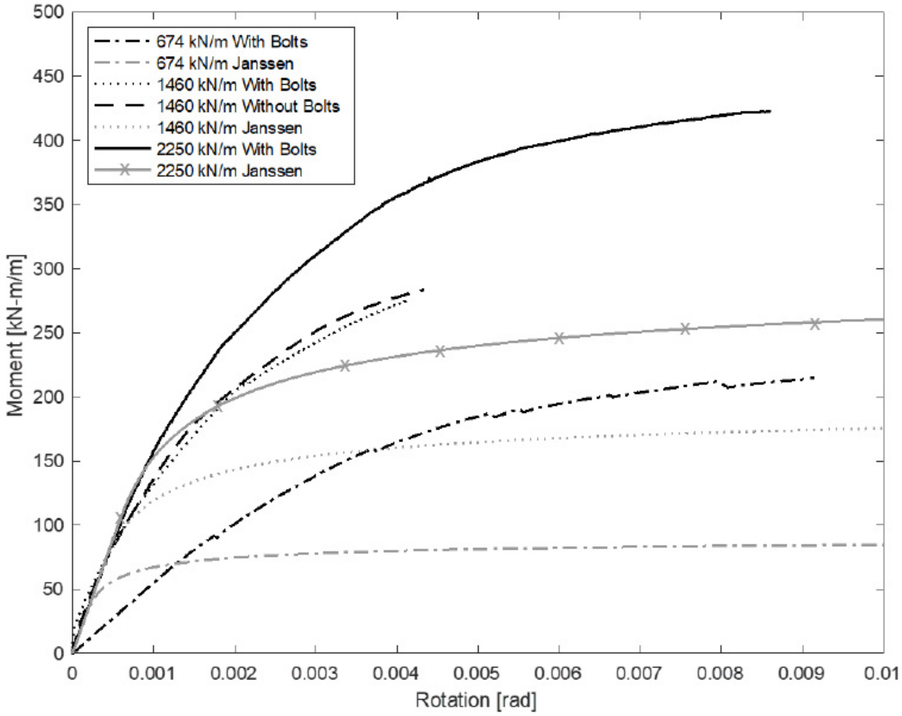

Figure 3-17. Moment-Rotation response to large rotation levels.

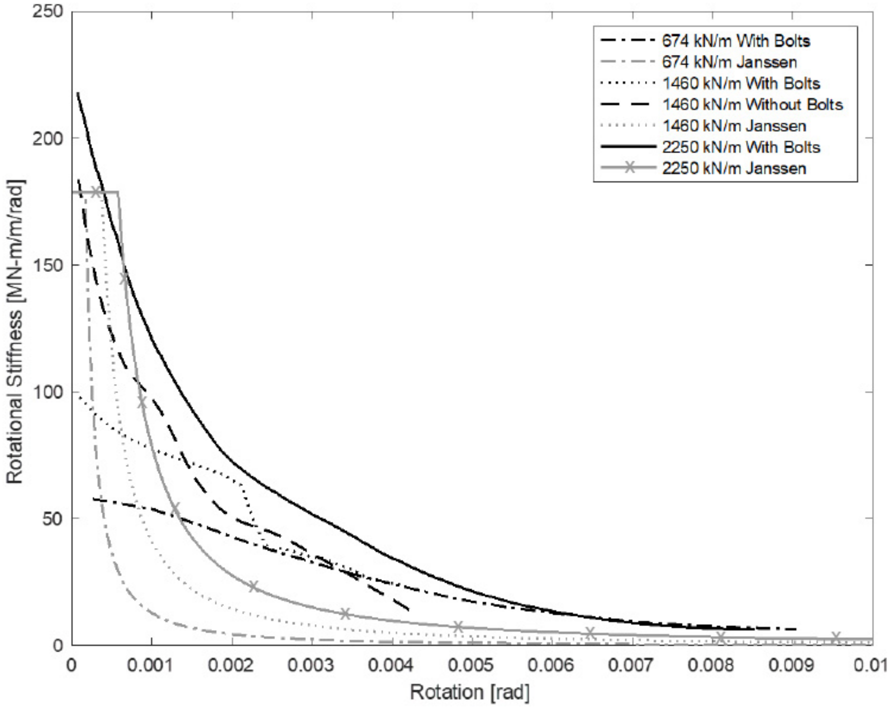

Figure 3-18. Rotational stiffness response to large rotation levels.

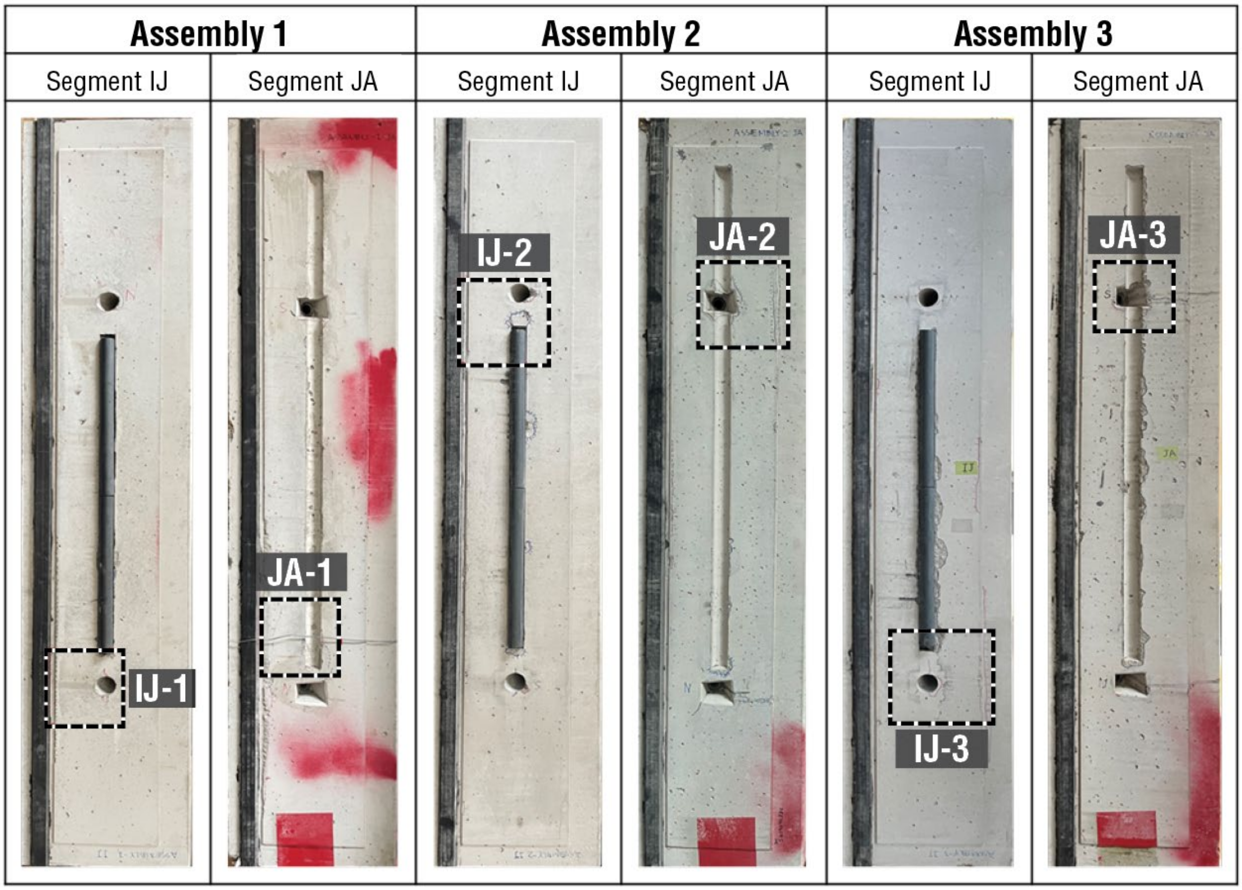

Figure 3-19. Post-test damage observations on joint.

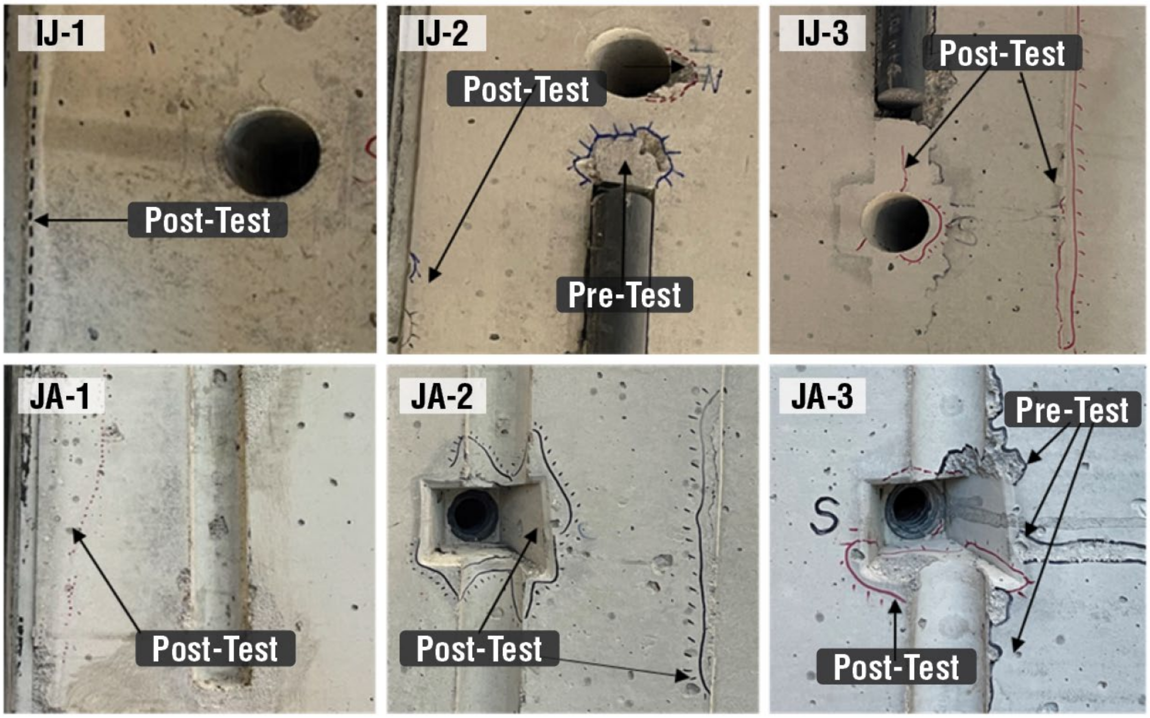

Figure 3-20. Damage details as marked in Figure 3-19.

3.5. Implications on Current Joint Moment Rotation Understanding

The results from experimental testing revealed increasing joint rotational stiffness magnitudes with increasing axial (thrust force) loading both when joints are closed and open. At axial load levels less than 2000 kN/m, the measured joint rotational stiffness at incipient opening was found to be less than that predicted by Janssen's model. To this end, Janssen's model overestimates joint rotation stiffness for these axial load levels. For the highest axial load level tested (2250 kN/m), the measured joint rotation stiffness effectively matched that predicted by Janssen. For design practice context, axial load levels of 2000 kN/m would correspond with ground loads at tunnel depths of approximately 15 m (50 ft). To this end, the results suggest that joint rotation stiffness is less than estimated by Janssen's model in shallow, low cover scenarios. It is worth mentioning that these are a limited array of tests and extrapolation beyond the geometries and load levels tested should be made with caution.

Additional findings were that closed radial joints were found to be 20-40% stiffer when subjected to negative moment than similar levels of positive moment, at all axial load levels tested. The measured joint moment-rotation response results in a much higher moment capacity at given rotation levels after joint opening occurs, compared to what is predicted by the Janssen model. The Janssen model underpredicts joint moment capacity, resulting in a conservative prediction of the plateau moment capacity. The use of bolts does alter the rotational stiffness of the joint, however the change in behavior is minimal. Joint damage at large rotations (0.004 to 0.010 radians) was limited to hairline cracking of the contact surface. No damage would be visible on the intrados under these elevated demands thus limiting the potential for in-situ inspection.

The joint used in this study represents a typical tunnel joint connection and includes both radial bolts and a gasket. These two facets used for construction of tunnels are not directly considered in the Janssen model and should be accounted for in future joint rotation model development.

4 PRESSURIZED SALT PONDING DURABILITY TESTING

4.1. Introduction

The AASHTO Load and Resistance Factor Design (LRFD) Road Tunnel Design and Construction Guide specifications (2017)[2] suggest designing PCTL for a service life for the structure of 150 years. However, a review of the literature revealed little information about the durability performance of concrete segments, including reinforcement steel corrosion, over such a long period of time. Additional research may be helpful to understand the durability performance of concrete segments over long periods of time. Steel fiber reinforced concrete (SFRC) has been adopted by many owners for tunnel liners due to its mechanical properties compared to traditional concrete. However, the potential damage caused by fiber corrosion in tunnel segments is not yet fully understood. Therefore, investigation of chloride penetration into SFRC segments may be crucial for ensuring the long-term safety and reliability of tunnel structure.

Large-diameter road tunnels can be subjected to high external groundwater pressures. Typical test methods to examine chloride ion penetration into concrete are performed under atmospheric pressure. The influence of elevated pressure on chloride ion penetration is unclear. Further, a review of the literature revealed little information about chloride ion penetration, and the resulting corrosion, through concrete containing micro-cracking under hydraulic pressures. Additional study of chloride ion penetration, and resulting corrosion, through concrete containing micro-cracking under hydraulic pressures may be needed. Micro-cracking is generally permitted in segmental lining design, typically up to crack widths of 0.2 mm (AASHTO 2017[2]) and in some cases less than 0.10 to 0.15 mm. The presence of cracks could accelerate chloride ion penetration and reinforcement corrosion. However, the influence of micro-cracking is not considered in chloride ion testing and durability design calculations.

Pressurized salt ponding testing was performed on 15 SFRC cylinders cored from the tunnel segments of the Chesapeake Bay Bridge Tunnel (CBBT) project. This chapter details the test program conducted and the test results observed.

4.2. Current Practice

Durability design of concrete structures is performed using *fib* Model Code for Concrete Structures (2010) through a performance-based approach. The limit state associated with the chloride ingress in concrete structures is described as follows:

$$P_f(t_{SL}) = P\{C_{crit} - C(x, t_{SL}) < 0\} < P_d \tag{4-1}$$

where P_f is the probability of failure, C_{crit} is the critical chloride content to achieve depassivation of the reinforcement, $C(x, t_{SL})$ is chloride concentration at depth x at the end of design service life t_{SL}, and P_d is target failure probability. C_{crit} and $C(x, t_{SL})$ are usually expressed as total chloride content relative to the weight of the binder (cement) or to the weight of concrete mass. A reliable value of C_{crit} is important for durability design. However, there is no general agreement on appropriate C_{crit} to be used. C_{crit} values reported in the literature are scattered, ranging over two orders of magnitude from 0.04 to 8.34 percent total chloride by weight of binder (Angst et al., 2009; Ann & Song, 2007; Cao et al., 2019; Glass & Buenfeld, 1997). In North America and European countries, a common practice is to assume C_{crit} to be 0.4 percent by weight of the binder (RILEM, 1994). Test results presented here will be compared to this RILEM (International Union of Laboratories and Experts in Construction Materials, Systems and Structures) reference.

According to *fib* Model Code (2010), the ingress of chlorides in a marine environment is assumed to obey the modified Fick's second law of diffusion:

$$C(x,t) = C_s - (C_s - C_i) \cdot \left[erf \frac{x}{2 \cdot \sqrt{D \cdot t}}\right] \tag{4-2}$$

where $C(x,t)$ is the content of chlorides in the concrete (percentage by weight of the concrete mass) at a depth x and at time t, C_s is the chloride concentration at the concrete surface, C_i is the initial chloride content of the concrete, D is the apparent coefficient of chloride diffusion through concrete, and *erf* is the error function. D is one of the key parameters and can be determined based on field data obtained via field/lab testing methods. Commonly used methods include the AASHTO T259[6] (2002) salt ponding test, Nordtest NTBuild 443[7], AASHTO T277[8] rapid chloride permeability test, electrical migration techniques (NT BUILD 492), and resistivity techniques (Hooton, 2016). However, these testing methods are performed under atmospheric pressure. No literature was found that addresses the influence of pressure. Chloride transport in concrete is a complex process, involving mechanisms such as diffusion, convection, capillary absorption, and flow with water, accompanied by physical and chemical binding (Luping et al., 2012). If such complex internal processes are simplified, with the assumptions of homogenous material, uniform pore distribution, no chemical reactions or physical bonding between chloride ions and materials, and a simple diffusion mechanism governs the chloride ingress, then Fick's second law can be used to access the diffusion problem phenomenologically.

4.3. Test Program

4.3.1. Sample Preparation

In this study, 15-cylinder core specimens were retrieved from five full-scale SFRC tunnel segments (Figure 4-1). The SFRC mix design included a cementitious content of 445 kg/m^3 and a w/c ratio of 0.35. Multi-hook 4D steel fiber was used. The fiber content was 38.5 kg/m^3 with 61 mm length, 7.5 mm diameter and 80 aspect ratio for each fiber. The average 28-day compressive strength of the SFRC was 65 MPa. The average 28-day split tensile strength was 7.1 MPa. The SFRC cores were approximately 36 months old before the salt ponding testing.

---

[6] Use of AASHTO T259, Standard Method of Test for Resistance of Concrete to Chloride Ion Penetration, is not a Federal requirement

[7] Use of NTBuild is not a Federal requirement

[8] Use of AASHTO T277, Standard Method of Test for Electrical Indication of Concrete's Ability to Resist Chloride Ion Penetration, is not a Federal requirement

Each full-depth core was cut into three disk specimens. Each disk specimen is about 75 mm tall and 100 mm in diameter (Figure 4-1). All faces except the top surface of each disk specimen were coated by epoxy resin to ensure one-dimensional chloride ingress.

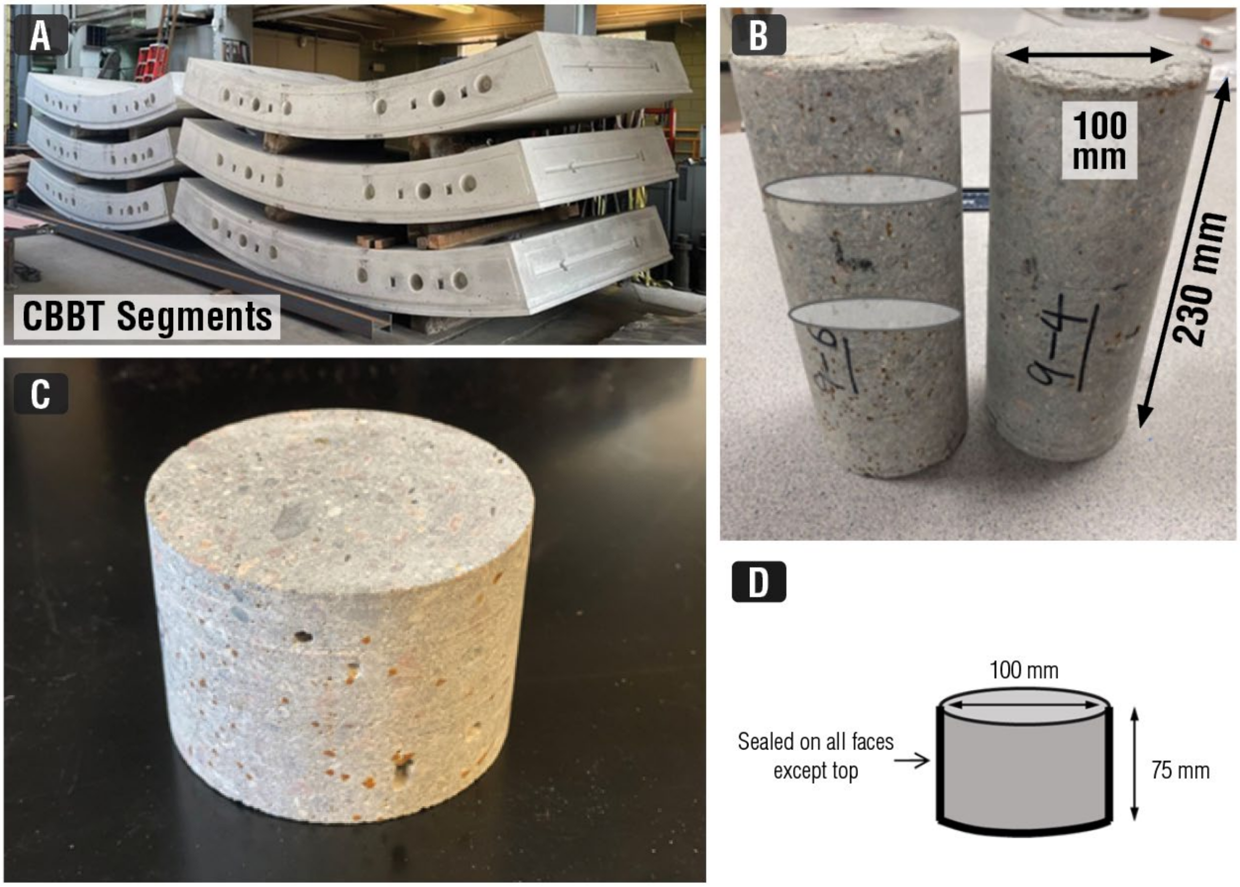

Figure 4-1. Sample preparation for pressurized salt ponding testing: (a) CBBT segments; (b) cored cylinder; (c) disk specimen; and (d) sealed locations.

4.3.2. Artificial Crack Generation

To study the influence of crack presence on chloride penetration, 18 SFRC disk specimens were cracked in a deformation-controlled indirect tension test. Figure 4-2 shows the indirect tensile testing to induce central cracks in SFRC specimens. The splitting tensile tests were performed using a displacement-control method with the actuator displacement rate of 0.02 mm/min. The crack opening at the center of the specimen surface was measured by extensometer in real-time as an estimate of average crack width.

Digital images of both sides of the specimen were captured. The final crack width of each specimen was determined based on an average crack width measured by imaging processing software as shown in Figure 4-3. The average crack width b_{ave} and maximum crack width b_{max} measured for each specimen are listed in Table 4-1. The distribution of b_{ave} for all specimens is shown in Figure 4-4. A mean value of 0.21 mm and a standard deviation of 0.06 mm were obtained. The crack widths on both sides of each disk are not consistent but the differences are below 0.2 mm in terms of b_{ave}. Cracks were usually initiated from one side and propagated through the other. Five disk specimens (20Day-100 kPa-CK1, 20Day-500 kPa-CK1, 40Day-100 kPa-CK1, 40Day-300 kPa-CK2, 60Day-500 kPa-CK2) only exhibit crack on one side without permeating through the specimen.

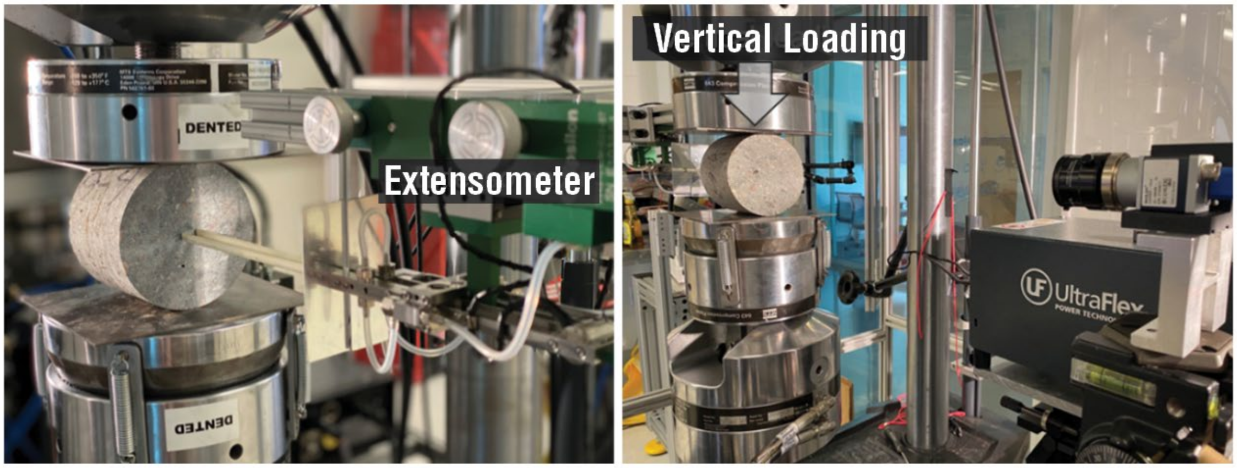

(a) **(b)**

Figure 4-2. Indirect tensile testing setup to induce cracking in SFRC specimen: (a) Extensometer to measure crack width and (b) camera to take crack photos.

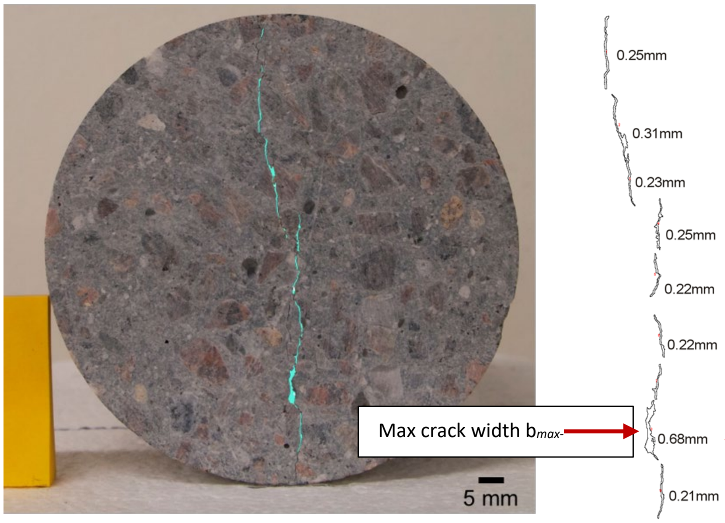

Average crack width:

$$b_{ave} = \frac{1}{n}\sum_{i=1}^{n} b_i = \frac{1}{n}\sum_{i=1}^{n} \frac{A_i}{L_i}$$

b_i = the width of the i^{th} crack section

n = the number of crack sections

A_i = the area of the i^{th} crack section

L_i = the length of the i^{th} crack section

(a) (b)

Figure 4-3. (a) Crack pattern and (b) measurement of crack width for one disk specimen.

Table 4-1. Crack widths of SFRC specimens.

Specimen	b_{ave} (mm)	b_{max} (mm)
20 Day-100 kPa-CK1	0.31	0.48
20 Day-100 kPa-CK2	0.33	0.51
20 Day-300 kPa-CK1	0.19	0.34
20 Day-300 kPa-CK2	0.28	0.68
20 Day-500 kPa-CK1	0.15	0.23
20 Day-500 kPa-CK2	0.25	0.28
40 Day-100 kPa-CK1	0.24	0.32
40 Day-100 kPa-CK2	0.29	0.53
40 Day-300 kPa-CK1	0.18	0.40
40 Day-300 kPa-CK2	0.27	0.58
40 Day-500 kPa-CK1	0.13	0.23
40 Day-500 kPa-CK2	0.14	0.23
60 Day-100 kPa-CK1	0.20	0.37
60 Day-100 kPa-CK2	0.21	0.40
60 Day-300 kPa-CK1	0.16	0.28
60 Day-300 kPa-CK2	0.20	0.36
60 Day-500 kPa-CK1	0.17	0.25
60 Day-500 kPa-CK2	0.13	0.30

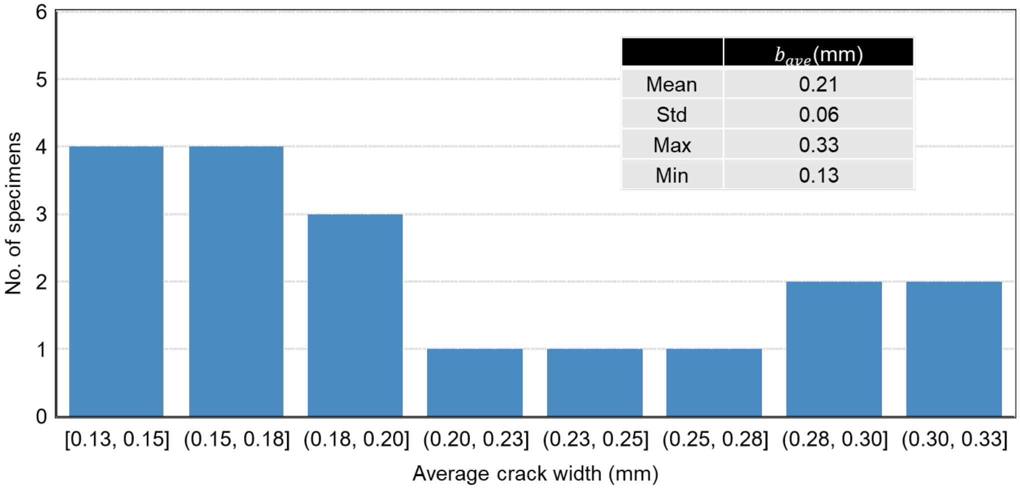

	b_{ave}(mm)
Mean	0.21
Std	0.06
Max	0.33
Min	0.13

Figure 4-4. Histogram and statistical information of crack widths.

4.3.3. Testing Arrangement

The test setup aimed to study chloride ion penetration into SFRC subjected to external groundwater pressures. The pressurized salt ponding test was conducted in general accordance with AASHTO T259[6], modified for different sample dimension, duration, and hydraulic pressure. Figure 4-5 shows the test fixture for the pressurized salt ponding testing. A total of 36 SFRC specimens, including 18 UCK (uncracked) specimens and 18 CK (cracked) specimens, were soaked in one open and two pressurized chambers with a 3.5 percent sodium chloride solution for 60 days. Table 4-2 summarizes the parameters used for the testing.

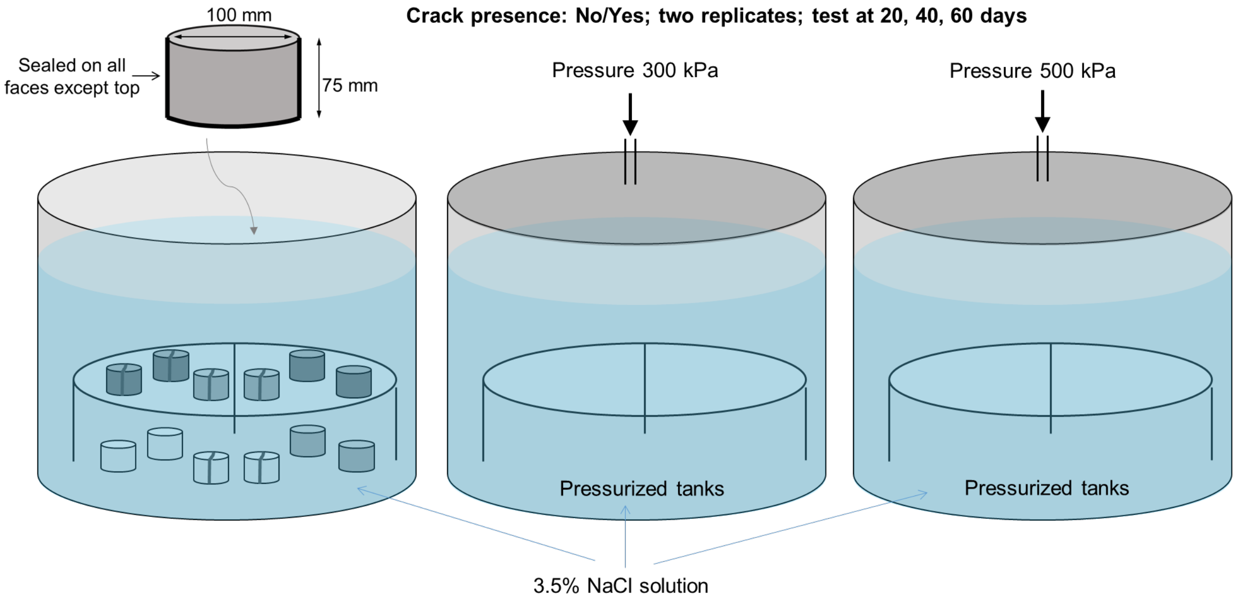

Figure 4-5. Pressurized salt ponding test setup (one open chamber and two pressurized chambers, each housing 6 UCK specimens and 6 CK specimens).

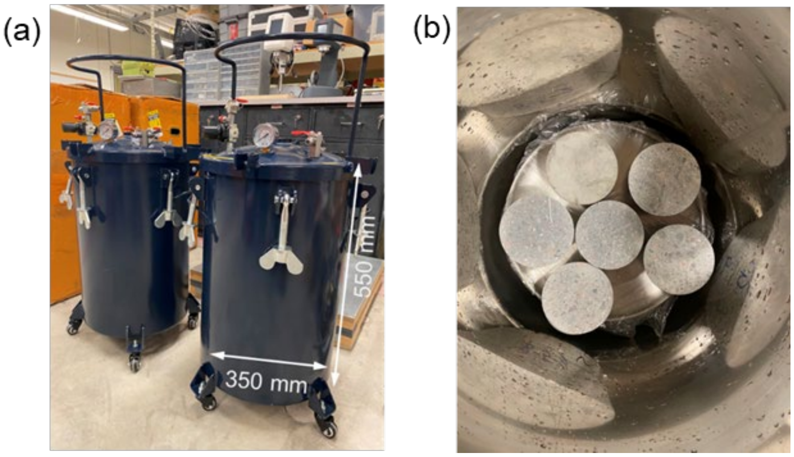

Figure 4-6. (a) Dimensions of the pressurized chambers and (b) specimen layout inside the chamber.

Table 4-2. Durability testing parameters.

Parameter	Magnitudes
Absolute (Abs) hydrostatic pressure [kPa]	100, 300, 500
Crack Presence	No, Yes (0.15 mm-0.35 mm)
Pressure duration [days]	20, 40, 60
Replicated samples	2
Total No. of samples	2x2x3x3=36

4.3.4. Measurement of Chloride Ingress

The hydraulic pressures applied in the pressurized chamber were continuously monitored to maintain constant levels. 12 SFRC specimens (6 uncracked and 6 cracked) were taken out for chloride analysis every 20 days. Each disk specimen was split in half for two types of analysis as shown in Figure 4-7. Part I of the freshly split portion was sprayed with 0.1 M silver nitrate (AgNO3) solution. The chloride penetration profile is visualized by the color difference on the cross-section surface. The chloride bonds with the silver to produce silver chloride which is a whitish substance. In the absence of chlorides, the silver bonds with the hydroxides in the concrete, presents a brownish color (Hooton, 2016).

The part II half disk was ground into powder samples at each depth Δx (2-5 mm). The powder samples were analyzed by ion chromatography (IC) technique to evaluate the chloride concentration at different depths. The IC measured the average concentration of chloride over a disc of diameter 100 mm. and thickness Δx. An average value of chloride percentage was reported, and the diffusion coefficients were calculated through Fick's second law.

Figure 4-8 shows the typical grinding procedure for SFRC specimens. The specimen was fixed on a base and a Dremel machine[9] equipped with a diamond grinding bit was used to pulverize the SFRC material. A vertical guide was attached to control the grinding depth as designed. After grinding, powder accumulated on the collecting paper, and 1 g powder sample was reserved for each layer. The 1g powder sample was first dissolved in deionized water to make a 40 ml solution. The solution was vibrated for 24 hours on an automatic vibrator and filtered to obtain a 10 ml solution. A 5 ml dilute solution was further made by mixing 2.5 ml filtered solution with 2.5 ml deionized water (Figure 4-9). The water soluble chloride in the 5 ml solution was quantified through ion chromatography analysis.

---

[9] The name of the equipment used is included for informational purposes only and is not intended to reflect a preference, approval, or endorsement of any one product or entity.

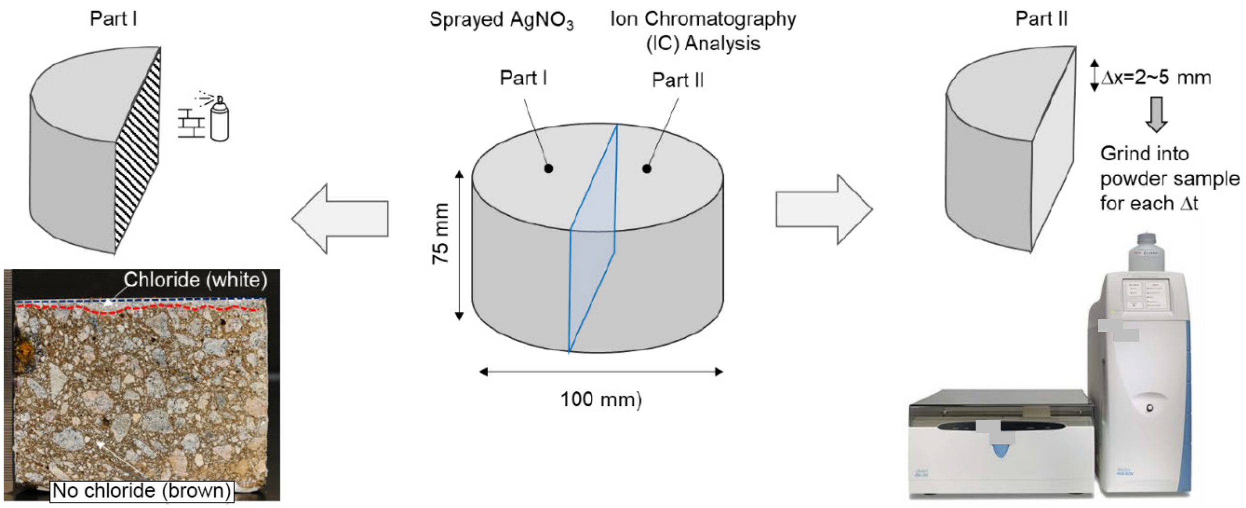

Figure 4-7. Chloride analysis procedure (Part I half disk is used for spraying $AgNO_3$, Part II half dish is used for IC analysis).

Figure 4-8. Grinding procedure to prepare sample for IC chloride analysis.

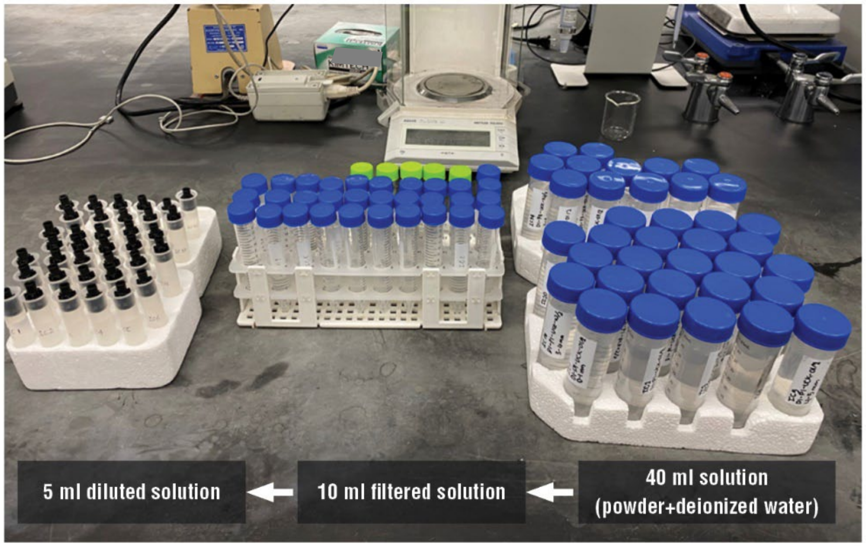

Figure 4-9. Preparation of solution for IC chloride analysis.

4.4. Test Results

4.4.1. Uncracked (UCK) SFRC Behavior

After subjecting disk specimens to pressurized saline solution for 20, 40 or 60 days, 0.1 M $AgNO_3$ solution was sprayed onto freshly split concrete specimens to visualize the chloride penetration profile. Figure 4-10 shows the color change of SFRC UCK specimens subjected to different pressure magnitudes and durations. The change of color is not clearly observed for all 20-day UCK specimens, indicating below threshold chloride concentration. However, it is known from the literature that the total chloride content at the color change boundary detected by silver nitrate varies widely, from 0.19 percent (Yuan, 2009) to 1.41 percent (Meck & Sirivivatnanon, 2003) by the mass of cement, and from 0.02 percent (Meck & Sirivivatnanon, 2003) to 0.5 percent (Otsuki et al., 1993) by mass of concrete, depending on the sample mix design and the measuring technique. Therefore, the quantitative chloride content within the SFRC specimens may need to be further investigated by other methods.

As shown in Figure 4-10(b), 40-day UCK specimens show less than 2 mm chloride penetration under 100 and 300 kPa. Approximately 3-5 mm chloride penetration depth was observed for 40-day UCK under 500 kPa pressure indicated by the formation of white regions near the top surfaces. The milk-white region near the center of the 40-day-500 kPa-UCK2 specimen is likely attributed to the dust adhering to the surface during the splitting process, and not due to the chloride ingress from the top free surface.

Two 60-day-100 kPa UCK specimens show approximately 3-5 mm chloride penetration depth. The chloride ingress fronts are not horizontal for 60-day-300 kPa UCK specimens, showing more chloride contents around the pores near the top surface. Pore structure tends to absorb water from penetration and thus attract more chloride ions during salt ponding. 60-day-500 kPa specimens show about 2 mm chloride penetration. Some areas close to the side boundaries also show whitish color after 60 days of exposure, indicating possible chloride penetration. This is mainly due to the imperfect sealing of the epoxy.

20Day-100kPa-UCK1 20Day-100kPa-UCK2

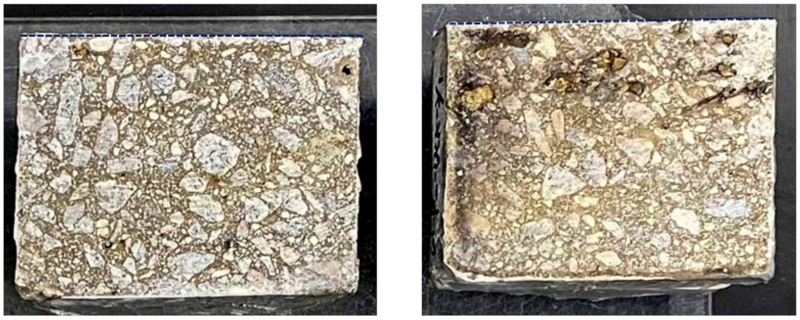

20Day-300kPa-UCK1 20Day-300kPa-UCK2

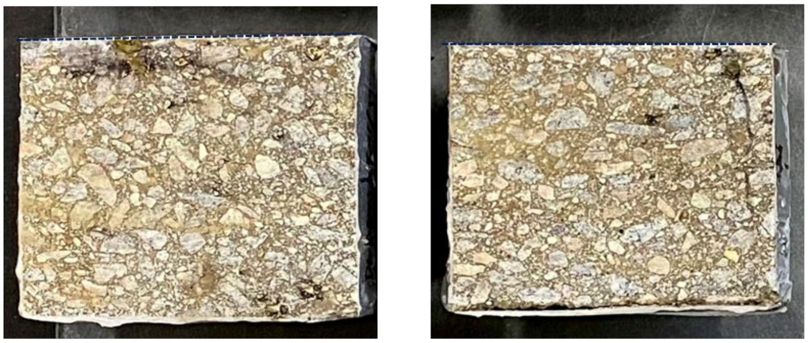

20Day-500kPa-UCK1 20Day-500kPa-UCK2

Figure 4-10(a). Chloride penetration through 20-day old UCK specimens visualized by spraying $AgNO_3$ solution (whitish substance indicates chloride presence while brownish color indicates absences of chloride).

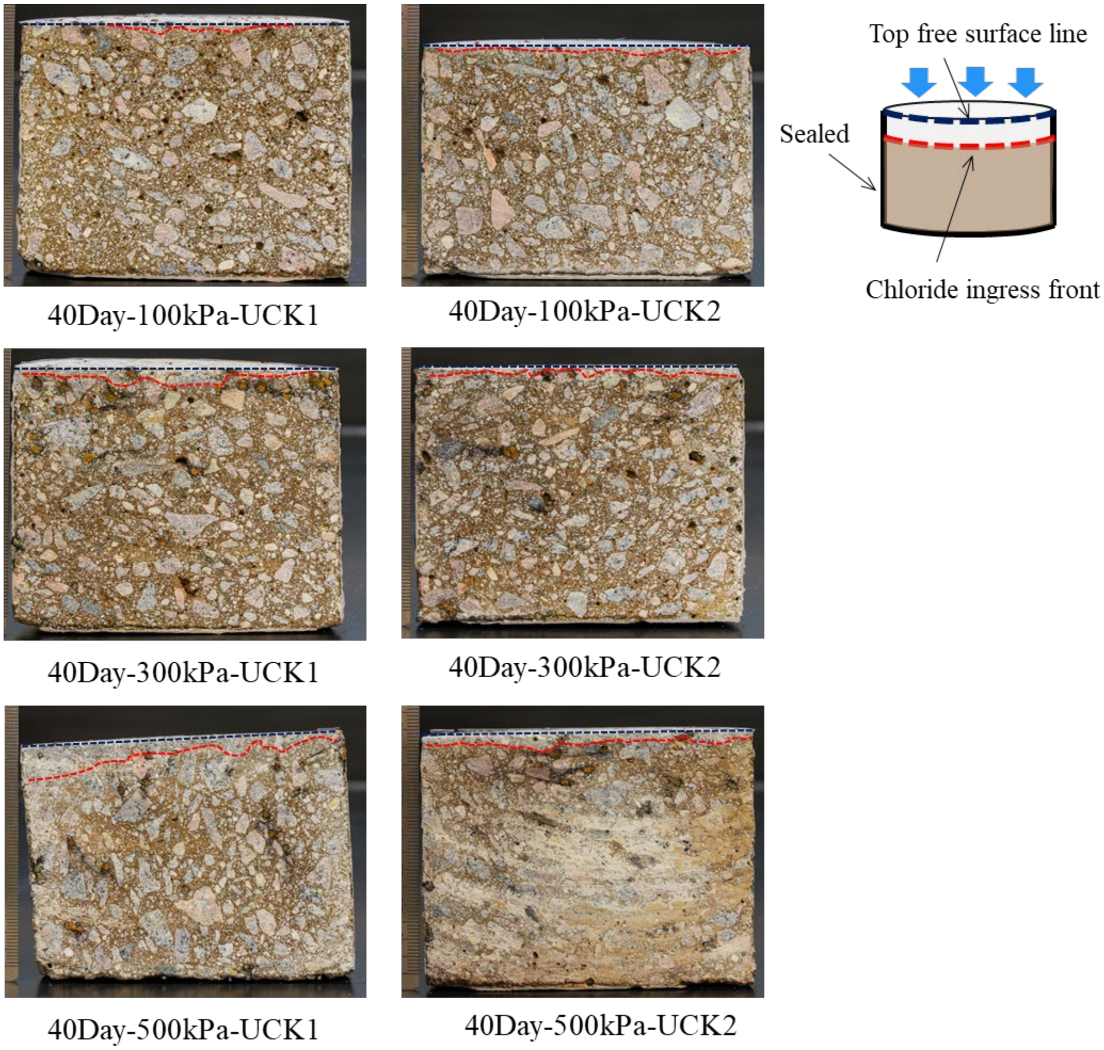

40Day-100kPa-UCK1

40Day-100kPa-UCK2

40Day-300kPa-UCK1

40Day-300kPa-UCK2

40Day-500kPa-UCK1

40Day-500kPa-UCK2

Figure 4-10(b). Chloride penetration through 40-day old UCK specimens visualized by spraying $AgNO_3$ solution (whitish substance indicates chloride presence while brownish color indicates absences of chloride).

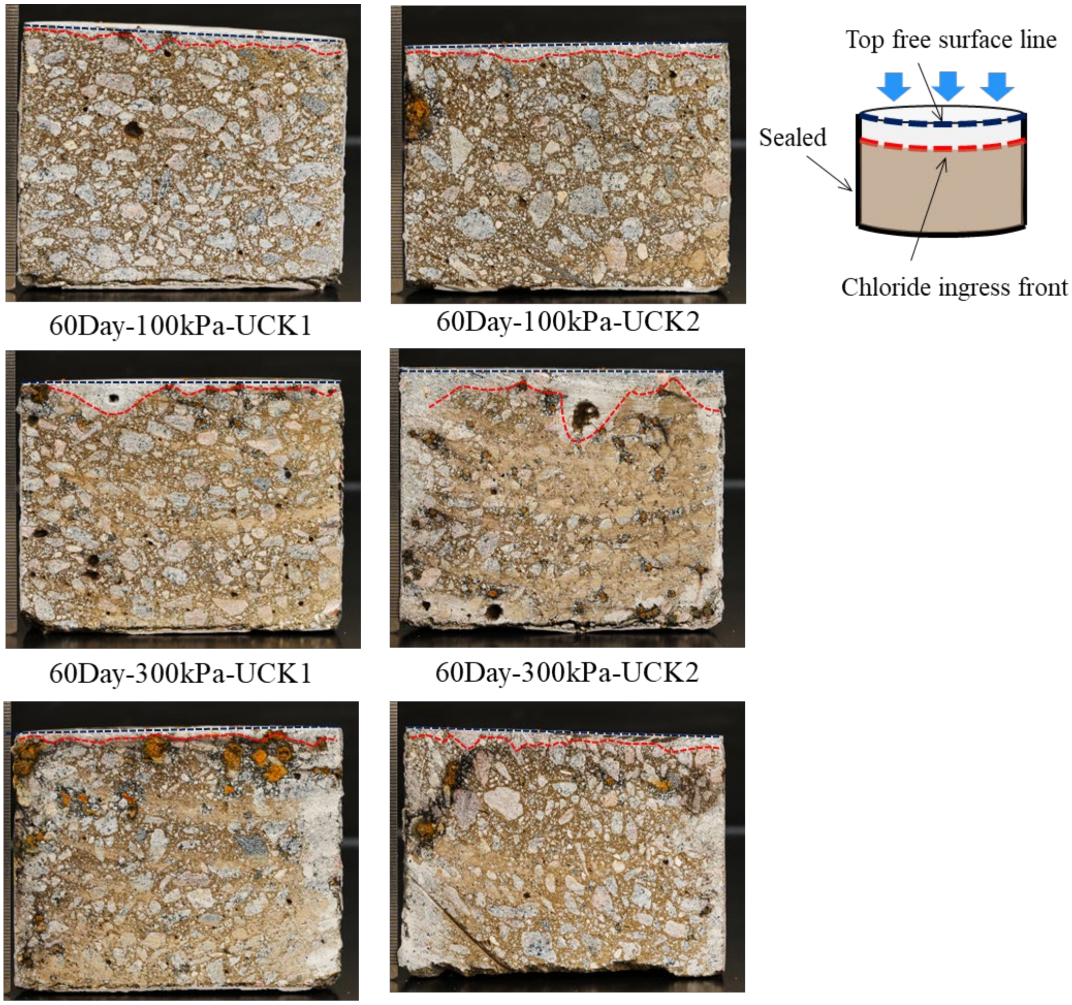

60Day-100kPa-UCK1

60Day-100kPa-UCK2

60Day-300kPa-UCK1

60Day-300kPa-UCK2

60Day-500kPa-UCK1

60Day-500kPa-UCK2

Figure 4-10(c). Chloride penetration through 60-day old UCK specimens visualized by spraying $AgNO_3$ solution (whitish substance indicates chloride presence while brownish color indicates absences of chloride).

To quantify chloride content within the SFRC specimens, the remaining SFRC disk specimen halves were used for Part II analysis as described in section 2.4. Chloride profiles were plotted showing chloride ion concentration (*C*) versus depth from the exposed surface as shown in Figure 4-11. The UCK specimens show similar chloride profile trends under various pressure levels. After 20 days of exposure to 3.5 percent NaCl solution, SFRC specimens exhibited 0.25 percent to 0.5 percent surface *C* in the 0-2 mm of the top surface, followed by a considerable decrease in *C* to approximately 0.1 percent at depth of 5 mm, followed by a gradual decrease approaching relatively low *C* less than 0.05 percent at specimen depths greater than 15 mm. The horizontal dash red lines shown in Figure 4.11 represent the C_{crit} value calculated based on 0.4 percent of weight of binder used in the SFRC mix design.

Similar decreasing with depth trends of chloride were observed for UCK specimens exposed for 40 and 60 days. In general, longer exposure time induced greater chloride penetration and surface chloride concentration. The increase in C with exposure time is more evident within the initial 8 mm depth of the specimens. The difference in C at different exposure times is lower at depths greater than 8 mm.

C generally increases with increasing exposure pressure. Higher chloride contents were measured at all depths in specimens immersed in 300 kPa and 500 kPa pressure compared to 100 kPa atmospheric pressure. However, the difference in C under 300 kPa and 500 kPa is not significant. During the grinding process, more pores were observed for 20Day-300kPa-UCK2, 40Day-300kPa-UCK1, and 60Day-300kPa-UCK2 specimens than others. This might have contributed to the relatively high C observed compared to the other specimens under the same pressure levels.

The apparent diffusion coefficient D and surface chloride concentration C_s were determined by fitting equation (4-1) to the chloride profiles. Table 4-3 summarizes D and C_s results for all UCK specimens. The diffusion coefficient varies from $3.3 \times 10^{-12}$to $38 \times 10^{-12} m^2/s$, and the surface chloride varies from 0.33 to 0.54 percent. The significant variability indicates the influence of the hydraulic pressure and duration of exposure on the durability of SFRC.

Generally, SFRC specimens under higher pressures show higher D than those under atmospheric pressure at all exposure times as shown in Figure 4-12. For instance, after 20 days of exposure, the diffusion coefficients of 300 kPa and 500 kPa specimens are about four times and eight times greater than that of 100 kPa specimens, respectively. This indicates a higher chloride penetration rate when SFRC linings are under high hydraulic pressures. In other words, the ability of SFRC linings to resist chloride penetration decreases with increasing hydraulic pressure.

D values remained constant with exposure time at 100 kPa pressure but varied for 300 kPa and 500 kPa specimens. There is no obvious trend of D changing with exposure time, although some previous studies reported a reduction of D with exposure time as a common phenomenon (Abbas et al., 2014; Costa & Appleton, 1999). In this case, this decreasing trend is not evident as the total duration time (60 days) is relatively short compared to months to years of measurement in the literature. The variation of D values observed for pressurized specimens is attributed to the combined effects of diffusion and convection under pressure and the inherent variability in the SFRC specimens.

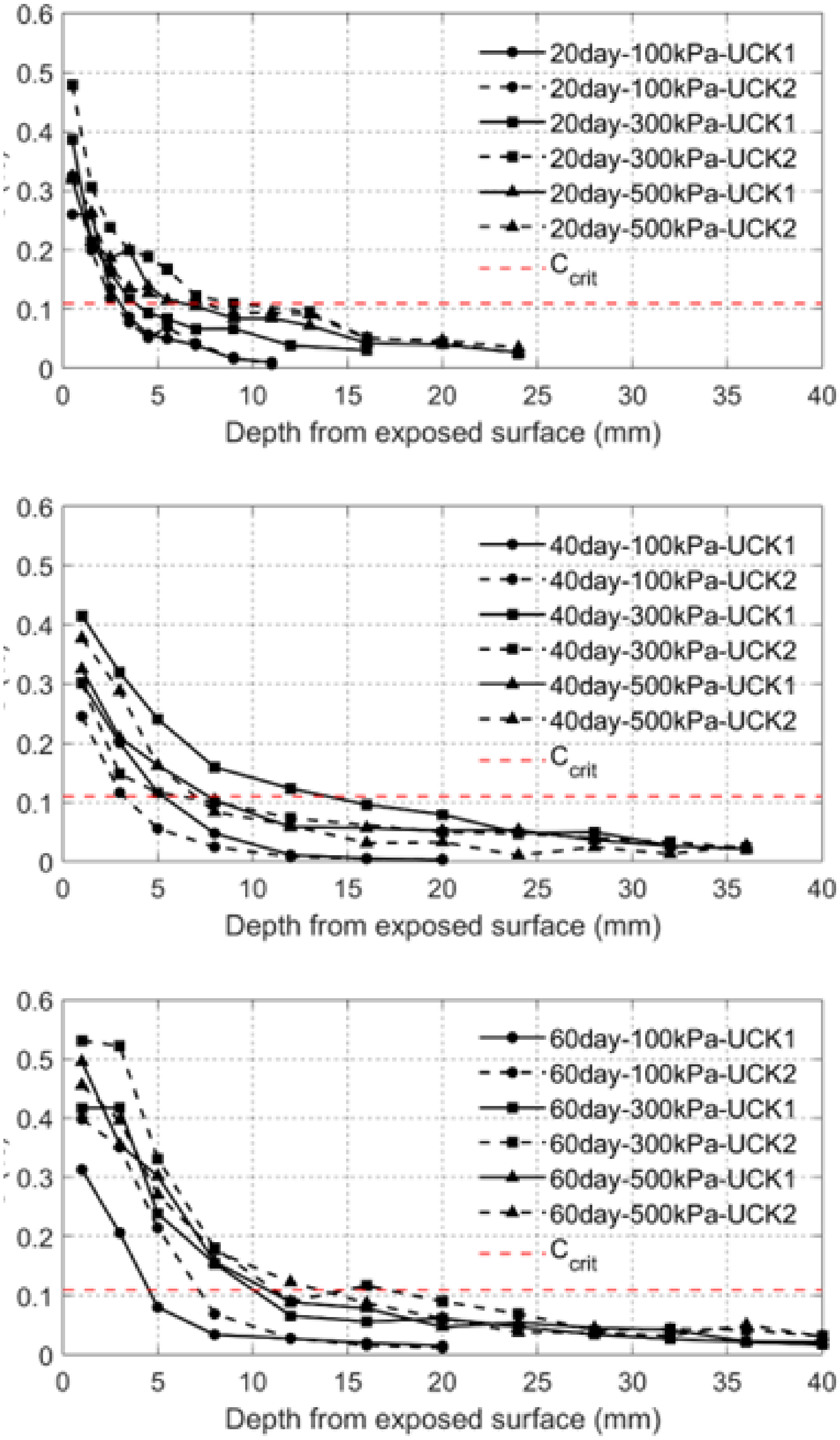

Figure 4-11. Chloride profiles for UCK specimens as a function of hydrostatic pressure magnitude (absolute) and pressure duration.

Table 4-3. Diffusion coefficient and surface chloride for UCK specimens.

Exposure time	20 days			40 days			60 days		
Abs pressure (kPa)	100	300	500	100	300	500	100	300	500
Diffusion coefficient D^* $(\times 10^{-12} m^2/s)$	3.3	13.6	27.9	3.5	20.9	37.7	3.4	11.3	32.6
Surface chloride C_s* (%)	0.33	0.44	0.35	0.33	0.38	0.38	0.43	0.54	0.50

* Averaged values of two specimens under the same condition.

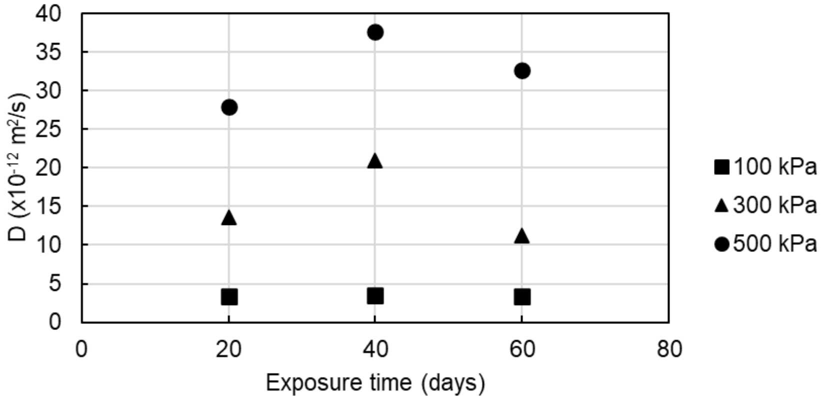

Figure 4-12. Diffusion coefficients versus exposure time.

4.4.2. Cracked (CK) SFRC Behavior

Figure 4-13 shows the sprayed $AgNO_3$ results of SFRC CK specimens for different ponding days and pressures. Unlike the UCK results, white bands were observed around the cracks for most specimens, indicating large amounts of chloride penetrating along the crack path.

In general, specimens immersed for 40 and 60 days show wider chloride bands around cracks than 20 days CK specimens. Also, relatively wider chloride bands were observed for specimens under higher pressures (300 kPa and 500 kPa) than those under atmospheric pressure (100 kPa).

When comparing the influence of crack width, as shown in Figure 4-10, specimens with larger crack widths do not exhibit an obvious increase in lateral penetration range. A similar phenomenon was also found in the salt ponding tests under atmospheric pressure (Rodriguez and Hooton, 2003). Based on the sprayed silver nitrate results, they concluded that the depth of chloride penetration is independent of the crack widths considered. However, the chloride penetration range is also influenced by the pressure in the study as most specimens with larger crack widths were immersed under atmospheric pressure.

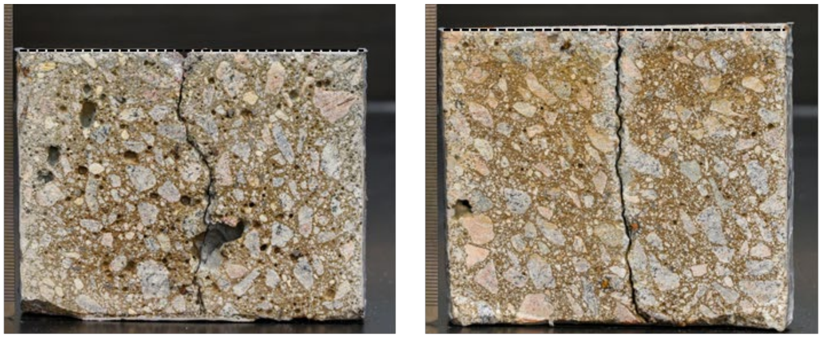

20Day-100kPa-CK1
b_{ave} = 0.31 mm

20Day-100kPa-CK2
b_{ave} = 0.33 mm

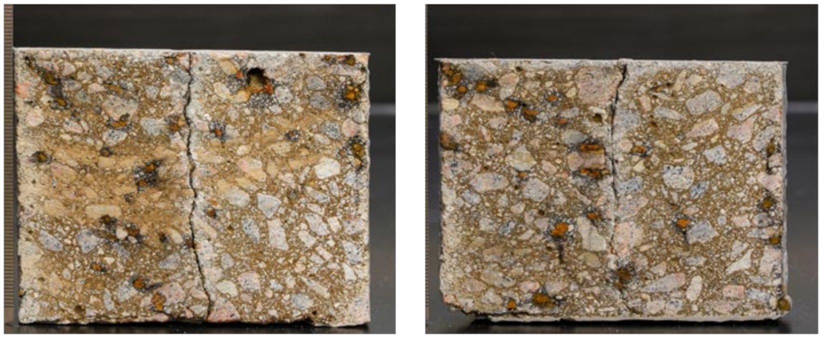

20Day-300kPa-CK1
b_{ave} = 0.19 mm

20Day-300kPa-CK2
b_{ave} = 0.28 mm

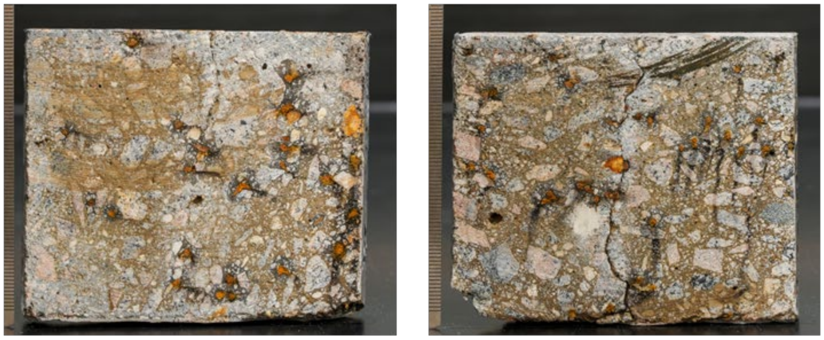

20Day-500kPa-CK1
b_{ave} = 0.15 mm

20Day-500kPa-CK2
b_{ave} = 0.25 mm

Figure 4-13(a). Chloride penetration through 20-day CK specimens visualized by spraying $AgNO_3$ solution (b_{ave} is the average crack width).

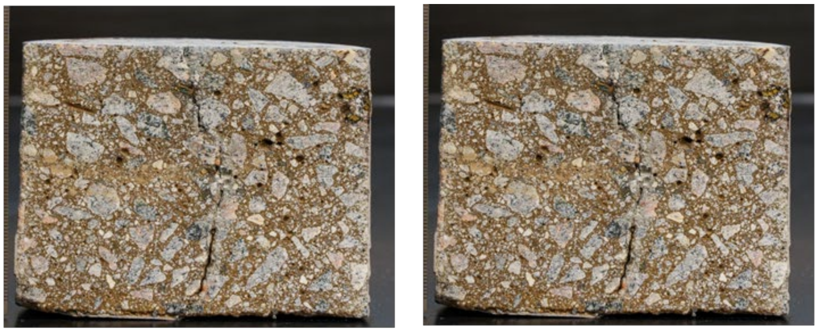

40Day-100kPa-CK1
b_{ave} = 0.24 mm

40Day-100kPa-CK2
b_{ave} = 0.29 mm

40Day-300kPa-CK1
b_{ave} = 0.18 mm

40Day-300kPa-CK2
b_{ave} = 0.27 mm

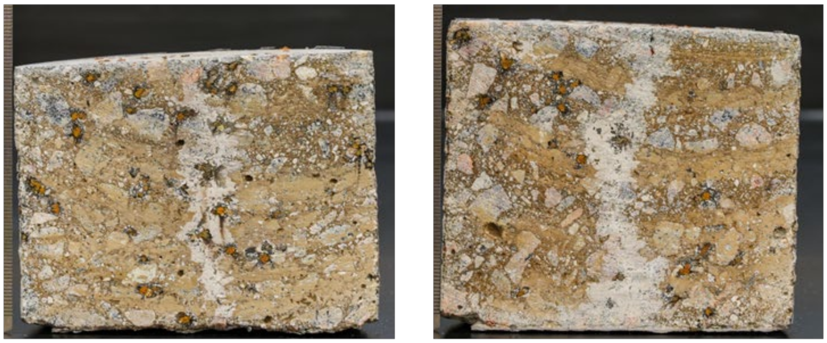

40Day-500kPa-CK1
b_{ave} = 0.13 mm

40Day-500kPa-CK2
b_{ave} = 0.14 mm

Figure 4-13(b). Chloride penetration through 40-day CK specimens visualized by spraying $AgNO_3$ solution (b_{ave} is the average crack width).

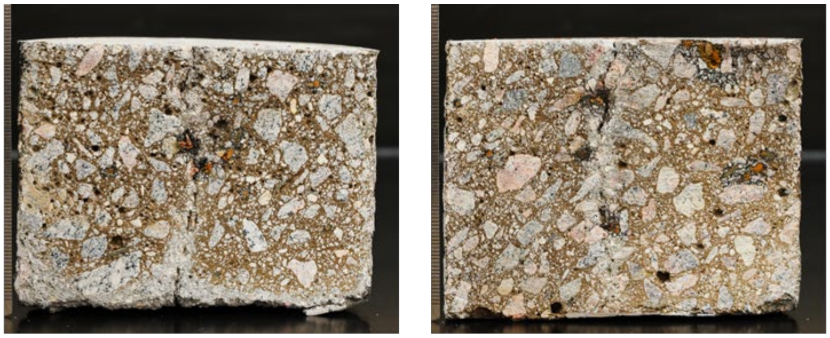

60Day-100kPa-CK1
b_{ave} = 0.20 mm

60Day-100kPa-CK2
b_{ave} = 0.21 mm

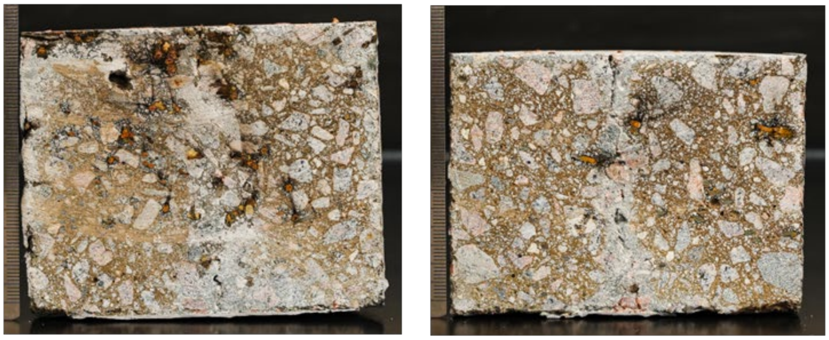

60Day-300kPa-CK1
b_{ave} = 0.16 mm

60Day-300kPa-CK2
b_{ave} = 0.20 mm

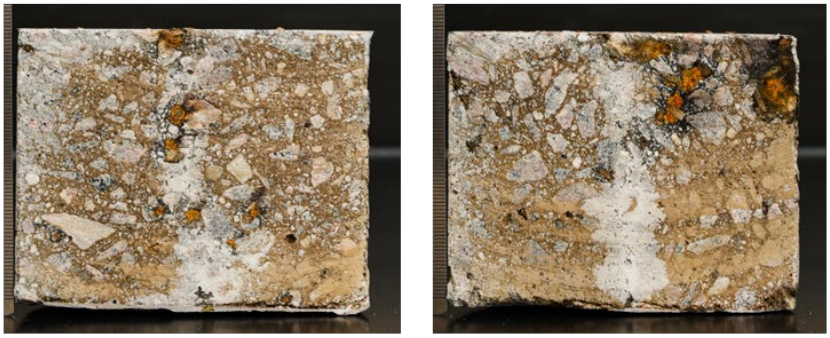

60Day-500kPa-CK1
b_{ave} = 0.17 mm

60Day-500kPa-CK2
b_{ave} = 0.13 mm

Figure 4-13(c). Chloride penetration through 60-day CK specimens visualized by spraying $AgNO_3$ solution (b_{ave} is the average crack width).

A different grinding configuration was used to quantify the chloride contents within the CK specimens. Several 10 by 10 by 10 mm slots were ground along the crack path for each specimen to investigate the chloride concentration near the cracked area as shown in Figure 4-14.

Figure 4-15 shows the chloride concentration profiles at different depths along the crack path for each CK specimen. Generally, CK specimens under 300 kPa and 500 kPa show higher chloride concentrations than those under atmospheric pressure. After 20 days of exposure, the 500 kPa-

CK1 specimen shows low chloride concentration versus others as the average crack width b_{ave} is 0.15 mm, which is considerably lower than other 20-day specimens. After 40 days of exposure, all CK specimens exhibit similar chloride profiles along the crack paths with slight differences close to the exposed surface. This might be attributed to the fact that the crack widths b_{ave} of the CK specimens decrease with applied hydraulic pressure as presented in Table 4-1.

A decrease in chloride in the vertical direction from the surface to the bottom is more evident after greater exposure time. This is because the general chloride contents close to the surface increase with salt ponding duration as illustrated in Figure 4-11 for UCK specimens. Under the same pressure, longer duration induced higher chloride concentrations near the top surface of the CK specimens as shown in Figure 4-16.

Compared to UCK specimens, the chloride concentrations near the surface (5 mm) of the CK specimens are comparable to the average values of the first 5 mm chloride concentrations for the UCK specimens, indicating a vertical chloride penetration through the concrete matrix dominates the behavior. Whereas, CK specimens still show relatively constant 0.1 to 0.25 percent chloride concentrations from near surface (15 mm) all to way down to the bottom. In comparison, gradually decreased chloride concentrations were observed to be below 0.1 percent beyond the depth of 20 mm for most UCK specimens. The presence of cracks induces hydraulic paths for water penetration and therefore is favorable for chloride ingress as well. The results show that cracks developed during construction or service life of tunnel lining, connecting to a surface exposed to a chloride environment, impair the durability performance of SFRC structure. Even with a micro-crack (0.1 to 0.2 mm width) presence, under higher hydraulic pressure, the chloride content can be as high as 0.1 percent at 70 mm deep from the surface after 60 days of exposure.

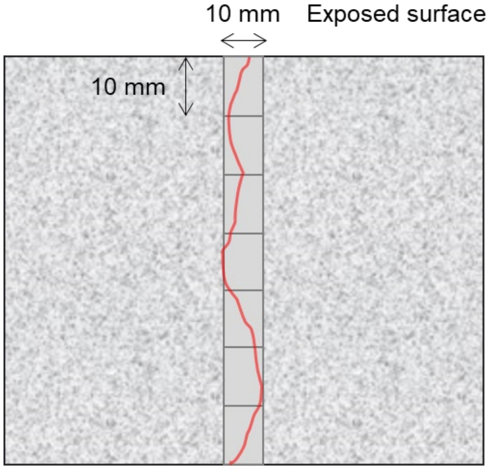

Figure 4-14. Grinding layout for cracked specimens.

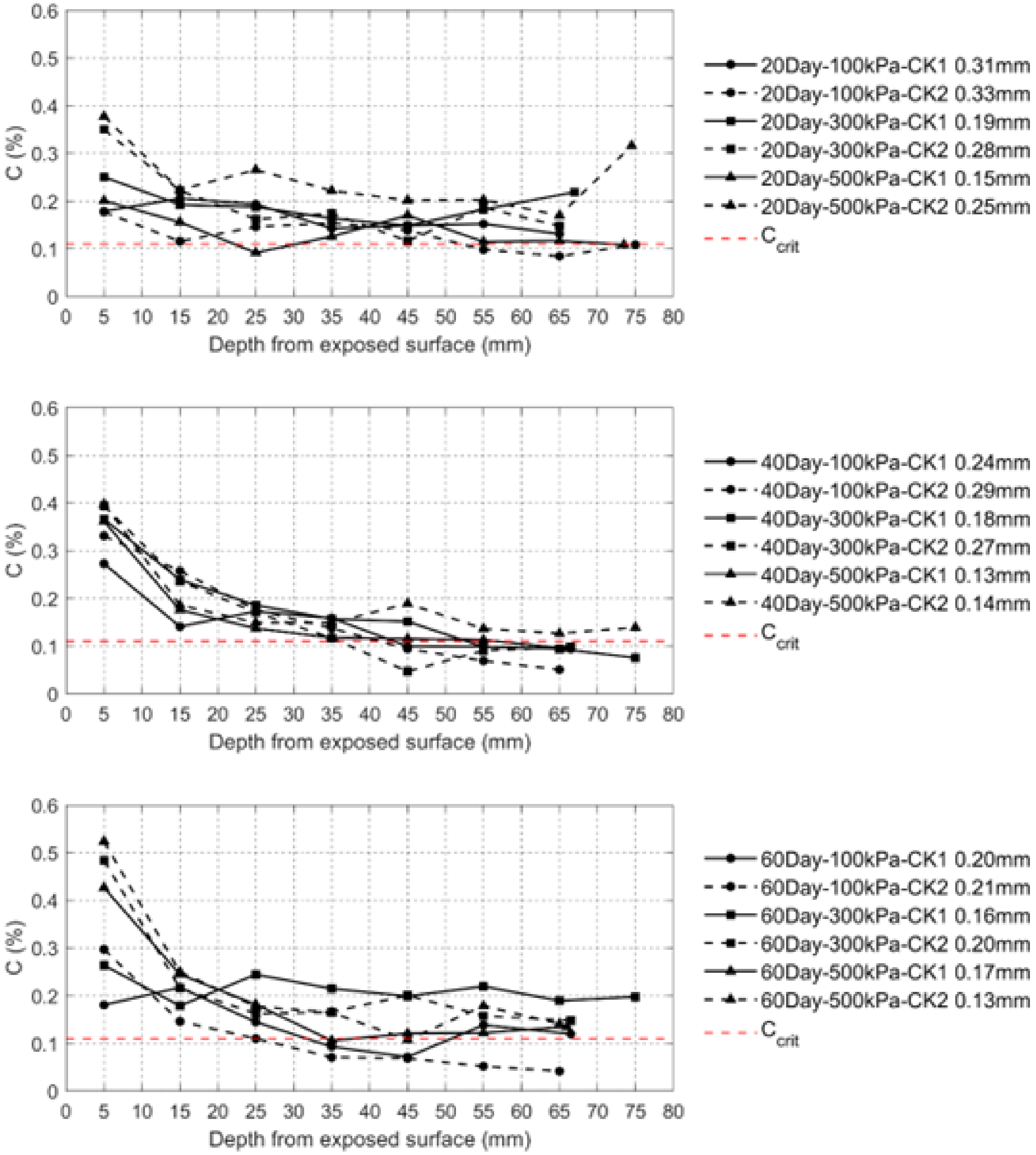

Figure 4-15. Chloride profiles for CK specimens as a function of pressure.

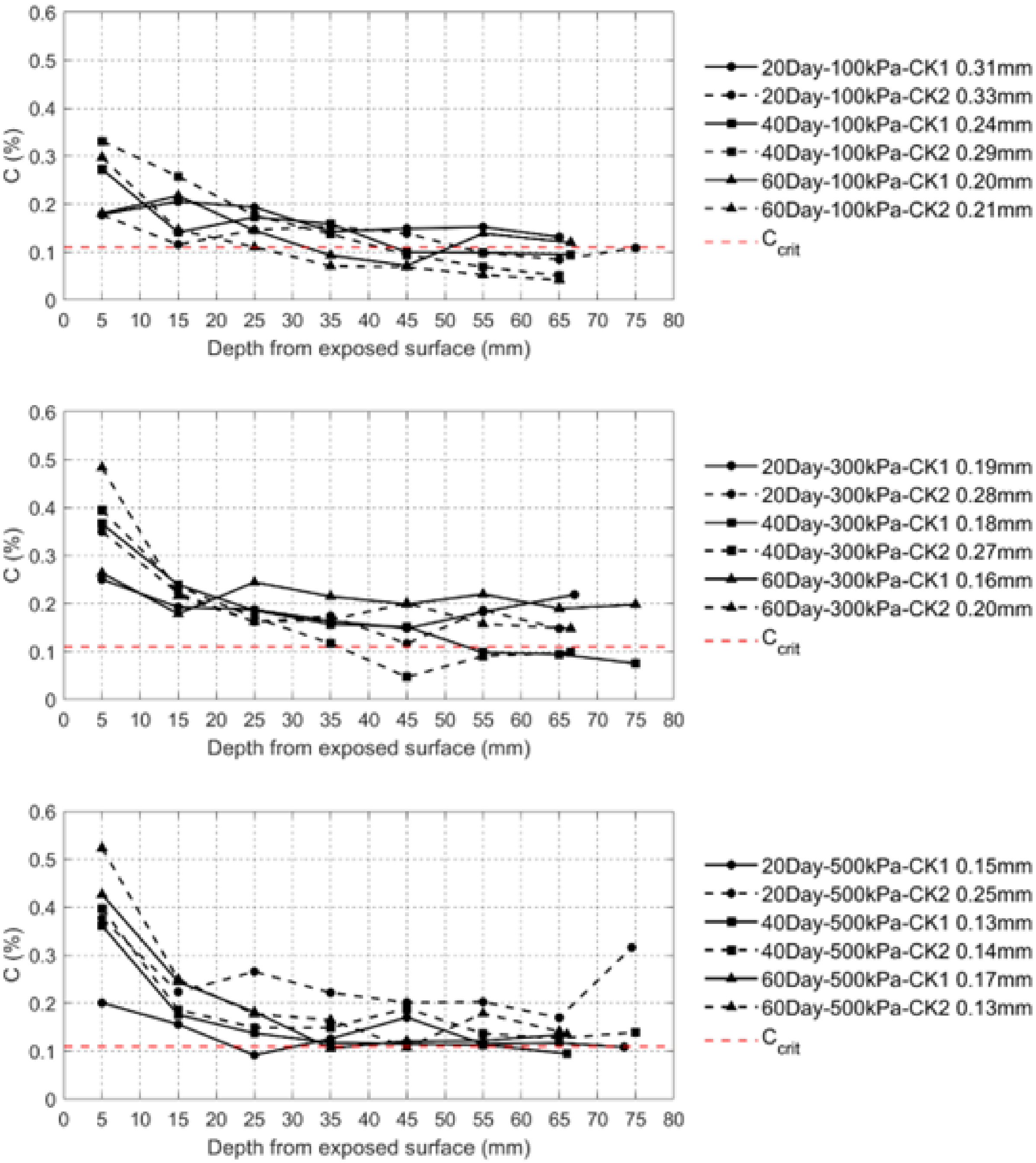

Figure 4-16. Chloride profiles for CK specimens as a function of duration.

4.5. Conclusions and Limitations

Pressurized salt ponding durability testing on SFRC specimens showed that:

- Higher hydraulic pressure induces higher chloride concentration for uncracked SFRC specimens. The diffusion coefficient of specimens under 500 kPa is 8-10 times greater than that of the specimens under atmospheric pressure.
- The presence of cracks creates new paths for chloride penetration, both vertical penetration from the top surface and lateral penetration from the cracking surface were observed.
- Higher hydraulic pressure generally induced higher chloride concentrations along the crack paths with a combined effect of the variability in crack width.
- Even with a micro crack developed (0.1 to 0.2 mm), under high hydraulic pressure, the SFRC specimen can exhibit chloride concentration higher than 0.1percent at 70 mm deep from the exposed surface after 60 days of salt ponding.

A number of limitations are noted. The number of specimens tested were limited. Only one mix design was investigated. The exposure time did not exceed 60 days. The SFRC specimens were cored from the field tunnel segments that contain variability and uncertainty during the casting and curing process. The crack width is not a quantitatively controlled variable in this study.

The influence of crack width on chloride penetration and the combined effects with hydraulic pressures should be further investigated. The internal cracking and porous structure also influence the chloride ingress pattern, which can be further characterized via techniques such as computerized tomography (CT) scanning. The penetration degree of chloride in the lateral direction from the free concrete surface created by cracks should be further quantified.

5 DESIGN FOR FIELD MONITORING OF FULL RING BEHAVIOR

5.1. Introduction

The response of fully assembled PCTL rings has been investigated in a few large-scale laboratories around the world. As described in Mooney et al. (2020) and illustrated in Figure 5-1, full ring tests are performed by erecting multiple rings on their side and assembling a load frame with many hydraulic jacks to apply axial and bending moments as well as longitudinal load. A substantial reaction frame should also be built to counteract the axial and moment loading. This approach to investigating full ring behavior can be costly. No full ring studies published in the United States were identified.

This chapter summarizes ways in which full PCTL ring behavior can be tested in-situ, within active construction projects. The main advantages to this approach is that (1) the tested rings are those that are being used during construction and (2) testing is more economically achievable (e.g., the cost of segment construction and ring assembly are eliminated). This chapter summarizes suggestions for implementing the instrumentation and the testing approach in-situ. The coordination for in-situ testing would need to begin during the tunnel planning phase.

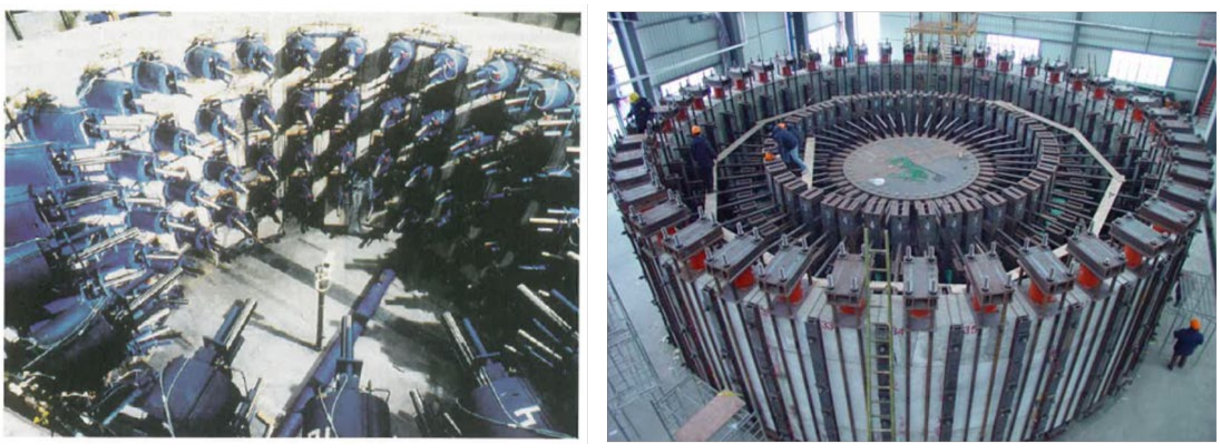

Figure 5-1. Setup of full scale PCTL ring load tests including for the 13.75 m diameter Elbe tunnel project in Germany (left) and for the 15.0 m diameter Shanghai Yangtze river tunnel project in China (right).

5.2. Objectives

The objectives of field monitoring of large diameter full PCTL rings include measuring:

- Thrust jack load induced tensile bursting and spalling stress.
- Annulus grouting-induced thrust and bending moments on segments, including joint rotation, and the progression of such load given non-uniform axisymmetric grouting.
- Earth and water pressure-induced loads and deformation, including any long term change in arching-induced and lateral earth pressure due to creep.
- Time-dependent transition from annulus grout-induced loads to earth and water pressure-induced loads and deformation.
- Load and deformation behavior during seismic loading.

5.3. PCTL Instrumentation

PCTL segments use internal instrumentation to measure axial (hoop) and bending strain/stress. The appropriate time to install instrumentation is during PCTL segment casting. Additional sensors, particularly at the joints, are external to the segment casting and therefore should be placed during or after ring installation. Because rings are built of numerous (8-10) individual segments, the collection of sensor data from each segment should be integrated and time synchronized. In the following sections, the description of segment and ring sensing is presented.

5.3.1. Internal Segment Instrumentation

Figure 5-2 shows the schematic layout of embedded sensors for each instrumented PCTL segment. Embedded instrumentation includes:

- Circumferential strain sensing near the extrados and intrados to measure and resolve both hoop (aka thrust, axial) load and bending moment at multiple clock positions circumferentially and at three longitudinal locations (near the leading edge, trailing edge and in the middle).
- Transverse (circumferential) and radial strain sensing beneath thrust jack load pads to measure transverse and radial bursting stresses and spalling stresses.

The number of strain gages can vary from project to project; therefore, the layout in Figure 5-2 is conceptually illustrative. The multiple locations circumferentially stems from the anticipated variation in bending and hoop loads circumferentially and as a radial joint is approached. The multiple locations longitudinally aim to characterize the influence of the circumferential joint between rings on bending moment and thrust load distribution. A variety of strain gage types can be employed, including single point vibrating wire, foil type, and optical strain gages or continuous distributed fiber optic sensing (DFOS). The placement approach for strain sensors will vary depending on the presence or absence of steel rebar. Gages are typically sistered to steel rebar or a wire frame if installed in SFRC without rebar for positional certainty and protection during segment casting.

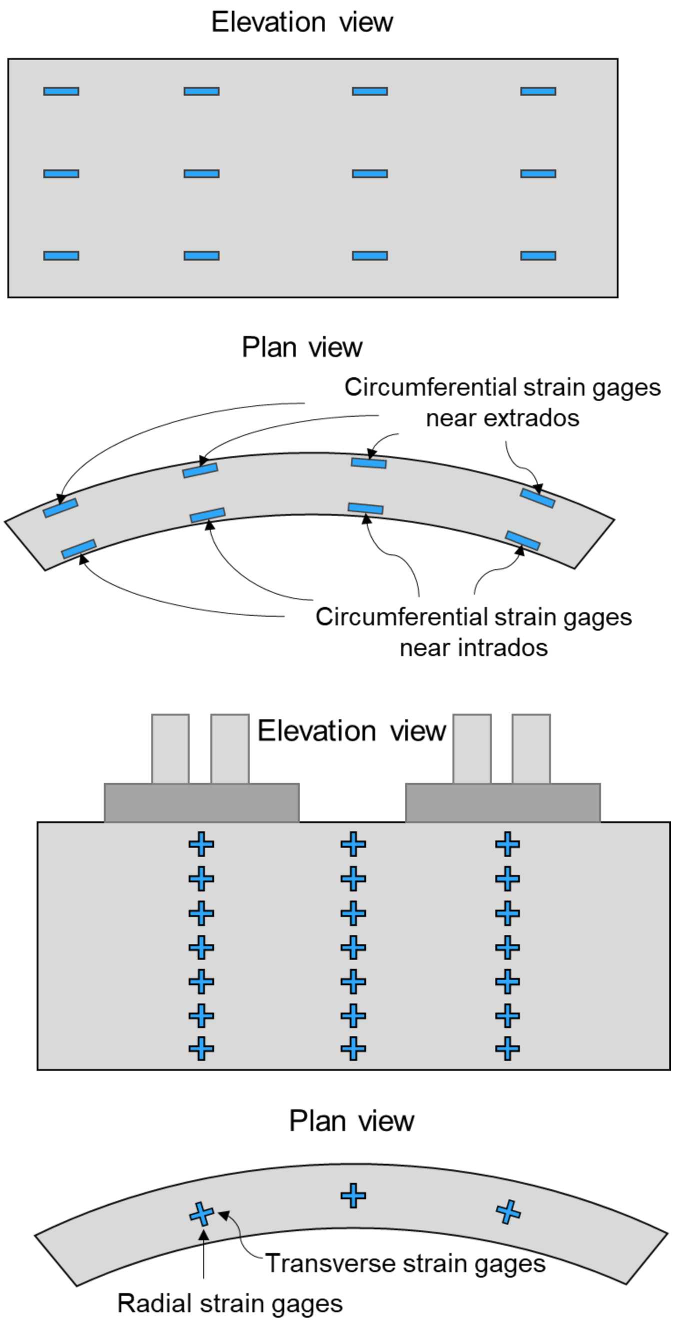

Figure 5-2. Plan and profile views of example embedded strain gage positions to measure: (a) hoop (axial) force, bending moment and related circumferential stresses; (b) thrust jack pad load bursting stresses in the radial and transverse (circumferential) directions.

Wires from each installed sensor should be terminated at one data collection hub on or near the intrados face for data collection. A data logger can be provided at or inside each data collection hub for analog to digital conversion or a communal local area data logger can be attached to the ring after ring assembly. In the latter case, the logger can connect wired or wirelessly to each segment's collection point (Figure 5-3).

There are multiple ways to record these data. Important aspects to keep in mind include sensor power, longevity of electronics, sampling frequency, and cost.

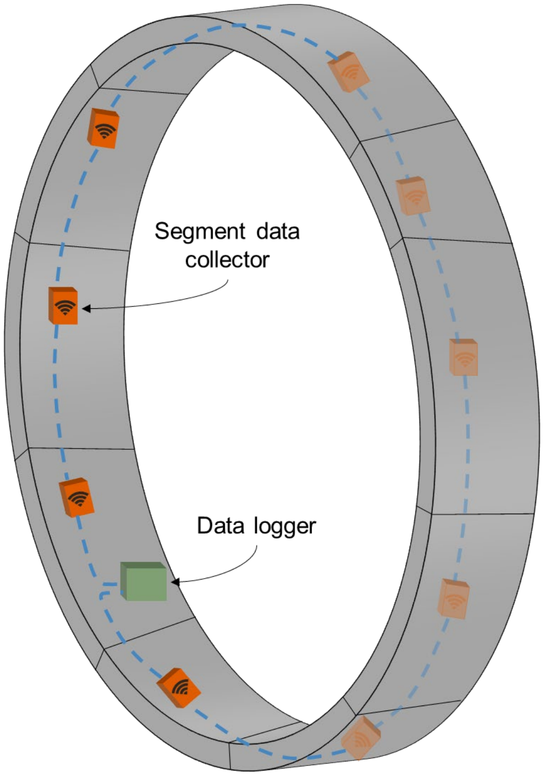

Figure 5-3. Sensor data within each segment is aggregated by a segment data collector. One local area data logger reads these data wirelessly.

5.3.2. Displacement and Joint Rotation

Each PCTL ring is assembled within the TBM shield and therefore is initially unloaded, except for self weight. The geometry of the unloaded ring should be measured both in terms of radial or cartesian position circumferentially and in terms of joint rotation. Joint rotation sensors can be added after ring assembly. Rotation can be measured by installing extensometers across the intrados joint or via tiltmeters attached to each segment near each joint (Figure 5-4).

The unloaded baseline radial convergence can be measured rapidly and with sufficient accuracy by lidar or by attaching an array of prisms to the segments and using automated total station technology. The combination of joint rotation measurements and displacements around the ring will enable the full resolution of ring kinematics. Ring deformation should be monitored: (a) as the TBM thrusts off the ring, (b) as the ring leaves the tail shield and annulus grout is injected to load the ring, (c) as the grout gels and hardens to transfer earth and groundwater loading to the ring, and (d) over time (hours to days to months to years as desired).

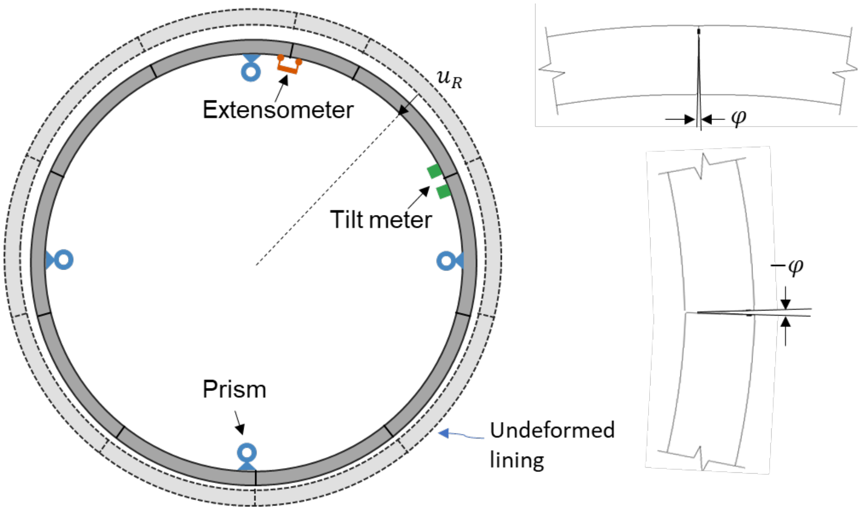

Figure 5-4. Measurement of radial convergence (or cartesian movement) via automated total station and prisms as well as joint rotation via tiltmeter and/or extensometers (only selected locations of sensors shown).

The data from all sensors (strain, displacement, joint rotation) are collected and time synchronized by each local data logger (Figure 5-3). The data logger can be programmed to record data at desired sampling rates. Multiple data loggers may be present throughout the tunnel (Figure 5-5). Several technologies can be used to relay information from the data logger, such as local area networks (LAN) or cellular technologies (4G/5G). Long-range communication (LoRa) is sometimes preferred as data can be transmitted over large distances with lower power consumption. Data collected by local wireless data loggers will be transmitted to a data server, usually a gateway hub, serving as a storage and export base station. Then the data will be collated and transferred to the internet. A data visualization platform can be utilized to view and analyze the monitored data (Figure 5-5).

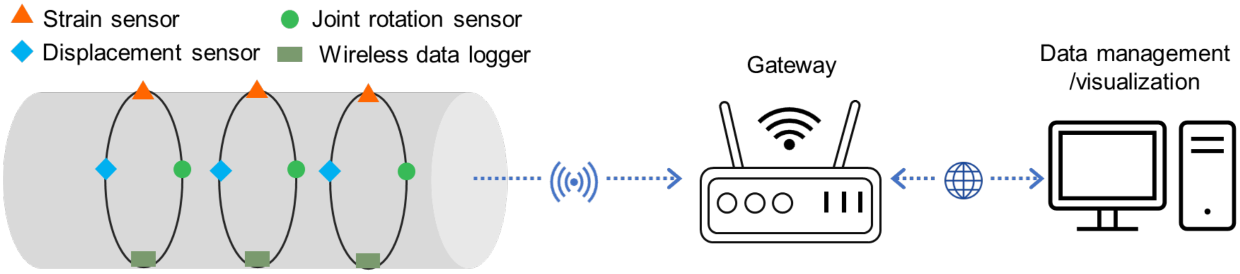

Figure 5-5. Data transport from in-situ instrumentation.

5.3.3. Digital Imaging of Crack Formation

As described in Chapter 4, the emergence and persistence of cracks in PCTL presents a durability concern. Tunnel cracks can appear during the construction and operational stages. Several factors contribute to the development of cracks in tunnel lining, including: (a) overloading during construction, e.g., thrust jack load induced bursting stress; (b) misalignment of segments; (c) ground movements surrounding tunnel; (d) inadequate or over pressurized nonuniform annulus grouting; (e) thermal expansion and contraction. As shown throughout this report, cracking also provides evidence of performance during thrust jack and flexural loading.

Timely detection of crack formation and proper mitigation of concrete cracks of extent and width beyond what is stated in the construction contract can be critical. High-quality digital images of segmental lining surfaces can be collected by a halo-based robotic inspection system, which mainly consists of a fixed ring with a circular sliding track, motorized arms, a visual camera, an ultrasonic sensor, and a data processing unit as shown in Figure 5-6. The system can be mounted to the segment erector for use immediately after full ring installation. Through the sliding track and robotic arms, the system can image the segment surface inside the tail shield of the TBM and then around the perimeter of the tailing gear. Each segment can be imaged before, during, and after loading.

A set of digital cameras can be mounted on the robotic arm with controllable lights and tilt mechanism. The image resolution is set based on the size of the crack of interest. For small or fine cracks with a size of around 0.05 mm, a resolution of 50-100 pixels/mm is suggested to ensure the quality and accuracy of the image post-processing.

After data collection, appropriate imaging processing techniques can be applied to characterize crack density and crack width, length, etc. This can be accomplished by traditional imaging processing techniques, such as edge-detection-based methods (Abdel-Qader et al., n.d.), the threshold segmentation method (Kamaliardakani et al., 2014; Lee et al., 2013). Image backgrounds may be complicated and noisy and so distinguishing cracks from tunnel lining backgrounds can be challenging. Alternative techniques such as deep learning-based methods have been advanced to detect and characterize tunnel lining cracks. Convolutional neural networks (CNN) have been widely used for crack detection from digital imagery (Figure 5-7).

Once cracks are identified, an ultrasonic sensor can be positioned by the robotic arm near the crack (with an accuracy of 5 cm) to measure the depth of the crack (Loupos et al., 2018). Traditional localized crack meters may be installed to monitor crack movement over time.

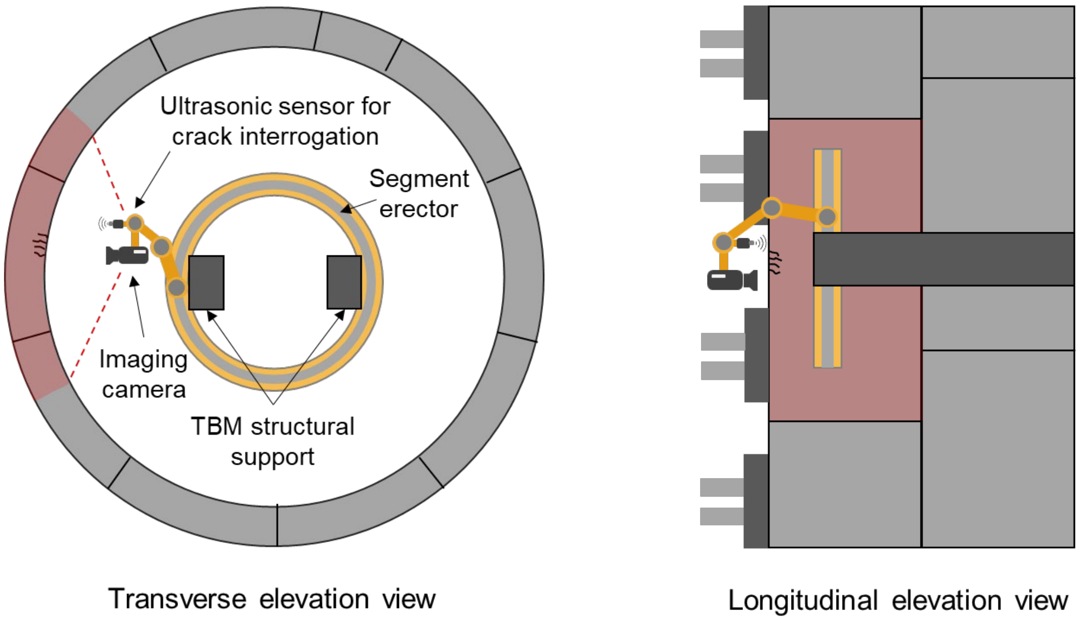

(a) (b)

Figure 5-6. Halo-based robotic system for crack inspection in (a) transverse elevation view and (b) longitudinal elevation view.

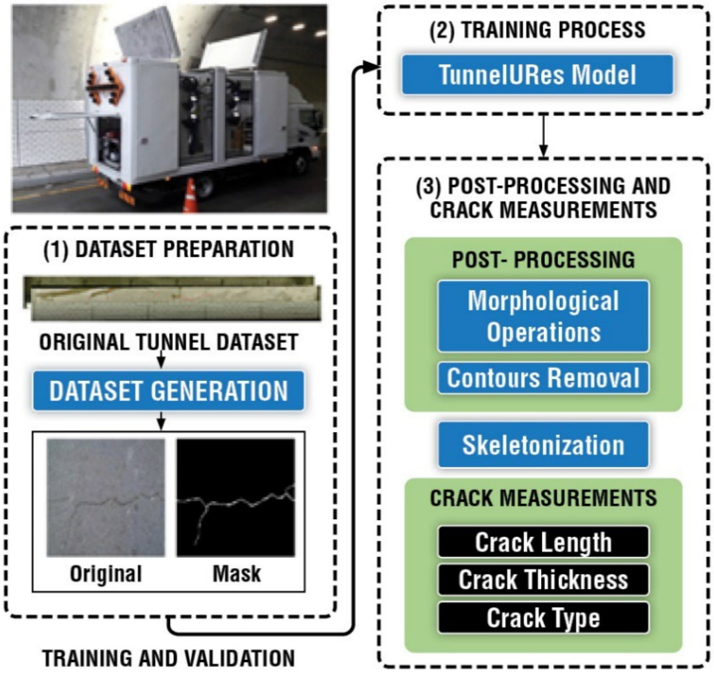

Figure 5-7. Deep learning framework for crack characterization, including data preparation, training process, post-processing and crack measurements.

5.4. Field Testing

The methodology and logistics of PCTL ring testing will depend on the specific objectives as well as project site constraints. Instrumented rings within the tunnel will be subjected to thrust jack loading, annulus grouting and earth/groundwater loading consistent with the commercial project specifications. These loads will vary with location along the alignment. Data collected from these instrumented rings will provide information though not about ultimate capacity. To this end, these data will provide information regarding service load performance. Special provision can specify testing full PCTL rings to their ultimate limit state, whether from thrust jack loading or axial-moment loading. While theoretically possible, it is unlikely that in-tunnel rings would be purposely damaged for the sake of testing. Such testing would involve the removal and replacement of the damaged rings.

Areas within a tunnel where sacrificial rings are adopted might provide an opportunity for ultimate limit state testing. This may include areas where an enlargement of the running tunnel is planned using the sequential excavation method, e.g., a station or adit, or at cross passage locations where installed rings will be significantly reinforced post-construction. Another location where full-scale testing may be possible is at the launch location where typically 4-6 temporary rings are erected to enable TBM launch (Figure 5-8). These rings are sacrificial and are disassembled after the TBM has successfully launched. It is possible that these rings could be left in place for axial-moment loading to failure. Some level of load frame and actuation would be used to impart hoop load and bending moments. Instead of the extensive array of individual longitudinal and transverse hydraulic jacks illustrated in Figure 5-1, cable tendons and selected jacks could be used to more economically load the rings to failure (see Figure 5-9).

© 2023 HS2 Ltd.

Figure 5-8. Sacrificial temporary rings used to launch TBM can be used for on-site load testing to failure.

Figure 5-9. Simplified hoop-moment loading applied using wrapped tendons as well as 12 o'clock and 6 o'clock jacks for moment loading.

BIBLIOGRAPHY

American Concrete Institute (ACI) Committee 544. (2016). *ACI 544.8R-16: Report on Indirect Method to Obtain Stress-Strain Response of Fiber-Reinforced Concrete (FRC)*. 22.

Abbas, S., Soliman, A. M., & Nehdi, M. L. (2014). Chloride ion penetration in reinforced concrete and steel fiber-Reinforced concrete precast tunnel lining segments. *ACI Materials Journal*, *111*(6), 613-622. https://doi.org/10.14359/51686991

Abdel-Qader, I., Abudayyeh, O., Asce, M., & Kelly, M. E. (n.d.). *Analysis of Edge-Detection Techniques for Crack Identification in Bridges*. https://doi.org/10.1061/ASCE0887-3801200317:4255

American Concrete Institute (ACI) Committee 318. (2014). *ACI 318-14*: *Building code requirements for structural concrete and commentary*.

American Concrete Institute (ACI) Committee 544. (2016) *ACI-544-7R-16: Report on Design and Construction of Fiber- Reinforced Precast Concrete Tunnel Segments*.

American Association of State Highway and Transportation Officials (AASHTO). (2002). *AASHTO T259 – Standard Method of Test for Resistance of Concrete to Chloride Ion Penetration*.

American Association of State Highway and Transportation Officials (AASHTO). (2017). *AASHTO LRFD Road Tunnel Design and Construction Guide First Edition*.

Angst, U., Elsener, B., Larsen, C. K., & Vennesland, Ø. (2009). Critical chloride content in reinforced concrete - A review. *Cement and Concrete Research*, *39*(12), 1122-1138. https://doi.org/10.1016/j.cemconres.2009.08.006

Ann, K. Y., & Song, H. W. (2007). Chloride threshold level for corrosion of steel in concrete. *Corrosion Science*, *49*(11), 4113-4133. https://doi.org/10.1016/j.corsci.2007.05.007

ASTM C1609/C1609M-12—Standard Test Method for Flexural Performance of Fiber-Reinforced Concrete (Using beam with Third-Point Loading). (n.d.).

Barros, J. A. O., Cunha, V. M. C. F., Ribeiro, A. F., & Antunes, J. A. B. (2005). Post-cracking behaviour of steel fibre reinforced concrete. *Materials and Structures/Materiaux et Constructions*, *38*(275), 47-56. https://doi.org/10.1617/14058

BS EN 14651:2005+A1:2007—Test Method for Metallic Fibre Concrete. Measuring the Flexural Tensile Strength (Limit of Proportionality (LOP), residual). (n.d.).

Cao, Y., Gehlen, C., Angst, U., Wang, L., Wang, Z., & Yao, Y. (2019). Critical chloride content in reinforced concrete - An updated review considering Chinese experience. *Cement and Concrete Research*, *117*(November 2018), 58-68. https://doi.org/10.1016/j.cemconres.2018.11.020

Costa, A., & Appleton, J. (1999). Chloride penetration into concrete in marine environment - Part I: Main parameters affecting chloride penetration. *Materials and Structures/Materiaux et Constructions*, *32*(4), 252-259. https://doi.org/10.1007/bf02479594

Dang, L. M., Wang, H., Li, Y., Park, Y., Oh, C., Nguyen, T. N., & Moon, H. (2022). Automatic tunnel lining crack evaluation and measurement using deep learning. *Tunnelling and Underground Space Technology*, *124*. https://doi.org/10.1016/j.tust.2022.104472

Deng, J., Lu, Y., & Lee, V. C. S. (2020). Concrete crack detection with handwriting script interferences using faster region-based convolutional neural network. *Computer-Aided Civil and Infrastructure Engineering*, *35*(4), 373-388. https://doi.org/10.1111/mice.12497

Federal Highway Administration (FHWA). (2020). *Precast Concrete Segmental Liners for Large Diameter Road Tunnels – Literature Survey and Synthesis, FHWA-HIF-20-036*.

fib Model Code for Concrete Structures. (2010).

Glass, G. K., & Buenfeld, N. R. (1997). The presentation of the chloride threshold level for corrosion of steel in concrete. *Corrosion Science*, *39*(5), 1001-1013. https://doi.org/10.1016/S0010-938X(97)00009-7

Groeneweg, T. W. (2007). *Shield driven tunnels in ultra high strength concrete* [PhD Thesis]. Delft University of Technology.

Hooton, D. (2016). *Testing the Chloride Penetration Resistance of Concrete : A Literature Review FHWA Contract DTFH61-97-R-00022 "Prediction of Chloride Penetration in Concrete" Testing the Chloride Penetration Resistance of Concrete : A Literature Review by University of. August*.

Iyengar, K. S. R. (1962). Two-dimensional theories of anchorage zone stresses in post-tensioned prestressed beams. *Journal of the American Concrete Institute*, *59*(59), 1443-1466.

Janssen, P. (1983). *Tragverhalten von Tunnelausbauten mit Gelenktübbings [Load carrying behavior of segmented tunnel linings]* [Ph.D. Thesis]. Technische Universität Carolo-Wilhelmina zu Braunschweig.

Jenkins, M. D., Carr, T. A., Iglesias, M. I., Buggy, T., & Morison, G. (2018). A Deep Convolutional Neural Network for Semantic Pixel-Wise Segmentation of Road and Pavement Surface Cracks. *26th European Signal Processing Conference (EUSIPCO)*, 2120-2124.

Kamaliardakani, M., Asce, S. M., Sun, Lu, & Ardakani, M. K. (2014). *Sealed-Crack Detection Algorithm Using Heuristic Thresholding Approach*. https://doi.org/10.1061/(ASCE)CP.1943-5487

Kim, B., & Cho, S. (2019). Image-based concrete crack assessment using mask and region-based convolutional neural network. *Structural Control and Health Monitoring*, *26*(8). https://doi.org/10.1002/stc.2381

Lee, B. Y., Kim, Y. Y., Yi, S. T., & Kim, J. K. (2013). Automated image processing technique for detecting and analysing concrete surface cracks. *Structure and Infrastructure Engineering*, *9*(6), 567-577. https://doi.org/10.1080/15732479.2011.593891

Loupos, K., Doulamis, A. D., Stentoumis, C., Protopapadakis, E., Makantasis, K., Doulamis, N. D., Amditis, A., Chrobocinski, P., Victores, J., Montero, R., Menendez, E., Balaguer, C., Lopez, R., Cantero, M., Navarro, R., Roncaglia, A., Belsito, L., Camarinopoulos, S., Komodakis, N., & Singh, P. (2018). Autonomous robotic system for tunnel structural inspection and assessment. *International Journal of Intelligent Robotics and Applications*, *2*(1), 43-66. https://doi.org/10.1007/s41315-017-0031-9

Luping, T., Nilsson, L.-O., & Basheer, M. (2012). *Resistance of concrete to chloride ingress: Testing and modelling*. Taylor and Francis.

Meck, E., & Sirivivatnanon, V. (2003). Field indicator of chloride penetration depth. *Cement and Concrete Research*, *33*(8), 1113-1117. https://doi.org/10.1016/S0008-8846(03)00012-7

Mooney, M., Epel, T., Wilson, A., Zheng, H., & Nitschke, A. G. (2020). Experimental Behavior of Large Diameter Segmental Lining Systems: A Review. *North American Tunneling: 2020 Proceedings*, 488-498.

Olesen, J. F. (2001). Fictitious crack propagation in fiber-reinforced concrete beams. *Journal of Engineering Mechanics*, *127*(March), 272-280.

Otsuki, N., Nagataki, S., & Nakashita, K. (1993). Evaluation of the AgNO3 solution spray method for measurement of chloride penetration into hardened cementitious matrix materials. *Construction and Building Materials*, *7*(4), 195–201.

DAUB. (2013). *Recommendations for the design, production and installation of segmental rings DAUB Deutscher Ausschuss für unterirdisches Bauen e. V. German Tunnelling Committee (ITA-AITES)*. www.daub-ita.de

RILEM. (1994). Draft recommendation for repair strategies for concrete structures damaged by reinforcement corrosion. *Materials and Structures*, *27*(7), 415–436. https://doi.org/10.1007/BF02473446

RILEM TC 162-TDF:2003-Test and Design Methods for Steel Fibre Reinforced Concrete. σ-ε Design Method: Final Recommendation. (n.d.).

Rodriguez, O. G., & Hooton, R. D. (2003). Influence of cracks on chloride ingress into concrete. *ACI Materials Journal*, *100*(2), 120-126. https://doi.org/10.14359/12551

Stephen, S. J., Raphael, B., Gettu, R., & Jose, S. (2019). Determination of the tensile constitutive relations of fiber reinforced concrete using inverse analysis. *Construction and Building Materials*, *195*, 405–414. https://doi.org/10.1016/j.conbuildmat.2018.11.014

Yang, X., Li, H., Yu, Y., Luo, X., Huang, T., & Yang, X. (2018). Automatic Pixel-Level Crack Detection and Measurement Using Fully Convolutional Network. *Computer-Aided Civil and Infrastructure Engineering*, *33*(12), 1090-1109. https://doi.org/10.1111/mice.12412

Yuan, Q. (2009). *Fundamental Studies on Test Methods for the Transport ofChloride Ions in Cementitious Materials.* Ghent University.

Zhang, A., Wang, K. C. P., Li, B., Yang, E., Dai, X., Peng, Y., Fei, Y., Liu, Y., Li, J. Q., & Chen, C. (2017). Automated Pixel-Level Pavement Crack Detection on 3D Asphalt Surfaces Using a Deep-Learning Network. *Computer-Aided Civil and Infrastructure Engineering*, *32*(10), 805-819. https://doi.org/10.1111/mice.12297

APPENDICES

Appendix A. Estimation of SFRC tensile properties

A1. Introduction

The design of SFRC segments subjected to thrust jack loading requires knowledge of the tensile strength and tensile stress-crack width relationship. However, estimating characteristic tensile properties of SFRC that can be adopted in existing design procedures may not be straightforward. The uniaxial tensile test that can directly capture post-cracking tensile behavior can be demanding and logistically expensive, and thus difficult to conduct. Therefore, flexural tests and split tensile tests are often performed. The equivalent tensile properties of SFRC can be derived from flexural tests by using analytical models combined with inverse analysis. Depending on the test methods used, there are multiple inverse analysis methods to estimate tensile stress-strain response. Similar tensile strength estimation can be performed with split tensile test results. The coefficients of prescribed equations are determined through inverse analysis by fitting experimental data using an elastic or inelastic method. Here, three methods were used to estimate SFRC tensile properties from BS EN 14651 test results.

ACI 544.7R-16[1] suggests the use of a post-crack residual tensile strength when designing for thrust jack load-induced bursting stress; however, the specific residual tensile strength is not clearly conveyed. The ACI 544.7R-16[1] Design Approach Section 3.3 cites *fib* Model Code 2010 and RILEM TC 162-TDF as suggesting that residual flexural strength corresponding to a crack mouth opening displacement (CMOD) equal to 0.5 mm be used in all calculations for serviceability limit state design. Thrust jack loading is not referenced in this section. The specific thrust jack loading Section 5.1 of ACI 544.7R-16[1] cites the use of residual tensile strength but does not state a specific criteria, e.g., CMOD level. Industry practice is also unclear about whether to use peak or residual tensile strength, and if residual strength at what crack width or strain level. Some designers use residual tensile strength assessed at various crack width values together with a strength reduction factor, while other designers use peak tensile strength and a stress reduction factor using ultimate limit state design adopting the philosophy that thrust jack loading should not crack the segments.

ACI 544.7R-16[1] does suggest the use of back analysis when estimating tensile strength from flexural test results. When inverting, residual flexural strengths at a net midspan deflection of $l/600$ (f_{600}^{D}) and $l/150$ (f_{150}^{D}) are typically used when ASTM C1609**Error! Bookmark not defined.** test is conducted, and residual flexural strengths $f_{R,1}$, $f_{R,3}$or $f_{R,4}$ (or the average of) are typically used for EN 14651 test method. The thrust jack load Section 5.1 of ACI 544.7R-16[1] states that SFRC splitting tensile strength may be used in place of the back calculated from flexural tests, provided that post-peak strength is greater than the first peak load (due to hardening behavior) as measured by a properly instrumented test setup.

A2. Splitting Tension Test Results

Splitting tensile tests were conducted on samples cored from the tested SFRC segments. The tests were performed in accordance with ASTM C496[10]. The results are summarized in Table A-1 and visualized in Figure A-1. Deformation measurements were not made during testing. The nominal ultimate tensile stress σ_{Nu} is estimated as shown below, where P_u is the ultimate load and D is the sample diameter. Corrections for load strip width (e.g., Denneman et al., 2011) were not made. Given the hardening nature of this SFRC, the measured P_u and calculated σ_{Nu} likely overestimate the initial uncracked peak tensile strength (Denneman et al., 2011). The magnitude of σ_{Nu} measured was less than that reflected in test result data provided by CSI Concrete Systems on 28-30 day cured specimens. The CSI-provided data was from 2019 pre-fabrication testing and not directly represented of the segments tested.

Table A-1. Splitting tensile testing results.

Test No.	σ_{Nu} (MPa) measured by CSI (age = 28-30 days)	σ_{Nu} (MPa) measured from cores (age = 650-700 days)
1	6.83	7.00
2	7.55	7.70
3	7.82	5.85
4	8.50	7.95
5	7.21	6.70
6	7.45	-
Ave	7.34	7.1
Std Dev	0.17	0.85

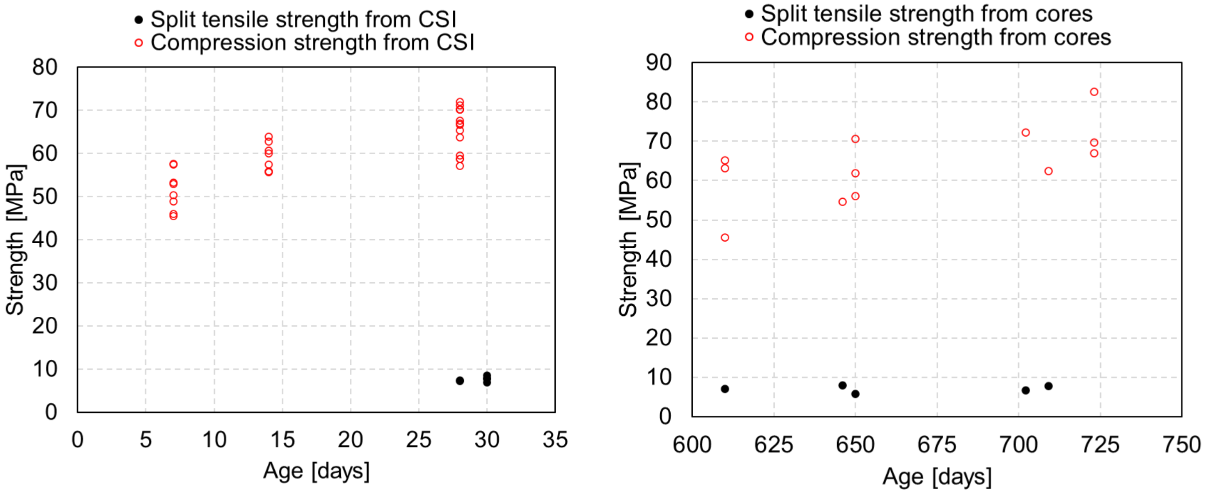

(a) (b)

Figure A-1. Splitting tensile and compression strength from (a) CSI and (b) cores.

---

[10] Use of ASTM C496, Standard Test Method for Splitting Tensile Strength of Cylindrical Concrete Specimens is not a Federal requirement.

A3. EN 16451 Flexural Beam Test Results

Twelve three-point bending tests were performed on SFRC specimens according to the BS EN 14651 procedure. The test setup is shown in a and a typical load versus CMOD response is shown in b. The peak flexural tensile strength $f_{t,fl}$ and residual flexural tensile strength $f_{R,j}$ were estimated from the load-CMOD relationship as suggested by *fib* Model Code (2010).

$$f_{t,fl} = \frac{3F_L l}{2bh_{sp}^2} \tag{A-1}$$

$$f_{R,j} = \frac{3F_j l}{2bh_{sp}^2} \tag{A-2}$$

where $f_{R,j}$ is the residual flexural tensile strength corresponding to *CMOD_j*, F_L is the peak load, F_j is the load corresponding to *CMOD_j*, l is the span length, b is the span width, and h_{sp} is the distance between the notch tip and the top of the specimen (125 mm). The load-CMOD curves obtained from 12 BS EN 14651 tests are shown in Figure A-3; the calculated flexural tensile strength values are summarized in Table A-2.

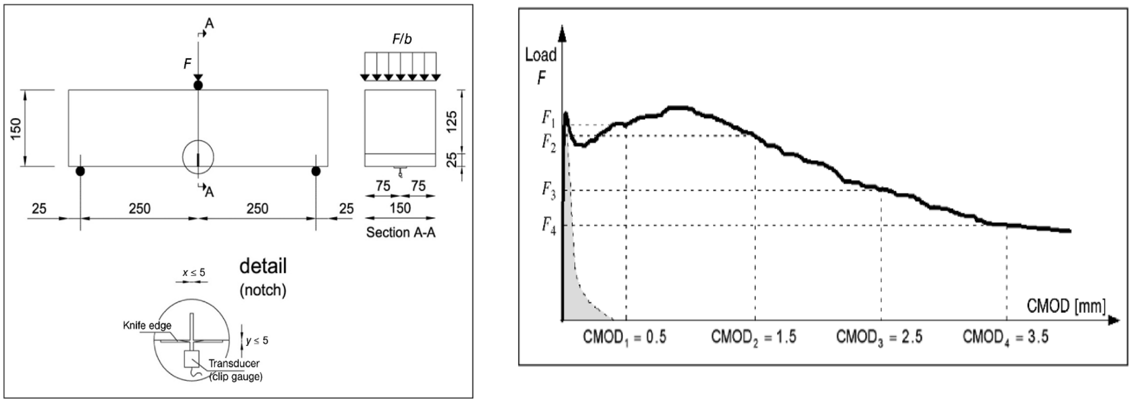

(a) (b)

© 2010 International Federation for Structural Concrete (fib)

Figure A-2. (a) Test set-up for BS EN 14651 (dimensions in mm); (b) load-CMOD curve for FRC.

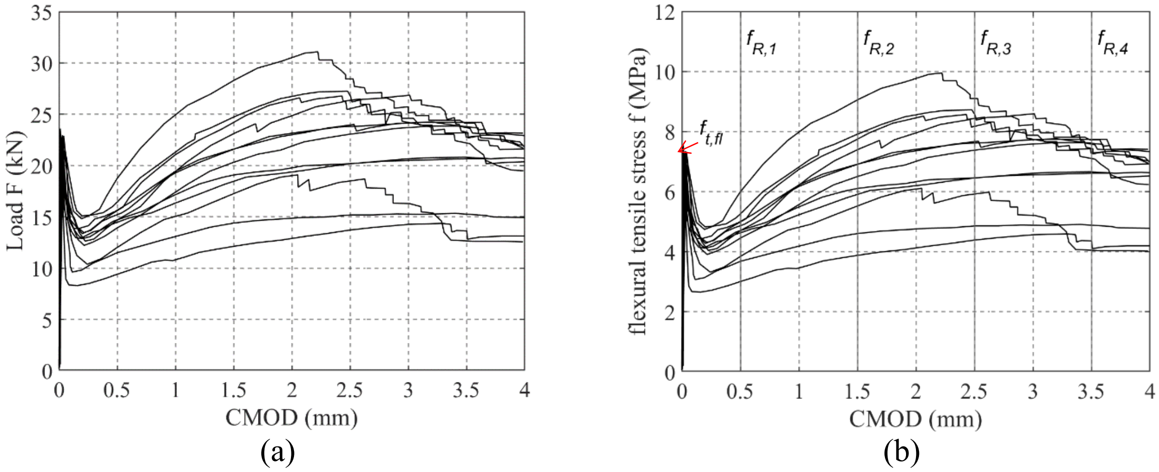

(a) (b)

Figure A-3. BS EN 14651 test results of 12 notched SFRC beams (a) load-COMD relationship; (b) flexural tensile strength versus CMOD (four test sets indicate four batches cast on different dates but all tested at an age of 28 days).

Table A-2. SFRC material properties.

Property	**CSI-measured value (MPa)**	**Measured from cores (MPa)**
Young's modulus	Not Applicable	30,940 ± 1,550
Compressive strength	65.6 ± 5.2	64.3 ± 9.5
CMOD peak $f_{t,fl}$	7.12 ± 0.32	Not Applicable
CMOD 0.5 mm $f_{R,1}$	4.57 ± 0.83	Not Applicable
CMOD 1.5 mm $f_{R,2}$	6.53 ± 1.52	Not Applicable
CMOD 2.5 mm $f_{R,3}$	6.96 ± 1.49	Not Applicable
CMOD 3.5 mm $f_{R,4}$	6.28 ± 1.30	Not Applicable

* ± reflects standard deviation

The general flexural tensile response observed involved the achievement of peak flexural tensile strength at CMOD less than 0.1 mm, followed by a considerable decrease to a minimum strength at CMOD equal to 0.1-0.3 mm, followed by a residual flexural tensile strength increase with additional CMOD. The residual flexural tensile strength grew to magnitudes greater than the peak flexural tensile strength at CMOD values of 2.0-2.5 mm. This represents a flexural hardening behavior of SFRC material. After the initial cracking peak load is reached, the fibers provide extra resistance by bridging cracks and redistributing tensile stress. The load-carrying capacity and residual flexural tensile strength gradually decreased at CMOD greater than 2.5 mm, representing the final softening branch. Per ACI 544.8R-16[11], a certain FRC presenting a hardening flexural behavior does not necessarily imply hardening tensile behavior.

The average peak flexural strength $f_{tm,fl}$ is 7.1 MPa, and the average flexural residual strengths at 0.5 mm CMOD and 3.5 mm CMOD are 4.6 MPa and 6.3 MPa, respectively. ACI 544.4R-18[12] suggests that, for design purposes, the tensile residual strength should be calculated from the flexural residual strength obtained from a beam test.

A4. Empirical Equation by RILEM TC 162-TDF

ACI 544.8R-16[7] suggests using an empirical equation proposed by RILEM TC 162-TDF (2003) to estimate SFRC peak and residual tensile strengths from BS EN 14651 flexural test results. The stress-strain diagram shown in Figure A-4 is a piecewise linearized response suggested by RILEM TC 162-TDF. The values of $\sigma_{i,E}$ and $\varepsilon_{i,E}$ are key stress-strain points defining the tensile response and can be directed related to BS EN 14651 test data to evaluate characteristic tensile strength values.

$$f_t = \sigma_{1,E} = C_1(1.6 - d) f_{tm,fl} \tag{A-3}$$

$$\sigma_{2,E} = C_2 f_{R,1} \tag{A-4}$$

$$\sigma_{3,E} = C_3 f_{R,4} \tag{A-5}$$

Here, f_t is the peak tensile strength, d is the depth of the beam's cross-section, and $f_{tm,fl}$ is the mean value of the peak flexural tensile strength $f_{t,fl}$, and is 7.1 MPa in this case. C_1, C_2 , and C_3 can be assumed as 0.52, 0.36, and 0.27, respectively (Barros et al. 2005). The tensile strain $\varepsilon_{1,E}$ at peak tensile strength is obtained following Hooke's Law ($\varepsilon_{1,E} = \sigma_{1,E}/E_c$), where E_c is Young's modulus of FRC. Other strain values ε_2 and ε_3 depend on the choice of modeling technique and are assumed as 0.12 percent and 10.4 percent according to Barros et al. (2005) The values were proposed by Barros et al. (2005) through an inverse analysis of experimental tests and numerical analysis results. In their tests, two types of DRAMIX steel fibers[13] were used: (1) RC 80/60 BN with a length of 60 mm, a diameter of 0.75 mm and an aspect ratio of 80, which is the same as the fibers used in the project; (2) RC 65/60 BN with a length of 60 mm a diameter of 0.92 mm and an aspect ratio of 65. The yield stress of their fiber is reported as 1100 MPa versus 1800 MPa for the fibers used in the project. Various percentages of fly ash were added to their mix design. The 28-day compressive strength of their SFRC is reported close to 40 MPa, which is lower than the 65

---

[11] Use of ACI 544.8R-16, Report on Indirect Method to Obtain Stress-Strain Response of Fiber-Reinforced Concrete (FRC), is not a Federal requirement

[12] Use of ACI 544.4R-18, Guide to Design with Fiber-Reinforced Concrete, is not a Federal requirement

[13] The name of the product used is included for informational purposes only and is not intended to reflect a preference, approval, or endorsement of any one product or entity.

MPa for the SFRC. The geometry of their test beams is the same as the standard beam used in BS EN 14651 test.

The estimated f_t = 5.5 MPa and the estimated residual tensile strengths $\sigma_{2,E}$ equals 1.6 MPa and $\sigma_{3,E}$ equals 1.7 MPa, as shown in Figure A-5. These back-calculated peak and residual tensile strengths differ by more than 300 percent and will convey significantly different thrust jack load capacities. The stress-strain relationship proposed by this method is a two-piece linear model without distinguishing the strain hardening and softening behavior observed in the BS EN 14651 test results. However, as mentioned in the previous section, there is no one-to-one correlation between flexural and tensile behavior. A strain-softening FRC can develop deflection softening or deflection hardening based on the residual stress level present (ACI 544.8R-16[7]).

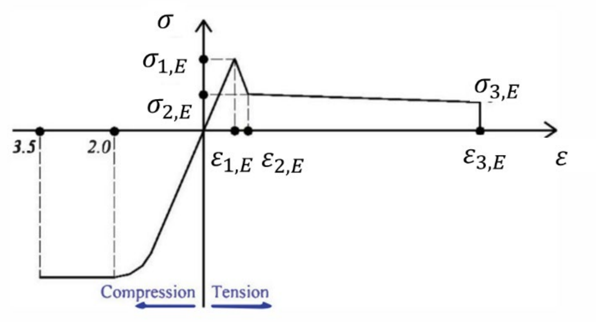

© 2016 American Concrete Institute (ACI)

Figure A-4. Stress-strain diagram for FRC in uniaxial tension and compression (from RILEM TC 162-TDF 2003).

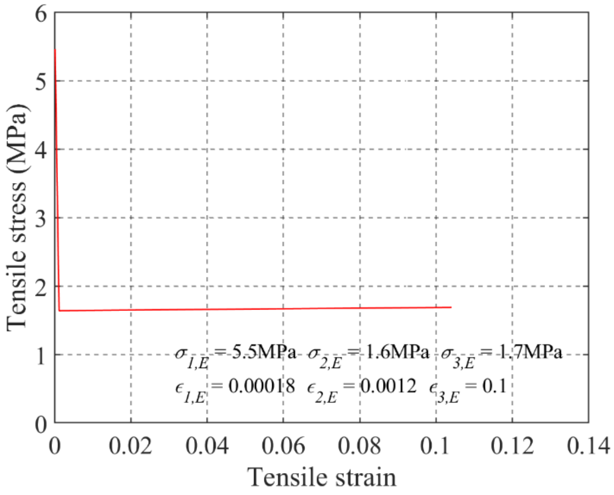

Figure A-5. Tensile strengths estimated by ACI empirical equation.

A5. Simplified Method Suggested by *fib* Model Code (2010)

The *fib* Model Code (2010) approach was also evaluated here to estimate residual tensile SFRC strength only, as the method does not estimate peak tensile strength. The *fib* Model Code (2010) proposes two simplified stress-crack width models based on the rigid-plasticity and linearelasticity tensile behavior of FRCs as shown in Figure A-6. The serviceability residual tensile strength f_{Fts} and the ultimate residual tensile strength f_{Ftu} can be estimated using BS EN 14651 test data. Peak tensile strength f_t is not estimated by the *fib* Model Code method.

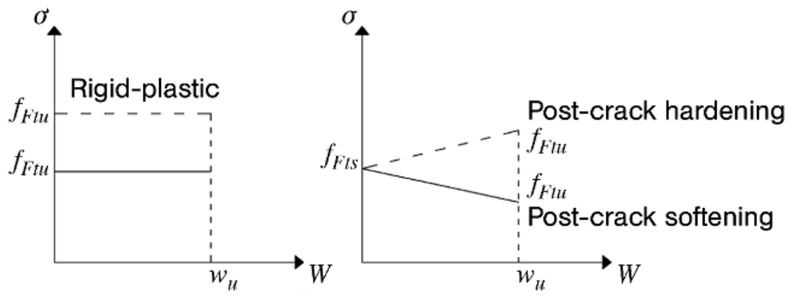

© 2010 International Federation for Structural Concrete (*fib*)

Figure A-6. Simplified post-cracking constitutive laws: stress-crack opening W (continuous and dashed lines refer to softening and hardening post-cracking behavior, respectively).

The rigid-plastic model is capable of estimating f_{Ftu} while the linear model is capable of estimating both f_{Ftu} and f_{Fts}.

The rigid-plastic model identifies a unique reference value based on the ultimate behavior:

$$f_{Ftu,R} = \frac{f_{R,3}}{3} = \frac{6.96}{3} = 2.32\ MPa \tag{A-6}$$

The linear model identifies f_{Ftu} and f_{Fts}, which are calculated through residual values of flexural strength:

$$f_{Fts,L} = 0.45 f_{R,1} = 0.45 \times 4.57 = 2.06\ MPa \tag{A-7}$$

$$f_{Ftu,L} = f_{Fts,L} - \frac{w_u}{2.5}\left(f_{Fts,L} - 0.5 f_{R,3} + 0.2 f_{R,1}\right)$$
$$= 2.06 - \frac{0.2}{2.5}(2.06 - 0.5 \times 6.96 + 0.2 \times 4.57) = 2.10\ MPa \tag{A-8}$$

where w_u is the maximum crack opening accepted in structural design (0.2 mm was used here).

A6. Inverse Method Proposed by Stephen et al. (2019)

The SFRC tensile strength and the tensile constitutive relations were also estimated through a full inverse analysis method proposed by (Stephen et al., 2019). The inverse analysis is based on a closed-form solution for relating the multi-linear stress-crack opening relation to the load-CMOD curve. A tetralinear model of the stress-crack opening curve was used as shown in Figure A-7b.

The analytical model is based on the concept of a non-linear hinge for simulating the three-point bending test of SFRC (Olesen, 2001). The nonlinear hinge is placed at mid-span with length *s* equal to half the beam depth. The hinge is modeled as layers of spring elements with behavior governed by the tensile constitutive relation of the concrete (Figure A-7b). When a beam of depth H, width b and span l is subjected to a load P at the center, the hinge undergoes an angular deformation φ as shown in Figure A-7a. For a strip at depth y, $w(y)$ is crack opening (different from CMOD, which is the opening deformation at the notch tip), $u(y)$ is the deformation of a strip, and $\sigma_w(y)$ is the tensile stress at w crack opening. y_0 is the neutral axis depth.

The parameters of the SFRC stress-crack width curve were found by fitting the CMOD curve obtained from BS EN 14651 tests on the SFRC (Figure A-3). The fitting parameters include the peak tensile strength f_t, the stress levels $\sigma_{1,I}$, $\sigma_{2,I}$, $\sigma_{3,I}$), and the corresponding crack openings $w_{1,I}$, $w_{2,I}$, $w_{3,I}$ at the kinks of the $\sigma - w$ curve shown in Figure A-7b. The inversion is conducted by fitting individual data from BS EN 14651 tests. A best-fit load-CMOD curve was obtained for each BS EN 14651 test and a set of best-fit tensile strength parameters was obtained. The statistics of the fitting parameters are summarized in Table A-3. The solid black line in Figure A-8a shows the load-CMOD curve using the average values of inverted parameters from individual tests. Figure A-8b shows the stress-crack width relationship using the average inverse parameters. The average peak tensile strength f_t estimated via the inverse analysis is 4.3 MPa. The estimated average residual tensile strengths corresponding to crack widths 0.05, 0.6, and 1.3 mm are 1.2, 2.2, and 2.8 MPa, respectively.

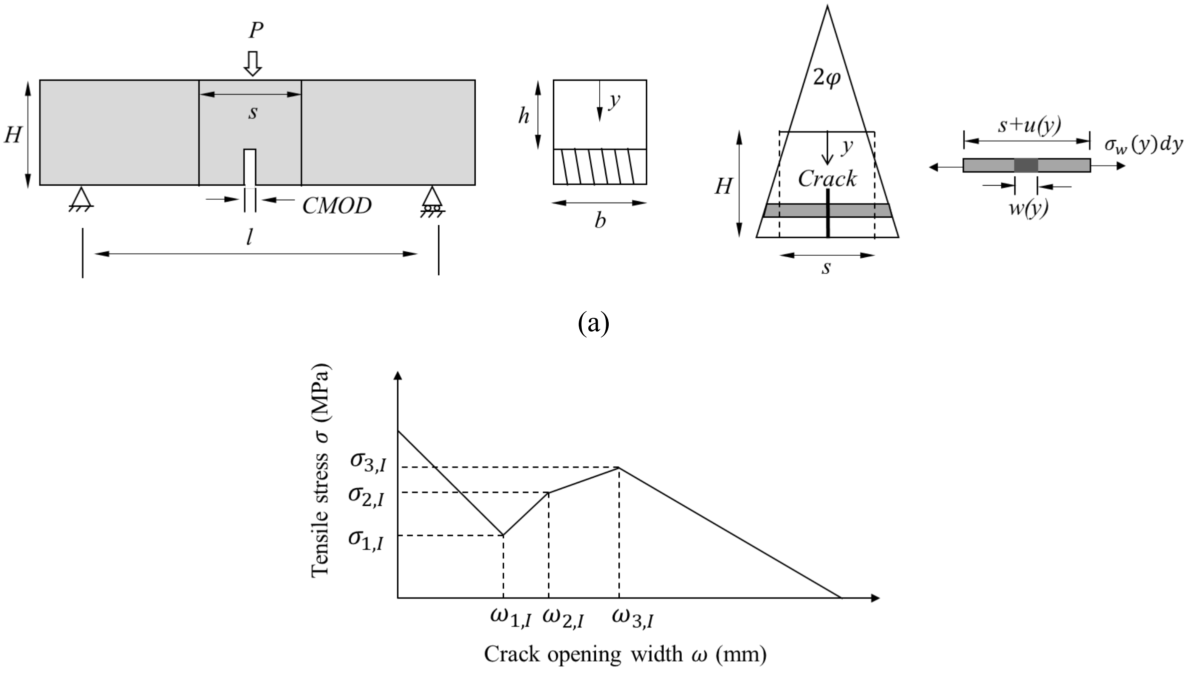

(a)

(b)

Figure A-7. (a) Cracked hinge model and (b) the tetralinear stress-crack opening relationship.

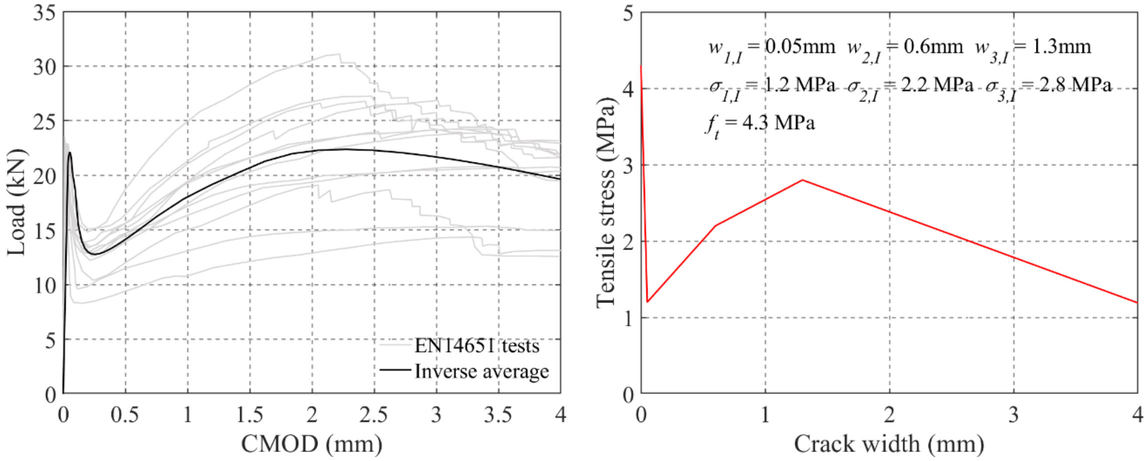

(a) (b)

Figure A-8. Inverse analysis results of (a) the load-CMOD curve and (b) stress-crack width relationship (mean values of fitting parameters).

Table A-3. Inverse analysis results using the tetralinear model (by fitting individual BS EN 14651 data).

-	f_t (MPa)	$\sigma_{1,I}$ (MPa)	$\sigma_{2,I}$ (MPa)	$\sigma_{3,I}$ (MPa)
Mean	4.3	1.2	2.2	2.8
Standard deviation	0.2	0.2	0.5	0.6
Minimum	4.6	1.6	3.2	3.8
Maximum	4.0	0.7	1.4	1.8

A7. Summary

Peak and residual tensile strengths were back calculated from BS EN 14651 beam test results using the three methods described above. The results are summarized in Table A-4. Given the measured average elastic modulus (30,940 MPa), the corresponding peak tensile strain limits were also calculated and are listed in Table 4. Peak tensile strengths were estimated to be 5.5 MPa (RILEM) and 4.3 MPa (Stephen inversion). For comparison, average splitting tensile strength was found to be 7.34 MPa; however, this magnitude reflects maximum hardened capacity and is not directly comparable to the peak tensile strengths that reflect the onset of cracking. The back-calculated residual tensile strength magnitudes were smaller than peak strength magnitudes, ranging from 1.2 to 2.8 MPa. For thrust loading design per ACI 544.7R-16[1], the allowable or ultimate thrust jack load will vary significantly depending on the assumed tensile strength.

The various inversion methods yield different results because assumptions regarding the shape of the stress-strain/crack width response affect the inversed parameters. For the purpose of comparison with the strain data and cracking behavior obtained in the thrust jack load tests, the peak tensile strength and strain are used as they represent the onset of the first cracking.

Table A-4. Estimated peak and residual tensile strength and strain.

-	Mean peak tensile strength (MPa)	Mean peak tensile strain ($\mu\varepsilon$)	Mean residual tensile strength (MPa)	
RILEM TC 162-TDF	5.5	180	$\sigma_{2,E}$	1.7
			$\sigma_{3,E}$	1.7
fib Model Code	-	-	$f_{Ftu,R}$	2.3
			$f_{Fts,L}$	2.1
			$f_{Ftu,L}$	2.1
Full inversion	4.3	140	$\sigma_{1,I}$	1.2
			$\sigma_{2,I}$	2.2
			$\sigma_{3,I}$	2.8

Appendix B. Detailed Thrust Jack Test Results

The results from each of the six thrust jack load tests are provided here. The test matrix is summarized in Table B-1. The plots of load-time histories of all tests are shown in Figure B-1 below, where the solid line plots represent the load-time histories for double point load tests, and the dashed line plots represent the load-time histories for single point load tests. Details of each test are demonstrated in the following sections.

Table B-1: Test matrix of thrust jack tests.

Test No.	Segment No.	Segment Type	Loading Condition	Age at Test Date (days)
1	1	Hybrid	Double Point, Concentric	199
2			Single Point, Concentric	203
3	2	SFRC	Single Point, Concentric	313
4	3	Hybrid	Double Point, Concentric	214
5			Single Point, Eccentric	216
6	4	SFRC	Double Point, Concentric	673

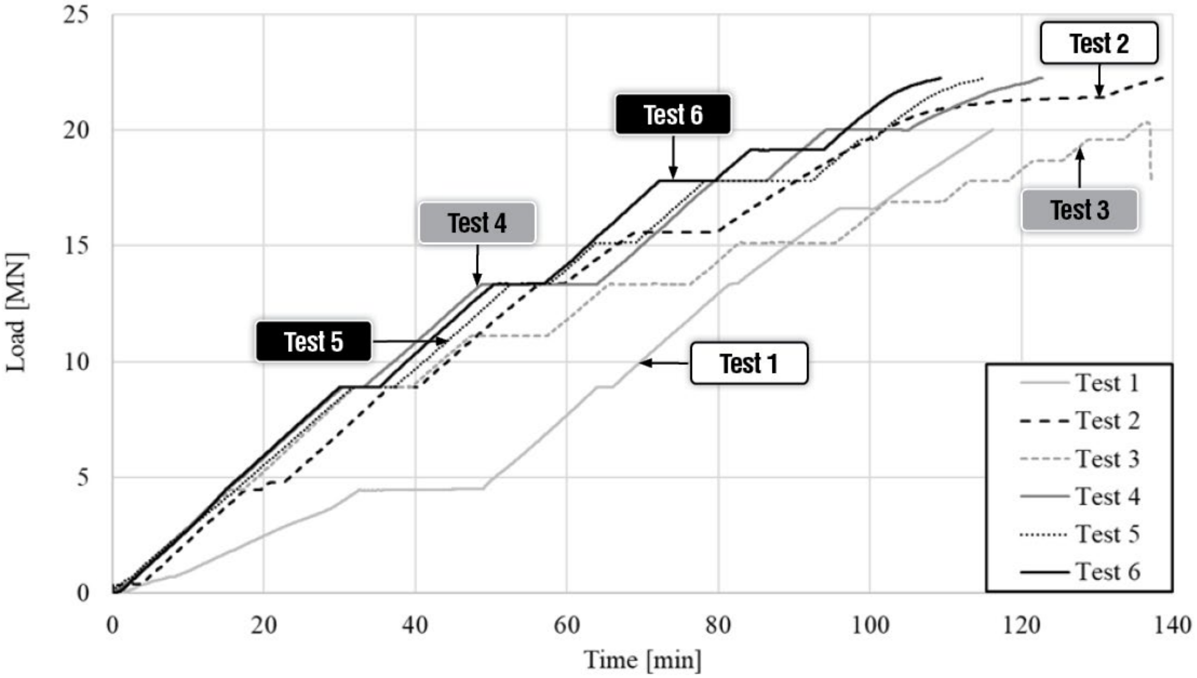

Figure B-1: Load-time histories for all tests.

B1. Test 1

This test examined the performance of a hybrid tunnel liner segment under concentric double point load. The loading rate was kept at approximately 296.6 kN/min. The detailed description of this test is presented in Table B1-1. Pictures of the segment before and after testing are shown in Figure B1-1. The geometry and dimensions of the tested segment is presented in Figure B1-2.

Table B1-1: Description of test 1.

Test No.	1
Previously Tested?	No
Segment Serial Number	SG 2006 9332
Segment Type	Hybrid
Segment Mold	GH-1
Age at Test Date	199 Days
Maximum Applied Load	20017 kN (4500 kips)
Description	Double Point Load Concentric

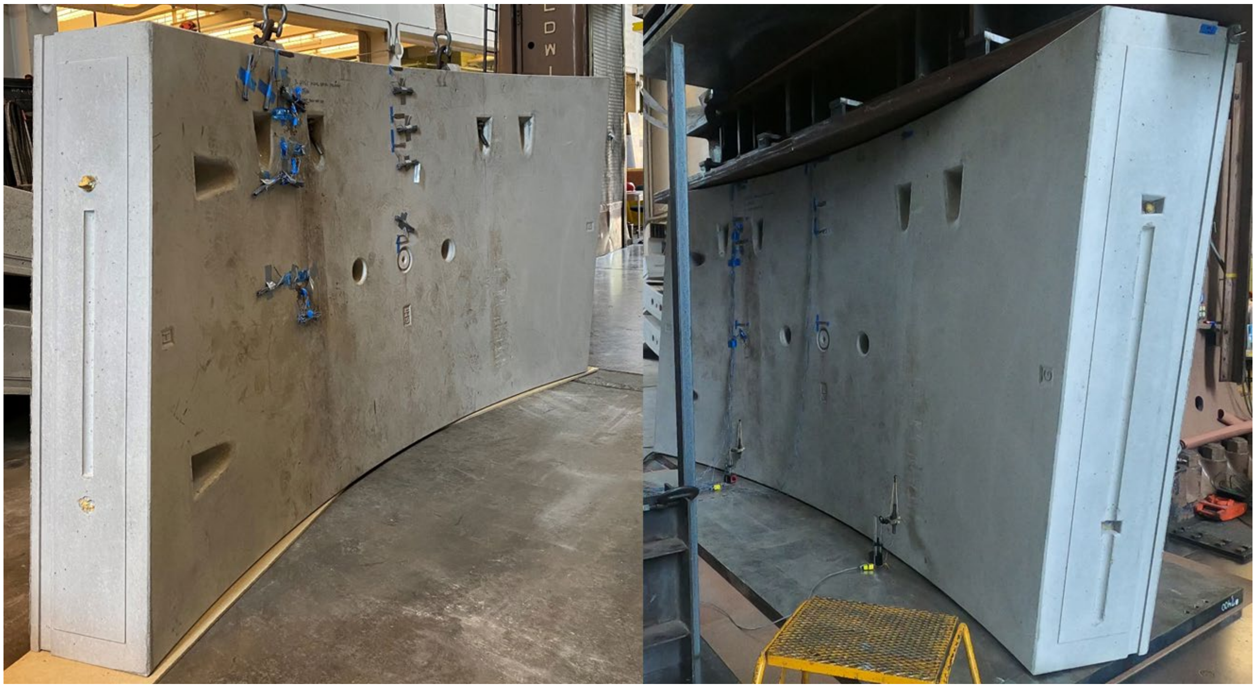

Figure B1-1: Intrados image of segment before (left) and after (right) testing.

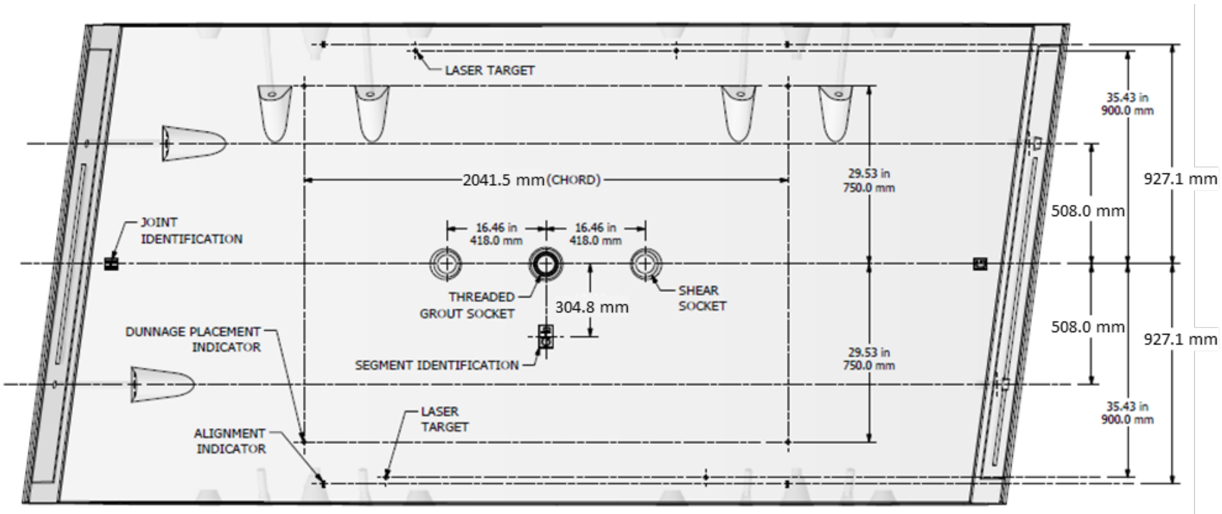

SEGMENT "GH" NORMAL TO CENTER VIEW OF INTRADOS

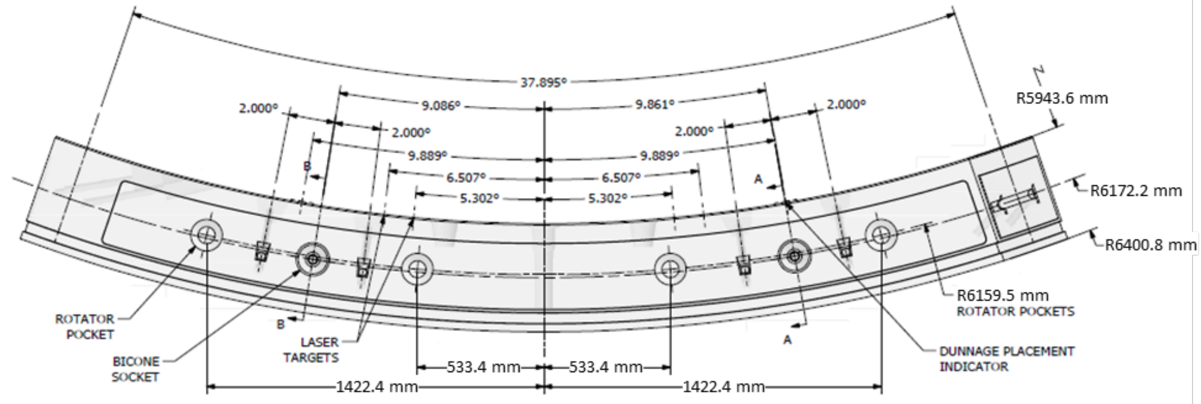

SIDE VIEW OF TRAILING EDGE

Figure B1-2: Geometry and dimensions of GH tunnel liner segment.

A double load pad configuration was used. This configuration is used at the top and bottom of the segment and is illustrated in Figure B1-3. The bearing pad layout is the same for both top and bottom locations.

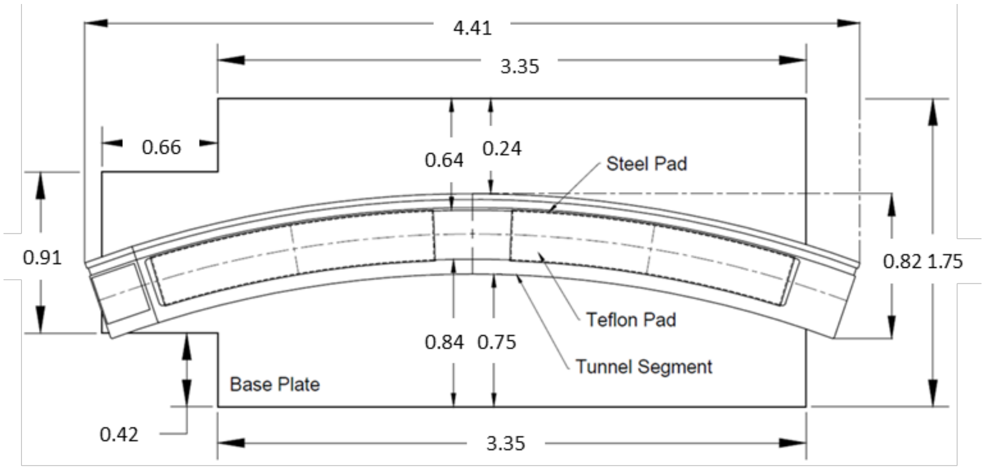

Figure B1-3: Plan view of load pad location at top and bottom of segment (dimensions in m).

Notes:

1. S1-S12 and S19 are surface bonded strain gages.
2. S13-S18 are radial strain gages, which are bonded to an epoxy stick before being inserted into the pre-drilled hole.
3. Strain gages S13, S15 and S17 are located at the mid-thickness of the segment, and S14, S16 and S18 are located 76 mm from intrados face.
4. Strain gage S15 was found malfunctioned before testing and is not presented in the data summary.

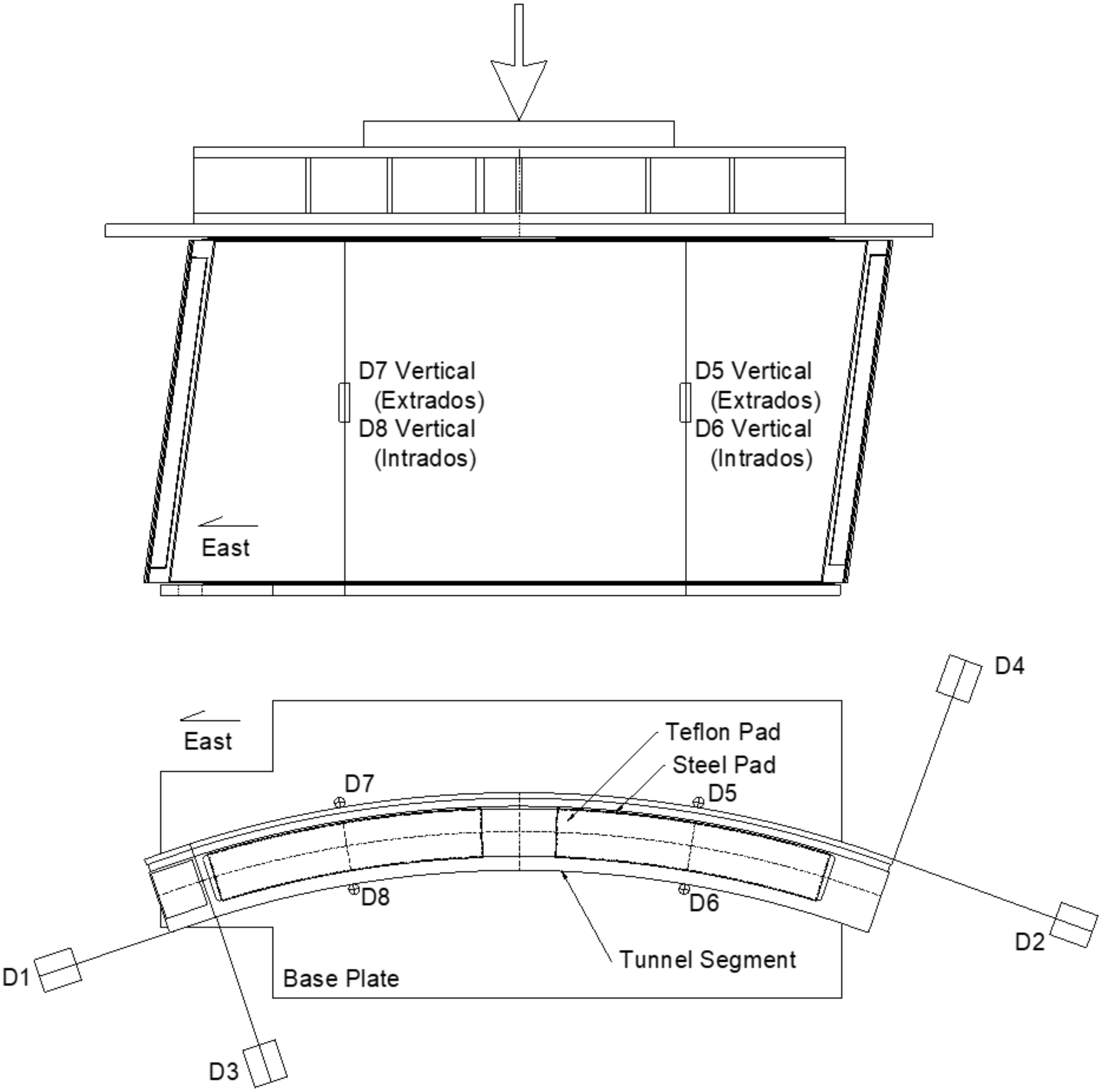

Figure B1-4: Displacement transducer layout.

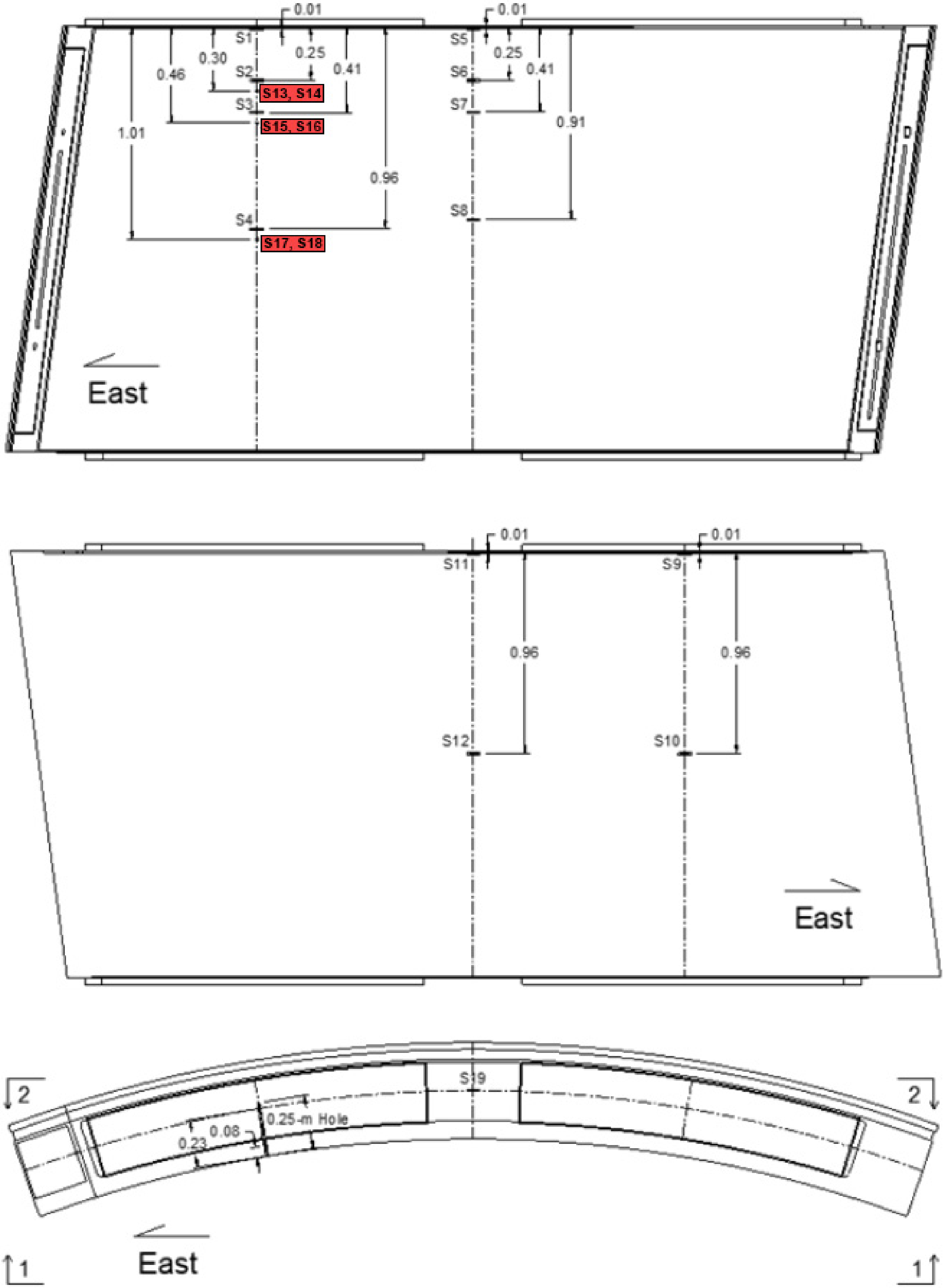

Figure B1-5: Strain gage layout.

B1.1. Load-Deformation

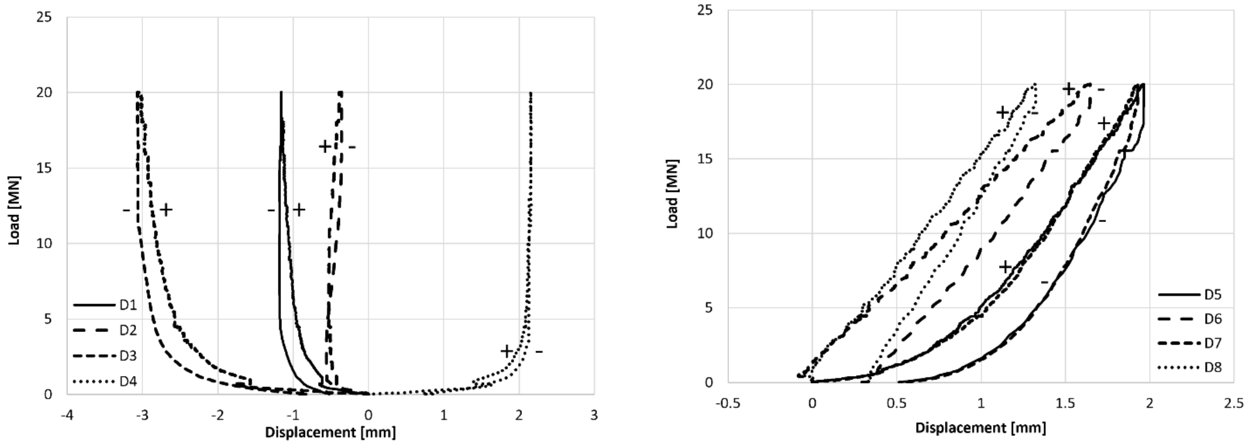

(a) (b)

Figure B1-6: Load versus (a) horizontal, and (b) vertical deformations of segment.

Notes: (1) Segment loading was paused a few key load levels to mark crack propagation; (2) The maximum applied load was 20.0 MN; (3) The segment exhibited no significant damage. A few small cracks were observed at the maximum applied load, 20.0 MN. The crack formation is illustrated in Figure B1-11.

B1.2. Strain Response

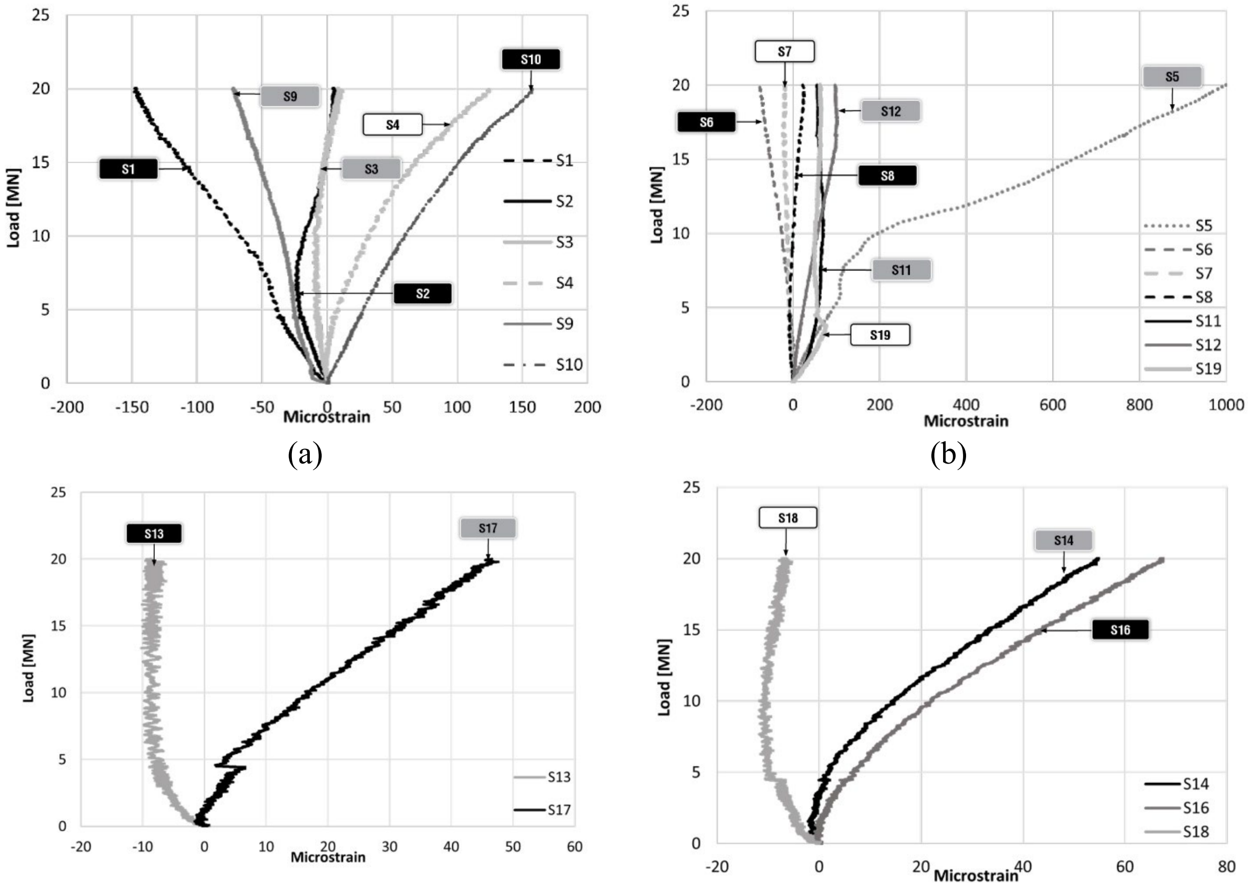

(a) (b)

(c) (d)

Figure B1-7: Strain gage data.

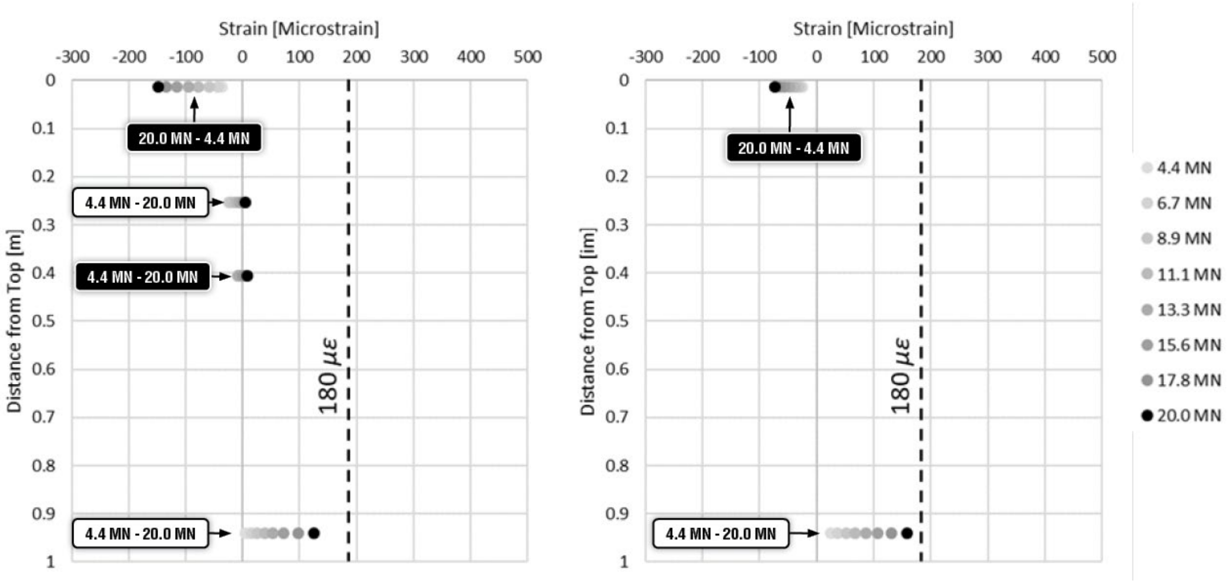

(a) (b)

Figure B1-8: Transverse strain for double-point-load tests at (a) load pad center intrados, and (b) load pad center extrados.

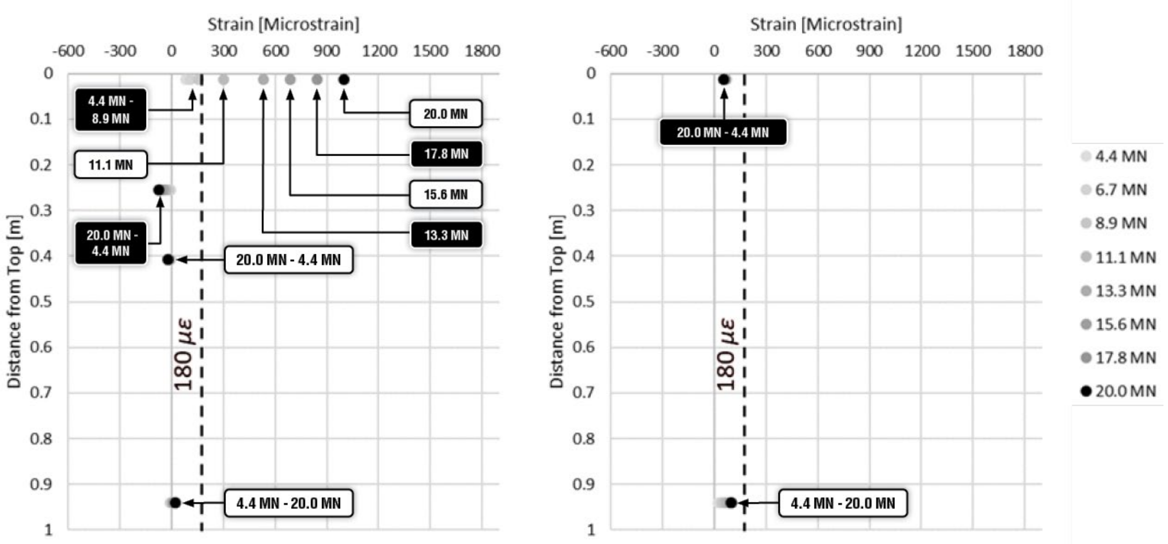

(a) (b)

Figure B1-9: Transverse strain for double-point-load tests at (a) midspan intrados, and (b) midspan extrados.

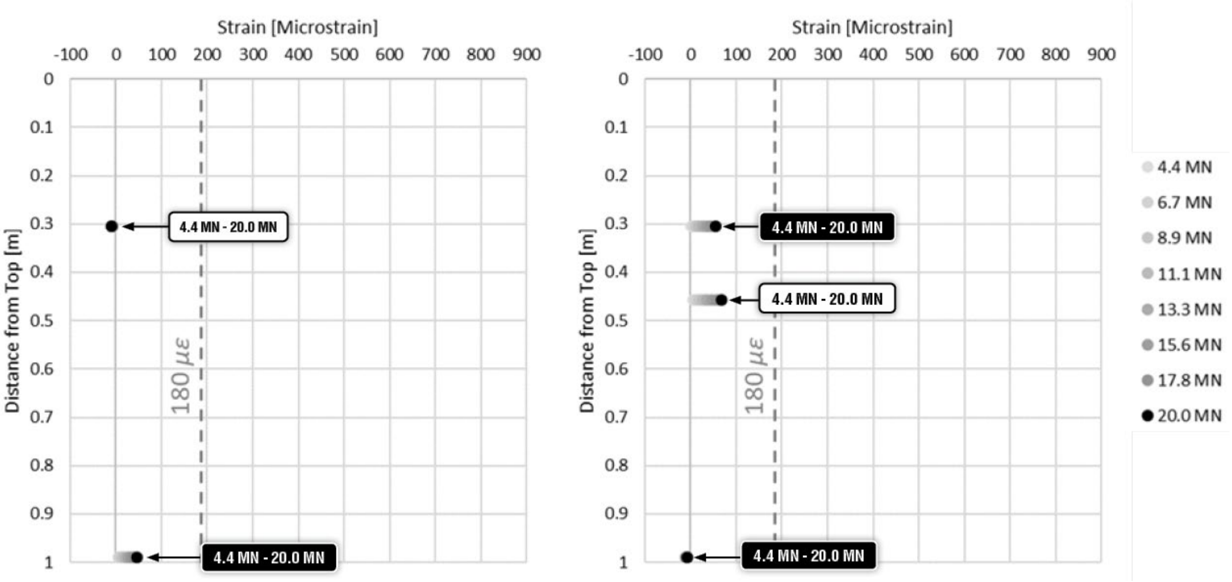

(a) (b)

Figure B1-10: Radial strain at (a) mid-thickness, and (b) 76 mm from intrados face.

B1.3. Cracking Response

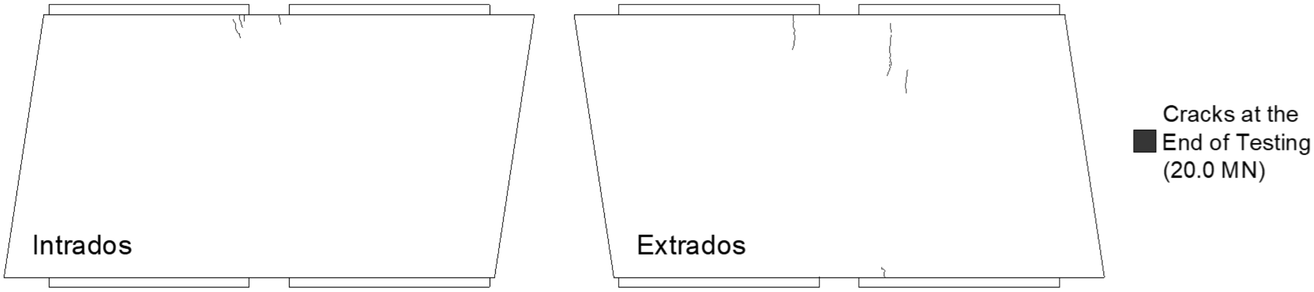

Figure B1-11: Crack propagation for test 1 on intrados face (left) and extrados face (right).

Notes:

1. No significant damage was observed at the end of testing. Only a few small cracks were found.

B2. Test 2

This test examined the performance of a hybrid tunnel liner segment under concentric single point load. The loading rate was kept at approximately 296.6 kN/min. The detailed description of this test is presented in Table B2-1. Pictures of the segment before and after testing are shown in Figure B2-1. The geometry and dimensions of the tested segment are presented in Figure B2-2.

Table B2-1: Description of test 2.

Test No.	2
Previously Tested?	Yes
Segment Serial Number	SG 2006 9332
Segment Type	Hybrid
Segment Mold	GH-1
Age at Test Date	203 Days
Maximum Applied Load	22224 kN (4996 kips)
Description	Single Point Load Concentric

Figure B2-1: Intrados image of segment before (left) and after (right) testing.

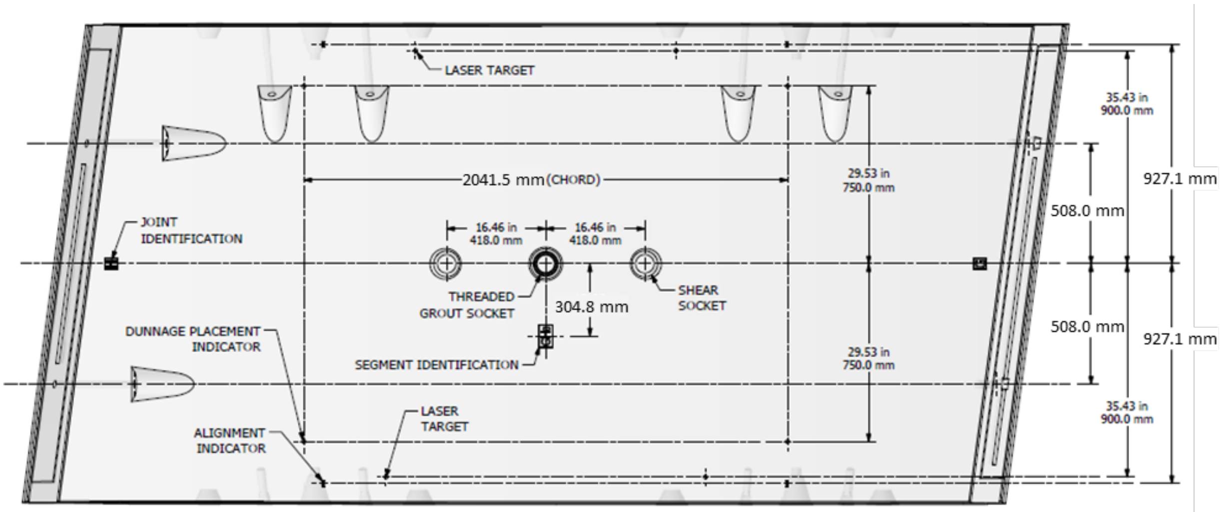

SEGMENT "GH" NORMAL TO CENTER VIEW OF INTRADOS

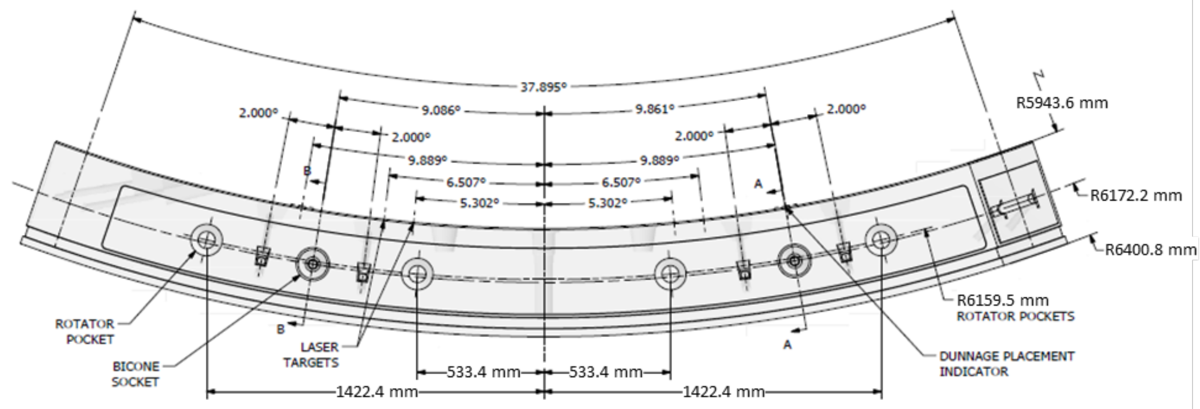

SIDE VIEW OF TRAILING EDGE

Figure B2-2: Geometry and dimensions of GH tunnel liner segment.

A single load pad configuration was used. This configuration is used at the top and bottom of the segment and is illustrated in Figure B2-3. The bearing pad layout is the same for both top and bottom locations.

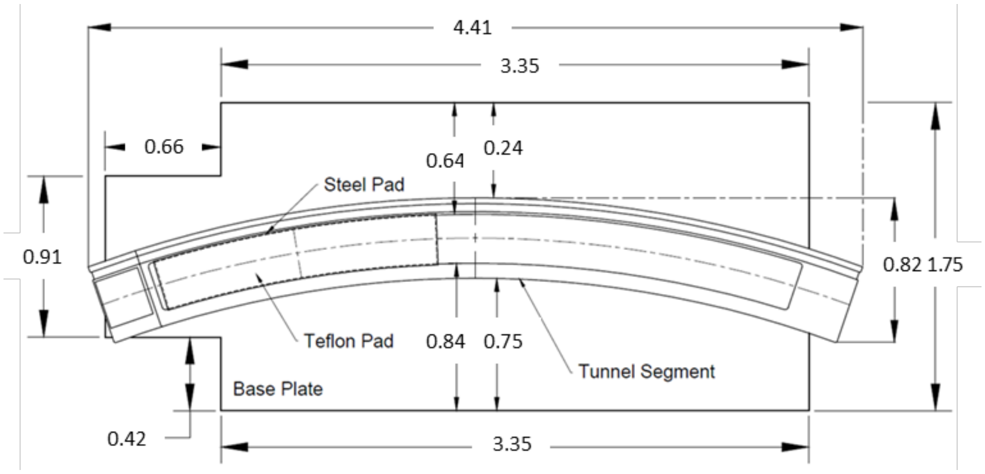

Figure B2-3: Plan view of load pad location at top and bottom of segment (dimensions in m).

Notes:

1. S1-S12 and S19 are surface bonded strain gages.
2. S13-S18 are radial strain gages, which are bonded to an epoxy stick before being inserted into the pre-drilled hole.
3. Strain gages S13, S15 and S17 are located at the mid-thickness of the segment, and S14, S16 and S18 are located 76 mm from intrados face.
4. Strain gage S15 was found malfunctioned before testing and are not presented in the data summary.

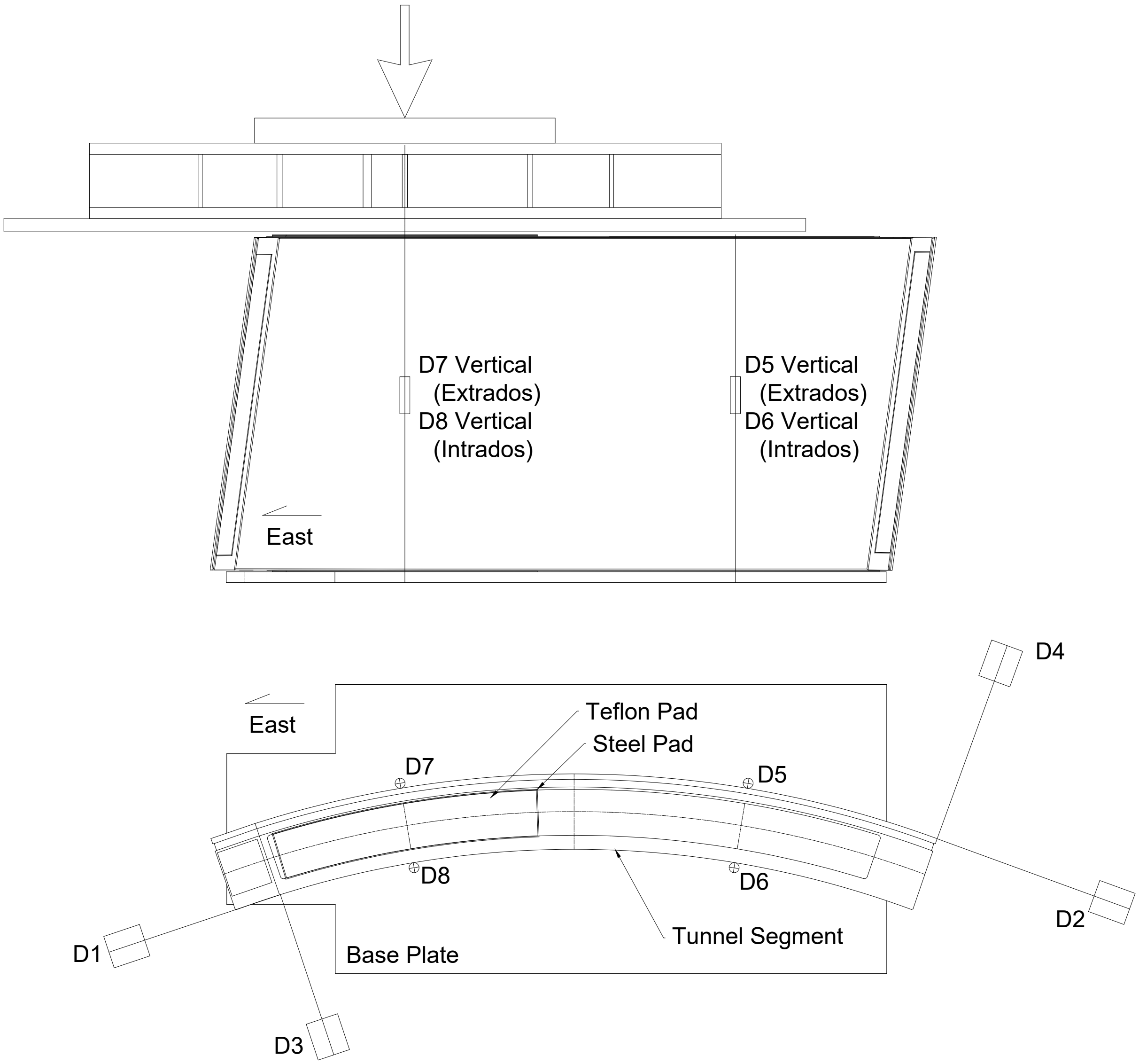

Figure B2-4: Displacement transducer layout.

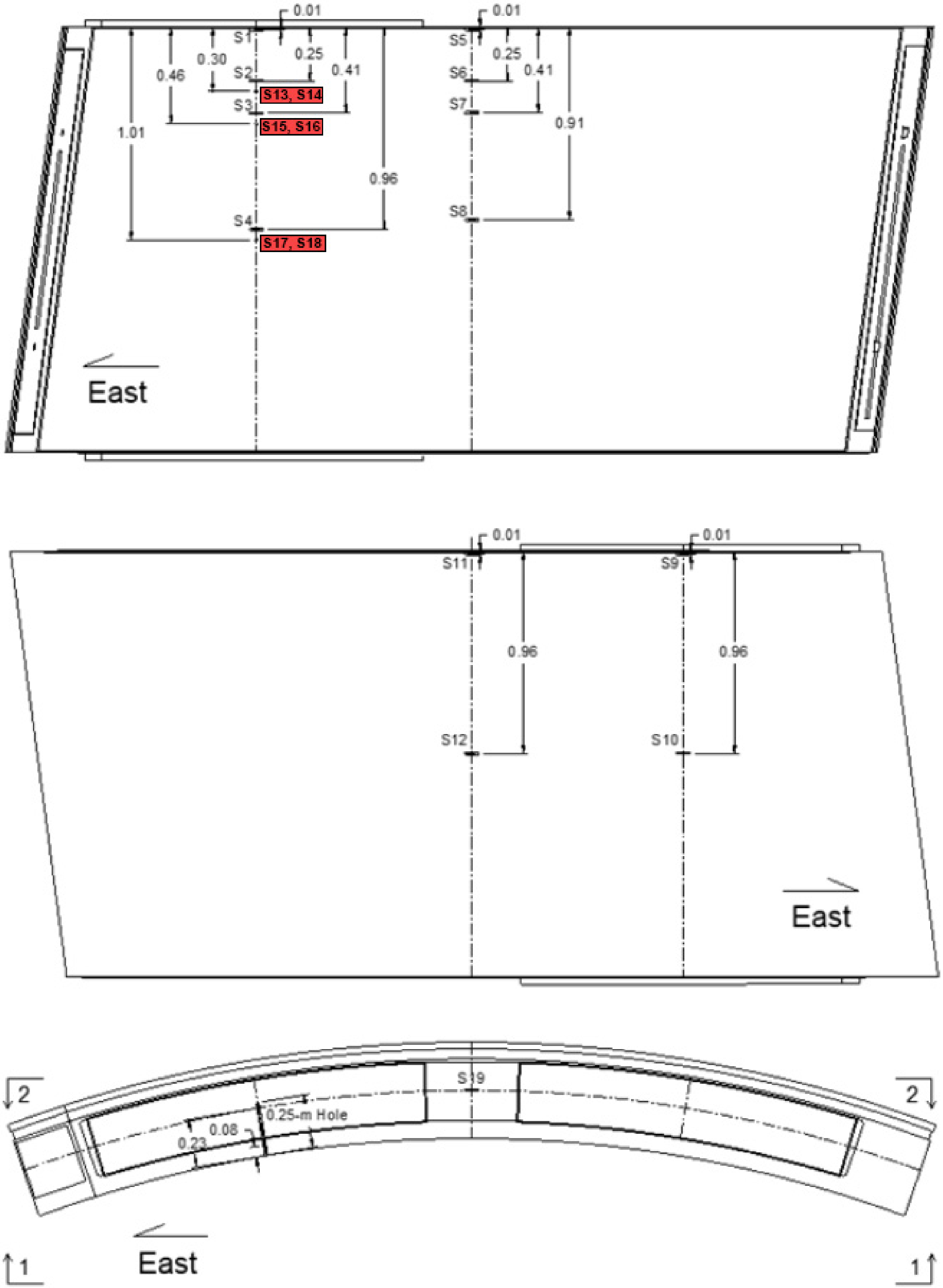

Figure B2-5: Strain gage layout.

B2.1. Load-Deformation

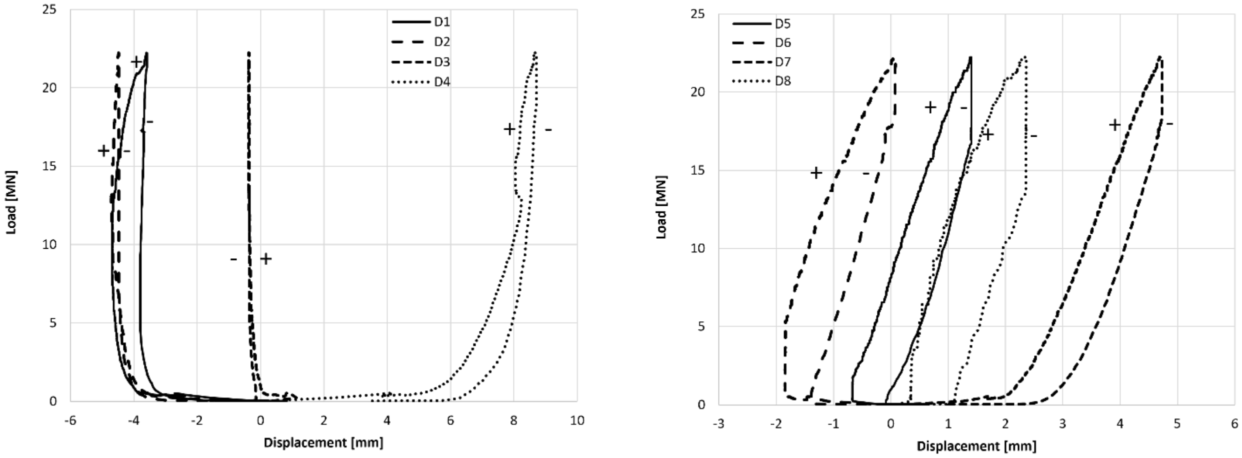

(a) (b)

Figure B2-6: Load versus (a) horizontal, and (b) vertical deformations of segment.

Notes: (1) Segment loading was paused a few key load levels to mark crack propagation; (2) The maximum applied load was 22.2 MN; (3) Significant cracking damage was observed at the end of testing as shown in Figure B2-7. Cracks started to develop at approximately 13.3 MN and increased in width and quantity with increasing load. The crack formation is illustrated in Figure B2-12.

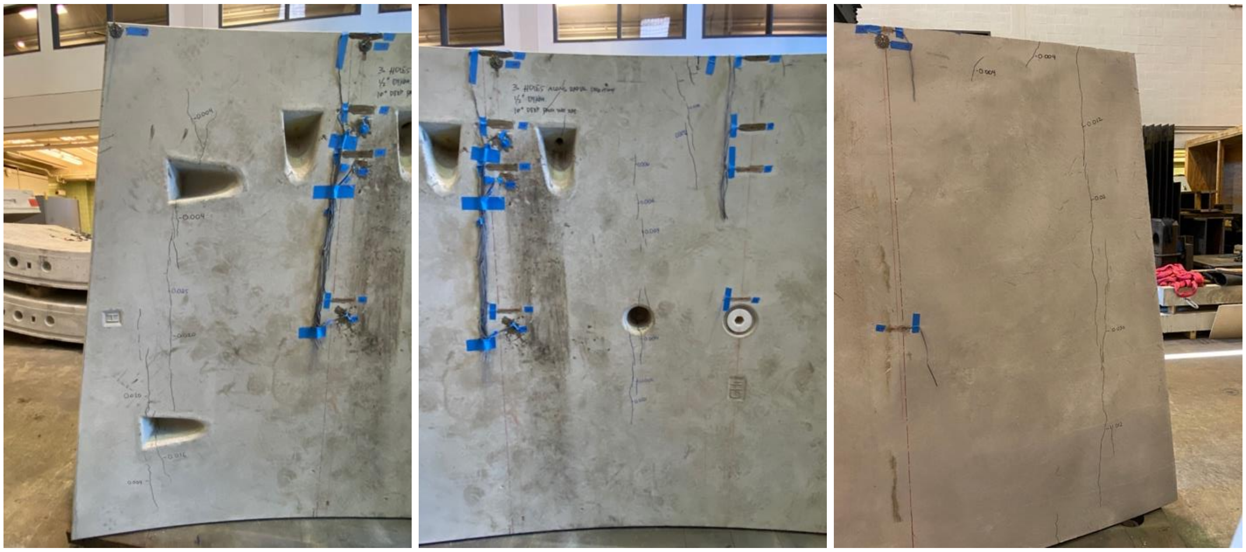

Figure B2-7: Damage of segment after Test 2 completion.

B2.2. Strain Response

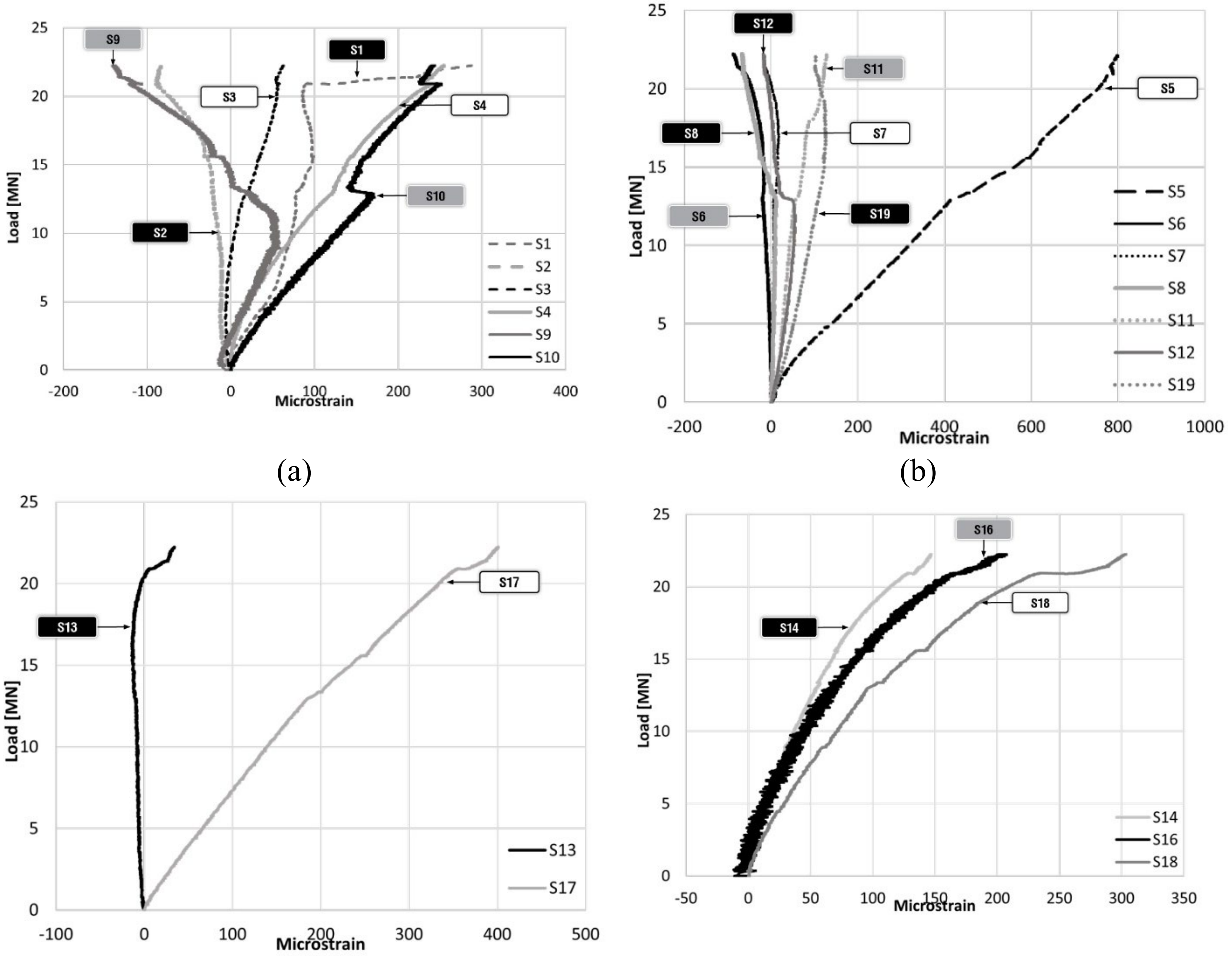

(a) (b)

(c) (d)

Figure B2-8: Strain gage data.

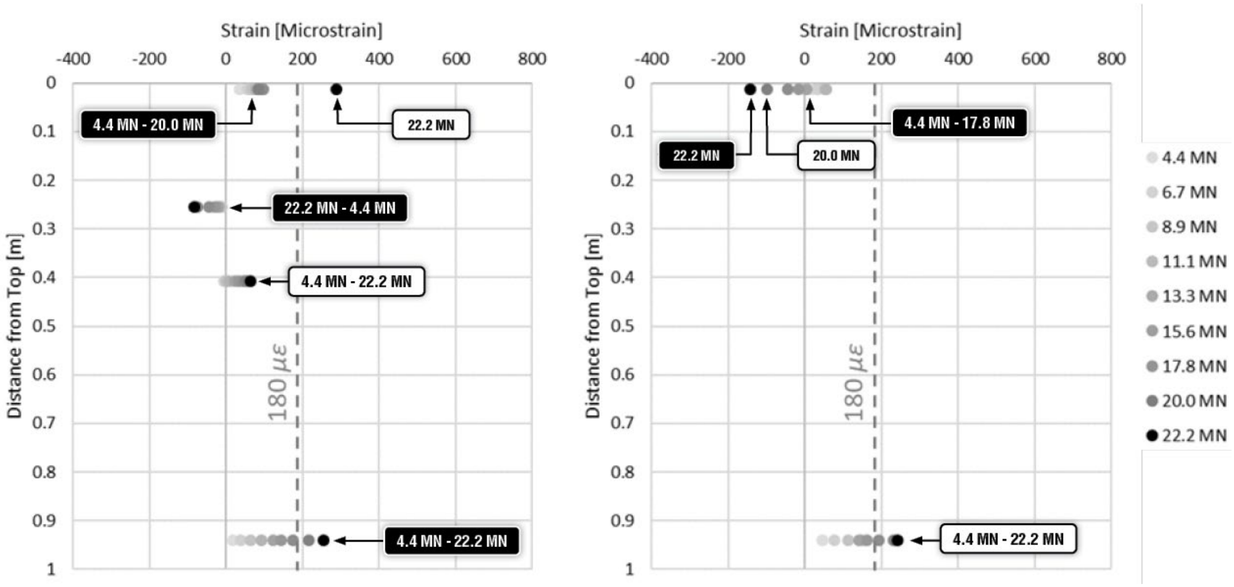

(a) (b)

Figure B2-9: Transverse strain for single-point-load tests at (a) load pad center intrados, and (b) load pad center extrados.

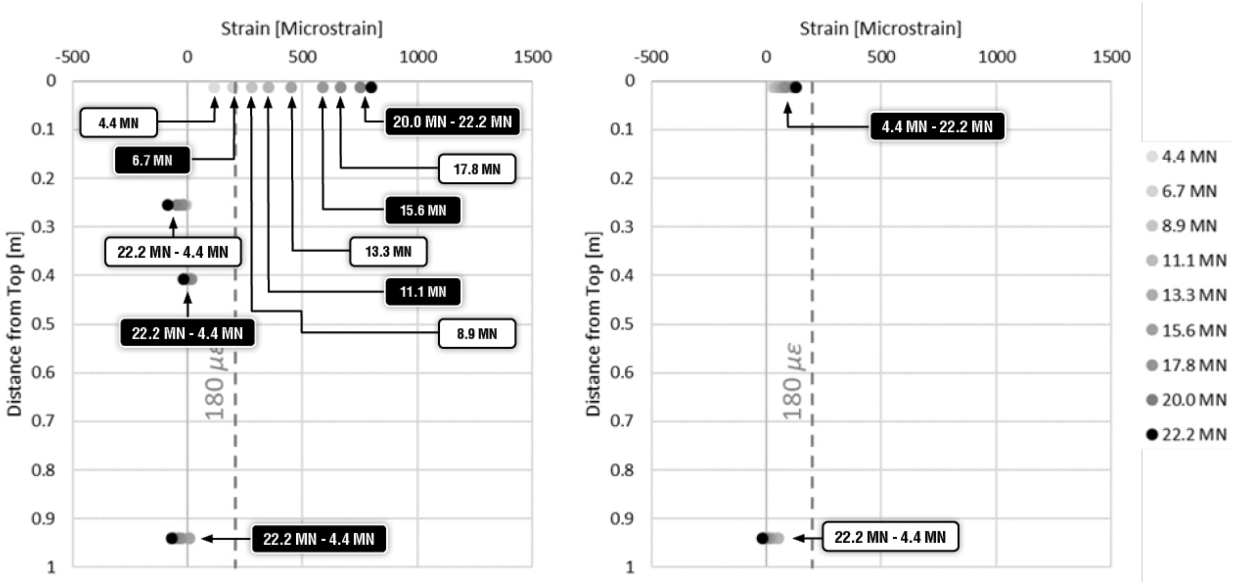

(a) (b)

Figure B2-10: Transverse strain for single-point-load tests at (a) midspan intrados, and (b) midspan extrados.

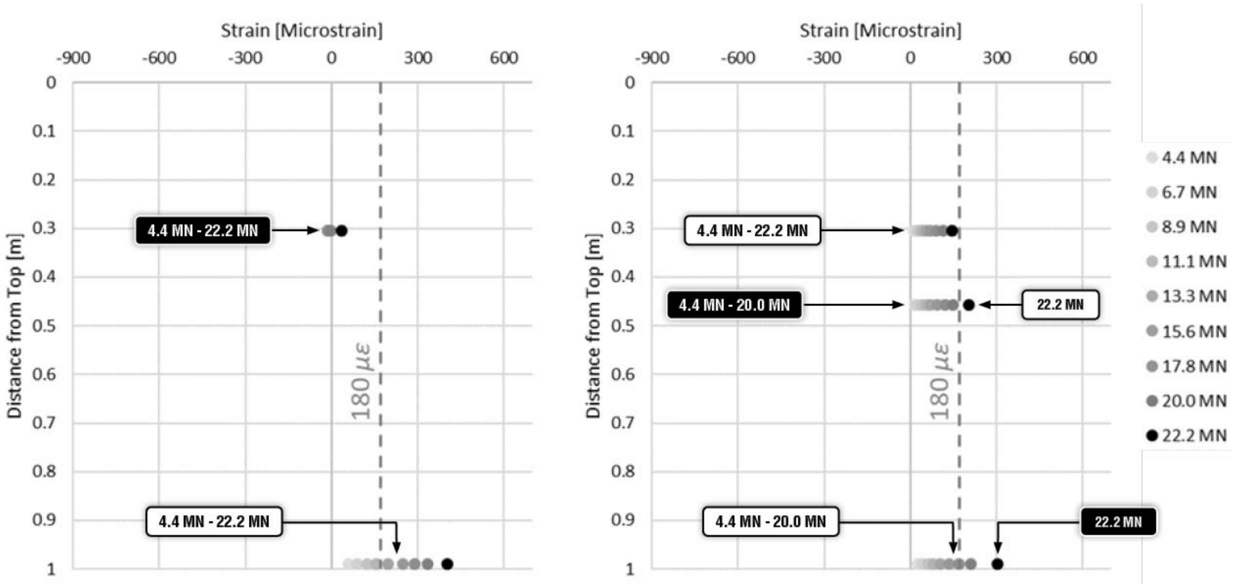

(a) (b)

Figure B2-11: Radial strain at (a) mid-thickness, and (b) 76 mm from intrados face.

B2.3. Cracking Response

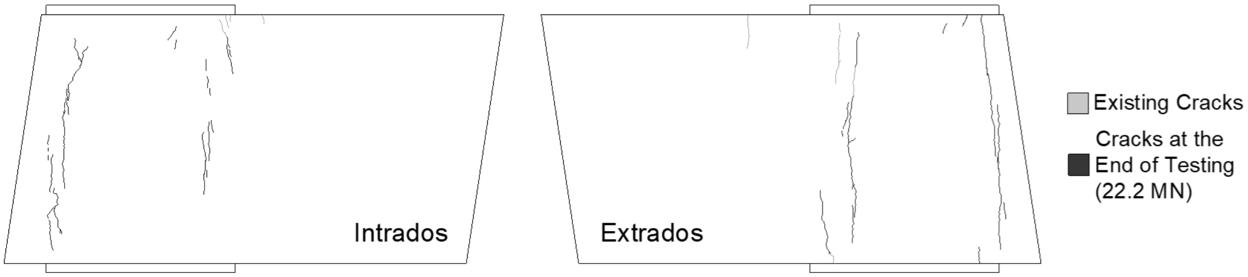

Figure B2-12: Crack propagation for test 2 on intrados face (left) and extrados face (right).

Notes:

1. The segment did not fail at the end of testing, but cracking appeared near the edge of the loading pad and base.
2. The cracks propagated approximately in straight lines along vertical direction. The first crack developed under approximately 13.3 MN near the edge of the loading pad or strain gage S5. Cracks developed gradually with increasing load.
3. More cracking occurred on the extrados face than the intrados face.

B3. Test 3

This test examined the performance of an SFRC tunnel liner segment under concentric single point load. The loading rate was kept at approximately 296.6 kN/min. The detailed description of this test is presented in Table B3-1. Pictures of the segment before and after testing are shown in Figure B3-1. The geometry and dimensions of the tested segment is presented in Figure B3-2.

Table B3-1: Description of test 3.

Test No.	3
Whether Previously Tested	No
Segment Serial Number	SG 2005 0569
Segment Type	SFRC
Segment Type and Mold	HI-1
Age at Test Date	313 Days
Maximum Applied Load	20.3 MN (4568 kips)
Description	Single Point Load Concentric

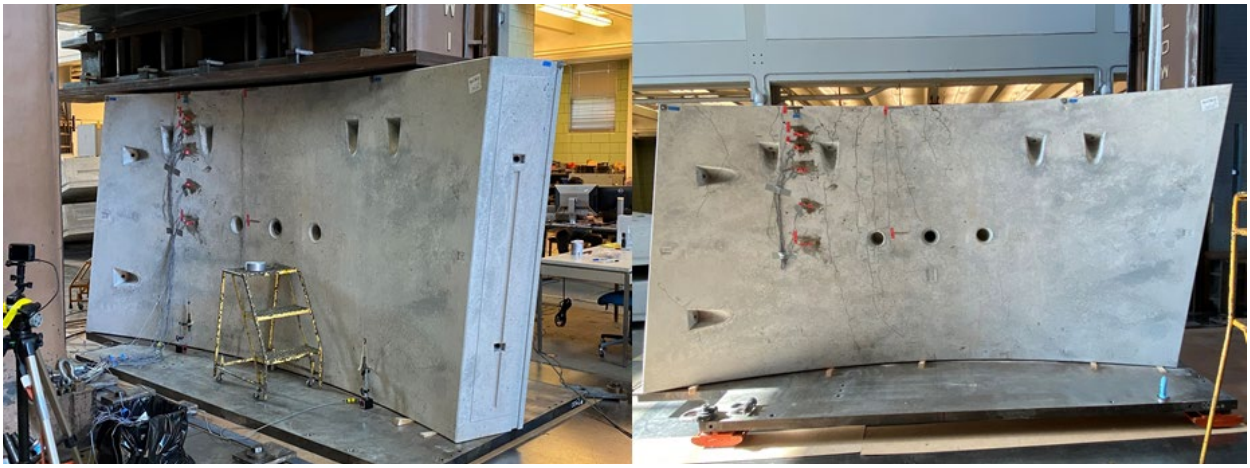

Figure B3-1: Intrados image of segment before (left) and after (right) testing.

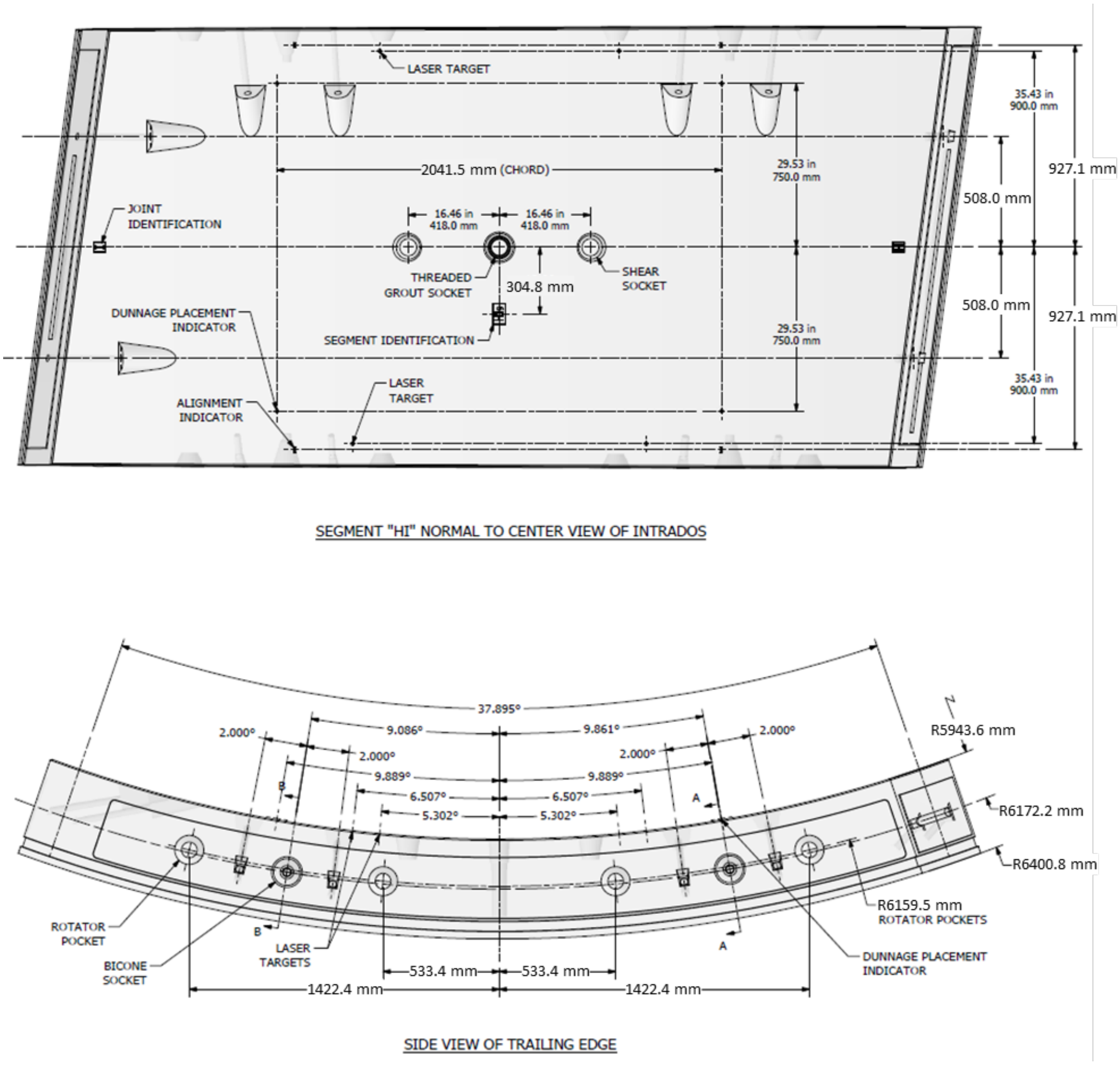

Figure B3-2: Geometry and dimensions of HI tunnel liner segment.

A single load pad configuration was used. This configuration is used at the top and bottom of the segment and is illustrated in Figure B3-3. The bearing pad layout is the same for both top and bottom locations.

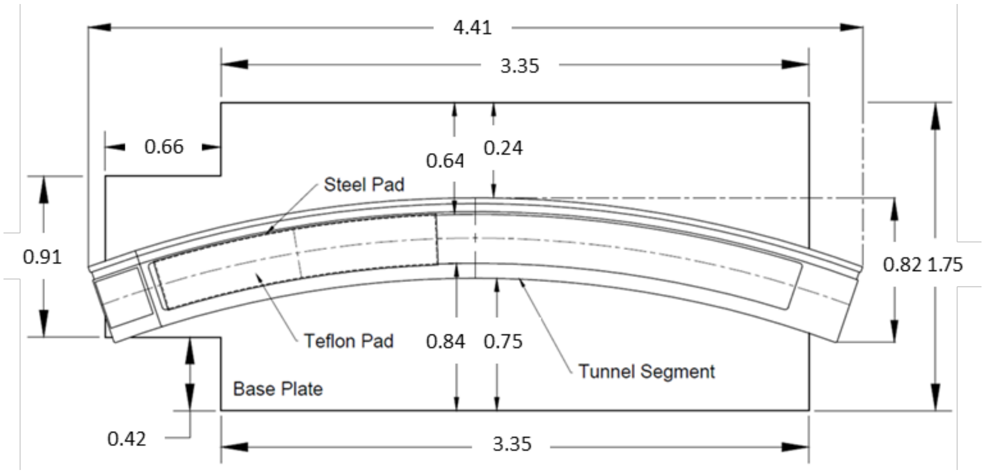

Figure B3-3: Plan view of load pad location at top and bottom of segment (dimensions in m).

Notes:

1. S1-S12 are surface bonded strain gages.
2. S13-S22 are radial strain gages, which are bonded to an epoxy stick before being inserted into the pre-drilled hole.
3. Strain gages S13, S15, S17, S19 and S21 are located at the mid-thickness of the segment, and S14, S16, S18, S20 and S22 are located 76 mm from intrados face.
4. Strain gages S13, S14, S15, S16, S17, S19, S21 and S22 were found malfunctioned before testing and are not presented in the data summary.

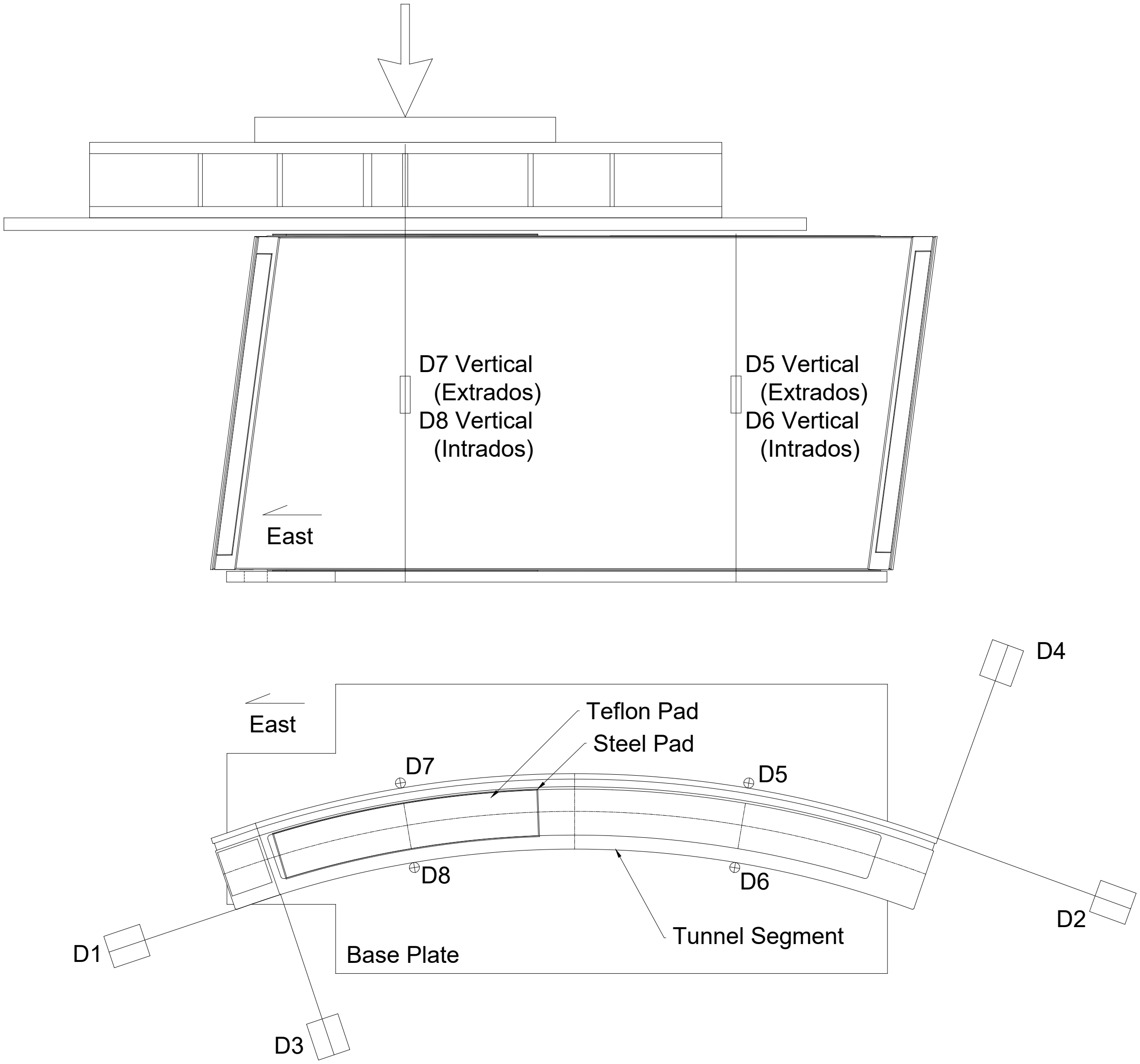

Figure B3-4: Displacement transducer layout.

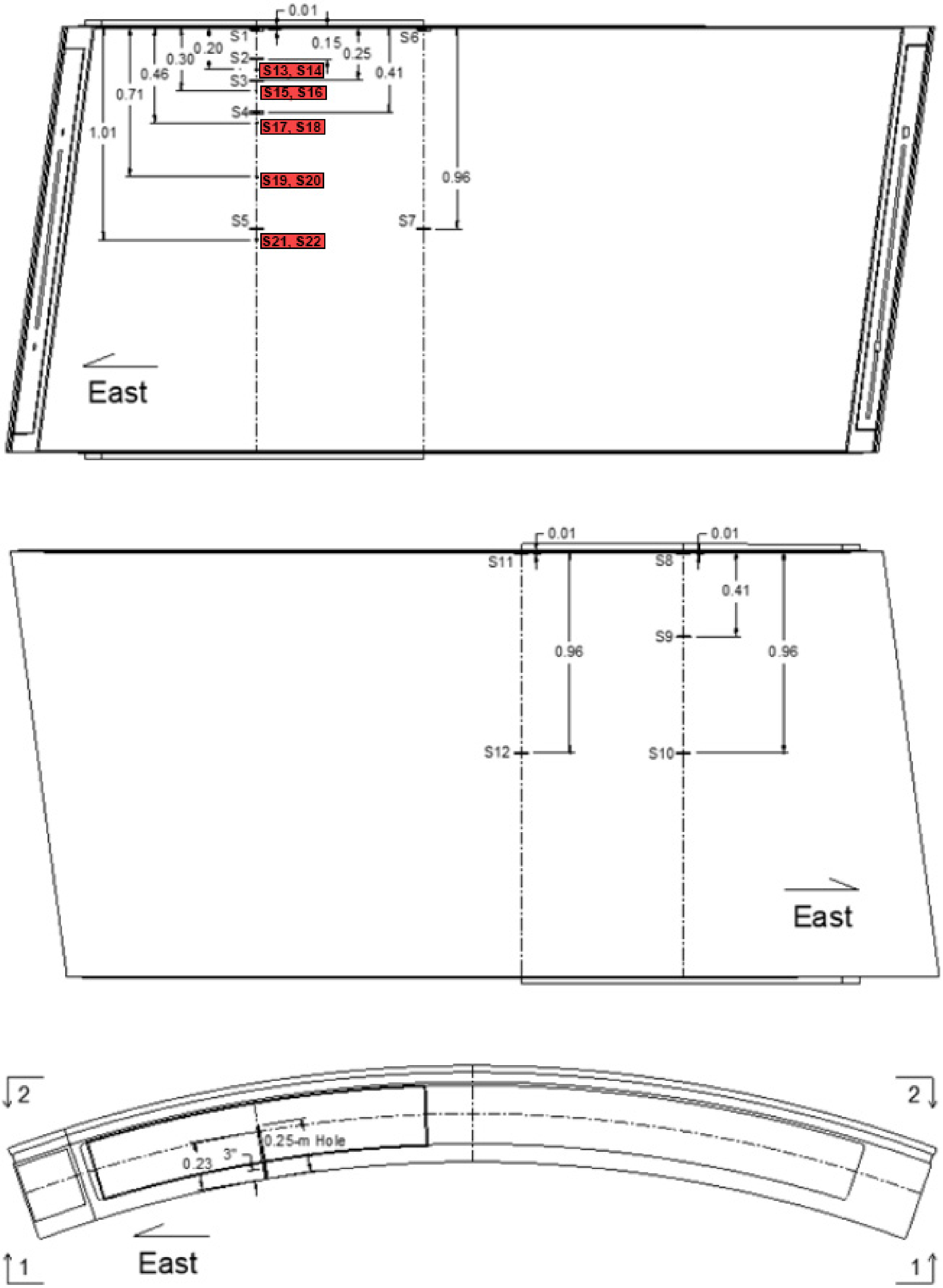

Figure B3-5: Strain gage layout.

B3.1. Load-Deformation

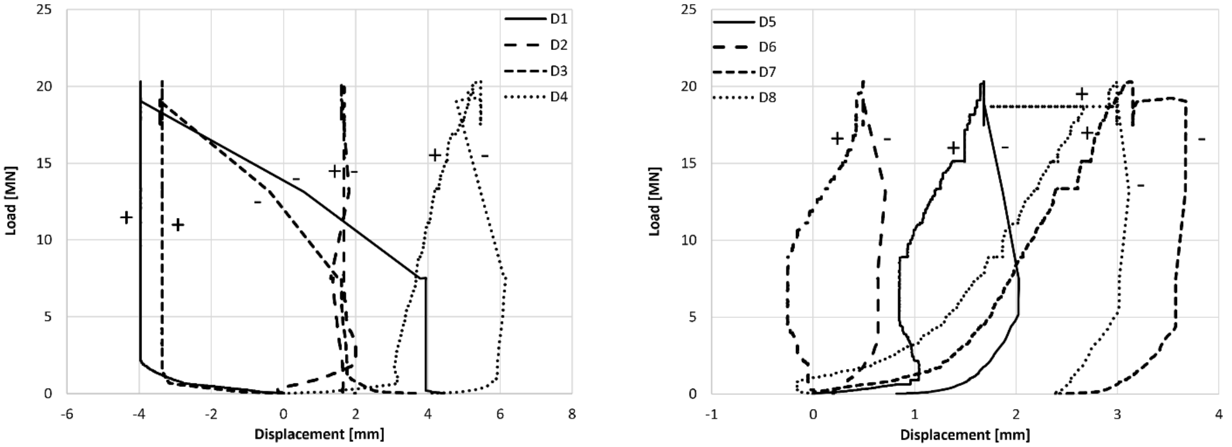

(a) (b)

Figure B3-6: Load versus (a) horizontal, and (b) vertical deformations of segment.

Notes: (1) Segment loading was paused a few key load levels to mark and measure crack propagation; (2) The maximum applied load was 20.3 MN; (3) The segment failed abruptly through crushing and vertical cracking under the load pad as shown in Figure B3-7. Cracks started to develop at approximately 8.90 MN and increased in width and quantity with increasing load. The crack formation and size are summarized in Table B3-2 and illustrated in Figure B3-12.

Figure B3-7: Damage of segment after test 3 completion.

B3.2. Strain Response

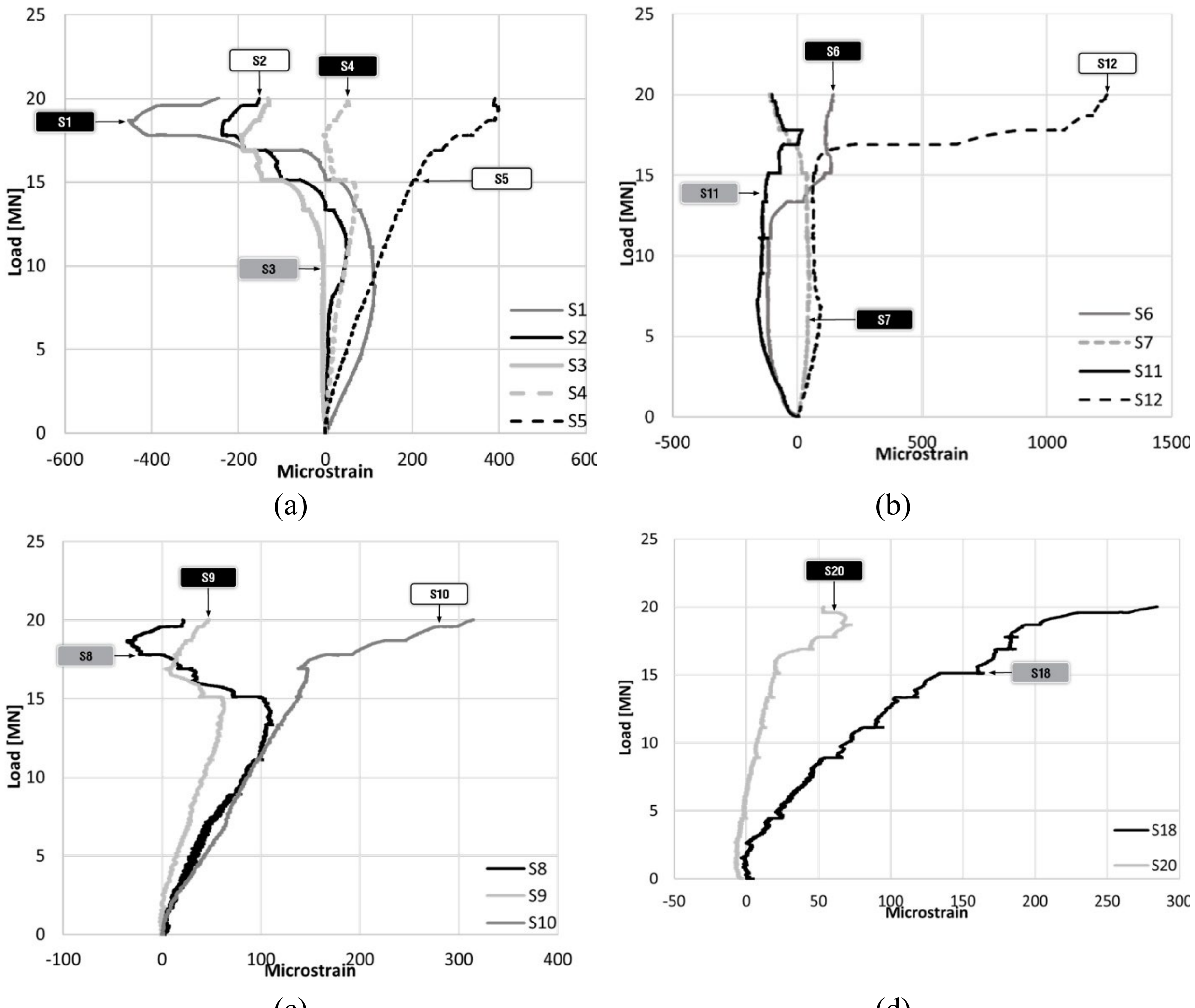

(a) (b)

(c) (d)

Figure B3-8: Strain gage data.

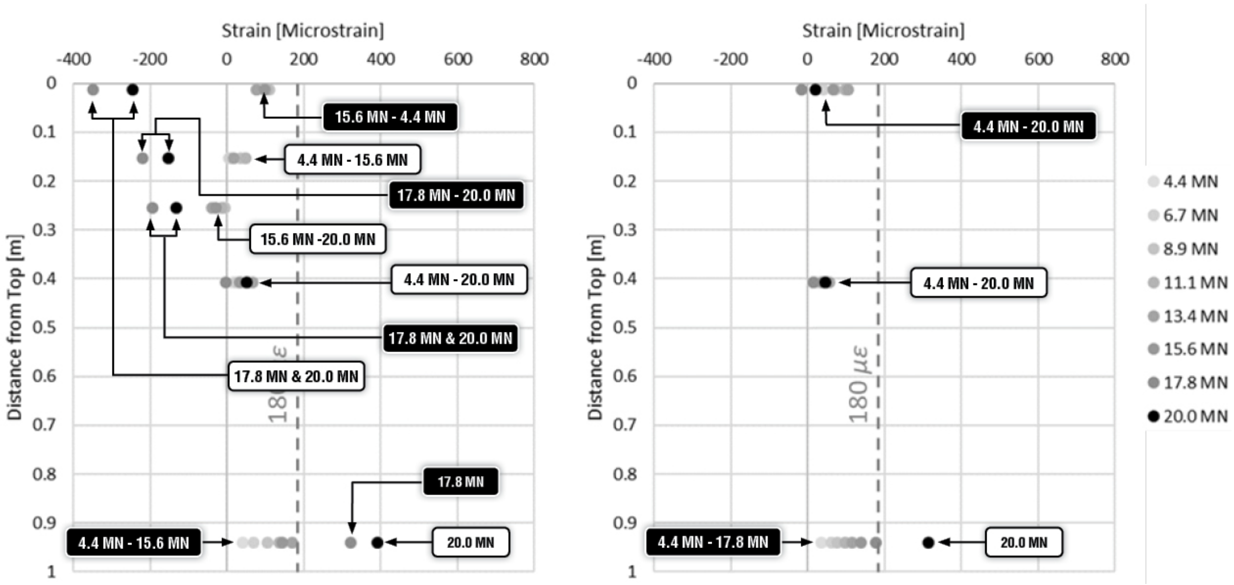

(a) (b)

Figure B3-9: Transverse strain for single-point-load tests at (a) load pad center intrados, and (b) load pad center extrados.

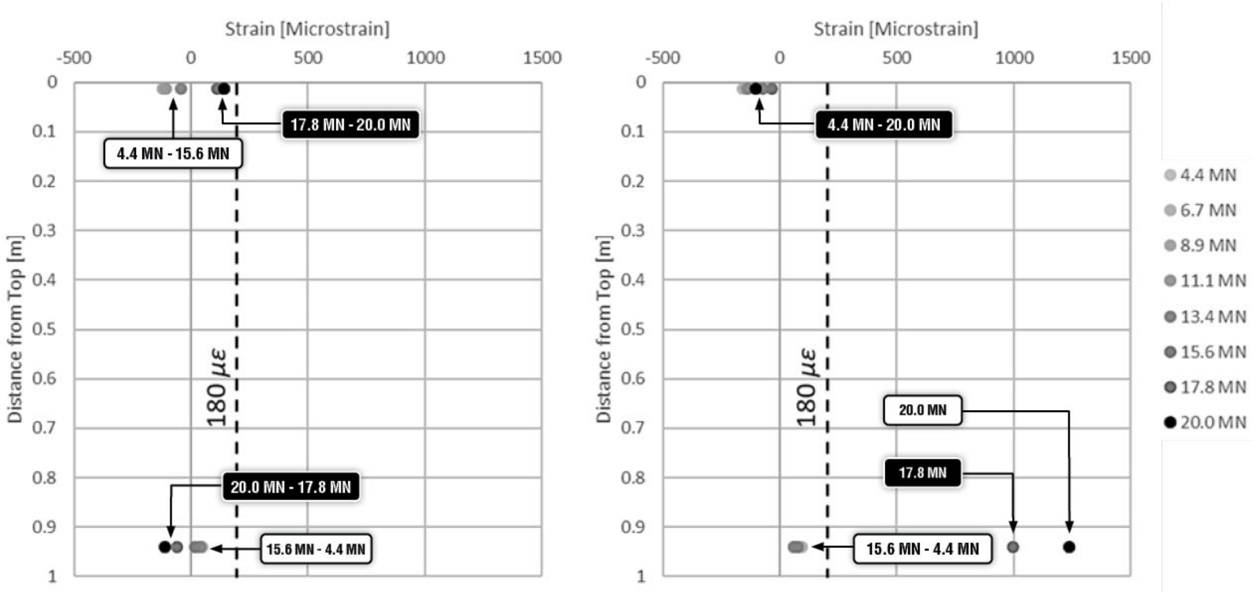

(a) (b)

Figure B3-10: Transverse strain for single-point-load tests at (a) load pad edge near midspan intrados, and (b) load pad edge near midspan extrados.

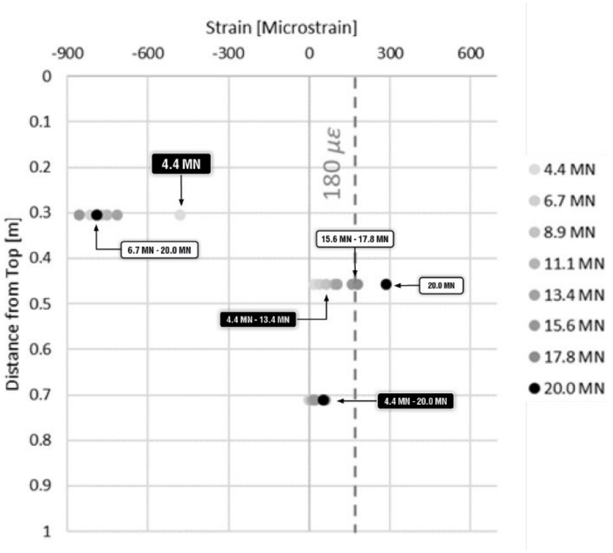

Figure B3-11: Radial strain at 76 mm from intrados face.

B3.3. Cracking Response

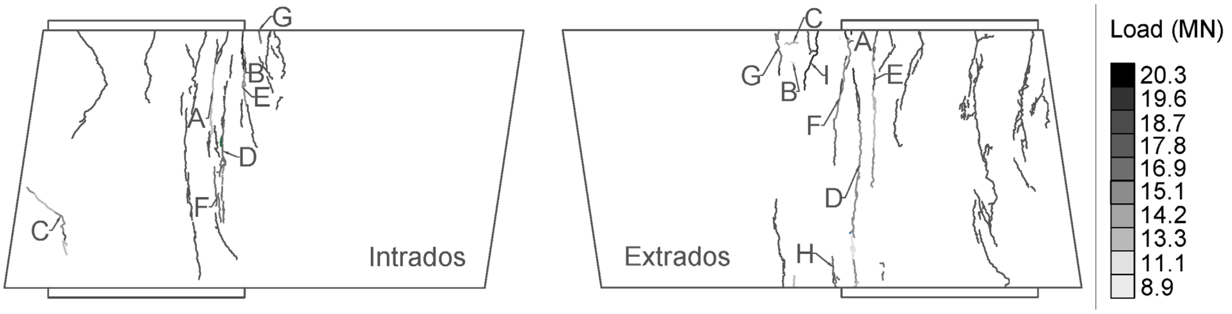

Figure B3-12: Crack propagation for test 3 on intrados face (left) and extrados face (right).

Table B3-2: Crack Width Development for Test 3

Load (MN)	Intrados Crack Width (mm)							Extrados Crack Width (mm)								
	A	B	C	D	E	F	G	A	B	C	D	E	F	G	H	I
4.4	0.00	0.00	0.00	0.00	0.00	0.00	0.00	0.00	0.00	0.00	0.00	0.00	0.00	0.00	0.00	0.00
8.9	0.00	0.00	0.00	0.00	0.00	0.00	0.00	0.10	0.05	0.10	0.00	0.00	0.00	0.00	0.00	0.00
11.1	0.05	0.00	0.00	0.00	0.00	0.00	0.00	0.10	0.08	0.15	0.23	0.00	0.00	0.00	0.00	0.00
13.3	0.10	0.05	0.10	0.00	0.00	0.00	0.00	0.10	0.10	0.18	0.23	0.15	0.00	0.00	0.00	0.00
15.1	0.15	0.05	0.15	0.10	0.10	0.00	0.10	0.10	0.10	0.18	0.23	0.18	0.18	0.00	0.00	0.00
16.9	0.23	0.08	0.15	0.15	0.10	0.10	0.10	0.10	0.10	0.18	0.25	0.18	0.18	0.10	0.15	0.00
17.8	0.23	0.10	0.15	0.15	0.10	0.10	0.10	0.10	0.10	0.18	0.64	0.25	0.18	0.10	0.15	0.00
18.7	0.23	0.10	0.15	0.15	0.18	0.10	0.10	0.10	0.10	0.18	0.76	0.30	0.51	0.10	0.18	0.00
19.6	0.25	0.15	0.15	0.15	0.18	0.10	0.10	0.18	0.15	0.23	0.81	0.30	0.51	0.15	0.23	0.18

Notes:

1. The first cracks to appear on this segment are the cracks labeled B and C on the extrados face of the segment. These cracks appeared horizontally at 8.9 MN but did not continue to increase in length or width much as loading continued.

2. Significant cracking began to propagate at 13.3 MN for both the intrados and extrados face.
3. Cracks grew significantly on the extrados face at 15.1 MN and 16.9 MN for the intrados face.
4. Inspection of the segment after a violent failure at 19.2 MN showed that the load pad moved below the top surface of the segment by approximately 64 mm.
5. Many more cracks appeared during the failure event as well and they were wider than any of the cracks measured under loading, but the widest crack to form during testing was crack D directly under the edge of the loading pad 0.813 mm.
6. Total failure of the segment occurred in Test 3 as evident by many of the cracks being labeled as failure.
7. More cracking occurred on this segment than any other test that was conducted.

B4. Test 4

This test examined the performance of a hybrid tunnel liner segment under concentric double point load. The loading rate was kept at approximately 296.6 kN/min. The detailed description of this test is presented in Table B4-1. Pictures of the segment before and after testing are shown in Figure B4-1. The geometry and dimensions of the tested segment is presented in Figure B4-2.

Table B4-1: Description of Test 4.

Test No.	4
Previously Tested?	No
Segment Serial Number	SG 2006 8946
Segment Type	Hybrid
Segment Mold	GH-1
Age at Test Date	214 Days
Maximum Applied Load	22241 kN (5000 kips)
Description	Double Point Load Concentric

Figure B4-1: Intrados image of segment before (left) and after (right) testing.

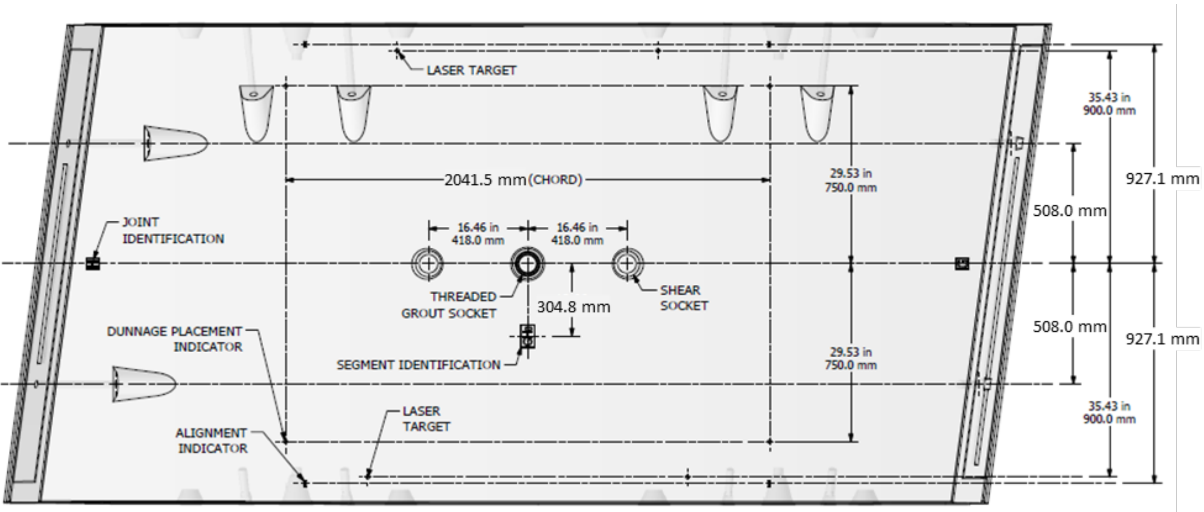

SEGMENT "GH" NORMAL TO CENTER VIEW OF INTRADOS

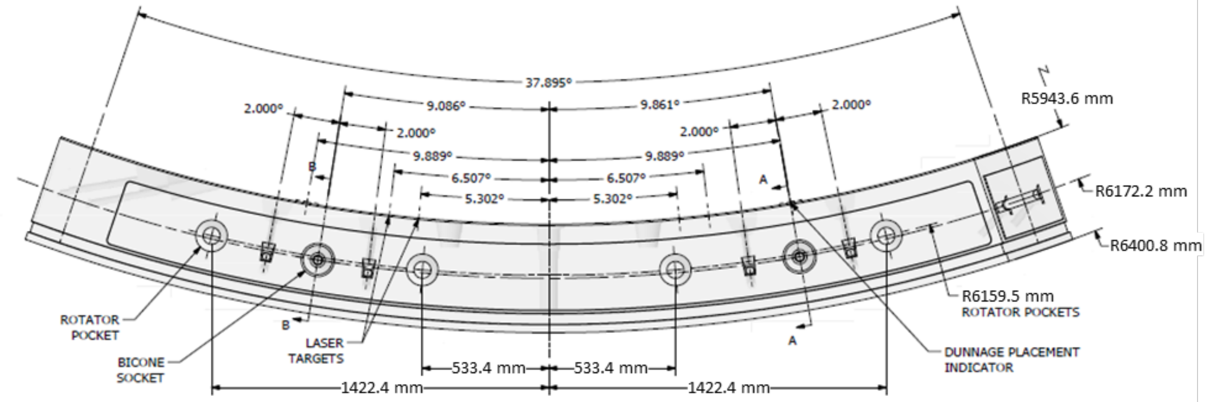

SIDE VIEW OF TRAILING EDGE

Figure B4-2: Geometry and dimensions of GH tunnel liner segment.

A double load pad configuration was used. This configuration is used at the top and bottom of the segment and is illustrated in Figure B4-3. The bearing pad layout is the same for both top and bottom locations.

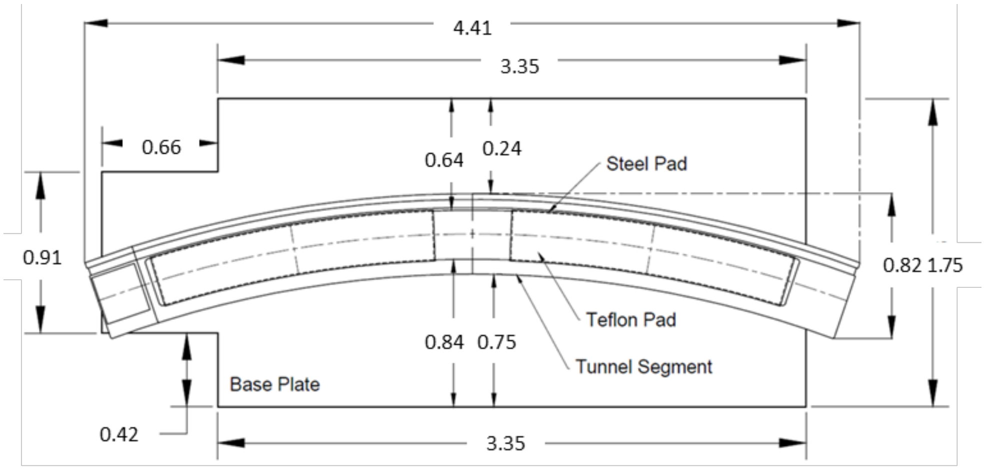

Figure B4-3: Plan view of load pad location at top and bottom of segment (dimensions in m).

Notes:

1. S1-S14 and S20 are surface bonded strain gages.
2. S15-S19 are radial strain gages, which are bonded to an epoxy stick before being inserted into the pre-drilled hole, and are located at the mid-thickness of the segment.
3. R1-R10 are internal steel gages installed on the reinforcement steel.

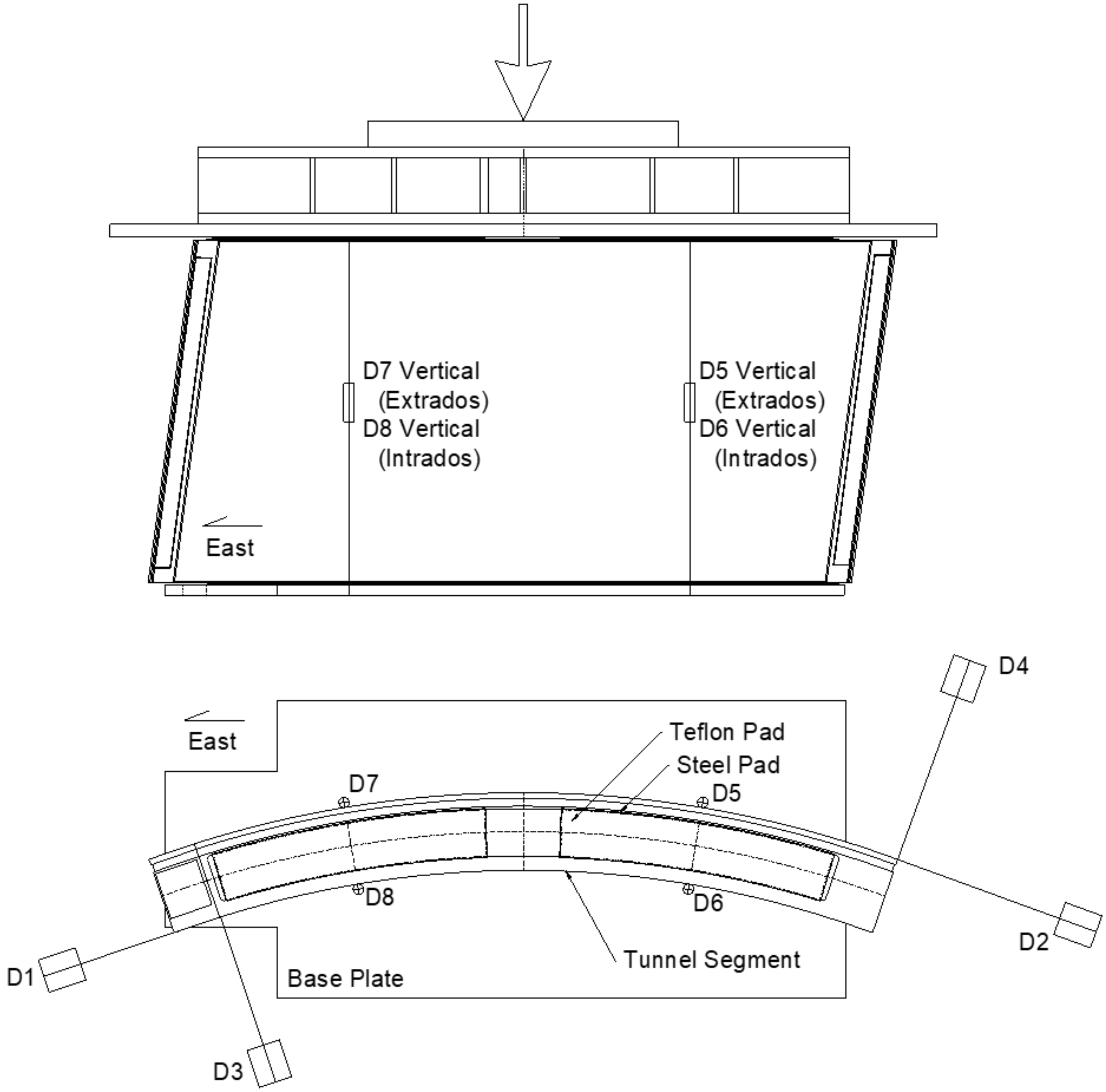

Figure B4-4: Displacement transducer layout.

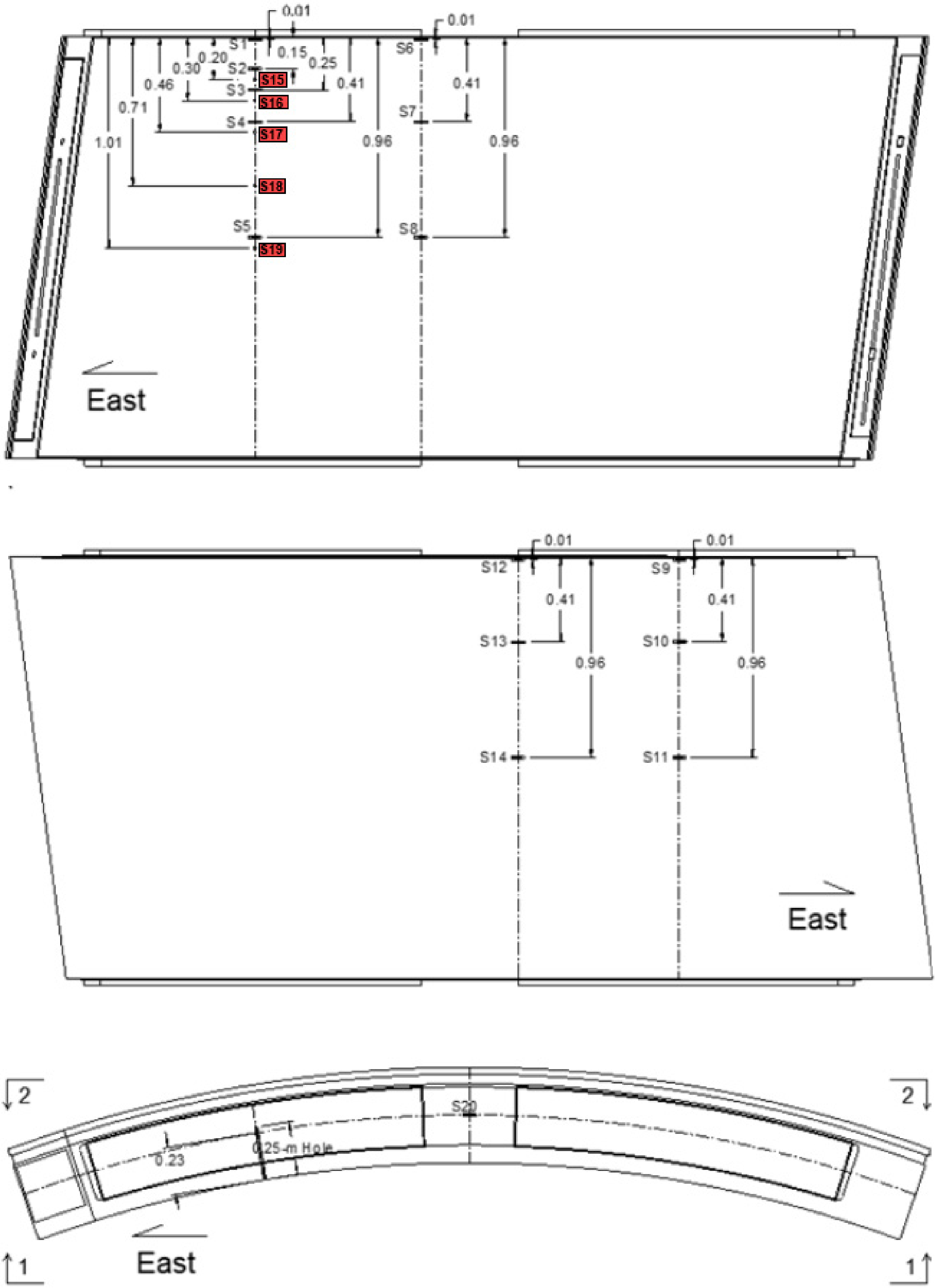

Figure B4-5: Strain gage layout.

Strain Gauges on the First Layer of Reinforcement

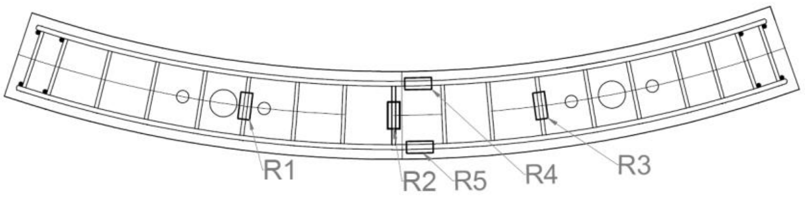

Strain Gauges on the Second Layer of Reinforcement

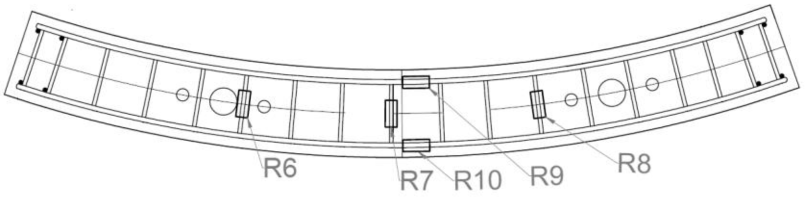

Figure B4-6: Internal strain gage layout.

B4.1. Load-Deformation

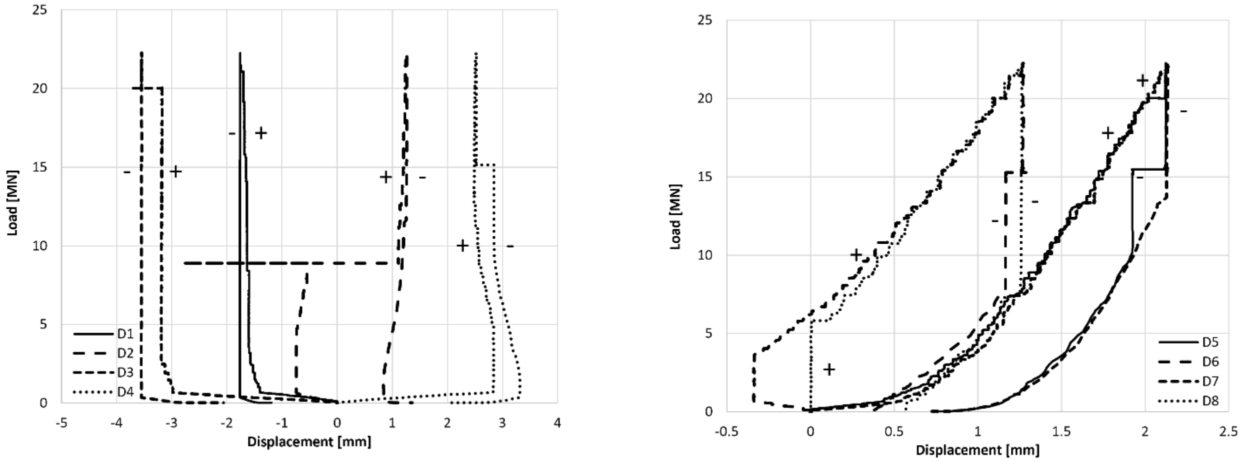

(a) (b)

Figure B4-7: Load versus (a) horizontal, and (b) vertical deformations of segment.

Notes: (1) Segment loading was paused a few key load levels to mark and measure crack propagation; (2) the maximum applied load was 22.2 MN; and (3) significant cracking damage was observed at the end of testing as shown in Figure B4-8. Cracks started to develop at approximately 13.3 MN and increased in width and quantity with increasing load. The crack formation and size are summarized in Table B4-2 and illustrated in Figure B4-13.

Figure B4-8: Damage of segment after test 4 completion.

B4.2. Strain Response

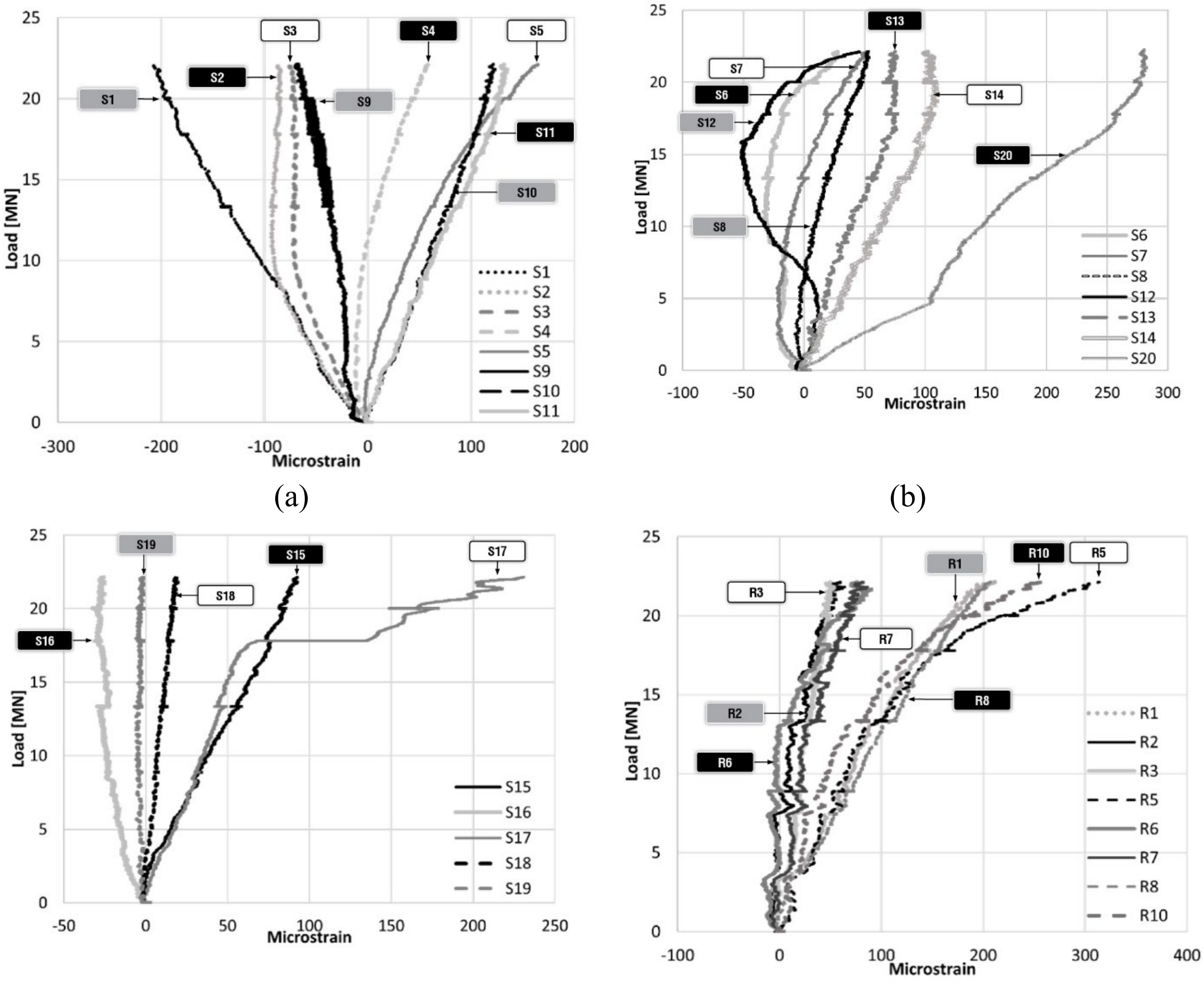

(a)

(b)

(c)

(d)

Figure B4-9: Strain gage data.

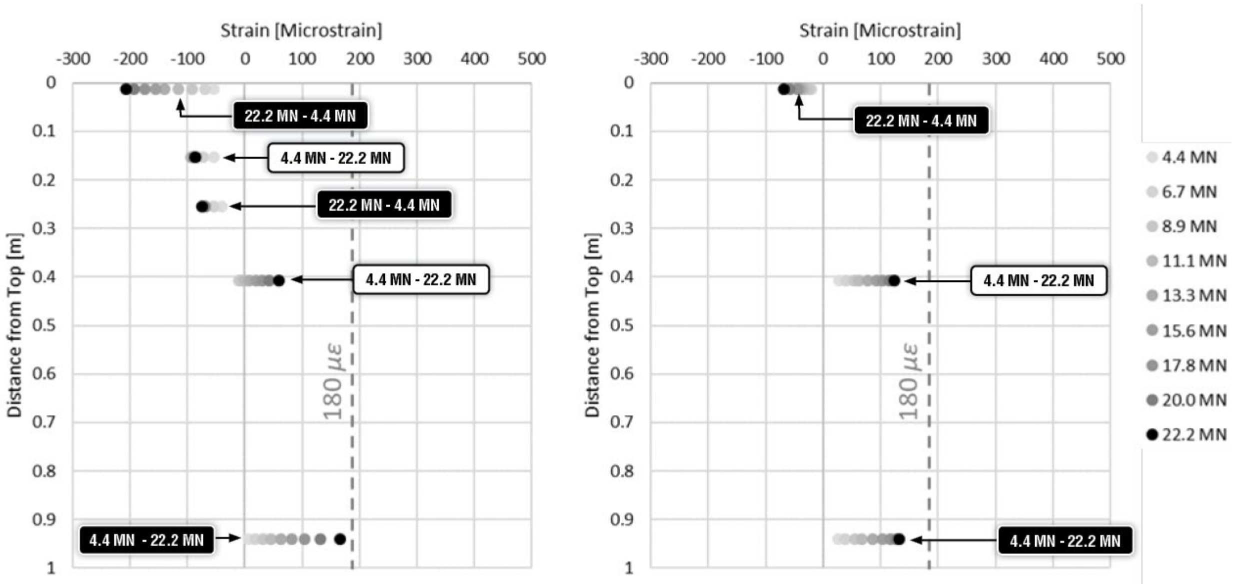

(a) (b)

Figure B4-10: Transverse strain for double-point-load tests at (a) load pad center intrados, and (b) load pad center extrados.

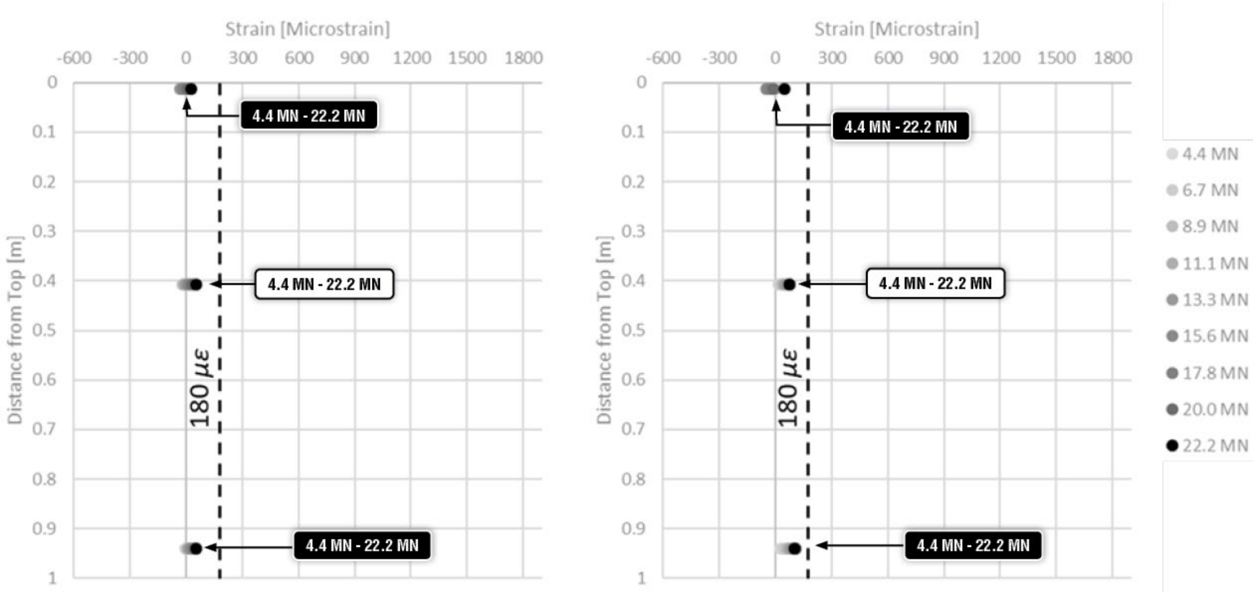

(a) (b)

Figure B4-11: Transverse strain for double-point-load tests at (a) load pad edge near midspan intrados, and (b) load pad edge near midspan extrados.

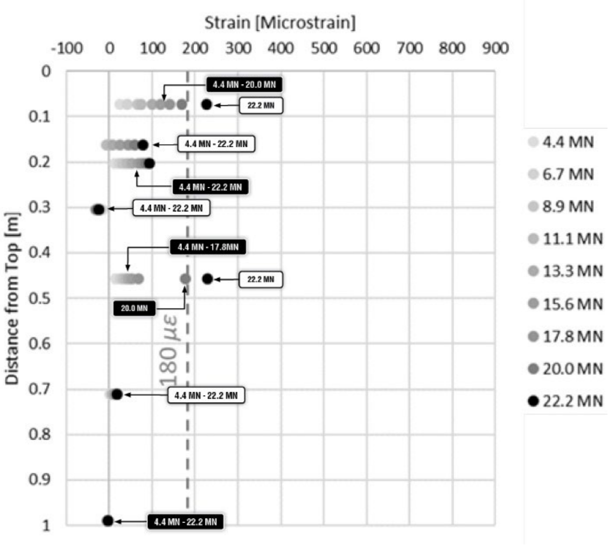

Figure B4-12: Radial strain at mid-thickness.

B4.3. Cracking Response

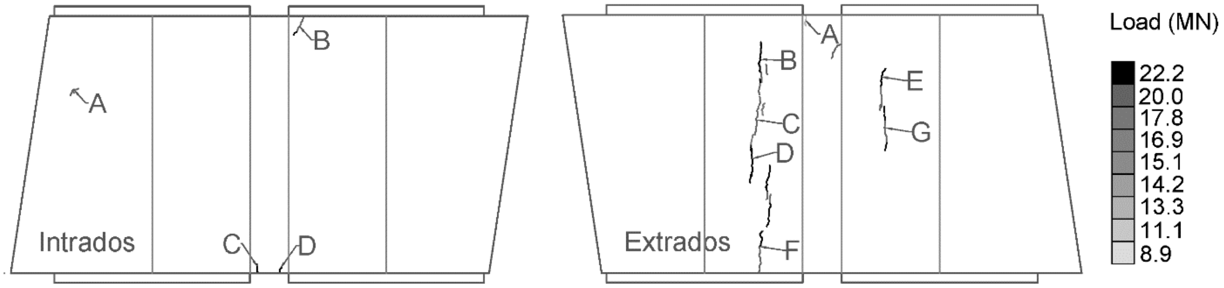

Figure B4-13: Crack propagation for test 4 on intrados face (left) and extrados face (right).

Table B4-2: Crack Width Development for Test 4

Load (MN_	Intrados Crack Width				Extrados Crack Width(mm)						
	A	B	C	D	A	B	C	D	E	F	G
4.4	0.00	0.00	0.00	0.00	0.00	0.00	0.00	0.00	0.00	0.00	0.00
8.9	0.00	0.00	0.00	0.00	0.00	0.00	0.00	0.00	0.00	0.00	0.00
13.3	0.00	0.00	0.00	0.00	0.05	0.00	0.00	0.00	0.00	0.00	0.00
17.8	0.00	0.00	0.00	0.00	0.05	0.05	0.08	0.08	0.00	0.00	0.00
20.0	0.05	0.00	0.00	0.00	0.10	0.10	0.10	0.10	0.05	0.18	0.10
22.2	0.05	0.10	0.10	0.10	0.15	0.10	0.10.	0.10	0.05	0.23	0.10

Notes:

1. The first crack to develop on this segment was crack A at 13.3 MN on the extrados face. However, this segment contained precast strain gages on the rebar cage inside the hybrid segment, and Crack A developed from the whole that was created by the wire leads coming out of the segment from the gages.

2. The next crack to develop was Crack C, at 17.8 MN. However, at 17.8 MN regions of bulging and micro cracking appeared around Cracks C and G, but with was before Crack G developed. These regions of micro cracking spread very slightly between 17.8 kN and 20.0 MN but cracks in these regions did not get wider and were too small to measure with a crack comparator card. The widest crack to develop was Crack F under the edge of the western load pad.

B5. Test 5

This test examined the performance of a hybrid tunnel liner segment under single point load with an eccentricity of 38 mm toward the extrados face. The loading rate was kept at approximately 296.6 kN/min. The detailed description of this test is presented in Table B5-1. Pictures of the segment before and after testing are shown in Figure B5-1. The geometry and dimensions of the tested segment is presented in Figure B5-2.

Table B5-1: Description of Test 5.

Test No.	5
Previously Tested?	Yes
Segment Serial Number	SG 2006 8946
Segment Type	Hybrid
Segment Mold	GH-1
Age at Test Date	216 Days
Maximum Applied Load	22241 kN (5000 kips)
Description	Single Point Load Eccentric toward Extrados at 38 mm

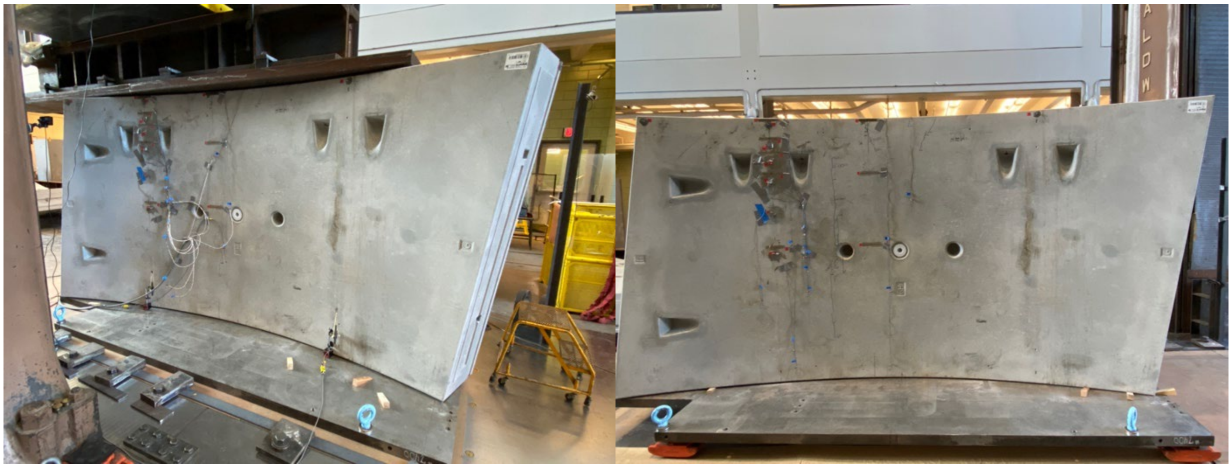

Figure B5-1: Intrados image of segment before (left) and after (right) testing.

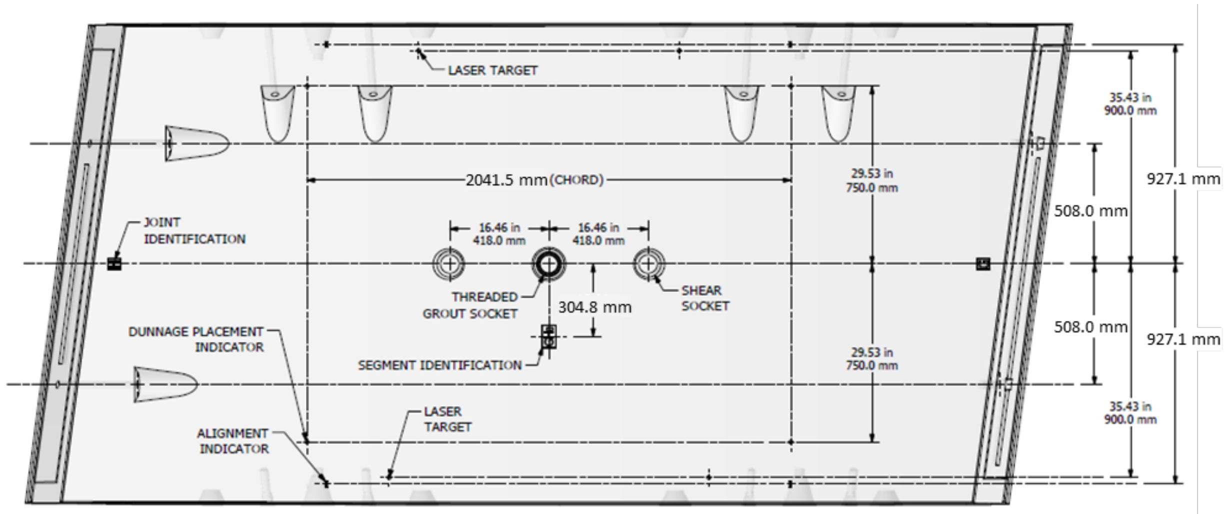

SEGMENT "GH" NORMAL TO CENTER VIEW OF INTRADOS

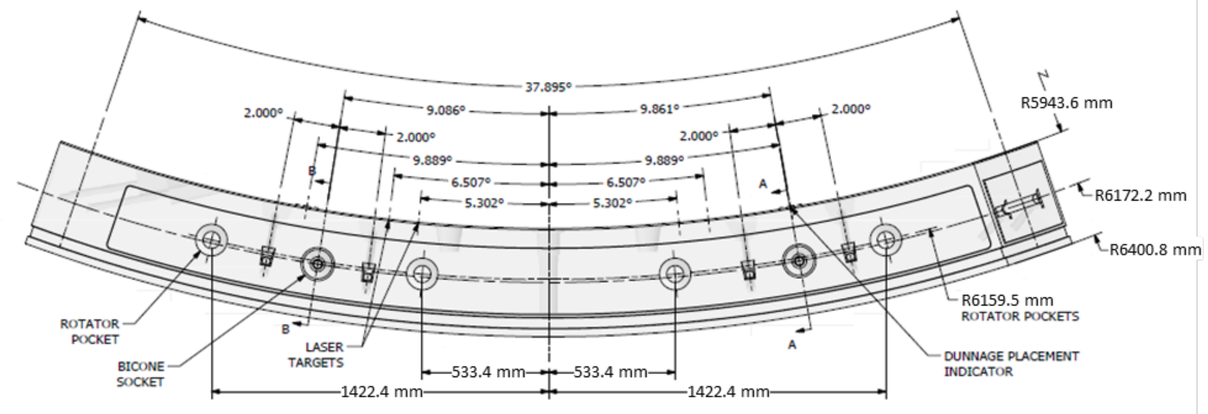

SIDE VIEW OF TRAILING EDGE

Figure B5-2: Geometry and dimensions of GH tunnel liner segment.

A single load pad configuration was used. This configuration is used at the top and bottom of the segment and is illustrated in Figure B5-3. The bearing pad layout is the same for both top and bottom locations.

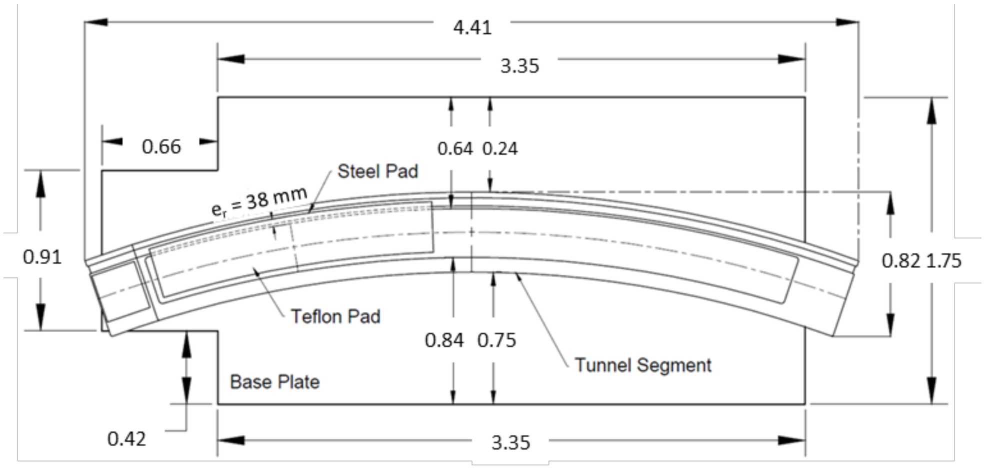

Figure B5-3: Plan view of load pad location at top and bottom of segment (dimensions in m).

Notes:

1. S1-S14 and S20 are surface bonded strain gages.
2. S15-S19 are radial strain gages, which are bonded to an epoxy stick before being inserted into the pre-drilled hole, and are located at the mid-thickness of the segment.
3. R1-R10 are internal steel gages installed on the reinforcement steel.

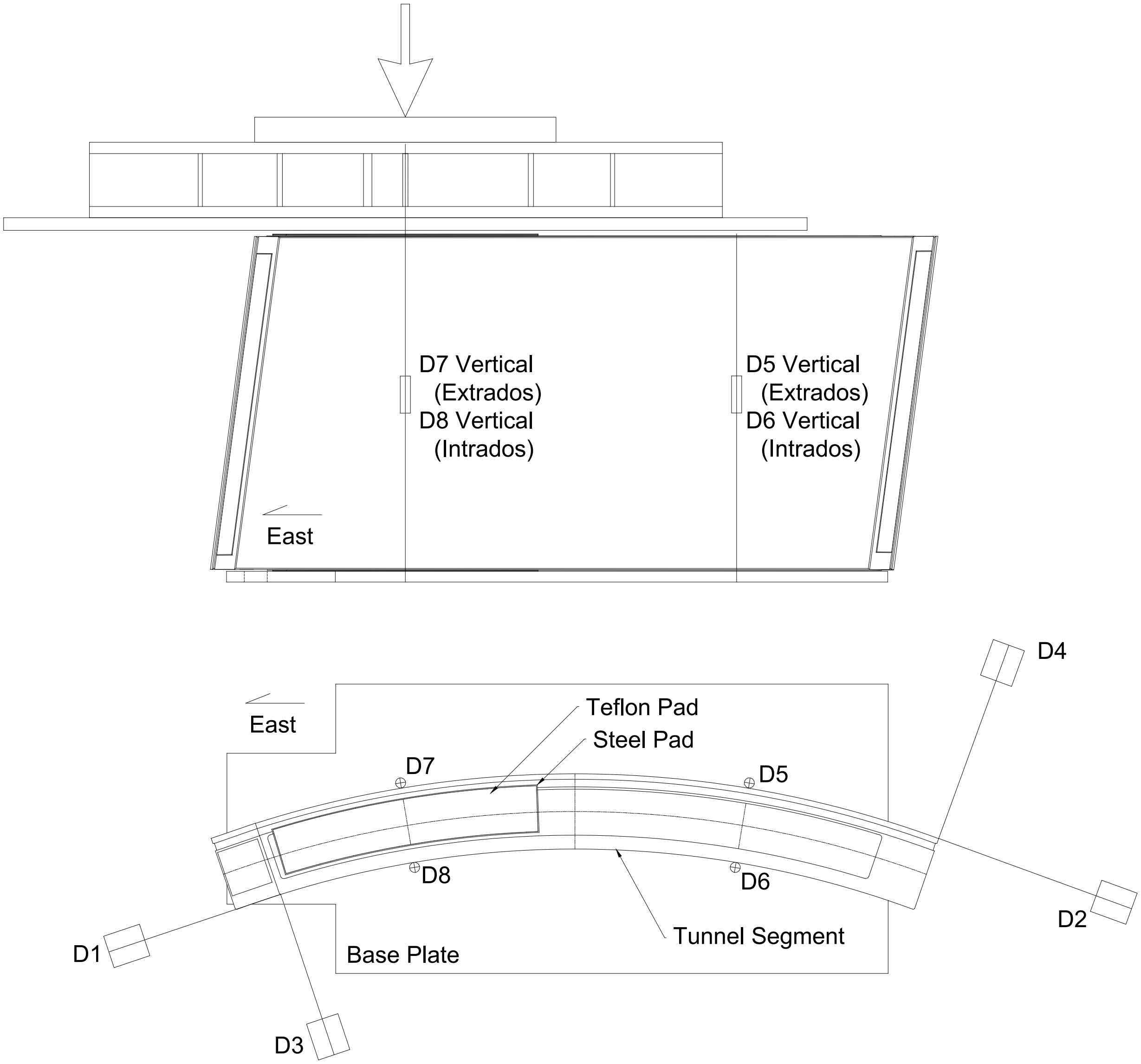

Figure B5-4: Displacement transducer layout.

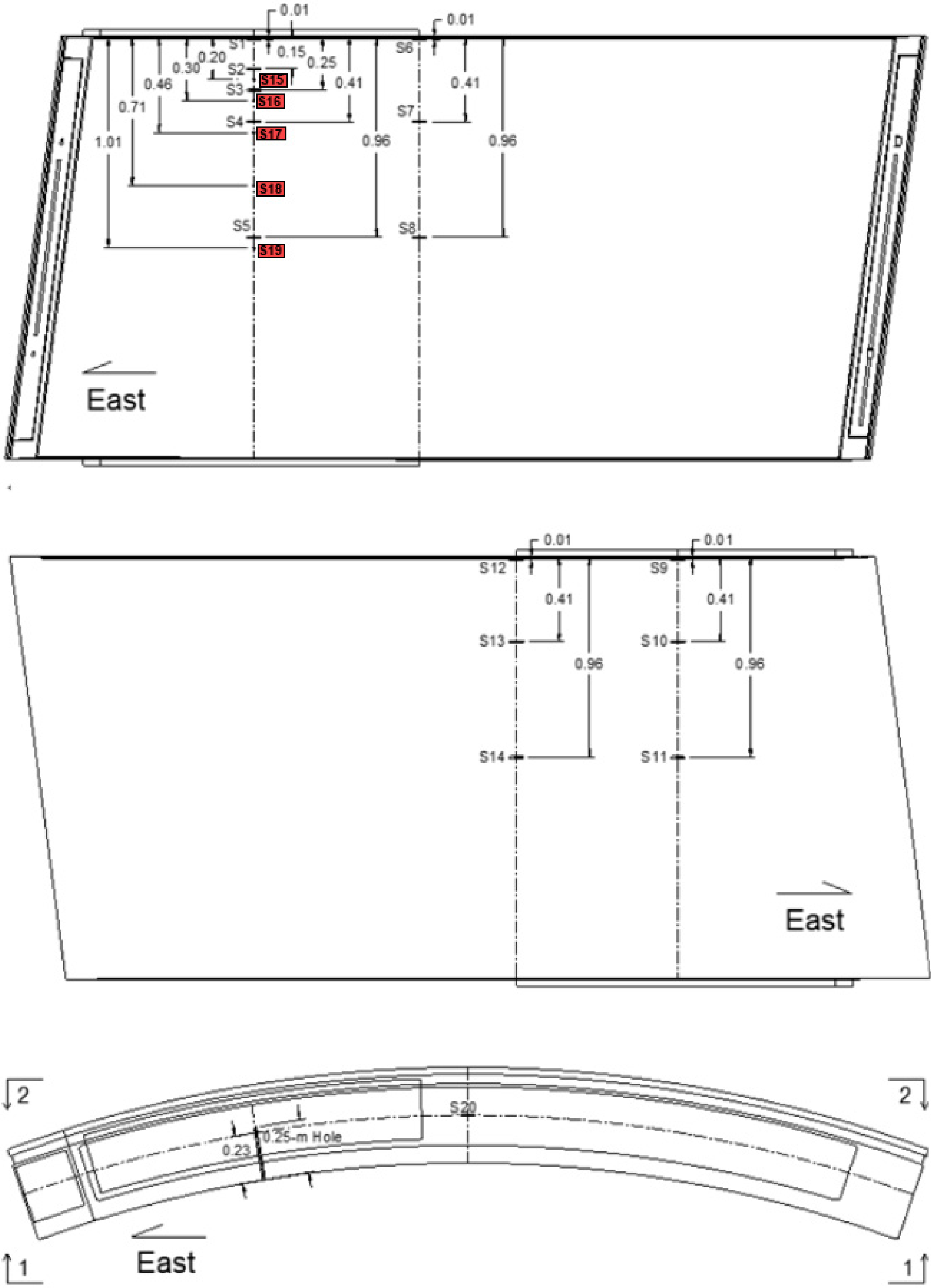

Figure B5-5: Strain gage layout.

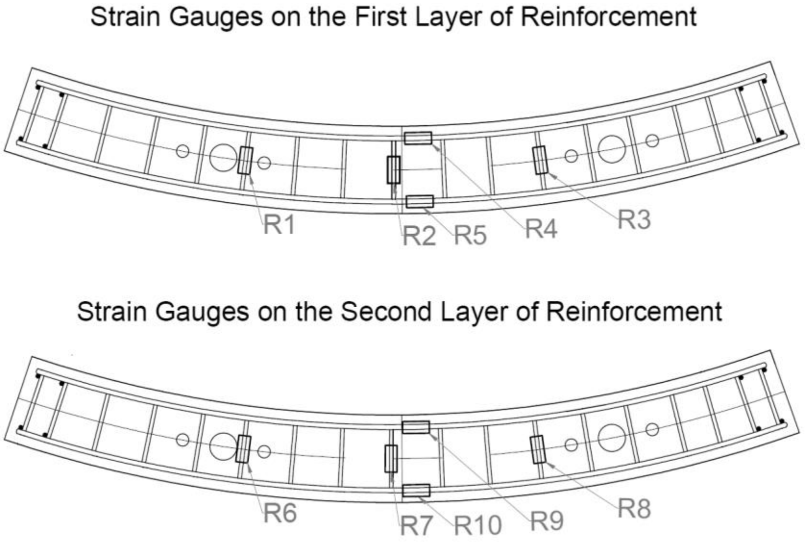
Strain Gauges on the First Layer of Reinforcement

Strain Gauges on the Second Layer of Reinforcement

Figure B5-6: Internal strain gage layout.

B5.1. Load-Deformation

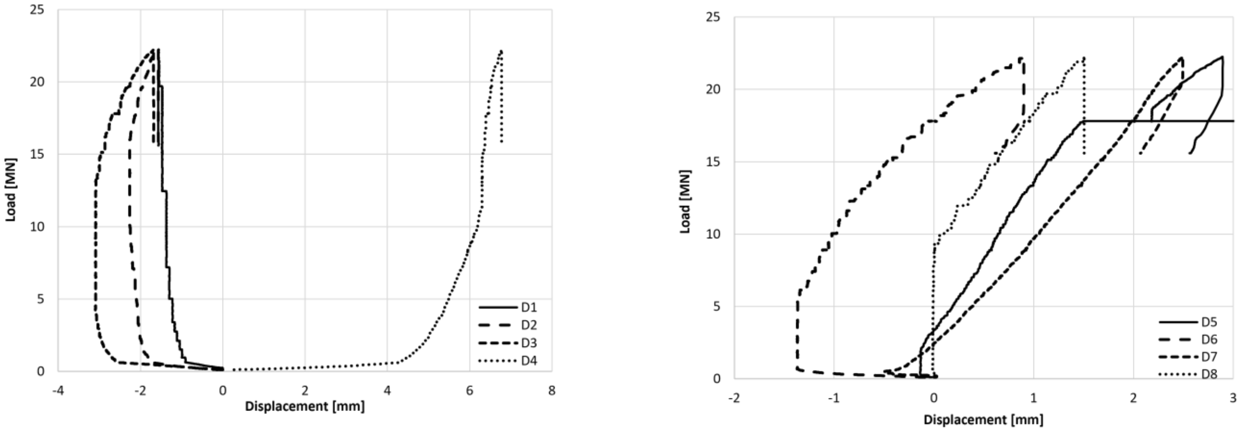

(a) (b)

Figure B5-7: Load versus (a) horizontal, and (b) vertical deformations of segment

Notes: (1) Segment loading was paused a few key load levels to mark and measure crack propagation; (2) The maximum applied load was 22.2 MN; (3) Significant cracking damage was observed at the end of testing as shown in Figure B5-8. Cracks started to develop at approximately 13.3 MN and increased in width and quantity with increasing load. The crack formation and size are summarized in Table B5-2 and illustrated in Figure B5-13.

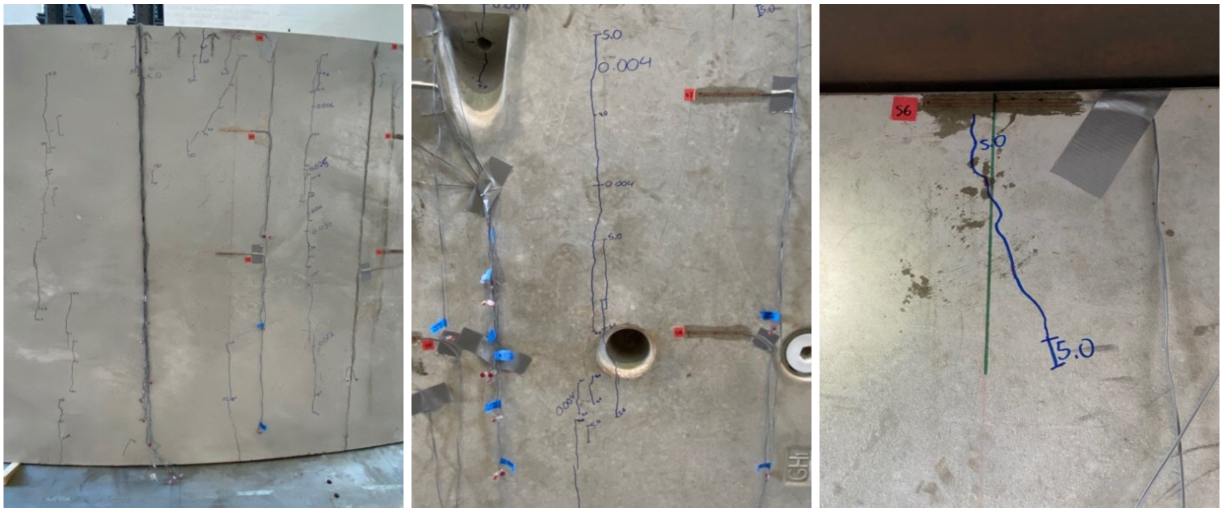

Figure B5-8: Damage of segment after test 5 completion.

B5.2. Strain Response

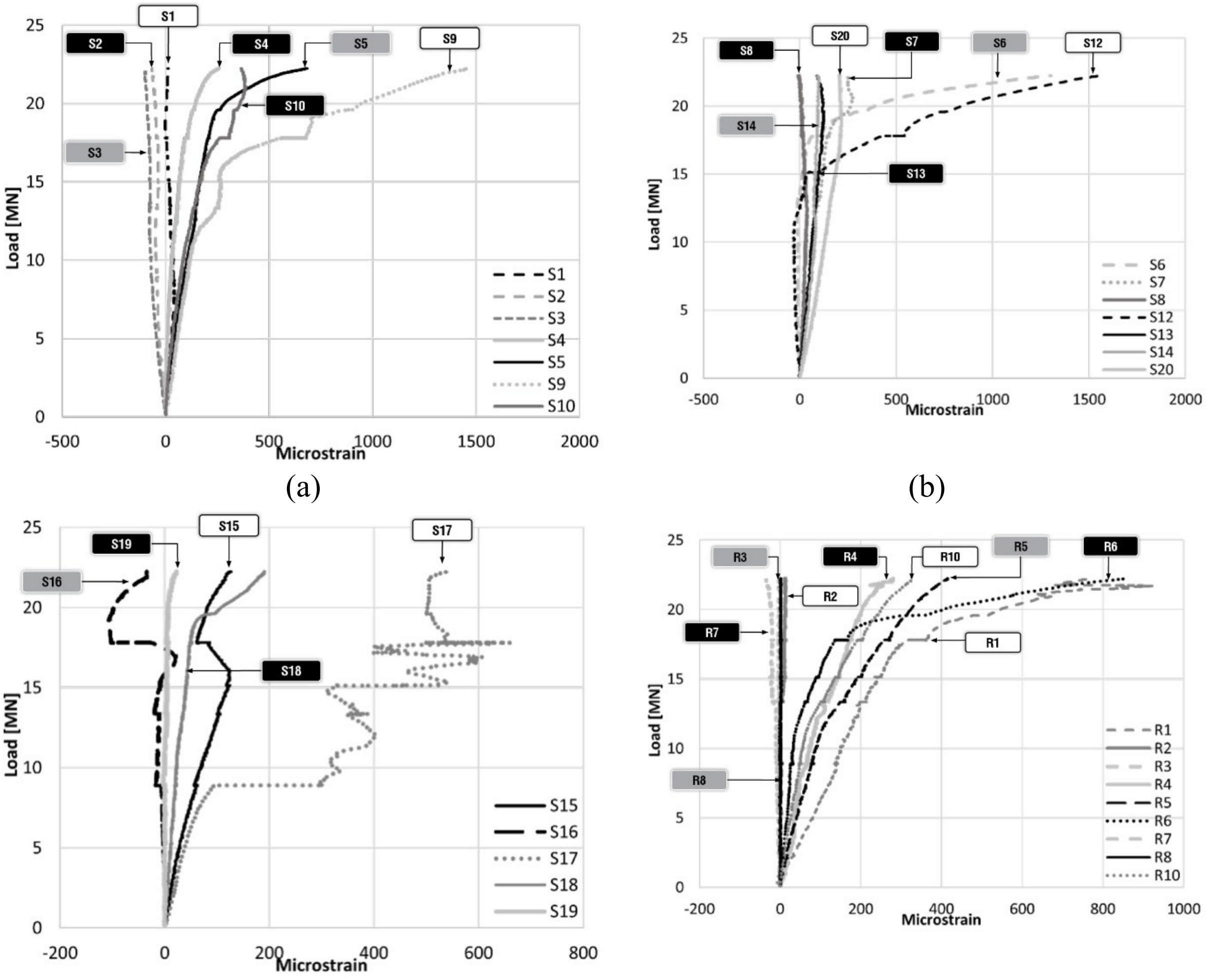

(a)

(b)

(c)

(d)

Figure B5-9: Strain gage data.

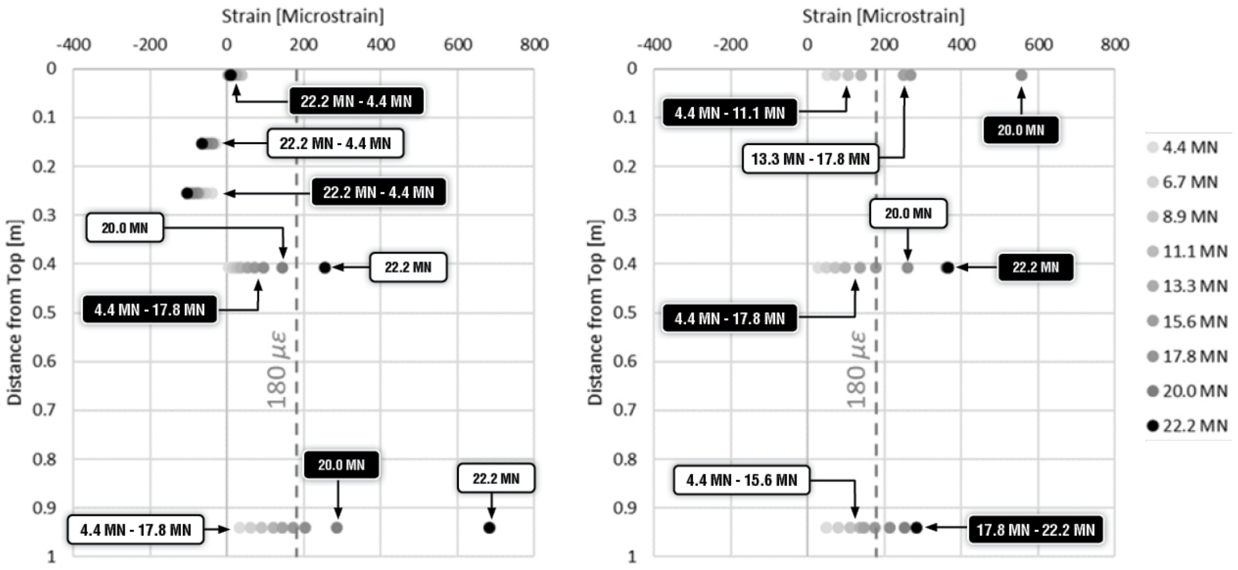

(a) (b)

Figure B5-10: Transverse strain for single-point-load tests at (a) load pad center intrados, and (b) load pad center extrados.

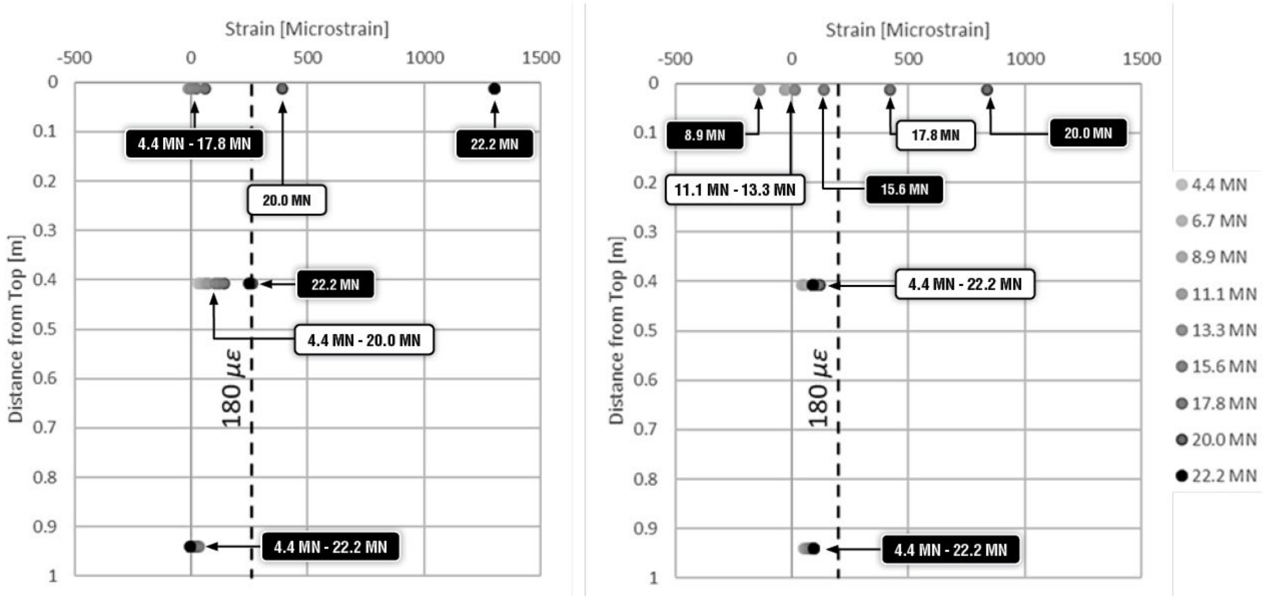

(a) (b)

Figure B5-11: Transverse strain for single-point-load tests at (a) load pad edge near midspan intrados, and (b) load pad edge near midspan extrados.

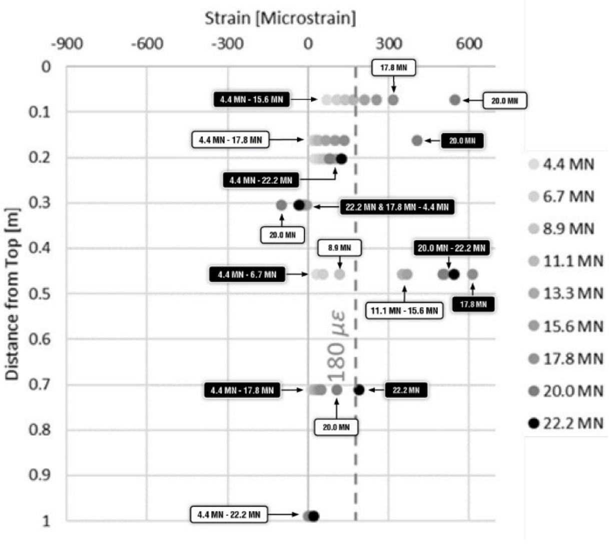

Figure B5-12: Radial strain at mid-thickness.

B5.3. Cracking Response

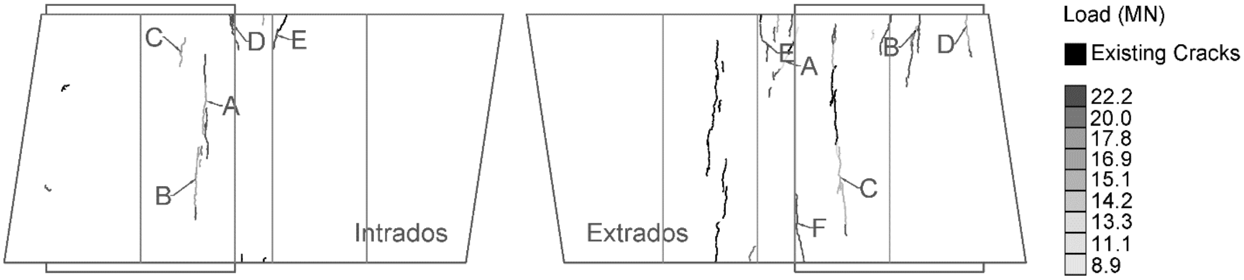

Figure B5-13: Crack propagation for test 5 on intrados face (left) and extrados face (right).

Table B5-2: Crack Width Development for Test 5.

Load	Intrados Crack Width (mm)							Extrados Crack Width (mm)								
(MN)	A	B	C	D	E	F	G	A	B	C	D	E	F	G	H	I
4.4	0.00	0.00	0.00	0.00	0.00	0.00	0.00	0.00	0.00	0.00	0.00	0.00	0.00	0.00	0.00	0.00
8.9	0.00	0.00	0.00	0.00	0.00	0.00	0.00	0.10	0.05	0.10	0.00	0.00	0.00	0.00	0.00	0.00
11.1	0.05	0.00	0.00	0.00	0.00	0.00	0.00	0.10	0.08	0.15	0.23	0.00	0.00	0.00	0.00	0.00
13.3	0.10	0.05	0.10	0.00	0.00	0.00	0.00	0.10	0.10	0.18	0.23	0.15	0.00	0.00	0.00	0.00
15.1	0.15	0.05	0.15	0.10	0.10	0.00	0.10	0.10	0.10	0.18	0.23	0.18	0.18	0.00	0.00	0.00
16.9	0.23	0.08	0.15	0.15	0.10	0.10	0.10	0.10	0.10	0.18	0.25	0.18	0.18	0.10	0.15	0.00
17.8	0.23	0.10	0.15	0.15	0.10	0.10	0.10	0.10	0.10	0.18	0.64	0.25	0.18	0.10	0.15	0.00
18.7	0.23	0.10	0.15	0.15	0.18	0.10	0.10	0.10	0.10	0.18	0.76	0.30	0.51	0.10	0.18	0.00
19.6	0.25	0.15	0.15	0.15	0.18	0.10	0.10	0.18	0.15	0.23	0.81	0.30	0.51	0.15	0.23	0.18

Notes:

1. Test 5 was the only eccentric test conducted, and it exhibited a single point load of a hybrid segment.
2. There was significant extrados cracking that occurred, which was expected because the load pads were shifted toward the extrados face for eccentric loading. Since this was the

second time this segment was tested, cracks E and G from the extrados face of Test 4 were the first to start increasing in length and width at 13.3 MN in Test 5. This is the crack labeled C on the extrados face of Test 5.

3. Crack A on the extrados face of test 5 also started to increase in length, but this crack originated from Test 4.
4. The first entirely new crack to develop in Test 5 was Crack D in the top right corner on the extrados face at 15.1 MN.
5. The widest crack that propagated was Crack C, at 0.64 mm, near the edge of the load pad used in single point testing.

B6. Test 6

This test examined the performance of an SFRC tunnel liner segment under concentric double point load. The loading rate was kept at approximately 296.6 kN/min. The detailed description of this test is presented in Table B6-1. Pictures of the segment before and after testing are shown in Figure B6-1. The geometry and dimensions of the tested segment is presented in Figure B6-2.

Table B6-1: Description of Test 6.

Test No.	6
Previously Tested?	No
Segment Serial Number	SG1903 4859
Segment Type	SFRC
Segment Mold	FG-3
Age at Test Date	673 Days
Maximum Applied Load	22241 kN (5000 kips)
Description	Double Point Load Concentric

Figure B6-1: Intrados image of segment before (left) and after (right) testing.

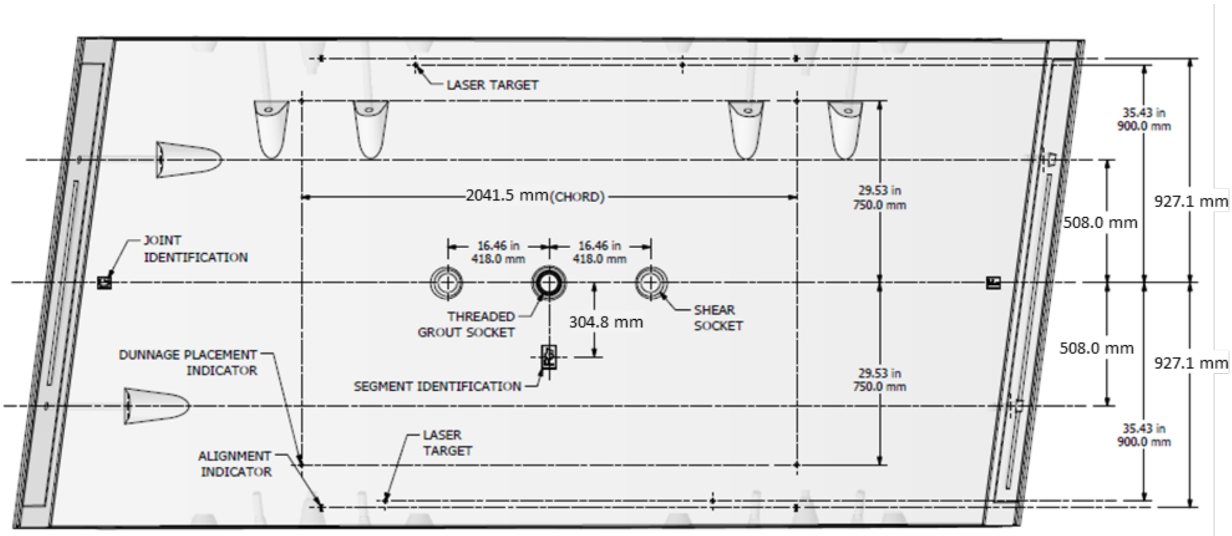

SEGMENT "FG" NORMAL TO CENTER VIEW OF INTRADOS

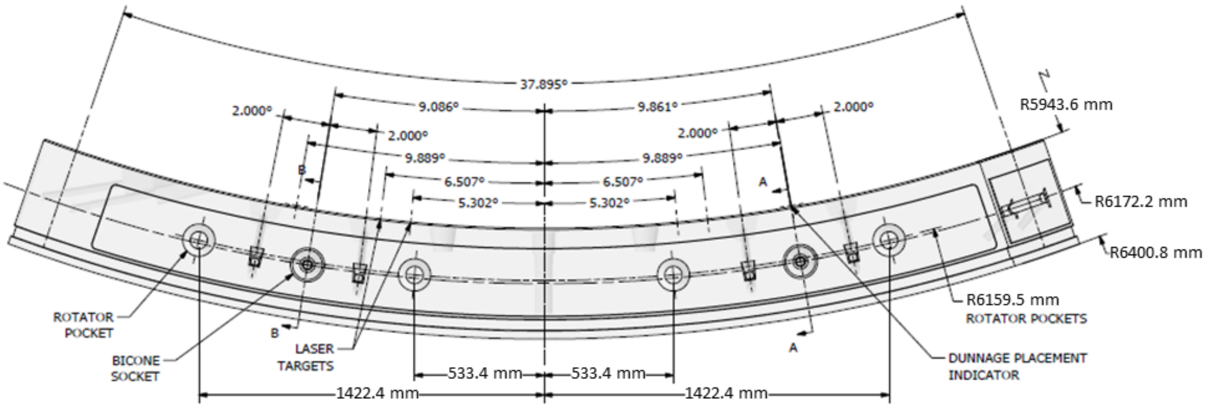

SIDE VIEW OF TRAILING EDGE

Figure B6-2: Geometry and dimensions of FG tunnel liner segment.

A double load pad configuration was used. This configuration is used at the top and bottom of the segment and is illustrated in Figure B4-3. The bearing pad layout is the same for both top and bottom locations.

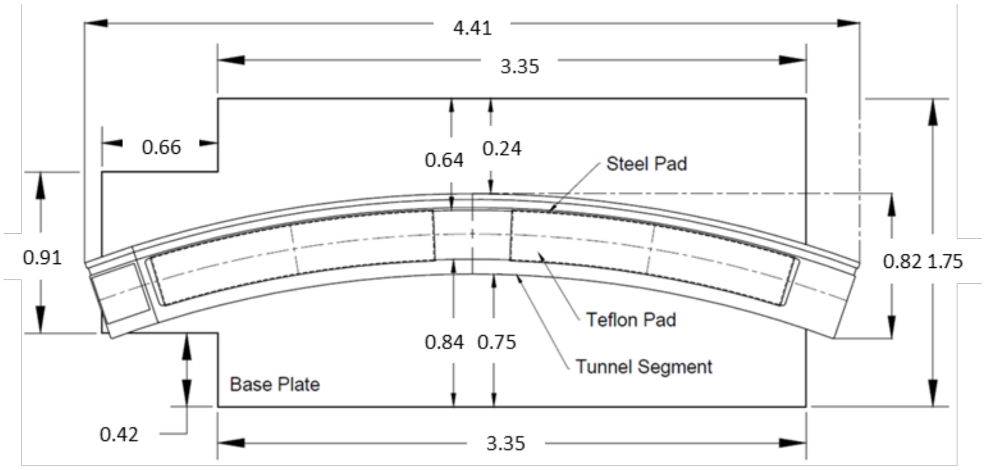

Figure B6-3: Plan view of load pad location at top and bottom of segment (dimensions in m).

Notes:

1. S1-S25 are surface bonded strain gages.
2. F1-F10 are fiber optic radial strain gages, which go through the pre-drilled through holes and are sealed with epoxy. The fiber optic gages measure the strain distribution profile along the radial direction. In Figure B6-8, only the strain data at the mid-thickness are presented. The strain distribution at various load levels are presented in Figure B6-14.

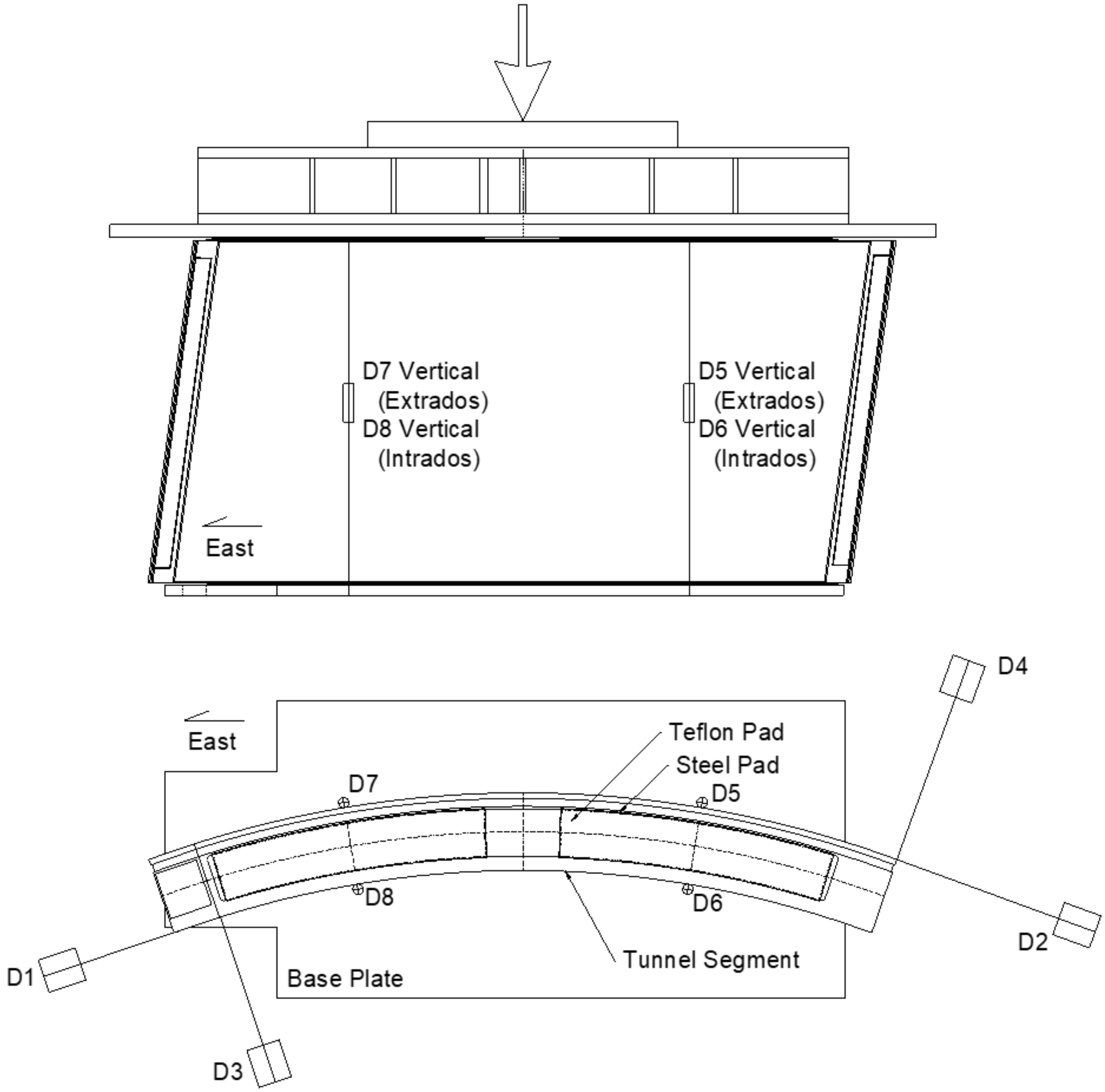

Figure B6-4: Displacement transducer layout.

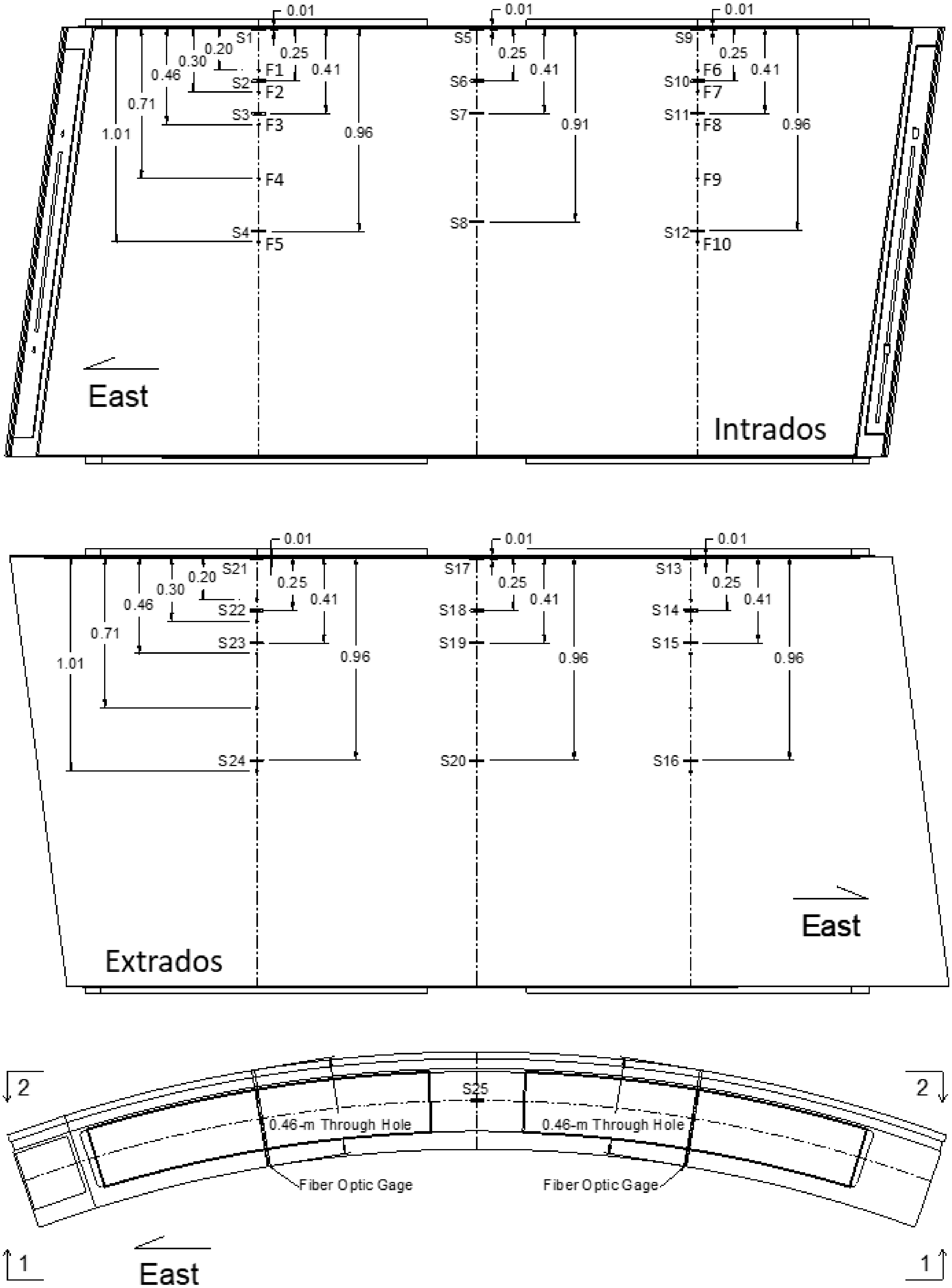

Figure B6-5: Strain gage layout.

B6.1. Load-Deformation

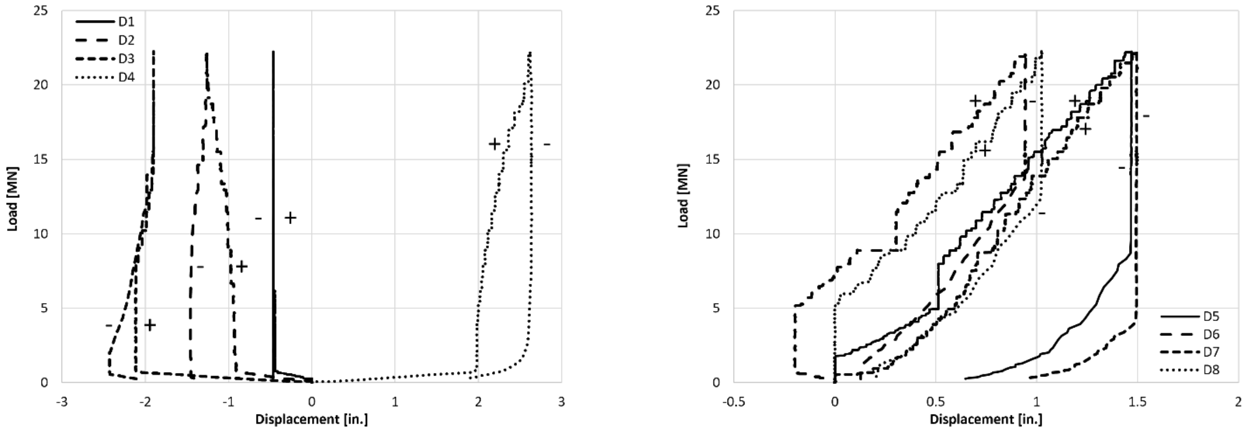

(a) (b)

Figure B6-6: Load versus (a) horizontal, and (b) vertical deformations of segment.

Notes: (1) Segment loading was paused a few key load levels to mark and measure crack propagation; (2) The maximum applied load was 22.2 MN; (3) Significant cracking damage was observed at the end of testing as shown in Figure B6-7. Cracks started to develop at approximately 19.1 MN and increased in width and quantity with increasing load. The crack formation and size are summarized in Table B6-2 and illustrated in Figure B6-15.

Figure B6-7: Damage of segment after test 6 completion.

B6.2. Strain Response

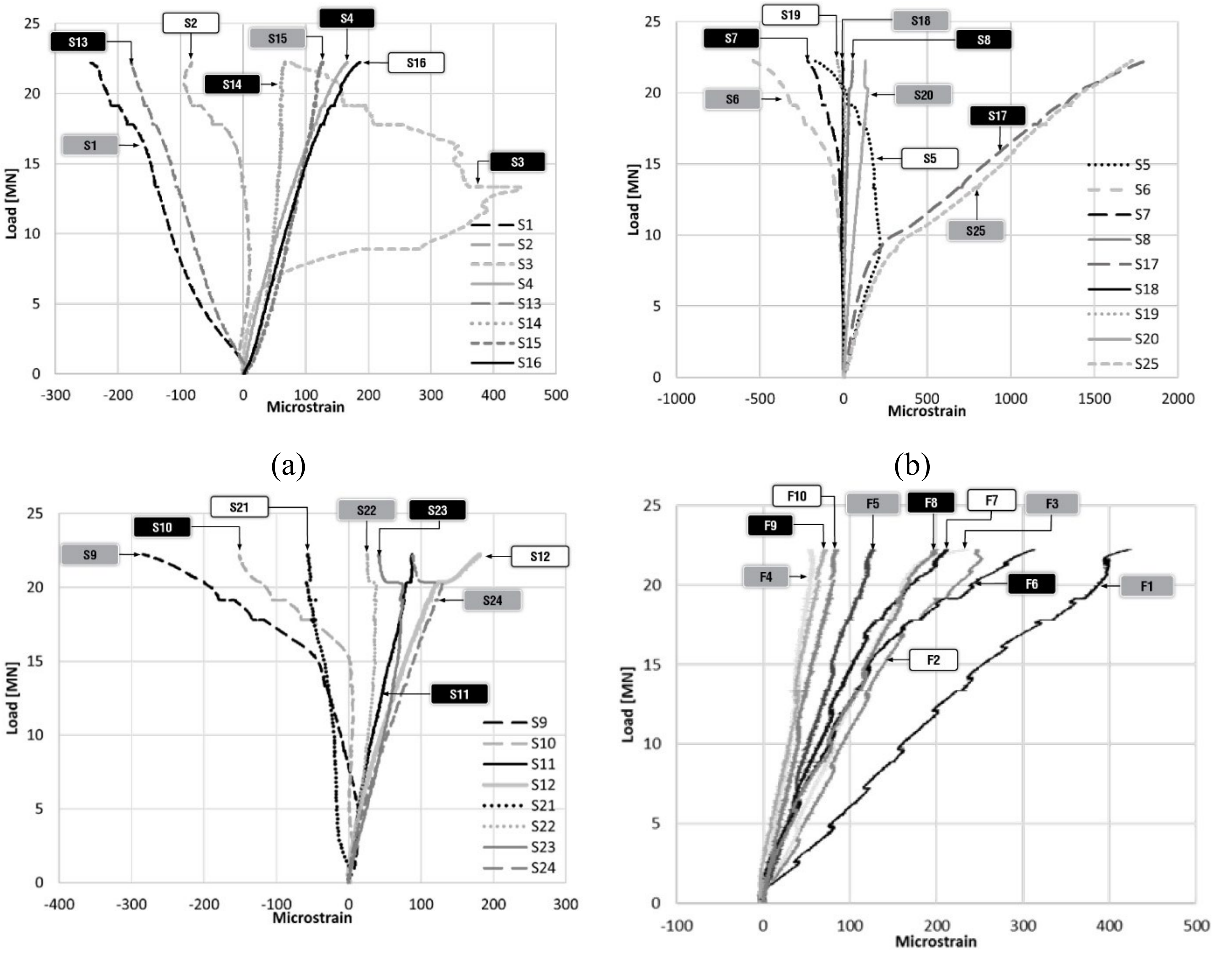

(a)

(b)

(c)

(d)

Figure B6-8: Strain gage data.

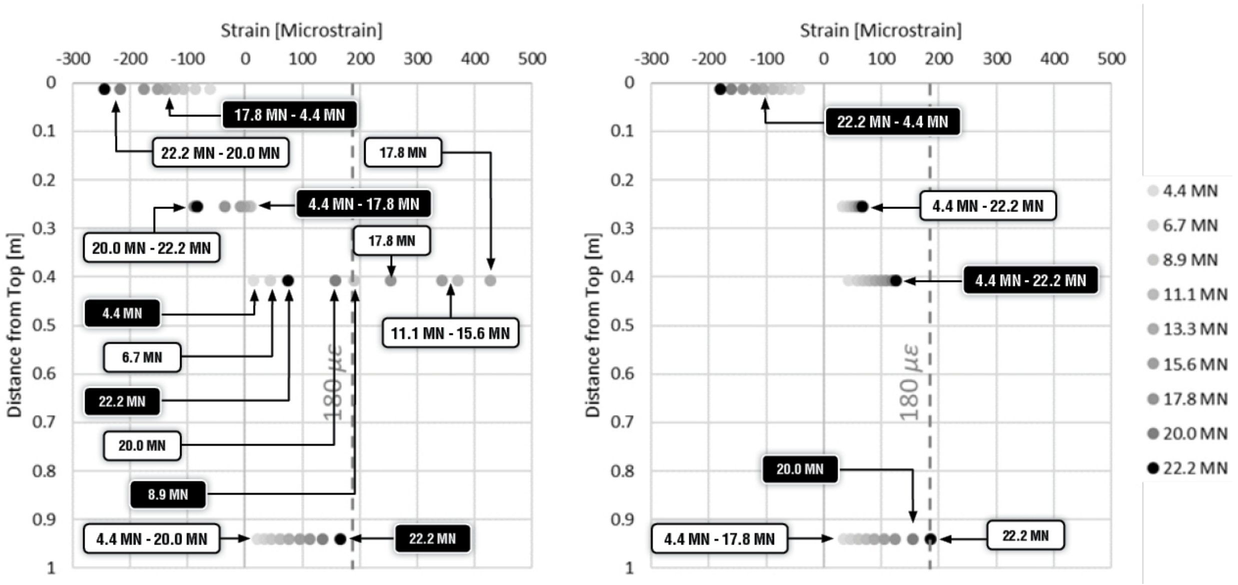

Figure B6-9: East transverse strain for double-point-load tests at (a) load pad center intrados, and (b) load pad center extrados.

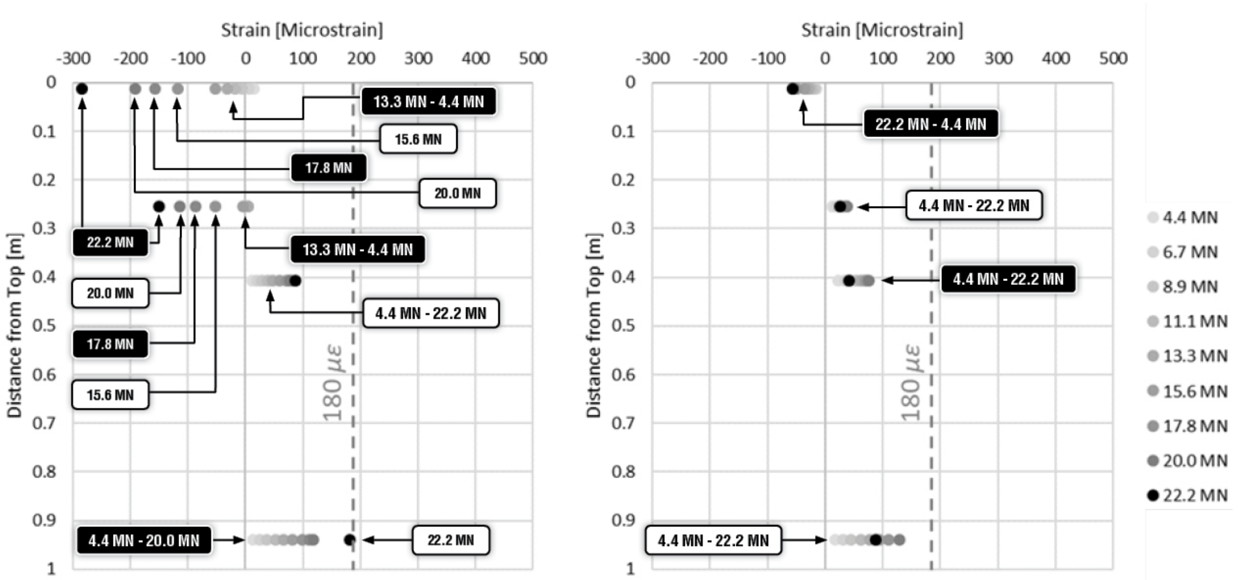

Figure B6-10: West transverse strain for double-point-load tests at (a) load pad center intrados, and (b) load pad center extrados.

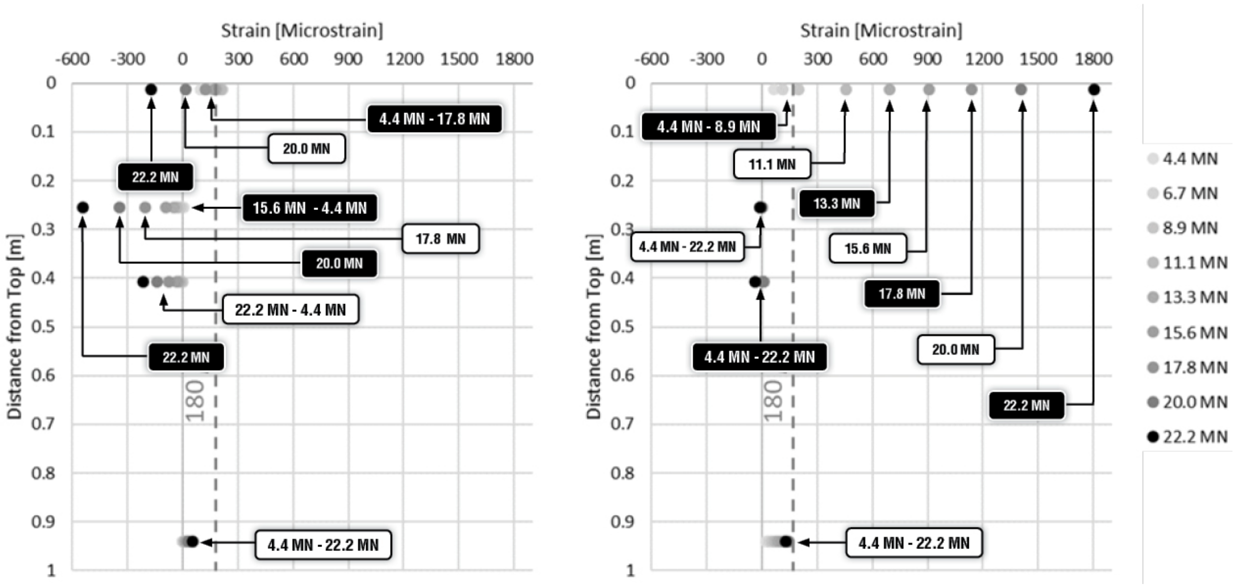

Figure B6-11: Transverse strain for double-point-load tests at (a) midspan intrados, and (b) midspan extrados.

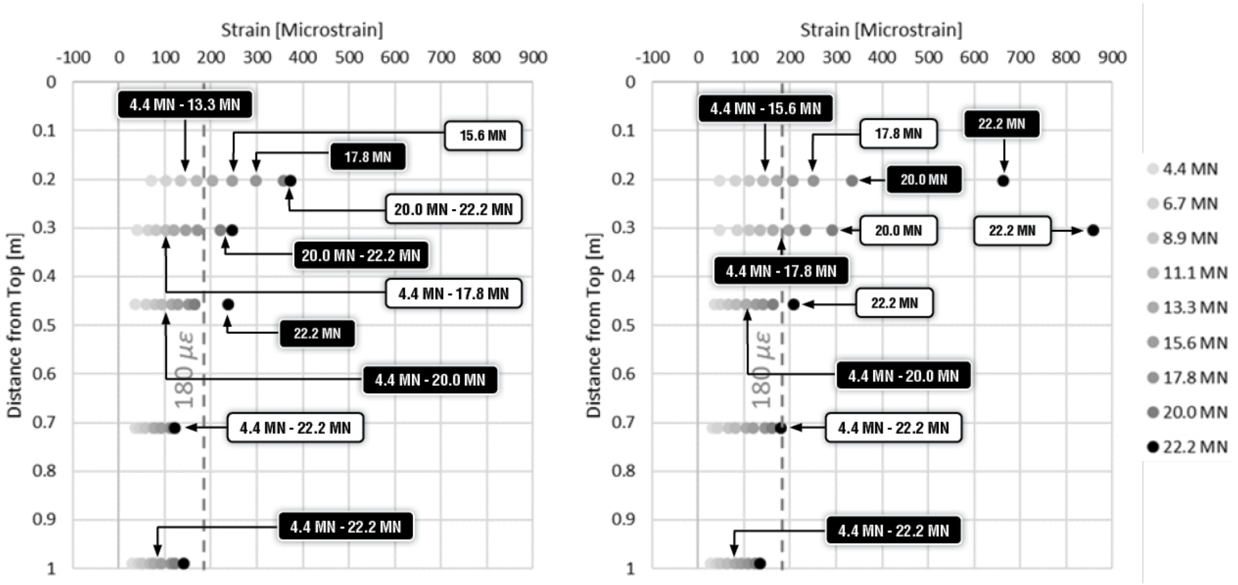

Figure B6-12: Radial strain at (a) mid-thickness and (b) 76 mm from intrados face.

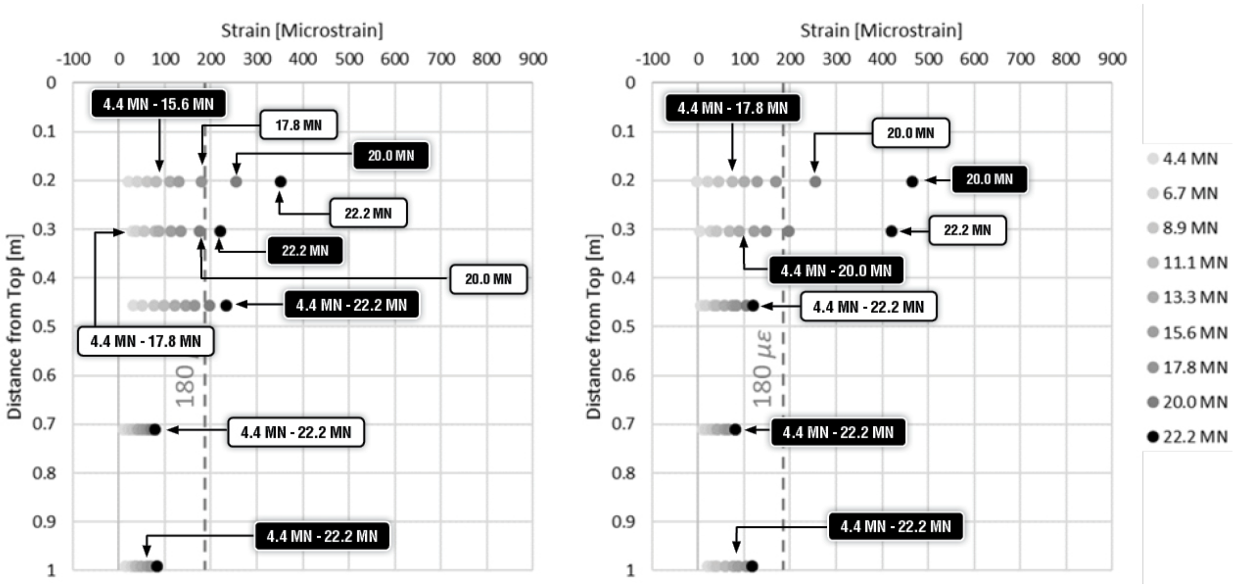

Figure B6-13: Radial strain at (a) mid-thickness and (b) 76 mm from intrados face.

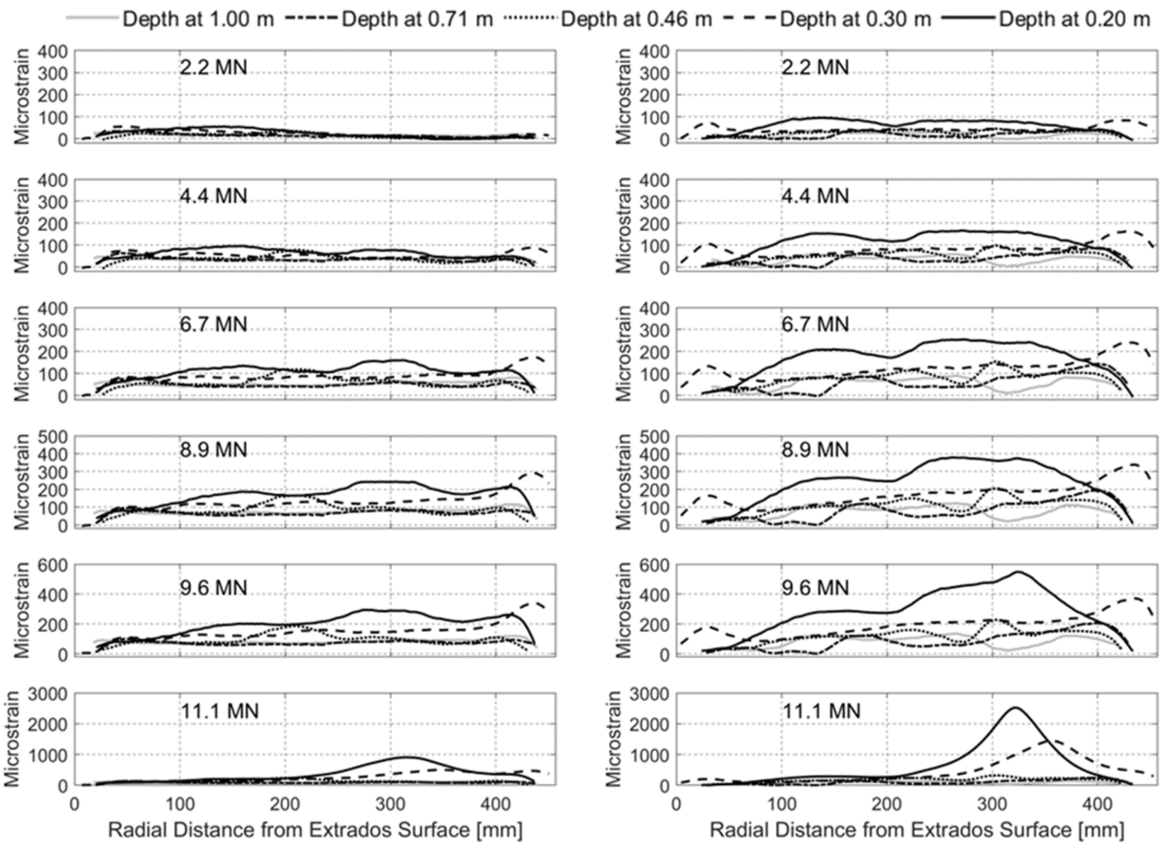

Figure B6-14: Radial strain distribution in radial direction under various load levels.

B6.3. Cracking Response

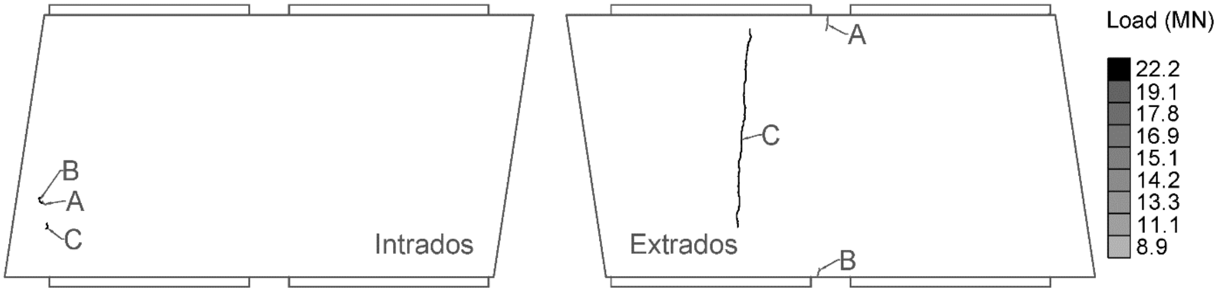

Figure B6-15: Crack propagation for test 6 on intrados face (left) and extrados face (right).

Table B6-2: Crack Width Development for Test 6.

Load (MN)	Intrados Crack Width			Extrados Crack Width		
	A	B	C	A	B	C
4.4	0.00	0.00	0.00	0.00	0.00	0.00
8.9	0.00	0.00	0.00	0.00	0.00	0.00
13.3	0.00	0.00	0.00	0.00	0.00	0.00
17.8	0.00	0.00	0.00	0.00	0.00	0.00
19.1	0.05	0.00	0.00	0.05	0.05	0.00
22.2	0.05	0.05	0.10	0.05	0.10	0.15

Notes:

1. Test 6, a concentric double point load of an SFRC-only segment, showed very little cracking.
2. The segmental tunnel liner in this test showed no observable cracking until 19.1 MN. At this load three small cracks developed: two on the extrados face (Cracks A and B), and one on the intrados face (Crack A). As testing proceeded, these cracks did not grow much in length or width.
3. After testing was taken to 22241 kN (5 million pounds) Crack C propagated on the extrados face of Test 6 and it was the most significant display of cracking on Test 6. It extended nearly the entire length of the segment and was 0.15 mm wide at its widest point.

Appendix C. Detailed radial joint test results

Three joint assemblies were examined through a series of six tests as summarized in Chapter 3. This appendix documents the results from each test. The test matrix is presented below in Table C-1.

Table C-1. Joint rotation test matrix.

Assembly	Test	Description
Assembly 1	Pretest	Calibration and nondestructive evaluation of setup and loading scheme
	1	Joint rotation stiffness evaluation and positive *M-φ* at *N* = 1460 kN/m with radial bolts
	2	Positive $M - \varphi$ at *N*= 674 kN/m axial load with radial bolts
Assembly 2	3	Negative/Positive joint rotation stiffness evaluation at *N*= 674, 1070, 1460, 1850 and 2250 kN/m with radial bolts
	4	Positive $M - \varphi$ at *N*= 2250 kN/m with radial bolts
	4a	Negative $M - \varphi$ at *N*= 2250 kN/m with radial bolts
Assembly 3	5	Negative/Positive joint rotation stiffness evaluation at *N*= 674, 1070, 1460, 1850 and 2250 kN/m without radial bolts
	6	Positive $M - \varphi$ at *N*= 1460 kN/m without radial bolts
	6a	Negative $M - \varphi$ at *N*= 1460 kN/m without radial bolts

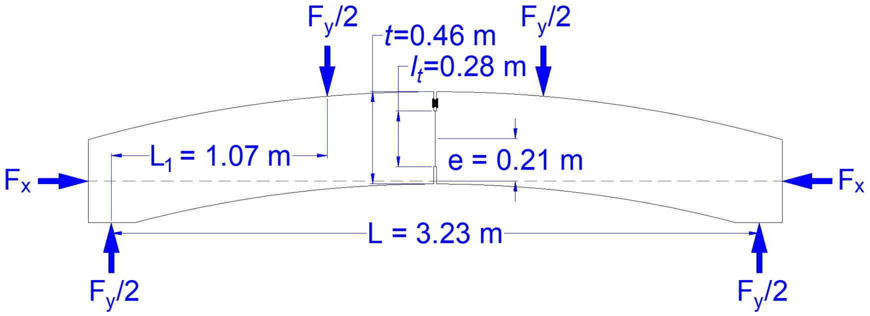

Figure C-1. Load application configuration.

Based on the test configuration, the load application can be simplified as shown in Figure C-1. The vertical load, F_y, provides positive bending moment, and the horizontal load, F_x, due to its eccentricity, provides negative bending moment. The expression of applied moment at the joint can be expressed as:

$$M = \frac{F_y \cdot L_1}{2} - F_x \cdot e \qquad \text{(C-1)}$$

Assemblies were outfitted with linear variable differential transformers (LVDTs) to measure joint openings, rotation meters to compare with LVDT data, displacement transducers for monitoring purposes, surface strain gages for monitoring purposes and bolt strain gages to measure the strain in bolts. The layout of LVDTs (L*i*), vertical and horizontal displacement transducers (VD*i* and HD*i*) and rotation meters (R*i*) are shown in Figure C-2. The bolt strain gages were installed in a 1-mm predrilled hole at the depth of 64 mm from the bolt head.

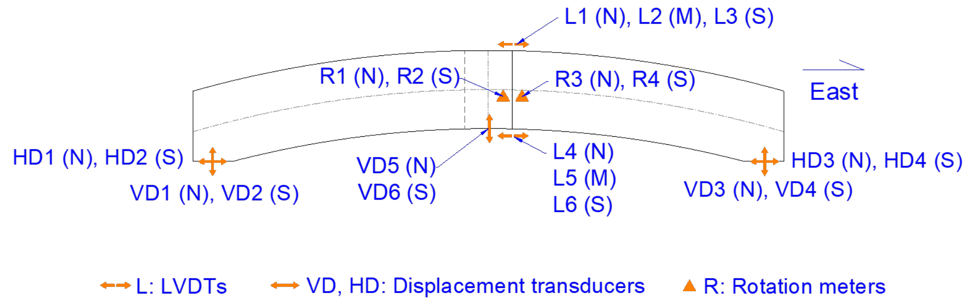

Figure C-2. Assembly instrumentation layout (N: North, M: Middle, S: South).

The rotation was measured through LVDTs. The calculated rotation using LVDT data can be expressed as:

$$\varphi = \frac{1}{3} \cdot \left(\frac{(L_4 - L_1)}{d_1} + \frac{(L_5 - L_2)}{d_2} + \frac{(L_6 - L_3)}{d_3} \right) \qquad \text{(C-2)}$$

where L_1 through L_6 are the displacement measured by LVDTs, and d_1 through d_3 are the distance between top and bottom LVDTs. It is important to note that the joint is at an 8-degree skew. The nonlinear geometric action is not directly examined.

C1. Assembly 1

C1.1. Pretest

The pretest intended to calibrate the load cell and evaluate the viability of the test configuration. The detailed description of this test is presented in Table C-2. Pictures of the assembly are shown in Figure C-3. Two axial load measurement systems were used. The Geokon load cells[14] with readout boxes are vibration wire based, which cannot be recorded by the data acquisition system that records data from resistance based sensors. To obtain real-time axial load data, the axial rods were instrumented with full-bridge strain gages, which were calibrated based on the readings of Geokon load cells. The calibration details are presented in Table C-3 and Table C-4. Linear regression analyses were performed to determine the relationship between the load from the Geokon load cell and millivoltage output of strain gage, as shown in Figure C-4.

---

[14] The manufacturer name is included for informational purposes only and is not intended to reflect a preference, approval, or endorsement of any one product or entity

Table C-2. Description of Test 1.

Assembly No.	1
Test No.	1
Whether Previously Tested	No
Radial Joint Type	J
IJ Segment Serial Number	SG 1903 9939
JA Segment Serial Number	SG 1904 6667
IJ Segment Age at Test Date	1114 Days
JA Segment Age at Test Date	1078 Days
Axial Load	1110 kN/m
Description	Calibration and nondestructive evaluation of setup and loading scheme

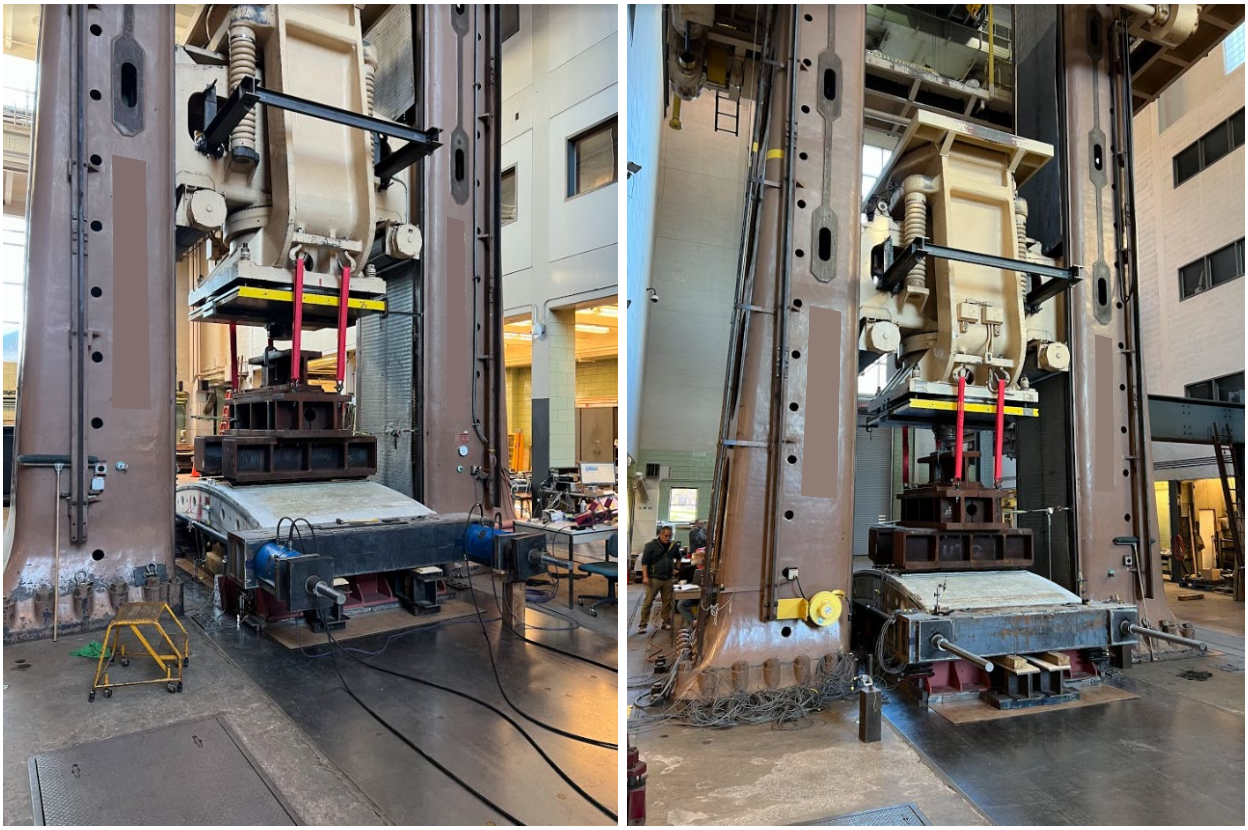

Figure C-3. Assembly pictures of west side (left) and east side (right).

Table C-3. Calibration data of the north rod.

Pressure [MPa]	Load [kN]	Predicted Reading	Geokon Reading	Load [kN]	Rod [mV]
2.07	65	-686	-	-	-
4.14	144	-587	-650	94	-1.45
4.14	144	-587	-640	102	-1.50
9.48	347	-330	-393	298	-3.30
13.10	485	-156	-219	435	-4.58
15.86	590	-23	-40	577	-5.78
15.86	590	-23	-32	583	-5.83
15.86	590	-23	-5	605	-6.00
19.31	721	142	137	717	-7.00
19.31	721	142	149	726	-7.09
22.75	852	308	250	806	-8.30
22.75	852	308	325	866	-8.33
26.20	983	474	493	998	-9.51
26.20	983	474	504	1007	-9.57
29.65	1114	640	671	1139	-10.84
29.65	1114	640	679	1146	-10.79
29.65	1114	640	677	1144	-10.78
29.65	1114	640	673	1141	-10.75
29.65	1114	640	672	1140	-10.73

Table C-4. Calibration data of the south rod.

Pressure [MPa]	Load [kN]	Predicted Reading	Geokon Reading	Load [kN]	Rod [mV]
2.07	67	784	-	-	-
4.14	146	898	860	120	1.48
4.14	146	898	864	122	1.43
9.48	349	1195	1114	294	-0.40
13.10	487	1395	1290	415	-1.67
15.86	592	1548	1365	466	-2.86
15.86	592	1548	1475	542	-2.92
15.86	592	1548	1497	557	-3.05
19.31	723	1739	1644	658	-4.05
19.31	723	1739	1660	669	-4.17
22.75	855	1930	1835	789	-5.38
22.75	855	1930	1840	793	-5.41
26.20	986	2121	2025	920	-6.63
26.20	986	2121	2035	927	-6.70
29.65	1117	2312	2220	1054	-8.03
29.65	1117	2312	2224	1057	-7.96
29.65	1117	2312	2227	1059	-7.98
29.65	1117	2312	2223	1056	-7.96
29.65	1117	2312	2223	1056	-7.93

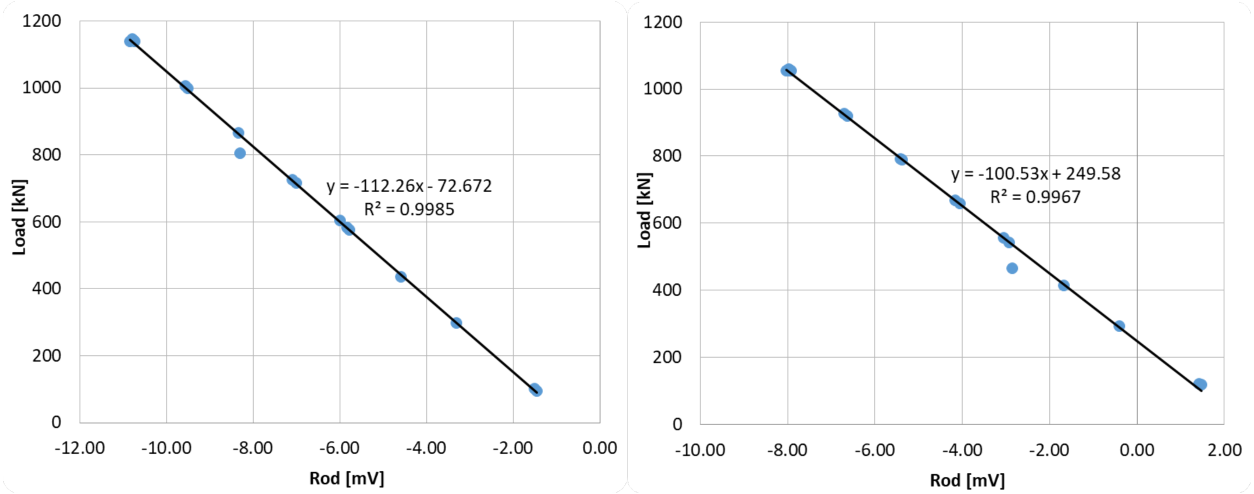

Figure C-4. Linear regression analysis of the calibration data of north rod (left) and south rod (right).

C1.2. Test 1

This test examined the performance of the radial joint of segmental tunnel liner under the demand of flexural and compressive load. The detailed description of this test is presented in Table C-5. Pictures of the assembly are shown in Figure C-3. The data from the experiment is included in the following graphs. This data includes the vertical and axial load measurements as a function of datapoint (Figure C-5), the applied moment history at the center of the joint contact surface (Figure C-6), the rotation history computed using the various measurement techniques noted in the main report (Figure C-7), the bolt strain history (Figure C-8), and the resulting moment – rotation history for the experiment (Figure C-9). Note that the moment – rotation data is processed further and the positive and negative bending performance is presented more clearly in the body of the report. In all cases the data was recorded at 1 Hz, thus for history plots the x-axis corresponds to the test duration in seconds.

Table C-5. Description of Test 1.

Assembly No.	1
Test No.	1
Whether Previously Tested	Yes
Radial Joint Type	J
IJ Segment Serial Number	SG 1903 9939
JA Segment Serial Number	SG 1904 6667
IJ Segment Age at Test Date	1115 Days
JA Segment Age at Test Date	1079 Days
Axial Load	1460 kN/m
Load Case	Joint rotation stiffness evaluation and positive *M*-*φ* at *N* = 1460 kN/m with radial bolts

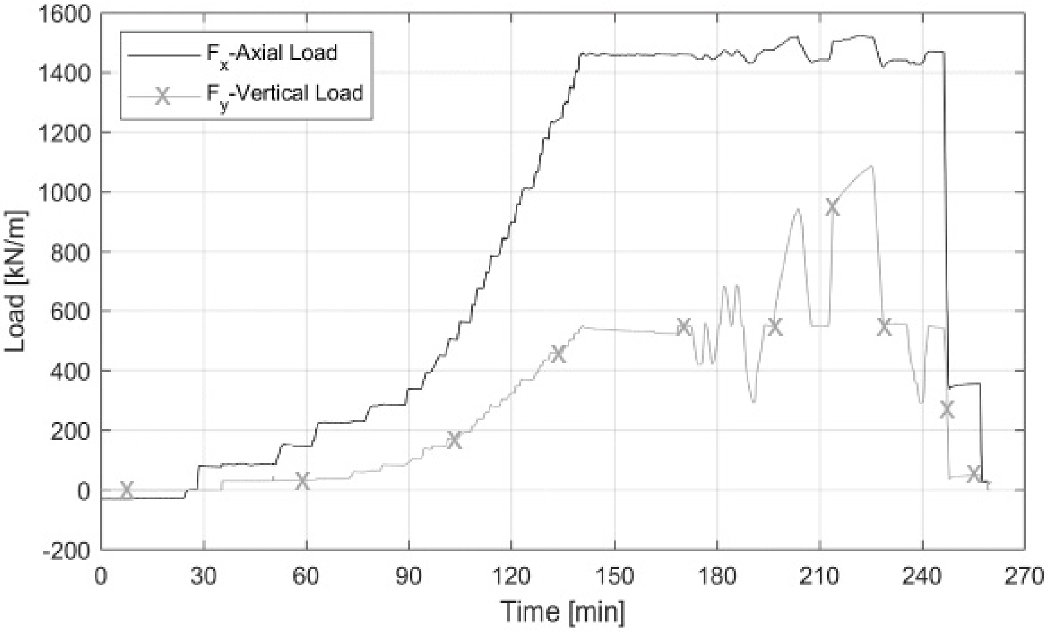

Figure C-5. Test 1 load time histories of total axial and vertical load.

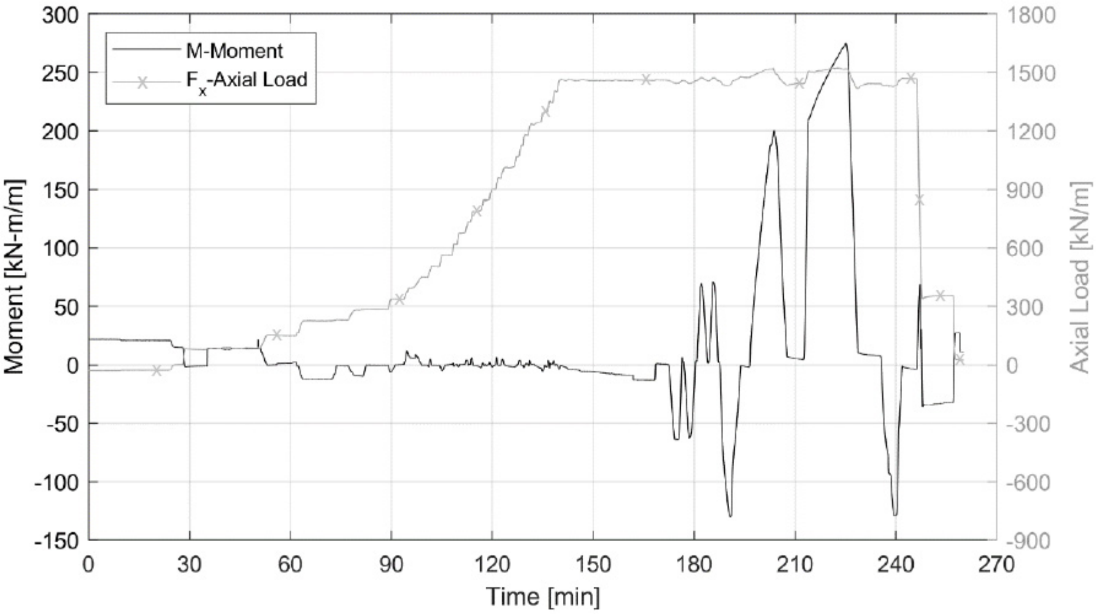

Figure C-6. Test 1 applied moment time history.

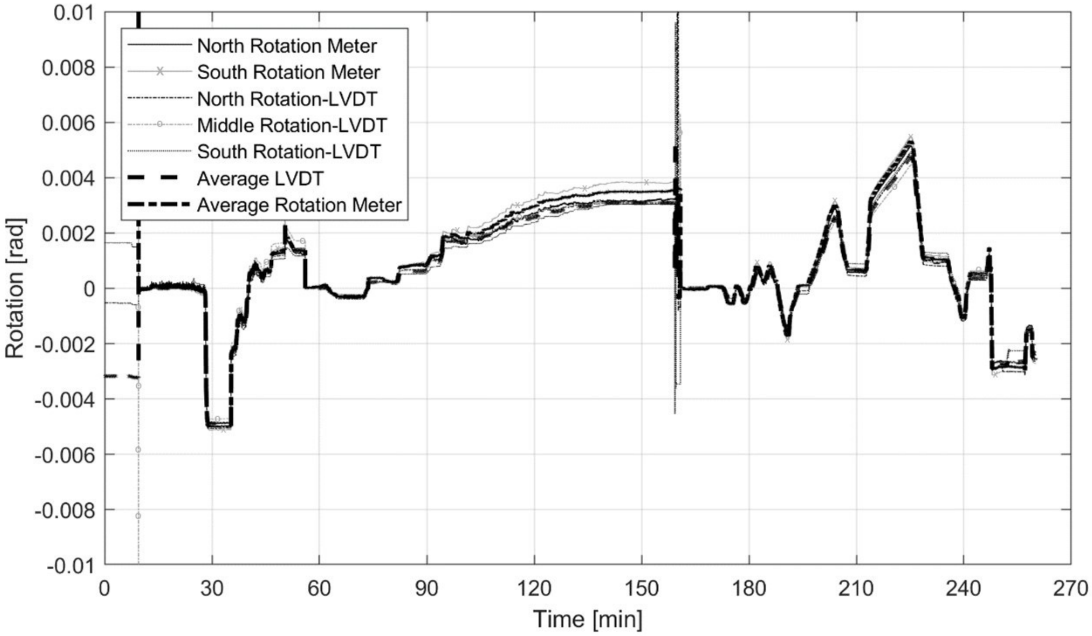

Figure C-7. Test 1 rotation time histories.

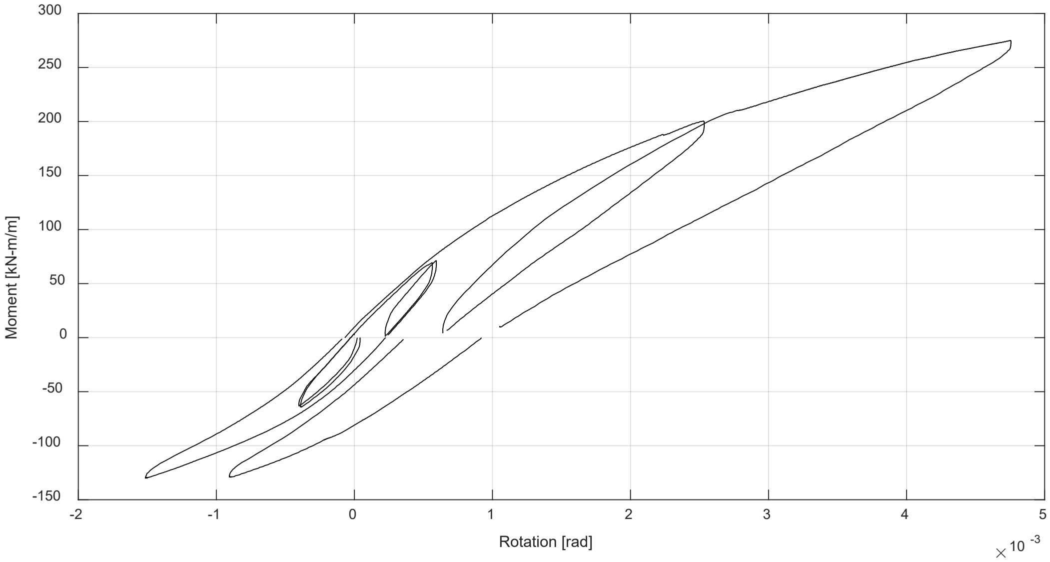

Figure C-8. Test 1 M-φ at N = 1460 kN/m with radial bolts.

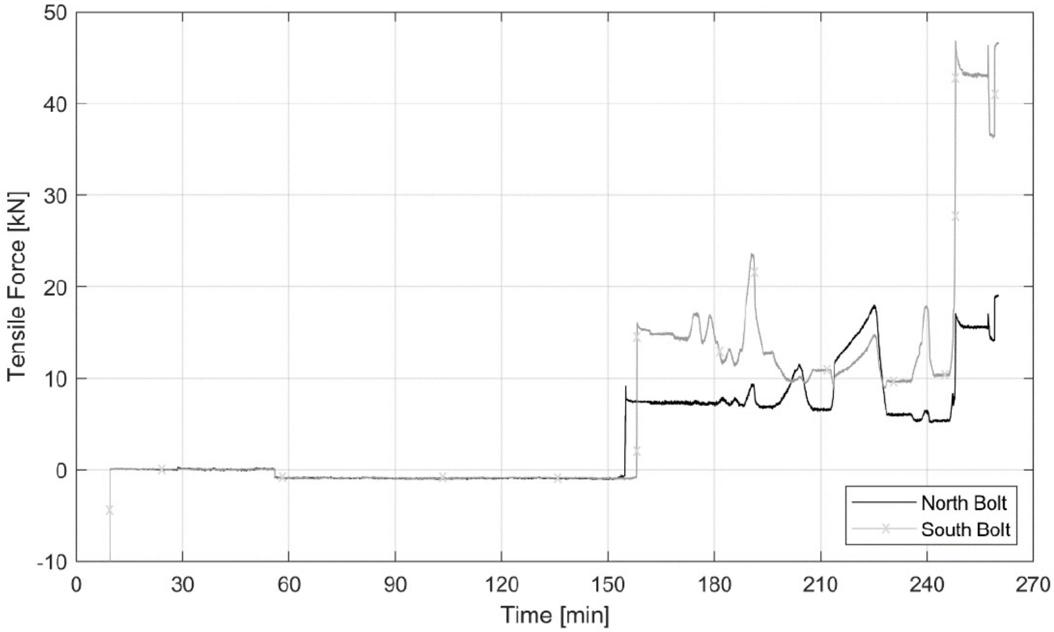

Figure C-9. Bolt strain time histories (measured microstrain multiplied by 0.0972).

C1.3. Test 2

This test examined the performance of the radial joint of segmental tunnel liner under the demand of flexural and compressive load. The detailed description of this test is presented in Table C-6. Pictures of the assembly are shown in Figure C-3. The data from the experiment is included in the following graphs. This data includes the vertical and axial load measurements as a function of datapoint (Figure C-10), the applied moment history at the center of the joint contact surface (Figure C-11), the rotation history computed using the various measurement techniques noted in the main report (Figure C-12), the bolt strain history (Figure C-14), and the resulting moment – rotation history for the experiment (Figure C-13). Note that the moment – rotation data is processed further and the positive and negative bending performance is presented more clearly in the body of the report. In all cases the data was recorded at 1 Hz, thus for history plots the x-axis corresponds to the test duration in seconds.

Table C-6. Description of Test 2.

Assembly No.	1
Test No.	2
Whether Previously Tested	Yes
Radial Joint Type	J
IJ Segment Serial Number	SG 1903 9939
JA Segment Serial Number	SG 1904 6667
IJ Segment Age at Test Date	1116 Days
JA Segment Age at Test Date	1080 Days
Axial Load	1460 kN/m
Description	Positive $M - \varphi$ at N = 674 kN/m axial load with radial bolts

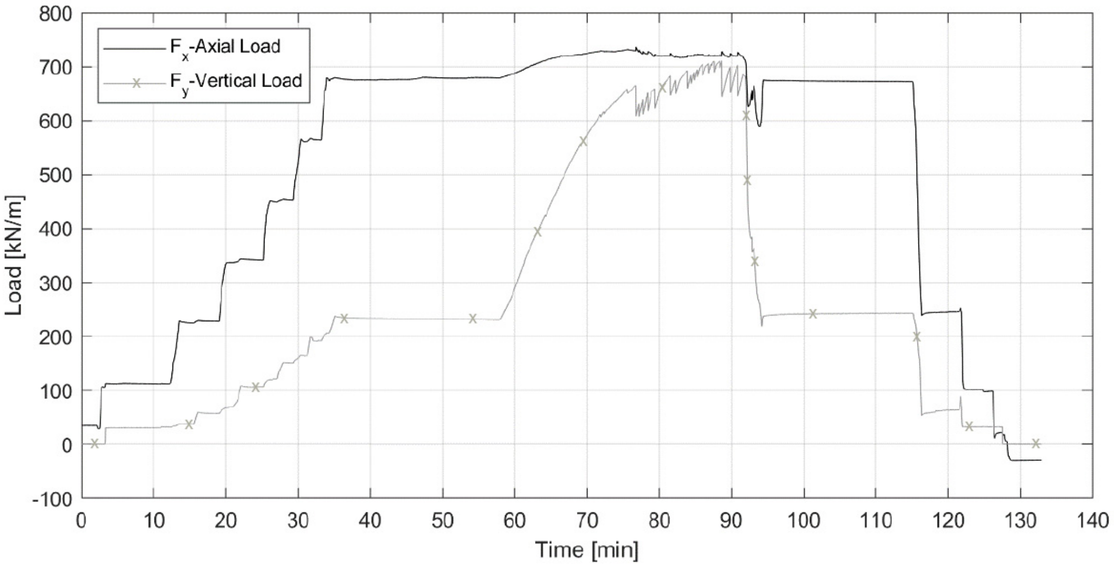

Figure C-10. Load time histories of total axial and vertical load.

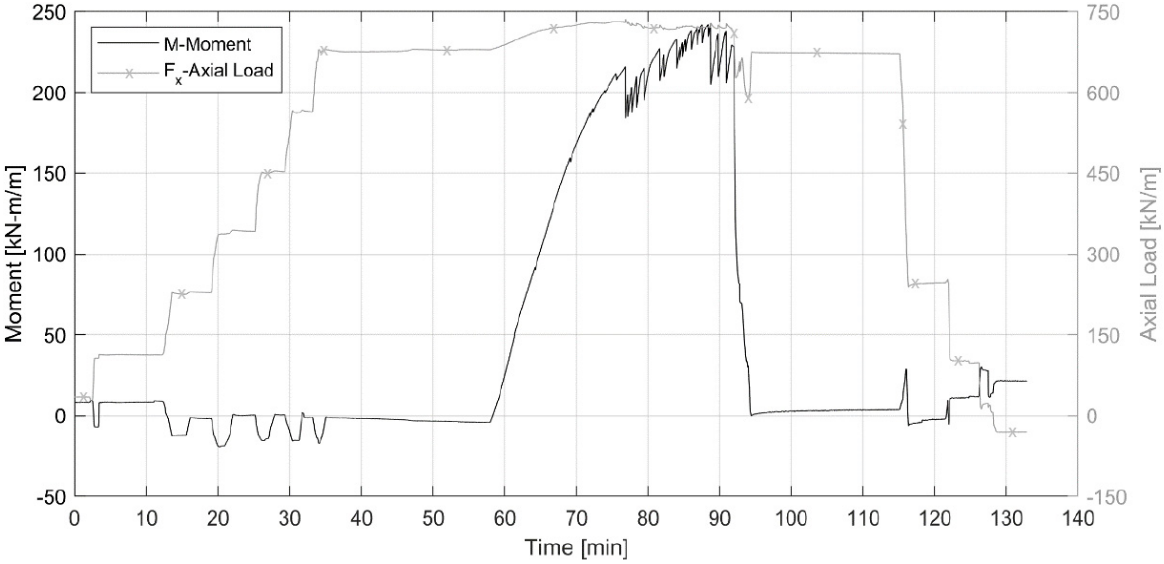

Figure C-11. Applied moment time history.

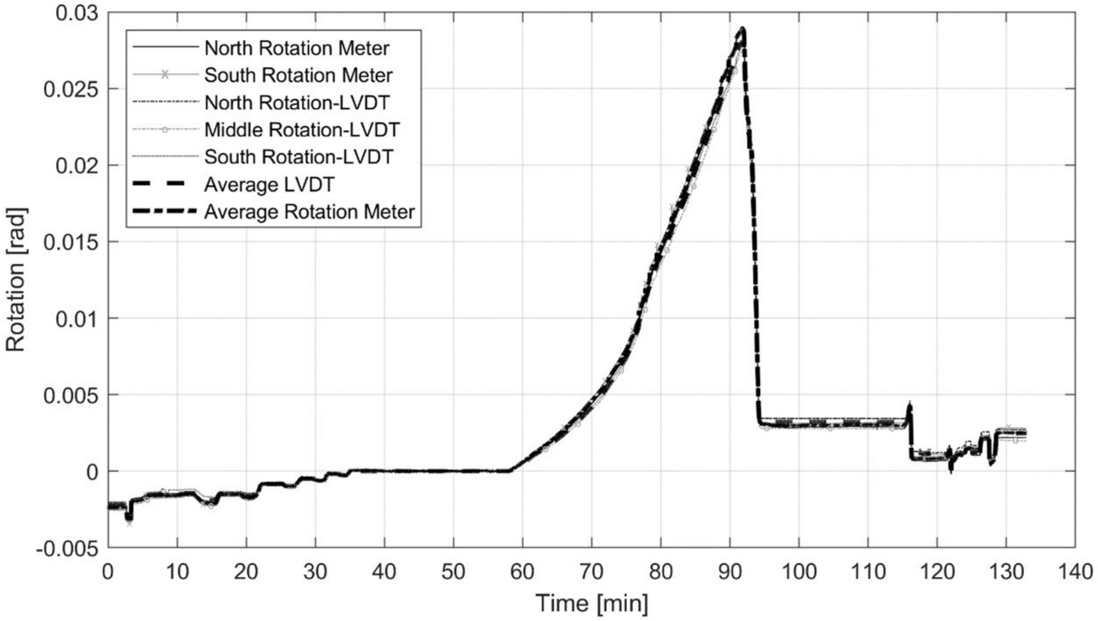

Figure C-12. Rotation time histories.

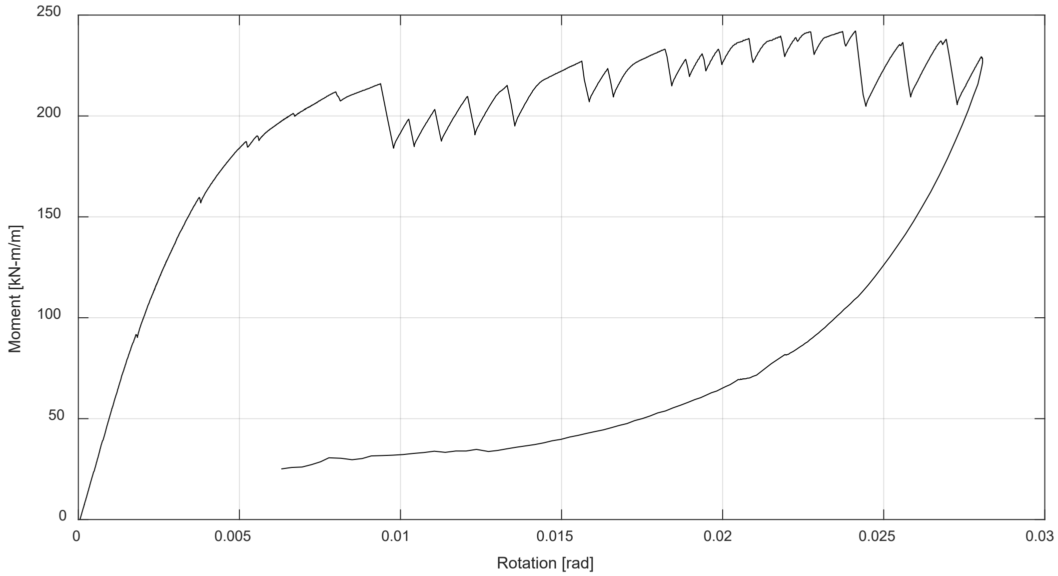

Figure C-13. M-φ at N = 476 kN/m with radial bolts.

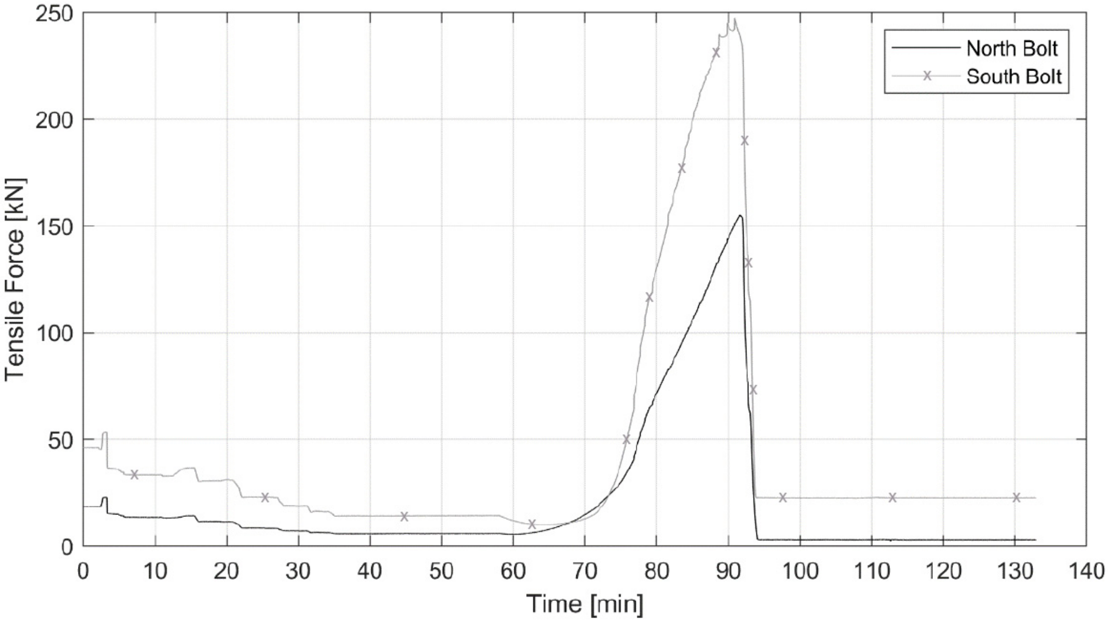

Figure C-14. Bolt strain time histories (measured microstrain multiplied by 0.0972).

C2. Assembly 2

This test examined the performance of the radial joint of segmental tunnel liner under the demand of flexural and compressive load. The detailed description of this test is presented in Table C-7. Pictures of the assembly are shown in Figure C-15. The data from the experiment is included in the following graphs. This data includes the vertical and axial load measurements as a function of datapoint (Figure C-16), the applied moment history at the center of the joint contact surface (Figure C-17), the rotation history computed using the various measurement techniques noted in the main report (Figure C-18), the bolt strain history (Figure C-20), and the resulting moment – rotation history for the experiment (Figure C-19). Note that the moment – rotation data is processed further and the positive and negative bending performance is presented more clearly in the body of the report. In all cases the data was recorded at 1 Hz, thus for history plots the x-axis corresponds to the test duration in seconds.

Table C-7. Description of Tests 3, 4 and 4a.

Assembly No.	2	
Test No.	3	4 and 4a
Whether Previously Tested	No	
Radial Joint Type	J	
IJ Segment Serial Number	SG 1904 6353	
JA Segment Serial Number	SG 1904 0382	
IJ Segment Age at Test Date	1087 Days	
JA Segment Age at Test Date	1120 Days	
Axial Load	674, 1070, 1460, 1850 and 2250 kN/m	2250 kN/m
Description	Negative/Positive joint rotation stiffness evaluation at N = 674, 1070, 1460, 1850 and 2250 kN/m axial load with radial bolts	Positive M-φ at N = 2250 kN/m axial load with radial bolts (Test 4) Negative M-φ at N = 2250 kN/m axial load with radial bolts (Test 4a)

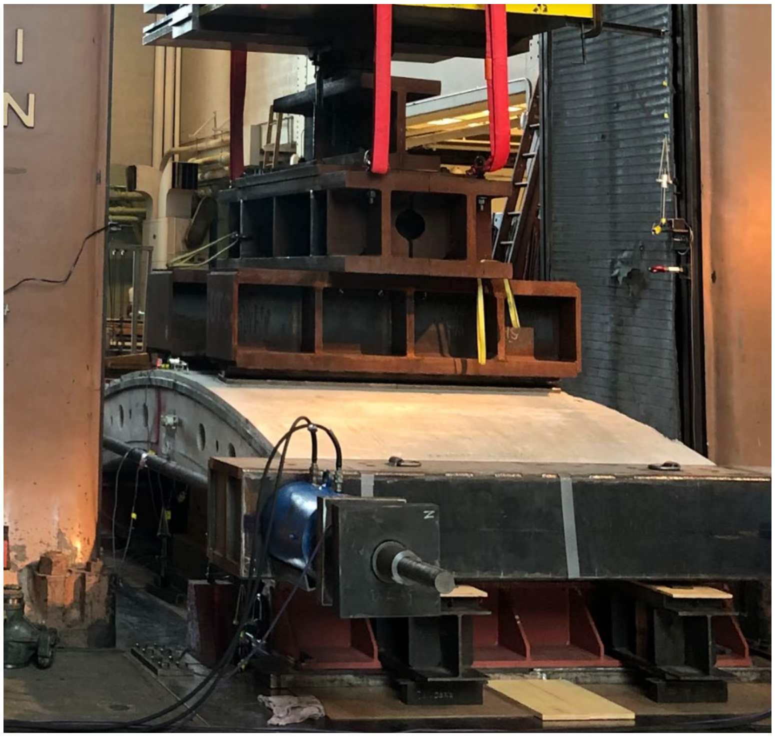

Figure C-15. Picture of radial joint assembly test setup .

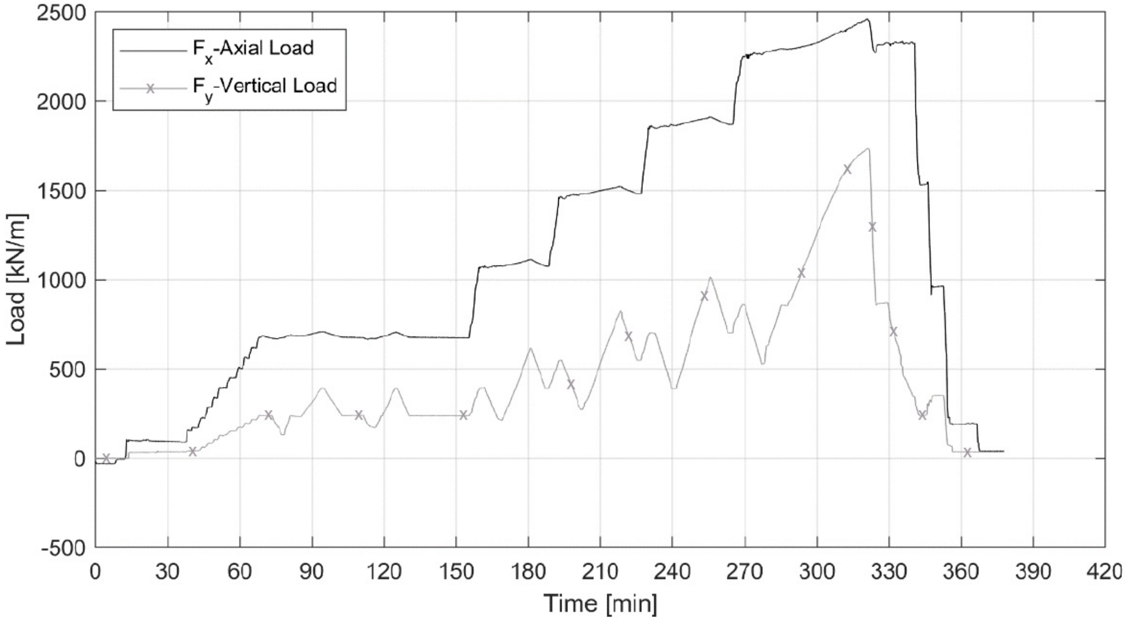

Figure C-16. Load time histories of total axial and vertical load.

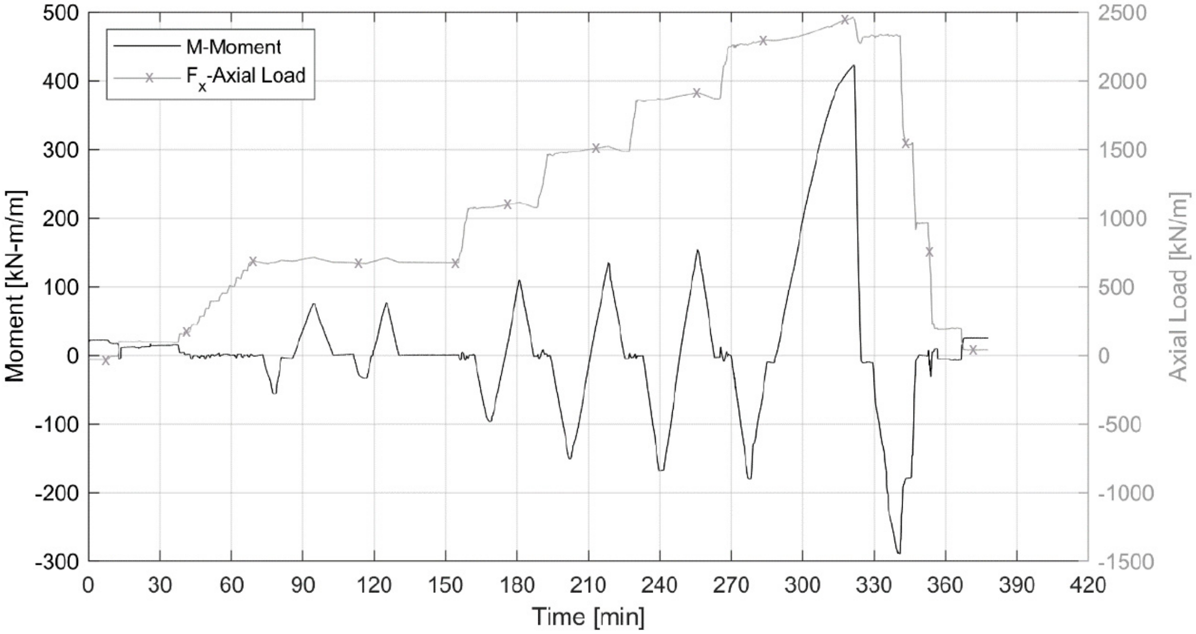

Figure C-17. Applied moment time history.

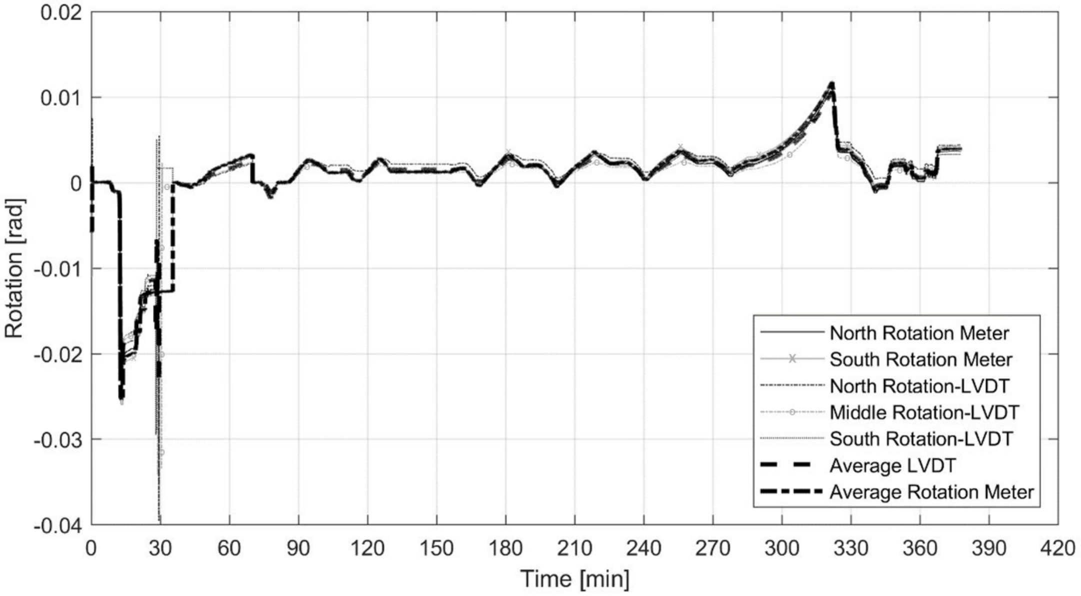

Figure C-18. Rotation time histories.

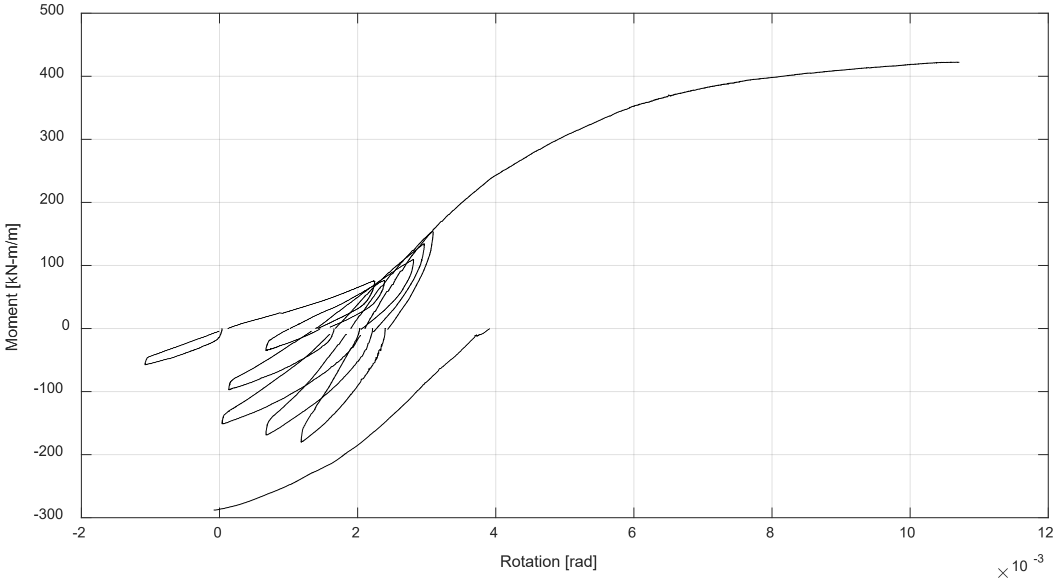

Figure C-19. M-φ of the assembly with radial bolts.

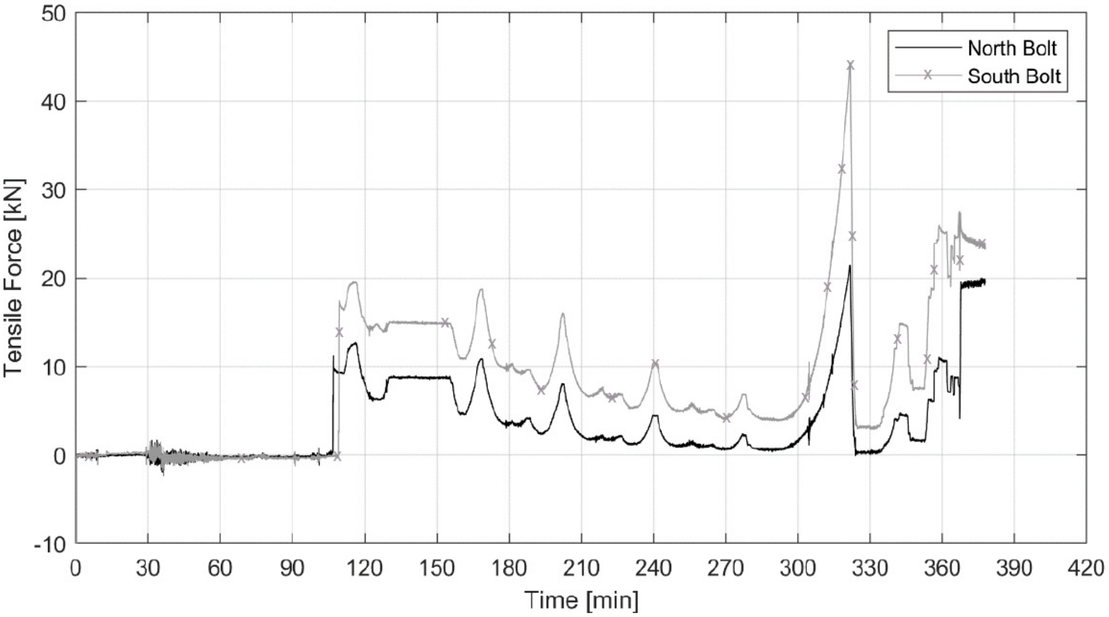

Figure C-20. Bolt strain time histories (measured microstrain multiplied by 0.0972).

C3. Assembly 3

This test examined the performance of the radial joint of segmental tunnel liner under the demand of flexural and compressive load. The detailed description of this test is presented in Table C-8. Pictures of the assembly are shown in Figure C-21. The data from the experiment is included in the following graphs. This data includes the vertical and axial load measurements as a function of datapoint (Figure C-22), the applied moment history at the center of the joint contact surface (Figure C-23), the rotation history computed using the various measurement techniques noted in the main report (Figure C-24), the bolt strain history (Figure C-25), and the resulting moment – rotation history for the experiment (Figure C-24). Note that the moment – rotation data is processed further, and the positive and negative bending performance is presented more clearly in the body of the report. In all cases the data was recorded at 1 Hz, thus for history plots the x-axis corresponds to the test duration in seconds.

Table C-8. Description of Tests 5, 6 and 6a.

Assembly No.	3	
Test No.	5	6 and 6a
Whether Previously Tested	No	
Radial Joint Type	J	
IJ Segment Serial Number	SG 1904 6845	
JA Segment Serial Number	SG 1903 9352	
IJ Segment Age at Test Date	1092 Days	
JA Segment Age at Test Date	1133 Days	
Axial Load	674, 1070, 1460, 1850 and 2250 kN/m	1460 kN/m
Description	Negative/Positive joint rotation stiffness evaluation at N = 674, 1070, 1460, 1850 and 2250 kN/m axial load without radial bolts	Positive M-φ at N = 1460 kN/m axial load without radial bolts (Test 6) Negative M-φ at N = 1460 kN/m axial load without radial bolts (Test 6a)

Figure C-21. Assembly pictures of west side (left) and east side (right).

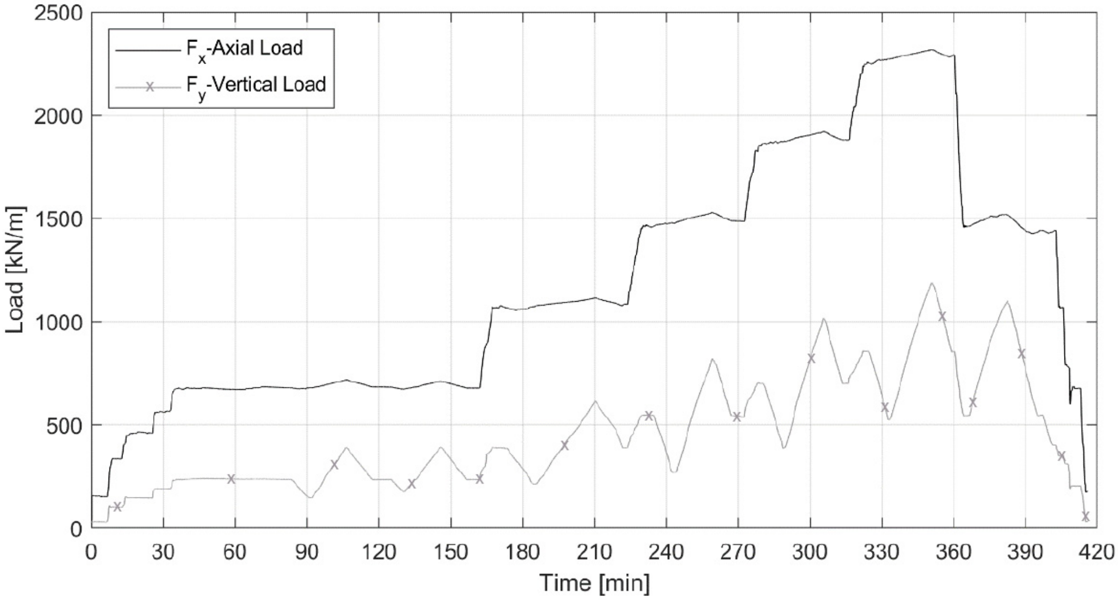

Figure C-22. Load time histories of total axial, F_x and vertical load, F_y.

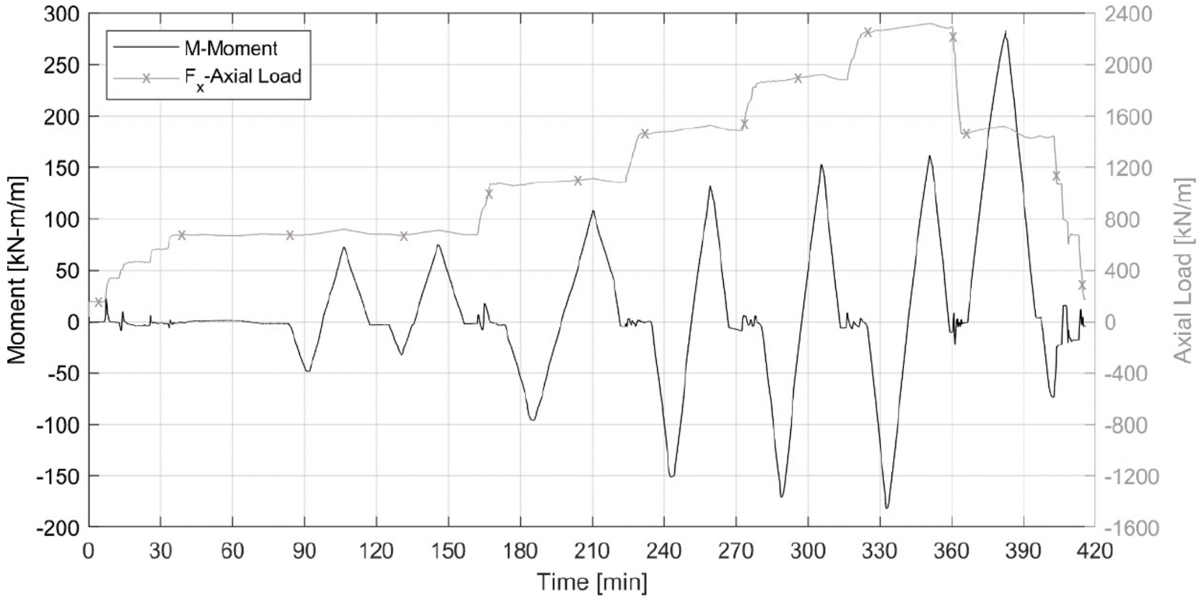

Figure C-23. Applied moment, M, time history.

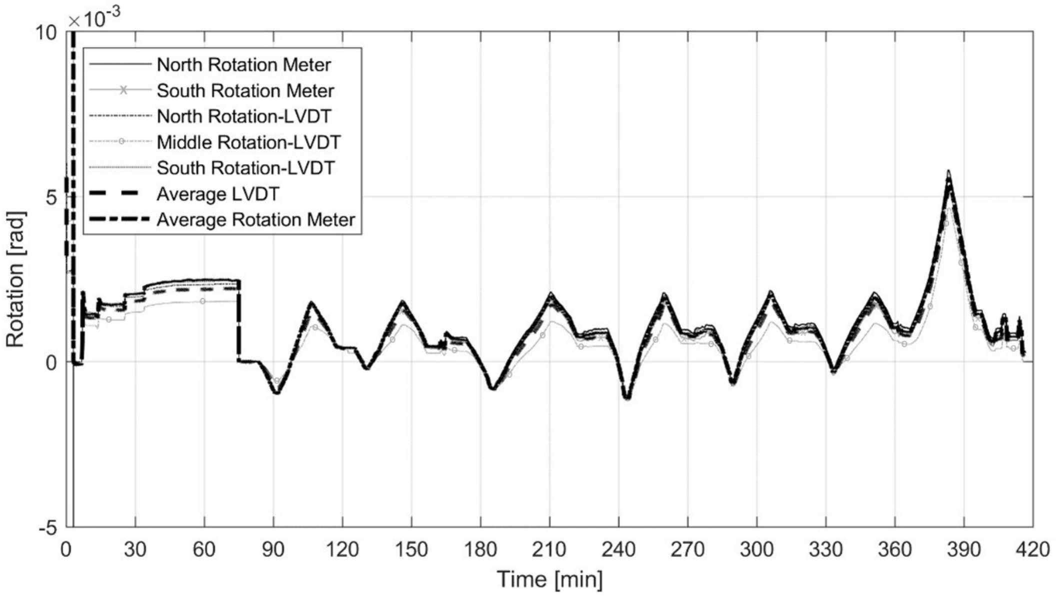

Figure C-24. Rotation, φ, time histories.

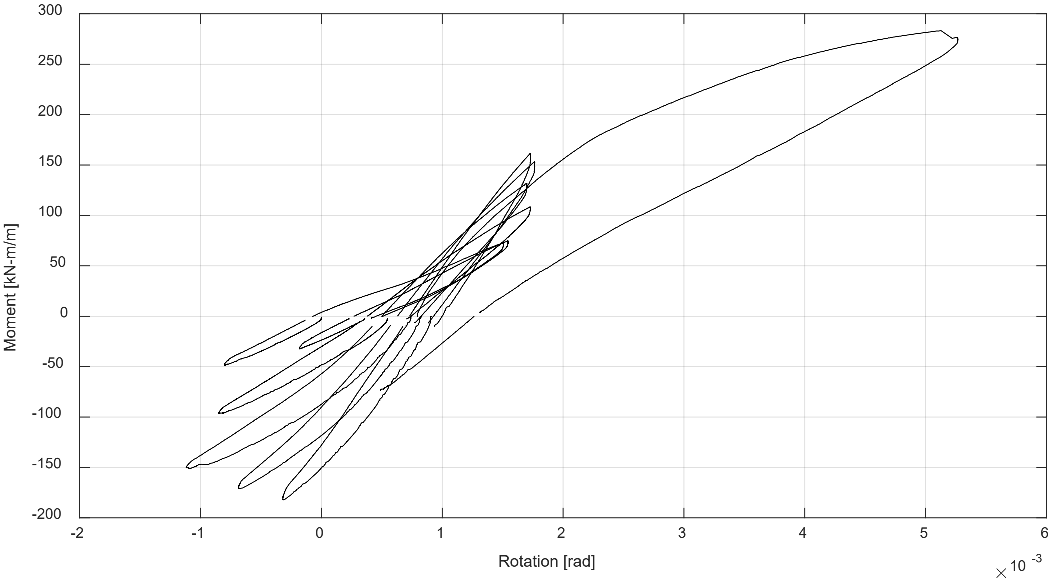

Figure C-25. M-φ of the assembly without bolts.

Appendix D. Radial bolt and gasket tests

D1. Radial Bolt Performance

The radial joint bolt system consists of an embedded socket and an ASTM A325[15] bolt. The specified yield based on a 0.2 percent offset is 480 MPa, the specified tensile strength is 724 MPa. The bolt system is illustrated in Figure D-1.

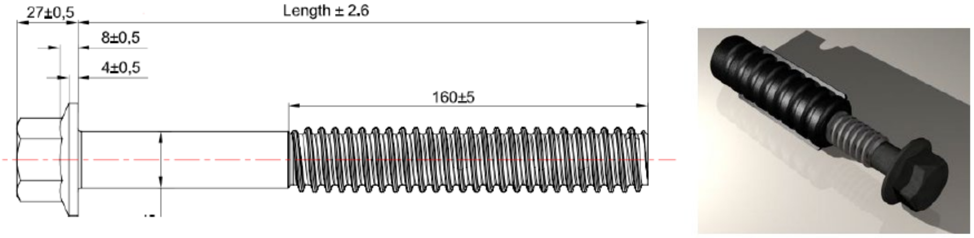

Figure D-1. Radial joint bolt (units: mm).

To assess the ultimate capacity of the radial joint bolt and the capability of the bolt gage a preliminary test on the instrumented bolt was conducted in a universal testing machine. One of the bolts provided with the liners were instrumented with two strain gages. One gage was consistent with the strain gage used on the flexural subassembly tests. In addition, a high elongation strain gage was added on the exterior of the bolt to measure the overall stress-strain performance. The stress-strain performance of the bolt is illustrated in Figure D-2. Based on the one test the tensile strength of the bolt is estimated at 846 MPa, the 0.2 percent offset yield strength is estimated at 630 MPa, both values exceed the specified values. The yield is estimated to occur at a strain of 4570 $\mu\varepsilon$. With a free length from the head of the bolt to the socket of 443 mm the amount of opening at the bolt location at yield can be estimated at 2.0 mm. Assuming rotation about the extrados face (at 229 mm from the bolt), this opening would be equivalent to approximately 0.089 radians. This amount of opening was only achieved on two of the nonlinear tests. Consequently, the bolt can be assumed to be elastic for most of the tests conducted.

---

[15] Use of ASTM A325, Standard Specifications for Structural Bolts, Steel, Heat Treated 120/105 ksi Minimum Tensile Strength, is not a Federal requirement.

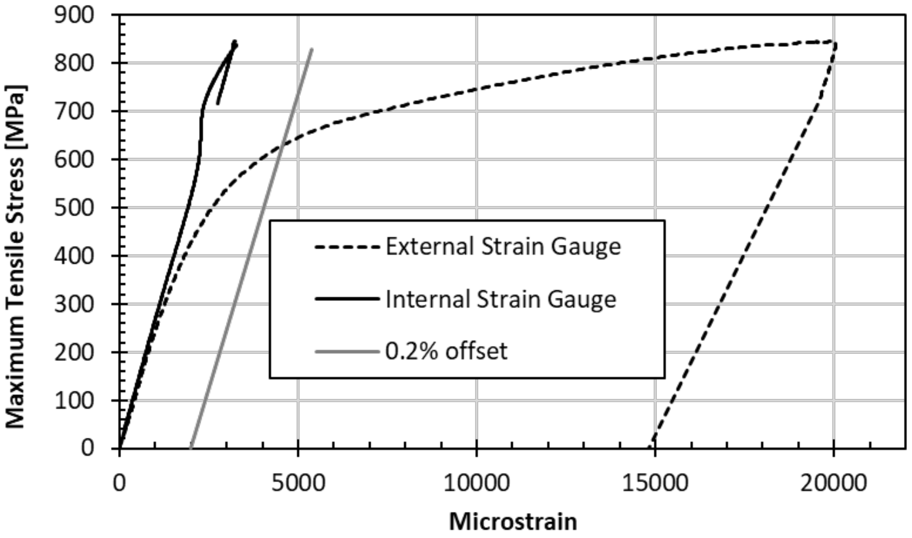

Figure D-2. Uniaxial tension test of the bolt.

D2. Compression Gasket

The stiffness of the compression gasket was examined through compression testing. A 3D printed fixture was fabricated that had the same pocket geometry as the tunnel liners. The height of the 3D printed elements was reduced slightly so that the gaskets could be compressed to a fully closed joint condition without the 3D printed pieces physically coming into contact. A gasket from one of the untested liners was sampled and used for evaluation. The gasket piece measured 76-mm long with the 3D printed plastic supports compressed in a universal testing machine as illustrated in Figure D-3. The gasket was tested eight times to assess repeatability.

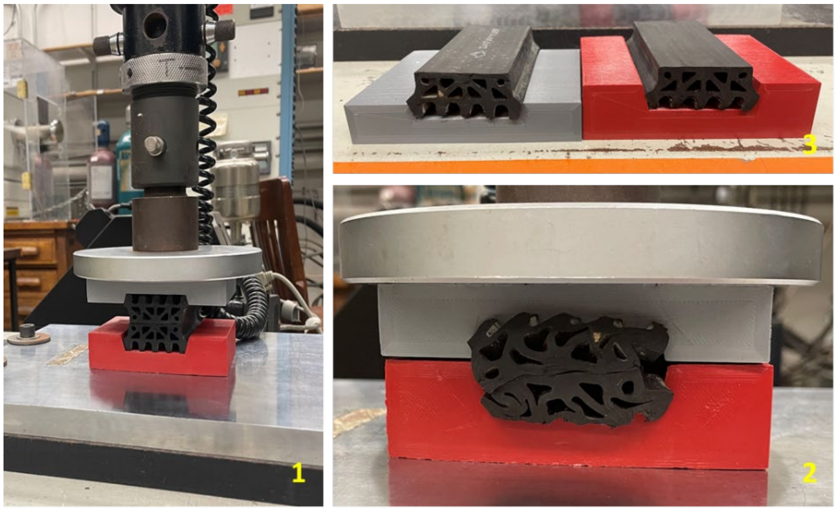

Figure D-3. Gasket Testing.

The load-displacement response of the 76-mm long gasket sample is presented in Figure D-4. As illustrated the first test produced marginally higher strengths. The remaining cycles were consistent. The estimated displacement to close the joint gap is 17.5 mm. At this displacement level the average resistance was 4.02 kN. Consequently, an axial force of 53.2 kN/m should be applied to the gasket to close the joint. This is much lower than the axial load levels applied. The centerline of the compression gasket to the centerline of the joint contact area is 187 mm, so it is estimated that the gasket contributes a negative moment of 9.95 kN-m/m to the joint.

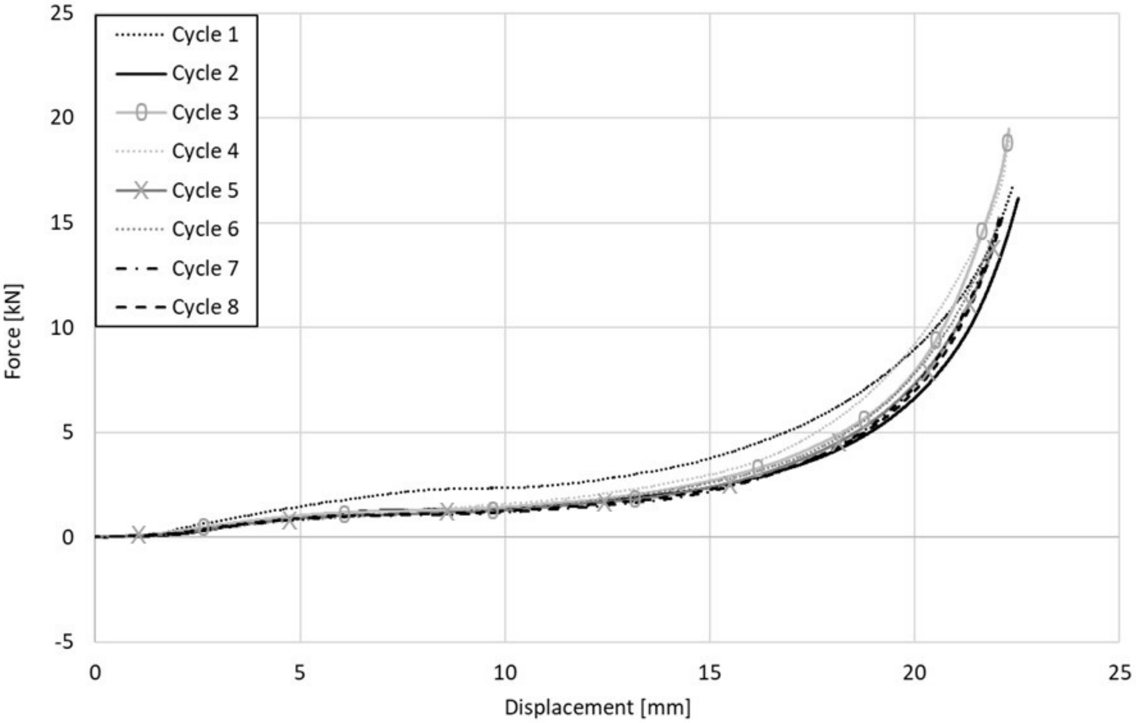

Figure D-4. 76-mm gasket force-displacement curves.